Development of Three-Dimensional Carbon Morphologies and their Surface Modification for Electrochemical Energy Applications

Thesis Submitted to AcSIR

For the Award of the Degree of

DOCTOR OF PHILOSOPHY

In

Chemical Sciences

By

Mr. Pranav K. Gangadharan

Registration Number: 10CC15A26033

Under the guidance of

Dr. Sreekumar Kurungot

CSIR-National Chemical Laboratory

Pune-411008, India

July 2020

CERTIFICATE

This is to certify that the work incorporated in this Ph.D. thesis entitled **"Development of Three-Dimensional Carbon Morphologies and their Surface Modification for Electrochemical Energy Applications"** submitted by **Mr. Pranav K. Gangadharan** to Academy of Scientific and Innovative Research (AcSIR) in fulfillment of the requirements for the award of the Degree of Doctor of Philosophy, embodies original research work under my guidance. I further certify that this work has not been submitted to any other University or Institution in part or full for the award of any degree or diploma. Research materials obtained from other sources have been duly acknowledged in the thesis. Any text, illustration, table etc., used in the thesis from other sources, have been duly cited and acknowledged. It is also certified that this work done by the student, under my supervision, is plagiarism free.

Pranav K. Gangadharan

(Student)

Dr. Sreekumar Kurungot

(Supervisor)

DECLARATION

I, hereby declare that all the experiments in thesis entitled **"Development of Three-Dimensional Carbon Morphologies and their Surface Modification for Electrochemical Energy Applications"** submitted for the degree of Doctor of Philosophy in Chemical Sciences to the Academy of Scientific and Innovative Research (AcSIR) have been carried out by me at the Physical and Materials Chemistry Division, CSIR-National Chemical Laboratory, Pune-411008, India, under the supervision of **Dr. Sreekumar Kurungot**. This work is original and has not been submitted to any other University or Institution in part or full for the award of any degree or diploma.

Mr. Pranav K. Gangadharan
Physical and Materials Chemistry Division,
CSIR- National Chemical Laboratory
Pune-411008, India.

Date: 22-07-2020

Acknowledgement

The most awaited time is reached; I am going to have the prestigious doctoral degree in my life. Thank god for being there for me and strengthening me in tough times. During this amazing journey, I must thank one and all who supported and motivated me; without any of them, this thesis would not have been possible. I take this opportunity to acknowledge them and extend my sincere gratitude for helping me and making this PhD thesis a possibility.

First and foremost, I would like to extend my sincere gratitude to my mentor, my research guide Dr. Sreekumar Kurungot for giving me the opportunity to do the research and providing me invaluable guidance throughout my research. His continuous support, enthusiasm, motivation and vast knowledge helped me a lot during my research days. I am very grateful to him for his immense help in planning and executing the present research work in time. He provided enough freedom in our lab, induced free-thinking capability to design a work, timely monitoring with suitable suggestions and made research life more systematic. His overly enthusiastic and comprehensive view on research and his adamant nature for high-quality research work is inspirable. His way of writing manuscripts is remarkable and he continuously guided me to polish my skills. My master's dissertation under his guidance inspired me, which became a motive to join in his lab. I am very much thankful to the Almighty to give the fortune to be associated with him.

I am thankful to Prof. Ashwini K. Nangia (Director, CSIR-NCL), Dr. Vijayamohanan K. Pillai (Former Director, CSIR-NCL) and Dr. Sourav Pal (Former Director, CSIR-NCL) for providing such a well-established laboratory and to use all the facilities available there. Also, I would like to thank Dr. P.A. Joy, Chair of Physical & Materials Chemistry Division, for providing all the facilities in the Division.

I express my heartfelt gratitude to the Doctoral Advisory Committee (DAC) members Dr. Venkat Panchagnula, Dr. J. Nithyanandhan and Dr. Vinod C. Prabhakaran for their timely and valuable suggestions during my DAC meetings. Despite their busy schedule, they used to review my work progress and made corrections. This significantly helped me to improve the quality of my work.

I would like to take this golden opportunity to express wholeheartedly my gratefulness to my senior Kuttetan. He provides full and unconditional support during my master's project and continued the same during my early research days. He is a role model for me and his dedication and hard work towards research inspired me to pursue the research field after the Master's degree. Under his constant support, I successfully overcame many difficulties and learned a lot.

I would like to thank my former teachers of the Department of Applied Chemistry, CUSAT. A special mention to Dr. K Girish Kumar for his motivation and encouragement. I acknowledge the help and encouragement from my former teachers of Sree Kerala Varma College, Thrissur, Dr. Indira and Dr. Eswary. Again my special regards to all my teachers because of whose teaching at the different stages of education has made it possible for me to complete the important task of my life.

I would like to thank the Student Academic Office (SAO) staff, Chairman Dr. B. L. V Prasad, former Chairman Dr. Mysore Shashidhar, AcSIR Coordinator Dr. Mahesh J. Kulkarni, Mr. Purushothaman, Mr. P. V Iyer, Mrs. Purnima Khole, Ms. Komal, Mrs. Vaishali, Mrs. Poornima and Mr. Santosh, for timely processing my Ph.D. related documents.

I am indebted to my many friends for providing a stimulating and fun-filled environment during my NCL stay. My thanks go in particular to Mavo who helped me a lot. I am ever indebted to Sanoop, Sarath, Vidya, Shibin, Ranjeesh, Shebeeb, Fayis, Vipin, Rashi, Munna, Khayum, Thaha, Sandy, Aswathy, Betsy, Anupriya, Zinoy and Sharathettan. I admire their distinguished helping nature.

My special appreciation goes to my lab mates Rajith, Siddhu, Vidya, Ayesha, Meena, Sachin, Manna, Geeta, Swati, Maria, Shilpa, Gaurav, Raji and Ajmal for their friendship and encouragement for making my lab hours very special, comfortable and memorable.

Most importantly, the deepest thanks from the bottom of my heart should be dedicated to all my senior members of our lab at NCL including Bihagikka, Vishalbayya, Palani anna, Harshitha deedi, Santosh bhai, Roby and Kashyap for their mentoring and care during my initial days in CSIR-NCL.

I would like to thank my former colleagues Sarath, Pandiaraj, Maya, Jeladhara and Ajith.

I extend my sincere word of thanks to Leena chechi, Arunettan, Jijiletan, Rakeshettan, Anumon chettan, Unniyettan, Remya chechi and Prajitha chechi for their brotherly love towards me.

I wish to acknowledge the extensive help from Rajith, Vidya and Ajmal during my research in CSIR-NCL.

My special thanks to Dr. Prasenjit Ghosh (IISER-Pune) and his student Nandha, Dr. Nirmalya Ballav (IISER-Pune) and his students Ranguwar Rajendra and Debashree, Dr. Amit Jaiswal (IIT-Mandi) and his student Prem Singh, Dr. Santosh Babu and his student Ranjeesh K. C for the fruitful research collaborations.

I would like to thank Mr. Gholap, Mr. Shriniwas Deo, Mrs. Rupali, Mr. Venkitesh, Mr. Harsha, Mr. Thushar and Mrs. Sheethal for their support to carry out the materials characterizations.

I express my gratitude towards Ms. Nazrin, Ms. Adrika, Ms. Roshni, Mr. Shijil and the project students who worked with me during their project internship in our lab.

Lastly, I would like to thank my family members, my uncle, my brothers, sisters, cousins and my father who always backed my decisions and provided all kinds of support, moral as well as financial. It was their love, care and patience which inspired me to carry on the research.

Finally, words are not enough to express my feelings for my beloved wife Aathi, for her care, love and support. I lost my courage at several steps but she helped me to stand, face and overcome my problems. I thank her for always being there for me.

List of Abbreviations

Abbreviation	Expansion
ADT	Accelerated Durability Test
AEM	Anion Exchange Membrane
AEMFC	Anion Exchange Membrane Fuel Cell
BET	Brunauer-Emmet-Teller
CA	Chronoamperometry
CE	Counter Electrode
CNT	Carbon Nano Tube
CN_x	Carbon Nitride
CO	Carbon Monoxide
CV	Cyclic Voltammetry
CTR	Charge Transfer Resistance
DFT	Density Functional Theory
ECSA	Electrochemical Active Surface Area
EDAX	Energy Dispersive X-ray Analysis
EIS	Electrochemical Impedance Spectroscopic
GDL	Gas Diffusion Layer
GC	Glassy Carbon

GO	Graphene Oxide
HER	Hydrogen Evolution Reaction
HOR	Hydrogen Oxidation Reaction
HR-TEM	High Resolution Transmission Electron Microscopy
HT-PEMFC	High Temperature Polymer Electrolyte membrane Fuel Cell
ICE	Internal Combustion Engine
LSV	Linear Sweep Voltammetry
LT-PEMFC	Low Temperature Polymer Electrolyte membrane Fuel Cell
MCFC	Molten Carbonate Fuel Cell
MEA	Membrane Electrode Assembly
MF	Melamine Foam
MOF	Metal Organic Framework
NPM	Non-Precious Metal
OCV	Open Circuit Voltage
OER	Oxygen Evolution Reaction
ORR	Oxygen Reduction Reaction
PAFC	Phosphoric Acid Fuel Cell
PBI	Polybenzimidazole
PEM	Polymer Electrolyte membrane
PEMFC	Polymer Electrolyte membrane Fuel Cell
RDE	Rotating Disk Electrode

RE	Reference Electrode
RHE	Reversible Hydrogen Electrode
RPM	Rotations per Minute
RRDE	Rotating Ring Disc Electrode
SEM	Scanning Electron Microscopy
SOFC	Solid Oxide Fuel Cell
STM	Scanning Tunneling Microscopy (STM)
TEM	Transmission Electron Microscopy
TPB	Triple Phase Boundary
UV	Ultra Violet
VC	Vulcan Carbon
WE	Working Electrode
XRD	X-ray Diffraction
XPS	X-ray Photoelectron Spectroscopy
ZAB	Zinc-Air Battery
3D	Three Dimensional

Table of Contents

Chapter 2

Chapter 3

Chapter 4

Chapter 5

Chapter 6

Preface

The energy demand is increasing globally with the rise in population and the exploitation of gradually depleting nonrenewable resources such as fossil fuel is not sustainable anymore. Already, the extensive use of fossil fuels has considerably contributed to the increased content of greenhouse gases in the atmosphere leading to environmental problems such as global warming and climate change. Nature has provided us with several renewable energy resources that are reliable to satisfy our futuristic energy demand. However, as of now, renewable energy technologies are not matured enough to replace well-established fossil fuels. Whatsoever, a gradual transition from fossil fuel to alternative energy storage and conversion technologies is inevitable in the long-run towards the goal of achieving energy sustainability, which demands intense research and investments.

In the current scenario, the generation of electrical energy from carbon-neutral fuels is receiving the utmost importance to satisfy the surplus of energy demand without impacting the ecosystem. In this regard, hydrogen (H_2) as a green fuel is generally accepted to be one of the promising resources for the sustainable and clean production of energy. The high energy density with zero-emission makes H_2 more attractive towards viable production of energy. Hydrogen fuel cells are energy conversion devices conceiving the conversion of chemical energy stored in H_2 to electrical energy. Fuel cells are operated by the consumption of H_2 fed into the anode, which ultimately produces water as the only by-product during the conversion to electrical energy. Due to the emission-free character, fuel cells can be considered as a perfect green energy technology. An ideal fuel cell is expected to operate with high energy efficiency compared to conventional fossil fuel-based internal combustion engine. Among the fuel cell family, polymer electrolyte membrane fuel cell (PEMFC) has gained much attention due to its high efficiency, low operating temperature, and relatively simple structure. Thus, PEMFCs have attained extensive research interest with the prospects of implementing as clean energy source in a wide variety of stationary and portable applications. However, the cathodic oxygen reduction reaction (ORR) in PEMFC is quite sluggish which plummets the energy conversion efficiency. To tackle this intricacy, precious Pt/C catalysts are widely employed in commercial fuel cells. This ultimately leads to a surge in the overall cost of the fuel cell-based appliances and often restricts their widespread adaptation.

To substantiate PEMFCs as a completely green energy technology, the production of H_2 is also required to be occurring through a green process. Steam reforming of natural gas and coal gasification are currently employed for the production of H_2, which expel environmentally hazardous gases to the atmosphere. This dilemma compels us to go after a clean and efficient method for the production of H_2. In this regard, water splitting attained paramount importance as a carbon-neutral strategy for the viable generation of H_2. Electrochemical water splitting is composed of two half-cell reactions; hydrogen evolution reaction (HER) on the cathode and oxygen evolution reaction (OER) on the anode. The efficiency of H_2 production of water electrolyzer is controlled by the complex four-electron transfer OER mechanism which requires high overpotential than HER. Therefore, efficient electrocatalysts are a quintessential part of electrolyzer to enhance the production of H_2 by reducing the overpotential. The precious metal catalyst systems such as Pt/C and RuO_2 have been widely used in the water electrolyzers as both cathode and anode. The high cost, scarcity, and low durability of the catalysts are the obstruction in the path of large scale production of H_2 *via* water electrolysis. The metal-air batteries are another class of electrochemical energy devices that can contribute to the sustainable production of energy along with fuel cells. A bifunctional air electrode is an important component of the metal-air battery. In rechargeable metal-air batteries, ORR and OER occur at the air electrode during the discharging and charging processes, respectively. The limited bi-functional activity of the *state-of-the-art* catalytic systems for ORR and OER is the bottleneck preventing the development of efficient metal-air battery systems.

The electrode reactions occurring in the electrochemical energy devices such as OER, ORR, HER, and HOR are collectively known as the electrochemical water cycle reactions since they involve the formation and dissociation of water. The practical intricacies associated with the commercialization of PEMFCs, metal-air batteries, and water electrolyzers are the lack of availability of efficient electrocatalysts for their operation. Significant efforts are required to crack the barriers associated with the catalyst development. The rational designing of efficient, cost-effective, and durable electrocatalysts for water cycle reactions has recently gained much research attention. The finely tuned three-dimensional (3D) carbon morphologies with active centers to facilitate the kinetics of the reactions are suitable for electrochemical water cycle reactions. The improved mass diffusion along with the structural integrity of the 3D morphologies makes these catalysts more fascinating towards their application in

electrochemical energy devices. In light of this, the present dissertation is focused on the development of 3D carbon morphologies to facilitate the water cycle reaction in energy devices such as PEMFCs, metal-air batteries, and water electrolyzers. The 3D carbon morphologies based on graphene and graphitic carbon were prepared by using melamine foam through environmentally benign methods. The catalytic active sites are induced in the material by the adaptation of different suitable strategies. The desirable properties of the catalysts such as electrical conductivity, active center density, porosity, and morphology are judiciously balanced and optimized in the prepared catalysts to enhance the efficiency of the systems. Organized development of the catalysts with the strong support of the literature review has been carried out to outperform the *state-of-the-art* catalytic systems. The outcomes of the individual chapters are highlighted below;

Chapter 1 starts with an overview of the current global energy scenario and the necessity of an H_2 energy economy. The fundamentals of electrochemical energy devices such as PEMFCs, metal-air batteries, and water electrolyzers are explained in this chapter. In continuation, this chapter introduced the electrochemical water cycle reactions and elaborates mechanisms of ORR, OER, HER, and HOR. The significance of the electrocatalysts for water cycle reactions is explained followed by a brief literature review of the different types of electrocatalysts reported so far for each individual reactions involved in the water cycle. The objectives and scope of the thesis are highlighted at the end of the chapter.

Chapter 2 discusses the development of metal-free electrocatalysts to facilitate the cathodic hydrogen evolution reaction (HER) of water electrolyzers. A simple strategy is proposed to synthesize a metal-free electrocatalyst for HER by a process involving high-temperature annealing of graphene oxide-coated melamine foam. The prepared catalyst possesses both structural and functional advantages with its three-dimensional (3D) interconnected arms of carbon nitride (CN_x) backbone wrapped with nitrogen-doped graphene (N-RGO) sheets (CN_x@N-RGO). The 3D interconnected nanostructure of CN_x@N-RGO retains a wide range of pores and adequate porosity for efficient mass transport. CN_x@N-RGO shows improved HER activity in the acidic condition in comparison to the many reported catalysts. CN_x@N-RGO faces only 193 mV overpotential to achieve a current density of 10 mA cm^{-2}, which is far superior to the previously reported Pt-free systems. With a low Tafel slope of 54 mV dec^{-1}, CN_x@N-RGO

follows a Volmer-Heyrovsky mechanism for HER. Along with a high exchange current density of $34.7 * 10^{-6}$ A cm^{-2}, CN_x@N-RGO exhibits high electrochemical stability in acidic conditions. DFT calculations show that the synergy between CN_x and N-RGO facilitates good electrical coupling between the two moieties and provides optimal binding to H^+ ions on the catalyst that in turn results in a more efficient reduction of hydrogen ion at a substantially reduced overpotential on the carbon atoms adjacent to the heteroatoms.

Chapter 3 explains the development a high performing electrocatalyst (Pt/3DNG) for PEMFC applications by using nitrogen-doped 3D graphene (3DNG) as the support material and an *in situ* grafted active "triple-phase boundary" to more precisely control the formation of the proton-conducting ionomer interface at the active sites. The advantages of the 3DNG morphology were compared by preparing and evaluating the performance characteristics of the Pt supported catalysts based on nitrogen-doped graphene (NRG) and Vulcan carbon (XC- 72) as the supports. With respect to the various performance indicators towards the electrocatalytic activities, Pt/3DNG outperforms the other two catalysts. It possesses the highest mass activity and specific activity of Pt along with enhanced durability among the three catalysts. Considering the 3D morphology of the system, during the electrode fabrication for realistic single-cell evaluation, the concept of *in situ* generation of the proton conducting-ionomer based "active triple-phase boundary" was introduced, which can potentially replace the conventional method of using Nafion ionomer for the electrode preparation. The monomers owing to their small-size can access the pores and inner regions of the 3DNG support, which on UV-curing, undergo polymerization and transform into an ionomer with the extended interfacial network into the nano regimes of 3DNG. Single-cell evaluation of the membrane electrode assembly (MEA) in a high-temperature polymer electrolyte membrane fuel cell (HT-PEMFC) by using phosphoric acid doped polybenzimidazole membrane displayed competency of the present strategy.

Chapter 4 illustrates the synthesis of a platinum-free (Pt-free) oxygen reduction electrocatalyst prepared by the annealing of polydopamine grown melamine foam. The prepared catalyst has a 3D interconnected bilayer network structure possessing the carbon nitride backbone wrapped by graphitic carbon layer bearing iron carbides and nitrides as the active centers (3D-FePDC). Interestingly, the 3D-FePDC catalyst displayed an ORR activity both under acidic and basic conditions. Whereas the ORR performance of 3D-FePDC closely matches that of the commercial

Pt/C in the basic medium, it displays only a low overpotential value of 60 mV under acidic conditions compared to its Pt counterpart. The kinetics of ORR on 3D-FePDC is found to be similar to the four-electron reduction pathway displayed by Pt/C. Testing of a PEMFC in single-cell mode by using 3D-FePDC as the cathode catalyst and Nafion membrane delivered a maximum power density of 278 mW cm^{-2}, which is a promising value expected from a system based on the non-precious metal cathode. Ultimately, as a cost-effective catalyst that can effectively perform irrespective of the pH conditions, 3D-FePDC offers significant prospects in areas like fuel cells and metal-air batteries which work in acidic and/or basic conditions.

Chapter 5 discloses the generation of a bifunctional electrocatalyst which is used as the air electrode in the rechargeable zinc-air battery. A high-performance catalyst that can facilitate both oxygen evolution reaction (OER) and oxygen reduction reaction (ORR) was developed by anchoring a $NiCo_2O_4$ nanowire array on a carbon nanotube sponge (NCS). The 3D morphology of NCS ensured the efficient transport of the reactants and products in the catalyst surface, thereby improving the activity of the material. The prepared catalyst showed remarkable OER activity, requiring an overpotential of 280 mV, which is comparable to that of the noble-metal catalysts. In addition to the noteworthy OER performance, the catalyst performed well with respect to ORR. The total oxygen electrode activity overpotential of the catalyst was found to be 0.83 V, which is lower than that of the commercial electrodes such as Pt/C and RuO_2. A rechargeable Zn-air battery constructed with NCS had an open circuit voltage of 1.42 V, a maximum power density of 160 mW cm^{-2}, and an energy density of 706 W h kg^{-1}. NCS exhibited bifunctional electrocatalytic activity and high stability for both OER and ORR, proving itself a good replacement for the noble metal electrode in rechargeable metal-air batteries.

Chapter 6 Summarizes the major observations and outcomes of each working chapter of the thesis. A brief introduction to the importance of the electrochemical energy devices and the significance of the electrocatalyst development for sustainable energy production is also included. The strategies adopted for developing efficient catalysts for electrochemical water cycle reactions are discussed. A brief discussion of the performance of the synthesized catalysts towards electrochemical reactions is stated. The future scope of the thesis work and the necessity of basic research and evolution needed in the current system for the effective commercialization of the respective electrochemical energy devices are presented in this chapter.

Chapter 1

Introduction: Electrocatalysts for Electrochemical Water Cycle Reactions

The present chapter starts with a short description on the global energy scenario, followed by a detailed discussion on electrochemical energy devices such as fuel cells, metal-air batteries, water electrolyzers, and electrochemical water cycle reactions in general. In the current scenario, overuse of fossil fuels and associated adverse environmental impacts demand the imminent transition to green and sustainable energy storage and conversion technologies. This can be realized by relying on electrochemical energy devices, which can contribute to the elimination of most of the concerns about the fossil fuel-based non-renewable energy technologies. Electrochemical water cycle reactions play a key role in the working of electrochemical energy devices. The hydrogen evolution reaction (HER), hydrogen oxidation reaction (HOR), oxygen reduction reaction (ORR), and oxygen evolution reaction (OER) are the individual reactions involved in the water cycle. The development of highly active and low-cost electrocatalysts for water cycle reaction has paramount importance in the path towards energy sustainability. In this situation, a vast literature survey by analyzing the progress in the path of catalyst development for water cycle reactions is thoroughly discussed in this chapter. The scope and objectives of the thesis are also presented at the end.

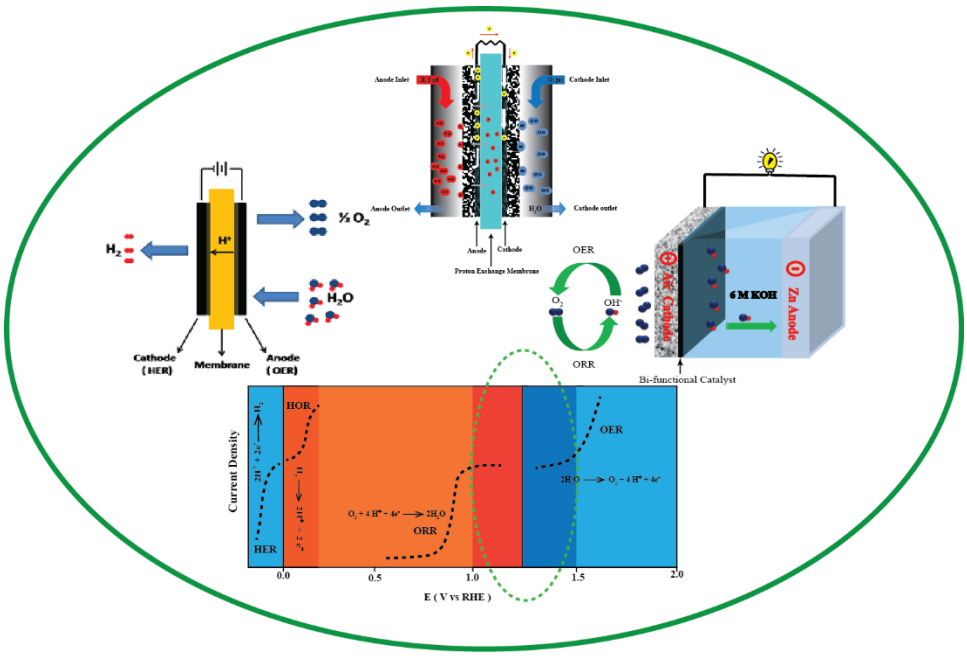

1.1 Introduction

Energy plays a vital role in our daily life and is a key element for the survival of mankind. The socio-economic progress of society is intimately connected with the amount of available energy. The energy demand of the world is increasing exponentially with the rise in population, whereas, our energy production is insufficient to match with the current demand.[1] The scarcity of non-renewable energy resources and their increased demand for energy generation are foreseen to lead the human race to big energy crisis in the nearby future. The energy resources that we are mainly dependent on for our needs are dominated by non-renewable fossil fuels. The extensive use of most of fossil fuels causes the emission of carbon dioxide and other greenhouse gases to the atmosphere driving global warming.[2] To avoid climate change by the overuse of the fossil fuel-based energy resources, a paradigm shift in the global energy policy is inevitable. A convenient balance between the development and environment is essential in the current situation to overcome the present issues of global climate change, which can be attained by the use of sustainable energy production methods. The world needs another industrial revolution in which our sources of energy are affordable, accessible, and sustainable. Energy efficiency and conservation, as well as decarbonizing our energy sources, are essential to this revolution.[3] Despite the significant dependence on the carbon-free renewable energy during the past two decades, it is worth noting that the fraction of energy production from these resources still lags behind that of the fossil fuel-based technologies. **Figure 1.1** depicts the current status of global energy production in terms of quantity and source.[4] It is visible from the figure that, from 1800 to 2018, the use of fossil fuels has shown a gradual increase per year. However, the use of renewable energy resources is less as compared to that of the non-renewable sources. Today, global energy use is growing dramatically due to steadily rising energy demand in developed nations and rapidly increasing demand in emerging economies. Our environment requires the development of high performance, low cost, and environmentally benign energy systems. Therefore, to accomplish more sustainable energy development with sufficient renewable energy and a considerable decline in pollution, more robust and efficient approaches in energy storage/conversion are needed.

Development of economically viable energy conservation methodologies has gained substantial attention in recent years. Nowadays, the conversion of chemical energy into electrical

energy is getting utmost importance due to the significance of the development of sustainable renewable energy systems.[5] In this context, desirable use of electrochemical energy devices such as metal-air batteries, fuel cells, and water electrolyzers, have the potential to substitute traditional energy systems. In the future, hydrogen (H_2), a promising green fuel, could have the potential to emerge as a source of energy by replacing the fossil fuels.[6] In recent years, the search for alternative energy sources has moved from an academic curiosity to an economic necessity. Improved technologies for the production and storage of electrical energy are indispensable for improving the way that society uses energy. Therefore, large-scale research efforts are underway in various locations around the world to develop fuel cells for the direct production of electricity from chemical energy and also to develop supercapacitors and advanced batteries for electrical storage purposes. These new technologies are particularly important to electrical/electronic devices as well as automotive applications.[7]

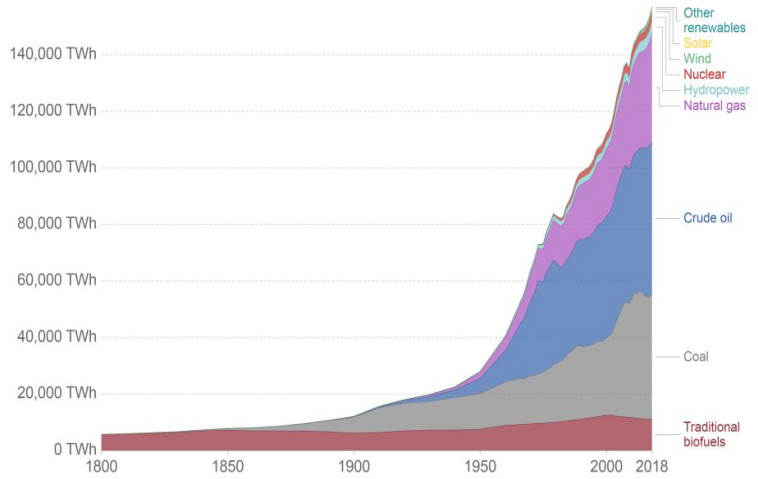

Figure 1.1 *The global energy consumption, measured in terawatt-hours (TWh) per year. (Courtesy: Vaclav Smil (2017). Energy Transitions: Global and National Perspectives. & BPStatistical Review of World Energy).*

1.2 Hydrogen as a future energy source

Hydrogen (H_2) is a fascinating energy carrier and burns cleanly without emitting any environmental pollutants. Hydrogen, with zero carbon content, has been considered as a promising energy carrier to fulfill our needs on future energy applications.[8] H_2 contains an energy density of 33 kWh per kilogram. Compared with the other fuels, such as natural gas and

diesel, H_2 contains two or three times more energy density.[9] Due to its low density and highly flammable nature, the storage of H_2 fuel is an unavailing task. H_2 production is a large and growing industry and 96% of global hydrogen production is based on fossil fuels. At present, the steam reforming method is efficient for the production of H_2. However, H_2 produced through steam reforming process accelerates fossil fuel depletion and carbon dioxide emissions.[10] The large market and sharply rising prices in fossil fuels have also stimulated great interest in an alternate, cheaper means of H_2 production. Hence, we need an alternative method from our renewable source for the production of H_2 and here water plays a crucial role.[11] Water splitting is a hot area of research that can provide a tremendous solution for climate change and is considered as a sustainable method for the production of H_2. The efficient and economical splitting of water provides a new pathway to meet contemporary and future energy demands.[12]

1.3 Fuel cells, metal-air batteries, and water electrolyzers

The electrochemical energy devices such as fuel cells, metal-air batteries, and water electrolyzers can contribute to sustainable energy production in the current global energy scenario. However, more focus should be given in these electrochemical devices to address the current problems associated with their commercialization. The fuel cell is an environmentally friendly energy device, which converts the chemical energy of a fuel into electrical energy without any emission of greenhouse gases.[13] In fuel cells, H_2 is being used as the fuel along with oxygen (O_2) as the oxidant to burn the fuel to release energy. The production of energy from H_2 initiates the establishment of a carbon-free energy economy. In the case of the metal-air battery, electricity generates through a redox reaction between metal and O_2 in the air. Among the many metal-air batteries, Zn-air batteries have received intensive research and development focus because of their high energy density, low cost, and safety. The battery uses Zn, which is an environmentally benign, earth-abundant metal, and the system has higher theoretical energy density than the Li-ion batteries.[14] However, the high overpotential due to the sluggish kinetics of the multistep ORR/OER precludes the practical commercialization of the rechargeable Zn-air batteries. The water electrolyzers are not direct energy devices; however, they have an integral role in the development of sustainable energy and the environment. Currently, we are depending on the fossil fuels for the production of green fuel H_2. However, for achieving the complete green energy economy, we need to ensure the environmentally benign production of the hydrogen. The

water electrolysis is one of the answers to this crisis; it enables environmentally viable production of H_2.[15] The electrochemical reduction of water is an economically feasible and greener approach for the synthesis of H_2.[16] All these energy systems involve two primary reactions, namely, the formation and dissociation of water. Among the different energy systems, Zn-air batteries and fuel cells are set apart by their high energy density.[17] One of the key elements in the pathway of the advancement of the electrochemical energy devices is the suitable catalyst development to drive the operation of devices. Since, the present thesis is focusing more on the catalyst development for polymer electrolyte membrane fuel cell (PEMFC), metal-air battery, and water electrolyzer, a brief discussion on the working principle of these energy devices is included in the following section.

1.4 Fuel cells

The fuel cell is an electrochemical device that converts the chemical energy stored in a fuel into electrical energy by means of electrochemical reactions. The hydrogen and small organic molecules such as methanol, ethanol, and formic acid are being used as the fuel in fuel cells. Since water and heat are the by-products of the fuel cell reactions, it will not contribute to global warming by expelling greenhouse gases to the atmosphere. The fuel cell is invented in 1839 by Sir William Grove (who is often referred to as the 'Father of the fuel cell').[18] The first commercial fuel cells were used in NASA space programs to generate power for satellites and space capsules.[19] Fuel cells have higher efficiency than that of the combustion engines. Unlike an internal combustion engine, the fuel is not combusted in a fuel cell but the energy is being released utilizing electrochemical reactions; this allows the fuel cell to be highly energy efficient.[20] Also, the zero-emission of the green-house gases makes the fuel cells more favorable over the combustion engines. The absence of any moving part in the fuel cells is an added advantage to achieve a high lifetime. As long as the fuel is supplied along with the oxidant, the fuel cell will generate electricity. The heat generated during the fuel cell operation can be used for external purposes, which helps to increase the efficiency of the overall system. A single cell produces an electrical potential of approximately 1.0 V, even though the theoretical potential is 1.23 V.[21] Higher power output can be generated by the combination series of cells. The size of the fuel cell is controlled according to the energy need or by the intended application. The fuel cell consists of two electrodes; a negative anode and a positive cathode separated by an

electronically insulating layer (electrolyte) which conducts the ions. The electrode at which the oxidation of the fuel occurs is the anode and the electrode at which the oxidant is getting reduced is the cathode. An electrolyte is one of the important components of the fuel cell, which separates the electrodes and transfers the electrically charged particles from one electrode to the other.

Table 1.1 *The classification of the different types of the fuel cells.*

	Low Temperature Fuel Cell			**High Temperature Fuel Cell**		
	DMFC Direct Methanol Fuel Cell	**PEMFC Polymer Electrolyte Membrane Fuel Cell**	**AFC Alkaline Fuel Cell**	**PAFC Phosphoric Acid Fuel Cell**	**MCFC Molten Carbon Fuel Cell**	**SOFC Solid Oxide Fuel Cell**
Electrolyte	Proton - Conducting Membrane	Proton/ hydroxyl ion -Conducting Membrane	Caustic Potash Solution	Concentrated Phosphoric Acid	Molten Carbonate	Ceramic
Temperature Range	<100˚C	<160˚C	<100˚C	200˚C	650˚C	800-1000˚C
Fuel	Methanol	Hydrogen	Hydrogen	Hydrogen	Natural gas, Coal	Natural gas, Coal
Power Range	Watts/Kilo watts	Watts/Kilo watts	Watts/Kilo watts	Kilowatts	Kilowatts/ Megawatts	Kilowatts/ Megawatts
Applications	Vehicles, small appliances	Vehicles, domestic supply, power stations	Outer space	Block type heat, power stations	Power plants, combined heat and power	Power plants, combined heat and power

There are several types of fuel cells and each differs in the mode of operation and the electrolyte employed. The basic workings of all the fuel cells are based on the same concept and it can be easily illustrated. But the fabrication of fuel cells for practical applications needs to overcome the following hurdles such as expense, efficiency, and reliability. In this context,

different types of fuel cells are popular with various sizes and shapes to get higher efficiency. The choice of the electrolyte differentiates each fuel cell even though all of them have the same working principle. In those fuel cells, the working components were designed compactly with the electrolyte used. The efficiency and the operating temperature of each type of the fuel cells are decided by the nature of the electrolytes used in it. Alkali, molten carbonate, phosphoric acid, polymer electrolyte membrane (PEM), and solid oxides are the common electrolytes used in the fuel cells. The first three are liquid electrolytes and the last two are solid ones. The liquid fuel cells have a circulation of electrolytes through the device, which requires extra parts to control the electrolyte movement. Each type of fuel cell has its advantages and drawbacks compared to the others. **Table 1.1** gives details of the classification of the different types of the fuel cells.

1.5 Polymer Electrolyte Membrane Fuel Cell (PEMFC)

Polymer electrolyte membrane fuel cell (PEMFC) is the most developed one among the different fuel cells, which has the advantage of small size and high power output. A solid membrane is used as the electrolyte in PEMFCs, which separates the electrodes coated with the active catalyst. Depending on the nature of the membrane and its molecular structure, it conducts either protons (H^+) or hydroxyl ions (OH^-). Based on the ion conduction in the electrolyte, PEMFC can be divided into proton exchange membrane fuel cells (PEMFCs) and anion exchange membrane fuel cells (AEMFCs). Polymer membrane fuel cell cells are low-temperature fuel cells which operate below 160 ^oC, and the working temperature may vary according to the membrane property. Also, in PEMFCs, the electrolyte membrane requires humidification to maintain high ionic conductivity except in the case of the acid doped PBI type membranes. The integral parts of the polymer electrolyte membrane fuel cells are porous electrodes, an electrolyte membrane, gaskets, sub gaskets, bipolar plates, and current collectors. Each component contributes to the overall efficiency of the system; however, the cathode catalyst is most important among them. The membrane electrode assembly (MEA) consists of a sandwiched membrane in between the electrodes, which is generally known as the heart of fuel cells. Apart from the MEA, other parameters like cell design, operating temperature, fuel and oxidant partial pressure, relative humidity, etc. would alter the fuel cell performance. The sluggish ORR is responsible for the majority of the activity losses in the fuel cells. Since, ORR has multi-electron steps, the low reaction rate of ORR leads to higher overpotential in the overall

performance of PEMFCs. This higher overpotential is one of the limiting factors in the energy conversion efficiency of PEMFCs. Also, the cost of the catalyst and other components used in the fuel cells hinders their prospects for widespread commercialization. Besides, highly expensive platinum (Pt) catalyst used in the electrodes of the commercial fuel cells covers almost 50 % of the total cost of the fuel cells. Other parts like bipolar plates, gas diffusion layer (GDL), current collectors, and membrane also contribute to the high price of the fuel cell system. Hence, the rational designing of all the components is required in the fuel cells to increase their performance and to reduce the cost.

1.5.1 Proton Exchange Membrane Fuel Cell (PEMFC)

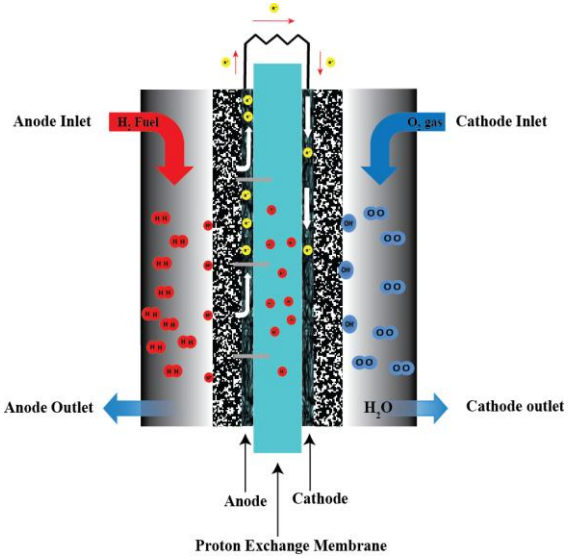

Figure 1.2 *Schematic illustration of the working principle of the proton exchange membrane fuel cell (PEMFC).*

Proton exchange membrane fuel cell (PEMFC) consists of a proton-conducting membrane (PEM) as a solid electrolyte in between the cathode and the anode. A PEMFC is typically fueled with pure H_2 at the anode, while O_2 or air is fed to the cathode. The H_2 is oxidized at the anode to produce positively charged protons and negatively charged electrons. The proton passes through the PEM to the cathode side whereas the electrons travel along an external circuit. At the cathode, O_2 is reduced by the electrons and combined with the protons to produce water and heat. Nafion, acid doped PBI, etc. are commonly used as the proton conducting membranes in

PEMFC. Some of the membranes required humidification for the fast conduction of protons through the membrane. The electrode reactions of a PEMFC are represented as below:[22]

At Anode: $2H_2 \longrightarrow 4H^+ + 4e^-$ ($E° = 0.00$ V) (1.1)

At Cathode: $O_2 + 4H^+ + 4e^- \longrightarrow 2H_2O$ ($E° = 1.23$V) (1.2)

Overall: $2H_2 + O_2 \longrightarrow 2H_2O$ ($E°$ cell = 1.23 V) (1.3)

1.5.2 Anion Exchange Membrane Fuel Cell (AEMFC)

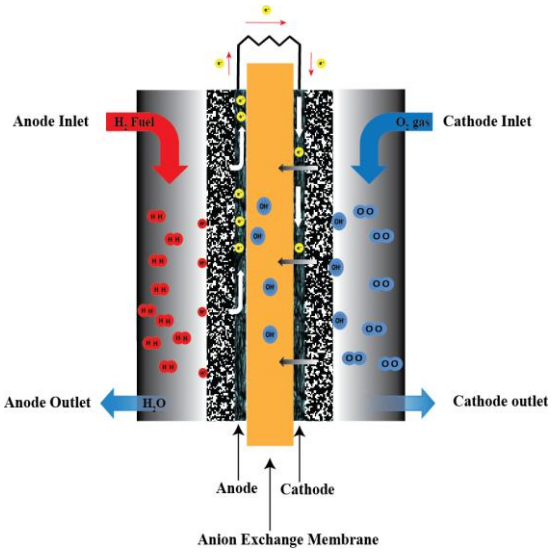

Figure 1.3 *Schematic illustration of the working principle of the anion exchange membrane fuel cell (AEMFC).*

In anion exchange membrane fuel cells (AEMFCs), hydroxyl ion-conducting membrane (anion exchange membrane (AEM)) is used as the solid electrolyte between the electrodes. The electrode reaction in AEMFC is quite different from that of PEMFC. At the cathode, hydroxyl ions (OH^-) are produced by the reduction of molecular oxygen. The OH^- ions produced transport towards the anode side through AEM and combine with the proton to form water. Electrons generated at the anode by the oxidation of H_2 travel through the external circuit towards the cathode and facilitating the oxygen reduction at the cathode. One of the drawbacks of AEMFC

compared to PEMFC is the lack of higher ionic conductivity of the membranes. The electrode reactions of AEMFC are given below:[23]

At Anode: $H_2 + 2OH^- \longrightarrow 2H_2O + 2e^-$ ($E° = 0.83V$) (1.4)

At Cathode: $½\ O_2 + H_2O + 2e^- \longrightarrow 2OH^-$ ($E° = 0.40\ V$) (1.5)

Overall: $H_2 + ½\ O_2 \longrightarrow H_2O$ ($E°\ cell = 1.23\ V$) (1.6)

1.6 Polymer Electrolyte Membrane (PEM)

Proton exchange membrane (PEM) is the important component in PEMFCs. PEM has high proton conductivity and electrically insulating. The advantage of using the PEM is that it has very good chemical/thermal stability, excellent mechanical properties, and low permeability of fuel molecules. It allows only protons (H^+) to transport from the anode to the cathode. The chemical structure of a solid polymer electrolyte membrane has two parts. The hydrophobic backbone chain and the hydrophilic functional groups forming continuous interconnected channels for proton conduction.[24] The proton transfer would occur through this channel either through the 'Grotthuss mechanism' or 'Vehicle mechanism'.[25] The transfer of proton between the hydronium ions occurs through the hydrogen bond in the Grotthuss mechanism. However, the vehicle mechanism involves the complete migration of the hydronium ions through the conduction channel. The proton conduction is faster in the Grotthuss mechanism compared to Vehicle mechanism. The polymer membranes also separate the anode and cathode reactants and acts as an insulating layer providing high ionic conductivity. Also, they are resistant to the temperature changes and reactive chemicals. Nafion, a high proton conducting membrane with a crystalline structure resembling that of Teflon, is being used in PEMFCs. Nafion is still relatively expensive. PEMFC industry is actively searching for more affordable alternatives. Recently, more research works are being carried out on acid doped polybenzimidazole (PBI) as the membranes in PEMFCs. Depending upon the use of the electrolyte and its operating temperature, the PEMFC is classified into two types, low-temperature PEMFC and high-temperature PEMFC. The low-temperature PEMFC (LT-PEMFC) needs the humidification and the proton exchange membrane must be hydrated throughout the operation and it operates below 80 ^oC. Here, the perfluoro sulfonic acid based membrane (Nafion) is generally used as an electrolyte which acts

as a water holder and helps to transport the proton. The high-temperature PEMFC (HT-PEMFC) is operated at around 160-200 ^{o}C in which phosphoric acid doped PBI (polybenzimidazole) is used as an electrolyte. The phosphoric acid acts as a proton transporter whereas PBI as a matrix to hold the acid. The main advantage of HT-PEMFC is its high CO tolerance.

1.7 Advantages of Polymer Electrolyte Membrane Fuel Cells

Compared to the other energy devices, a PEMFC has its own advantages. The PEMFCs are clean alternative energy systems for internal combustion engines (ICE) in the aspects of energy density, cost-effectiveness, and durability. Since a PEMFC does not use conventional fuels, the system eliminates the pollution caused by the burning of fuels like oil or gas, and the only byproduct formed is water. The H_2 produced from the electrolysis of water can be used further and it ensures the complete green energy production. This product enhances the distribution of the fuel and the attractive part is its higher efficiency than the petroleum based or gas engines. The maintenance of PEMFC is very simple compared to the other energy devices. PEMFC is found to be more convenient due to the absence of movable parts and it is completely noise-free. The absence of combustion and moving parts means that PEMFC technologies are expected to provide much-improved reliability over traditional combustion engines. The LT-PEMFCs have low heat transmission which makes them ideal for military applications. At the same time, the installation of smaller stationary PEMFCs leads to a more stabilized and decentralized power grid. Operating duration is much longer than that with batteries since, doubling the operating time needs only doubling the amount of the fuel and not the doubling of the capacity of the unit itself. The solid electrolyte reduces the corrosion and electrolyte management problems in PEMFC, which helps to achieve a high lifetime.[26]

1.8 Zinc-Air Battery

Metal-air batteries, especially zinc-air batteries, have the potential to deliver larger energy density at lower production cost than that of the other available batteries. Zn-air batteries have various applications in electronic devices since, their size can be adjusted according to the need. Size of the Zn-air batteries varies from a button cell to a large grid battery. It can be used in hearing aids, film cameras, electric vehicles, etc. Even though it is termed as the battery, it has

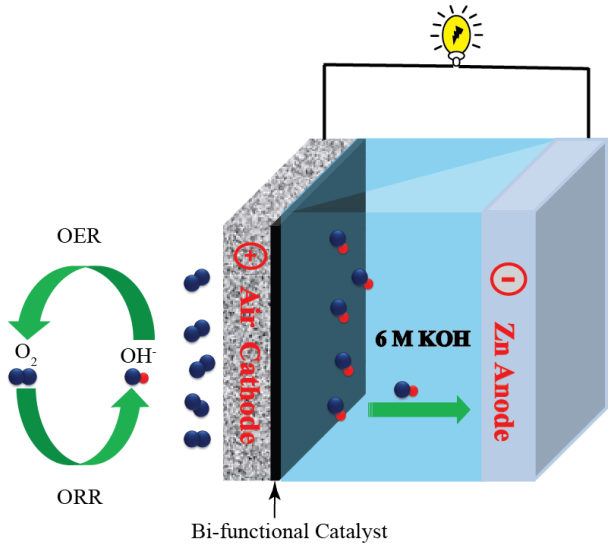

Figure 1.4 *Schematic illustration of the rechargeable zinc-air battery.*

some similarities with the functioning of fuel cells along with the battery features. Here, Zn is used as the fuel and O_2 is used as the oxidant, which controls the reaction rate. Since molecular oxygen is used as the active material in Zn-air batteries, the system delivers a higher energy density. In the Zn-air battery, the oxygen evolution reaction (OER) and oxygen reduction reaction (ORR) take place at the air electrode during the charging and discharging processes, respectively. The Zn-air batteries are matured technologies; their further development is hampered by the lack of low-cost and robust bifunctional catalysts for ORR and OER.[27-28] A rechargeable Zn-air battery is schematically illustrated in **Figure. 1.4**, which is composed of three main components: a Zn metal anode, an alkaline electrolyte, and an air cathode (usually a porous and carbonaceous material). In the discharging process, the O_2 supplied at the air cathode undergoes reduction to form hydroxyl ions. As-generated hydroxyl ions diffuse towards the anode side of the battery and react with the Zn ions, which are generated by the anodic oxidation of the Zn electrode to produce the intermediate zincate ($Zn(OH)_4^{2-}$) ions. The as-formed intermediate further decomposes into zinc oxide (ZnO) at a supersaturated concentration. During the charging of the battery, reverse reactions occur at the respective electrodes, *i.e.*, OER will occur at the air electrode interface with the release of O_2, and the generated ZnO gets redeposited from the electrolyte at the anode. The reactions produce a theoretical voltage of 1.65 V; however, due to the overpotential in the electrode reaction, the obtained voltage would reduce in practical cells.[29] The associated electrode reactions of a Zn-air battery are given below:

Discharge

Anode: $Zn + 4OH^- \rightarrow Zn(OH)_4 + 2e^-$ (1.7)

$Zn(OH)_4^{2-} \rightarrow ZnO + H_2O + 2OH^-$ (1.8)

Cathode: $O_2 + 2H_2O + 4e^- \rightarrow 4OH^-$ (1.9)

Overall reaction: $2Zn + O_2 \rightarrow 2ZnO$ (1.10)

Recharge

Anode: $ZnO + 2H_2O \rightarrow Zn(OH)_2 + H_2$ (1.11)

$Zn(OH)_4^{2-} + 2e^- \rightarrow Zn + 4OH^-$ (1.12)

Cathode:

$4\ OH^- \rightarrow O_2 + 2H_2O + 4\ e^-$ (1.13)

Overall reaction: $2ZnO \rightarrow 2Zn + O_2$ (1.14)

1.9 Water Electrolyzer

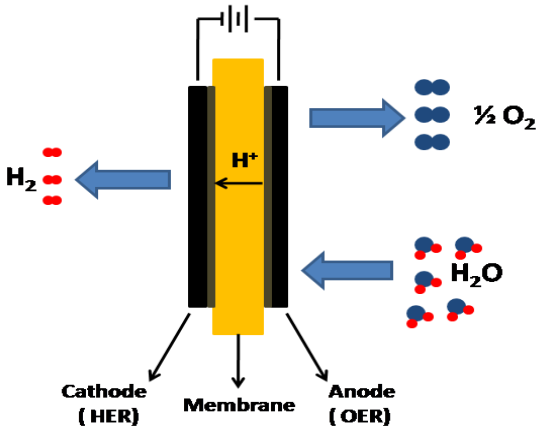

Figure 1.5 *Schematic illustration of the working principle of the polymer electrolyte membrane water electrolyzer.*

'Water splitting' is the general term for a chemical reaction in which water is separated into O_2 and H_2. Efficient and economical water splitting would be a key technological component of the hydrogen economy. Electrolysis of water is considered as one of the best methods for the production of H_2 since, the process employs renewable feedstock water and produces O_2 as a by-product along with H_2. The water electrolysis contributes to only 4% of the total global H_2

production due to the technological and economic issues. However, compared to the other H_2 production sources, water electrolysis ensures highly efficient production of H_2 with purity. The electrolysis can be driven by the DC input powered by sustainable energy sources such as solar, wind, etc. A water electrolyzer consists of an anode and a cathode separated by a polymer membrane. PEM water electrolyzer has similarities with PEM fuel cells, both use solid membranes as the electrolyte. The polymer membrane manages the transport of ions; it separates the product gases, and acts as an electrical barrier between the electrodes. Oxygen evolution reaction (OER) and hydrogen evolution reaction (HER) occur at the anode and cathode, respectively, during the electrolysis. The external potential drives the oxidation of the hydroxyl ion to molecular oxygen at the anode and at the same time the proton gets reduced to hydrogen gas at the cathode. The amount of H_2 generated is twice of O_2 according to ideal faradaic efficiency. The water electrolysis has a thermodynamic potential of 1.23 V in both the acidic and alkaline electrolytes. The overpotential to overcome the activation barriers associated with both the electrode reactions causes the shift in the potential to a higher value than that of the thermodynamic potential. The overpotential reduces the efficiency of the water electrolyzer since extra energy is needed to facilitate the reactions, which increases the cost of the system. The four-electron oxidation of the hydroxyl ion suffers higher overpotential than that of the two-electron reduction of the proton to hydrogen. The reduction of the overpotential is essential for achieving better production efficiency in the water electrolyzer. In this scenario, a suitable electrocatalyst can help to overcome the overpotential associated with the water-splitting electrodes. Therefore, highly efficient, cost-effective catalysts for OER and HER are playing a crucial role in the sustainable development of the water electrolyzer for the production of H_2. Also, in terms of the environmental impact, the water electrolyzer is the most favorable technology for the production of pure H_2. The lower operation temperature (30-80 ^oC), compact design, high current efficiency and purity of the hydrogen output make the water electrolyzer favorable among the different types of H_2 production technologies.

1.10 Electrochemical Water Cycle Reaction

Electrochemical water cycle reactions are the most important electrochemical reactions which take place in the electrochemical energy devices such as metal-air batteries, fuel cells, and water electrolyzers.[30] The electrochemical water cycle reaction is nothing but merely the splitting of

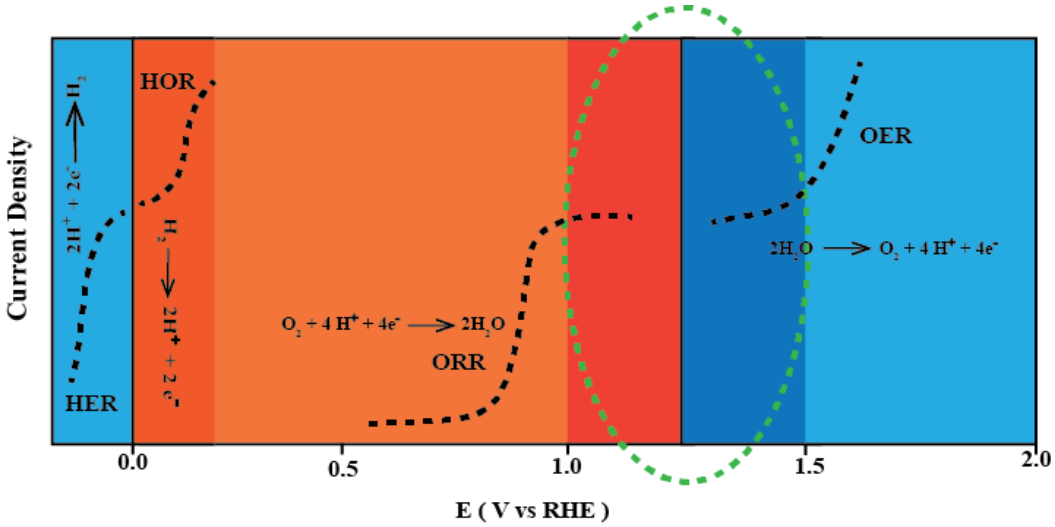

Figure 1.6 *Representation of the electrochemical water cycle reactions.*

water into H_2 and O_2 and the formation of water from its constituent elements. The electrochemical water cycle reactions include four elementary reactions such as oxygen evolution reaction (OER), hydrogen evolution reaction (HER), oxygen reduction reaction (ORR), and hydrogen oxidation reaction (HOR). Among these four reactions, the first two are the part of water splitting reactions (HER and OER) and the next two are the part of water formation reaction (HOR and ORR). In a water-splitting device such as a water electrolyzer, HER is the cathodic half-cell reaction, and OER is the anodic half-cell reaction. However, in a fuel cell device, ORR occurs at the cathode, and HOR takes place at the anode. In the case of a rechargeable metal-air battery, OER takes place during charging and ORR occurs during the discharge process. For carrying out these four reactions in the real application, suitable catalysts are required to enhance the reaction kinetics. The detailed description of each of the electrochemical water cycle reactions is given below.

1.10.1 Hydrogen Evolution Reaction

Hydrogen evolution reaction (HER) is the cathodic half-cell reaction of water electrolyzers. During HER, the protons in the reaction medium are getting reduced into molecular hydrogen. The HER is a typical example of a two-electron transfer reaction with the adsorbed proton (H*) as the intermediate species. HER requires suitable electrocatalysts to curtail the overpotential associated with the reaction.[31]

1.10.1a Mechanism of Hydrogen Evolution Reaction (HER)

Primary discharge step (Volmer reaction)

$$H_3O^+ + 1e^- \longrightarrow H_{ads} + H_2O \quad (1.15)$$

Electrochemical desorption step (Heyrovsky reaction)

$$H_{ads} + H_3O + 1e^- \longrightarrow H_2 + H_2O \quad (1.16)$$

Recombination Step (Tafel reaction)

$$H_{ads} + H_{ads} \longrightarrow H_2 \quad (1.17)$$

HER kinetics depend more on hydrogen adsorption free energy. HER reaction proceeds through either 1.15-1.16 or 1.15-1.17 pathways.[32] Here, in this first step, the protons from the electrolyte get adsorbed at the catalyst surface as they will be reduced by accepting one electron. It is known as the discharge step of HER. The next step is either chemical conversion or electrochemical conversion of the adsorbed hydrogen into molecular hydrogen. Chemical conversion occurs through the recombination step. In the recombination step, the two adsorbed H-atoms combine to form the H_2 molecule. This is also known as Tafel Reaction. The electrochemical reaction is through the desorption step. Here, the adsorbed H accepts a proton from the solution and gets converted to H_2 molecule.

The real mechanism of hydrogen evolution remains a mystery. Usually, the Tafel slope is used to elucidate the kinetics of HER. Tafel slopes for the discharge, desorption, and recombination steps are 118, 39, and 29.5 mV/ decade respectively.[33] At lower overpotentials, desorption or recombination, step is considered as the rate-determining step. However, at high overpotentials, the hydrogen adsorption on the catalyst surface approaches saturation, and the initial discharge step becomes the rate determining. The Gibbs free energy for the adsorption also depends on the rate-determining step. [34]If ΔG_{H^*} is positive, then the H-adsorption step will be the rate-determining step. If it is negative, then H desorption step will be the rate-determining step. Adsorption of the H atoms on the catalyst surface and the subsequent bond formation should be weak; otherwise, it is tough to proceed the further steps by desorption of H atoms. Therefore, it should have a moderate hydrogen binding energy. In the case of metals, during the

reaction, it forms a metal-H bond at the surface, but for the non-metal system, it is still a matter of discussion. Also, the free energy for hydrogen adsorption plays a vital role in determining the activity of the electrocatalysts for hydrogen evolution.

1.10.1b Electrocatalysts for HER

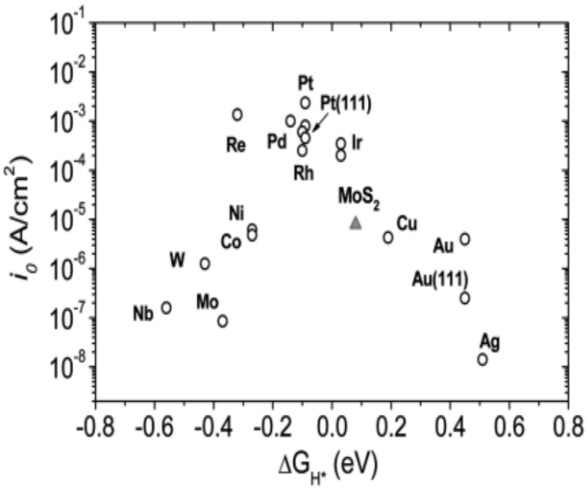

Figure 1.7 *Volcano plot constructed for HER by plotting exchange current density versus free energy of adsorption of hydrogen calculated from DFT analysis.*[35] *(Reprinted with permission, Copyright © 2007,* ***American Association for the Advancement of Science, License Number: 4870140994250****).*

A volcano plot can be obtained by plotting the experimentally measured exchange current density against the free energy of adsorption (ΔG_H). According to the Sabatier principle, an active catalyst binds the intermediate neither too strong nor too weak. A volcano plot with the free energy of adsorption of hydrogen at the x-axis and exchange current density at the y-axis provides insight into the optimum catalyst for HER. The catalyst which sits at the top of the volcano plot is ideal for HER. **Figure 1.7** shows the typical volcano plot for the HER.[35] The metal on the left side of the volcano has high hydrogen coverage, and metal on the right side of the volcano has low hydrogen coverage. Platinum (Pt) sits at the top of the volcano plot for HER with almost zero ΔG_H and with the highest exchange current density. This deduces that Pt is the most active catalyst for HER, which requires very low overpotential to achieve a high reaction rate. Pt catalysts show Tafel slope values near to 30 mV/dec and exchange current density in the

order of 10^{-4} A/cm^2.[36] The high cost and low abundance of Pt hinder their commercial use as HER catalyst in water electrolyzers. The surface modifications of the Pt catalysts by increasing the surface to volume ratio is a favorable strategy to overcome these situations. Structural modifications in the Pt surface are achieved by the synthesis of Pt alloys, core-shell materials, and by using support materials. To an extent, the Pt surface modification has helped in reducing the cost for the electrodes of HER. However, as a permanent solution, researchers have focused on earth-abundant noble-metal-free electrocatalysts as potential alternatives for the Pt catalysts.

Non-precious metal catalysts are frequently applicable in HER. Non-precious metal derived HER catalysts are based on transition metal alloys, and their chalcogenides, carbides, boride, phosphides etc.[37-42] Nickel is one of the most explored catalysts for HER.[43] However, due to the higher overpotential in the system forces the use of various nickel compounds instead of metallic nickel.[44] In this context, nickel alloys with other transition metal catalysts have gained the research attention.[45] The Ni-Mo alloys are reported as active catalysts for HER, which have shown comparable electrochemical performance with the precious metal systems.[46] Metal chalcogenides are another class of transition metal compounds which exhibit higher activity for HER. The chalcogenides of molybdenum are the most attractive one among these categories of electrocatalysts. Compared to bulk MoS_2, layered structures are more active towards HER. Like MoS_2, its isoelectronic species WS_2 also has shown excellent activity towards HER. The selenides of Mo and W are also having a comparable HER performance similar to the sulfide compounds. Many other transition metal chalcogenides show HER activity, but on comparing with Mo, their activity is insufficient. Also, carbides of transition metals, mostly Mo and W are shown positive response towards HER with low overpotential values.[38]

Since most of the nonprecious metal catalysts were shown higher activity for HER, the HER catalyst research moved away from the precious metal to low-cost earth-abundant metals. MoS_2 based catalysts are already proven to be capable enough to act as a replacement for Pt in HER. From the volcano plot, it can observed that MoS_2 has very low free energy value towards hydrogen binding. However, the basal planes of MoS_2 exhibit higher value (1.92 eV) towards the hydrogen adsorption, which indicates that MoS_2 edges are more active than the bulk phase. Jaramillo *et al* studied and illustrated the practical evidence of improved activity of MoS_2 edges

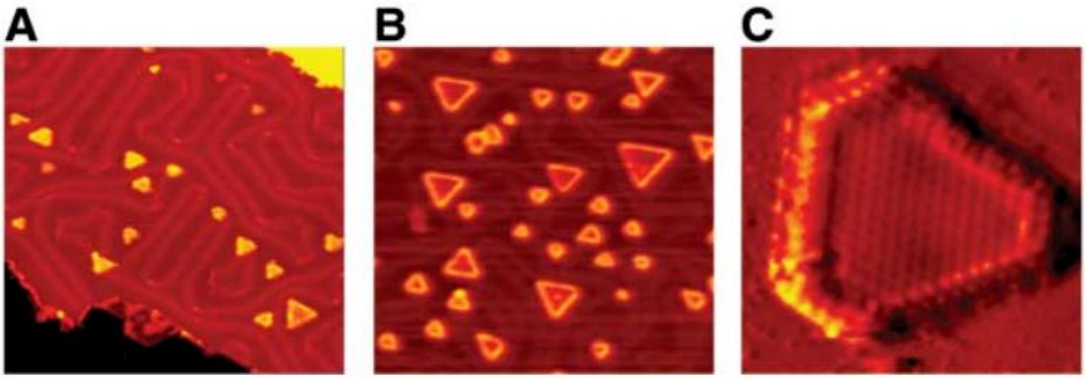

Figure 1.8 *The STM images of the MoS_2 nanoparticles having polygon morphology with exposure of conducting edges on Au(111).*[35] *(Reprinted with permission, Copyright © 2007,* ***American Association for the Advancement of Science, License Number: 4870140994250****).*

(**Figure 1.8**).[35] In their work, they have calculated the MoS_2 edge length with the help of STEM analysis and found that the activity is linearly dependent on the perimeter of the MoS_2 particle rather than the area. The coalition of the theoretical and experimental results triggered the development of more edge active sites on MoS_2. There are many MoS_2 based catalysts that were studied for HER by tuning their structure to improve the intrinsic activity of the material. The structural fine-tuning of the material helps to create more active edges, which will improve the activity of the system. The activity of an HER electrocatalyst is evaluated by analyzing two significant parameters, such as overpotential required to reach the 10 mA/cm^2 current density and turnover frequency. The tuning of MoS_2 for HER was accepted by the scientific community, and enormous efforts are taken in that direction, which result in the formation of different MoS_2 based structures. Mostly, three different categories of MoS_2 are known for the HER applications; we can classify them as crystalline MoS_2, amorphous MoS_2, and molecular MoS_2.[47]

The crystalline MoS_2 structures are designed in such a way by increasing the accessible edges per geometric area. The high-density active sites baring morphologies such as nanoparticles, nanowires, and thin films come under this category. These materials have 2H hexagonal crystal structures, which are mostly semiconducting. This type of crystalline MoS_2 was mostly synthesized by gas phase sulfidation or by hydrothermal treatment. MoS_2 nanoparticles with high dispersion give access to the active sites than the agglomerated particles.

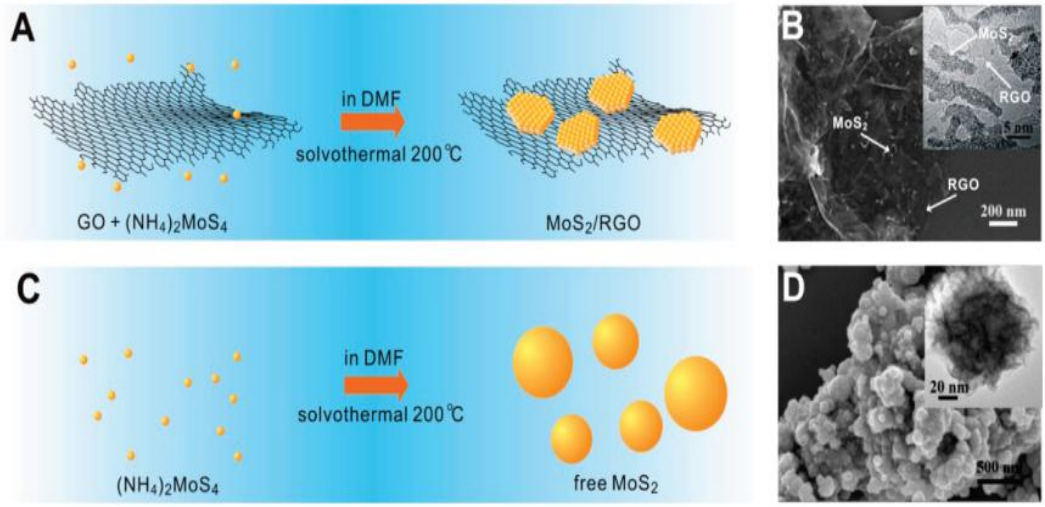

Figure 1.9 *(A) Illustration of solvothermal synthesis of MoS_2/RGO hybrid, and respective (B) SEM and (inset) TEM images (C) Schematic solvothermal synthesis of MoS_2 particles without GO sheets and respective (D) SEM and (inset) TEM images of the free particles.*[33] *(Reprinted with permission, Copyright © 2011,* ***American Chemical Society****).*

However, to attain the maximum dispersion and to expose the active edges, the anchoring of the MoS_2 nanoparticles on carbon support will help. MoS_2 nanoparticles deposited on reduced graphene oxide show substantial improvement in the activity compared to the free MoS_2 nanoparticles (**Figure 1.9**). During the synthesis, the electronic interaction by the conducting support material helps to form more dispersed nanoparticles with slightly different morphology than that of the unsupported nanoparticles. The above-mentioned catalyst has a low Tafel slope value of 41 mV/dec, which is lowest for any MoS_2 materials so far reported. The same catalyst also has a low overpotential of 150 mV at a current density of 10 mA/cm^2.[48] The MoS_2 loaded on mesoporous graphene gives good activity with almost 200 mV overpotential to attain the current density of 100 mA/cm^2. There are some reports of MoS_2 nanoparticles over carbon support; in all cases, it gives better performance than the unsupported MoS_2 and physically mixed MoS_2 over the carbon morphology. Another crystalline MoS_2 was prepared by sulfidation of MoO_3 nanowire, which results in the formation of MoO_3-MoS_2 core-shell nanowire.[49] The MoO_3 core helps the charge transfer to the shell, which improves the electron accessibility of the shell and ultimately improves the activity. MoO_3 is highly unstable in the acidic environment; the thin layer of acid-stable MoS_2 protects the MoO_3 core from acid leaching and MoO_3 shell provides necessary electronic support for the MoS_2 shell for the reduction of protons. Also, the

above catalyst has shown exceptional stability than that of the normal MoS_2-based catalysts. The vertically aligned MoS_2 thin film could favor the exposure of more active sites towards the electrolyte interface helping in the fast reactant transport.[50] This type of peculiar morphology helps to reduce the resistive loss formed due to the out of plane electron transfer from the basal plane. The double gyroid nanostructure shows good activity for HER due to its nanoscale curvature, which reduces the formation of the extended basal planes, resulting in a high density of the exposed active edge sites.[51]

The amorphous MoS_x possesses high electrocatalytic activity due to its high surface area. The amorphous MoS_x can be synthesized by wet chemical method or electrodeposition without any thermal treatment such as high-temperature sulfidation process. Mostly, the amorphous molybdenum sulphides have MoS_3 type structure. On the progress of the reaction, the amorphous structure changes to crystalline MoS_2.[52] Another advantage of the MoS_x amorphous structure is the easiness of doping of a second metal such as Fe, Co, Ni to improve the HER performance.[53] The molecular cluster of MoS_2 is another class of promising catalysts for HER since it has undercoordinated sulfur at the surface mimicking the MoS_2 edges. The incomplete cubane $[Mo_3S_4]^{4+}$, thiomolybdate $[Mo_3S_{13}]^{2-}$, etc., are the few known HER active MoS_2 clusters.[54, 55]

1.10.1c Non-metal catalysts for HER

The bottlenecks in the path of commercialization of the metal chalcogenides are the low stability of the material, inherent corrosion susceptibility and passivation in acidic proton water electrolyzing conditions. In this regard, metal-free carbon based electrocatalyst development for HER is a hot area of research. Non-metal catalysts are very less explored for HER. A good HER catalyst requires an active center for proton adsorption and then electronic conductivity for the reduction of the adsorbed hydrogen atom into molecular hydrogen. Both the properties should be managed simultaneously to get an active catalytic system. The non-metal category of the electrocatalysts consists of mostly carbon nitrides and heteroatom doped carbon morphologies. Since these systems have defects in their matrix along with high electron conductivity, they can promote proton adsorption with active sites. However, the pristine carbon morphologies are inactive towards HER.

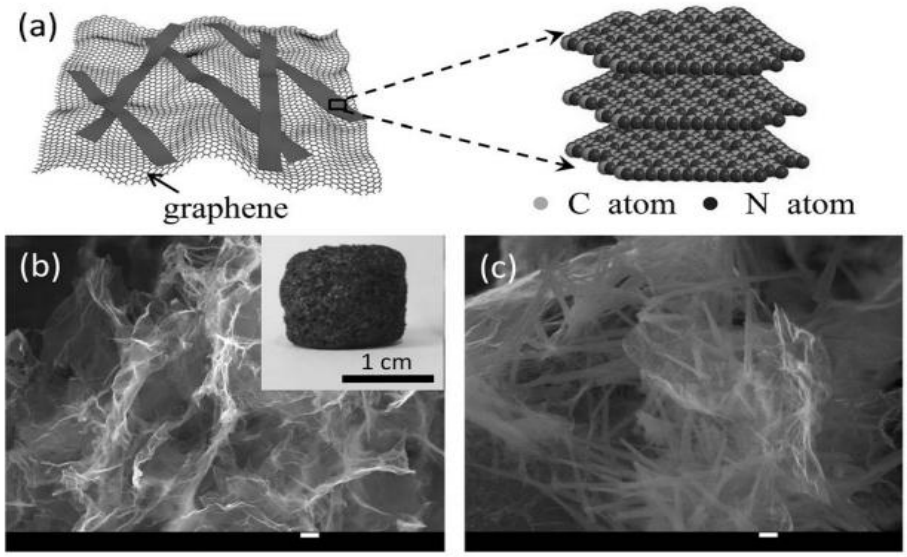

Figure 1.10 *Representation of the structural model of g-C_3N_4 nanoribbon-G with its SEM image.*[56] *(Reprinted with permission from* ***John Wiley and Sons, License Number: 4870041114537).***

The C_3N_4@NG hybrid material is one of the highly active catalysts for HER, and was reported by Qiao *et al*.[57] The material is synthesized from GO and dicyandiamide through chemical vapor deposition method. The hybrid structure formed by the coupling of graphitic carbon nitride (g-C_3N_4) with nitrogen-doped graphene (NG) possesses unique molecular structure and electronic properties having the advantage of synergetic effect, which was shown high electrocatalytic activity for HER. Here, g-C_3N_4 provides the active site for hydrogen adsorption and N-doped graphene helps to facilitate the electron transfer for successive reduction of the adsorbed hydrogen. The above catalyst recorded an overpotential of 240 mV to attain the current density of 10 mA/cm^2. Another highlight of the hybrid material is the high resistance to inherent corrosion in acid media due to its strong covalent interaction between g-C_3N_4 and NG. Qu *et al* reported an HER electrocatalyst based on graphitic carbon nitride ribbons on a graphene sheet.[56] It is the best ever report came in the category of the non-metallic HER catalysts because of the low overpotential. They have prepared a 3D architecture by *in situ* assembling through one-pot hydrothermal treatment. It shows an overpotential of 207 mV to reach a current density of 10 mA/cm^2 with a low Tafel slope of 54 mV/decade and the exchange current density of 39.8 μA/cm^2. These activity parameters substantiate the potential of the catalyst to drive the hydrogen

evolution economically. In this system, g-C_3N_4 gives highly active site for H binding and it also facilitates electron transfer through coupling with a graphene sheet. The above two catalysts validate the importance of g-C_3N_4 in facilitating hydrogen adsorption, which on coupling with electronically conducting substrate enhances the reduction of the adsorbed species.

Another group of the catalyst which has shown activity for HER is the heteroatom doped graphene. Chen *et al* reported N-S co-doped graphene for HER with low overpotential.[58] In this work, they highlighted that synergistic interaction of dual doping along with the defects played a crucial role in performing HER. The catalyst material is synthesized by nanoporous Ni-based chemical vapour deposition. They have also tried the single doping approach; however, the activity was poor compared to the dual doped systems. The NS-500 catalyst recorded an overpotential of 280 mV to reach the benchmark current density of 10 mA/cm^2. Also, it has a low Tafel slope of 80.5 mV/dec. These values are comparable with that obtained on the transition metal dichalcogenides. The free energy of the adsorption of hydrogen was calculated for the above catalyst by DFT analysis and the measured value is 0.12 eV, which is closer to that of the Pt catalyst (0.09 eV). Besides this N-S co-doped system, Qiao *et al* reported N-P co-doped system with enhanced activity for HER.[59] In this work, they have used DFT calculation to examine the effect of heteroatom doping in the graphene lattice with different heteroatoms such as P, N, O, S, B, F etc. In this study, it was observed that the N and O doping gave negative charge population and all the others gave positive charge population. Along with the single-atom doping, they have tried dual doping combinations of atoms by selecting one element from negative and one from the positive charge population category. On comparison with the single doped graphene system, dual doping has lower Gibbs free energy of adsorption of H. In different combinations, the N-P system is found to be more ideal for HER. Also, among different doped nitrogen species, the pyridinic nitrogen contributes more towards hydrogen evolution. Not only the doping but also the porosity of the catalyst contributes to its electrocatalytic activity. Wang *et al* detailed the relevance of pore size in hydrogen evolution performance. They have synthesized mesoporous graphene by template-assisted method using GO, commercial triblock copolymer Pluronic F127 and Cyanamid. The material shows high pore size of 25 nm in the system and displays a large surface area of 916 m^2/g. The N-doping and mesopores structure together synergistically played to facilitate hydrogen evolution activity in the system. It shows a low overpotential of 239 mV to attain the benchmark current density of 10 mA/cm^2. However, non-

porous N-doped graphene having low surface area was found to be poorly active for HER. Sun *et al* reported functionalized carbon nanotube pMWCNT-ao-cp as the active catalyst for HER.[60] Since pristine CNT is inactive towards HER, they have tuned the activity by acidic oxidation followed by cathodic pretreatment. The catalyst shown an overpotential of 220 mV corresponding to 10 mA/cm^2 current density. Also, a good exchange current density of 16 $\mu A/cm^2$ and a Tafel slope of 71.5 mV/dec were recorded for the above system.

1.10.2 Hydrogen Oxidation Reaction (HOR)

The hydrogen oxidation reaction (HOR) is the anodic half-cell reaction in the fuel cells, which results in the formation of the proton from the hydrogen fuel. HOR involves the same reaction steps as HER except that it is reverse of the former; similar to HER, the precious metal Pt is at the top of the volcano plot for HOR as well. In the real PEMFC application, the anodic electrode requires only small amounts of Pt (ca.0.05 mg_{Pt}/cm^2_{geo}) to catalyze the hydrogen oxidation without any performance loss. Identical to HER, the free energy of adsorption of hydrogen is an important theoretical parameter for HOR. The volcano plot derived from the theoretical calculation confirms that Pt is the highest active catalyst for HOR in acidic medium, which also is confirmed from the experimental pieces of evidence. The overall steps of HOR are written with involvement of either proton or hydroxide ions, which depends upon the reaction medium.[61]

Acidic medium: $H_2 \longleftrightarrow 2\,H^+ + 2e^-$ (1.18)

Basic medium: $H_2 + 2\,OH^- \longleftrightarrow 2\,H_2O + 2\,e^-$ (1.19)

In the acidic conditions, the reaction is believed to be composed of two out of three microscopic steps (Tafel/Volmer or Heyrovsky/Volmer):

Tafel step: $H_2 \longleftrightarrow 2\,H_{ad}$ (1.20)

Heyrovsky step: $H_2 \longleftrightarrow H_{ad} + e^- + H^+$ (1.21)

Volmer step: $H_{ad} \longleftrightarrow H^+ + e^-$ (1.22)

In the basic conditions, the Heyrovsky and the Volmer steps have conventionally been written with the hydroxides rather than the protons as the reactants:[62]

Heyrovsky step:

$$H_2 + OH \longleftrightarrow H_{ad} + e^- + H_2O \quad (1.23)$$

Volmer step:

$$H_{ad} + OH \longleftrightarrow H_2O + e^- \quad (1.24)$$

However, other than Pt, no other materials are following the HER volcano trend in the case of HOR. The research is still underway to find this difference in the volcano plot for the precious and non-precious catalyst performances for HOR. The hydrogen surface coverage is considered as one of the reasons for the unexpected deviation in the volcano plot. The Pt shows a high affinity for H coverage, which gives better activity for HER and HOR. However, MoS_2 shows less affinity compared to Pt and behaves differently for both HER and HOR. Another possibility for the low activity of the transition metals for HOR may be due to the surface oxidation happening during the course of the reaction. Hence, more precise theoretical models that consider the operating condition along with the catalyst surface are challenging in electrocatalysis. The hunt for high-performance catalysts with high conductivity and invariant hydrogen coverage to overcome the hurdles in the path of HER and HOR continues in the direction of exploring with the earth-abundant materials.

1.10.3 Oxygen Reduction Reaction (ORR)

Oxygen reduction reaction (ORR) is an important reaction that occurs in electrochemical energy devices like fuel cells and metal-air batteries. The ORR influences the overall performance and efficiency of the energy devices. It is the cathodic half-cell reaction of the fuel cells and metal-air batteries. In the fuel cell cathode, molecular oxygen is converted to hydroxyl ion, which further reacts with a proton to form water as the end product. In alkaline exchange membrane fuel cell, the hydroxyl ions migrate through the membrane and reach the anode side and react with the proton formed at the anode to get the water end product. However, the water formation reaction occurs at the cathode side in the case of a proton exchange membrane fuel cell. Also, in the case of metal-air batteries, the hydroxy ions formed at cathode move towards the anode. Since the

O=O bond is very strong, it is challenging to reduce oxygen with minimal energy. The oxygen reduction reaction is a four-electron transfer reaction, which converts molecular oxygen into H_2O. Along with direct four-electron transfer, an inefficient two-electron pathway also known to exist with a higher concentration of the intermediate peroxide formation. ORR is following different pathways in the acidic and alkaline electrolytes. The mechanisms of ORR in the acidic and alkaline media are giving below:

Acidic Medium:

Four-electron pathway:

$$O_2 + 4\,H^+ + 4\,e^- \rightarrow 2\,H_2O \qquad (E^o = 1.23\ V) \qquad (1.25)$$

Two-electron pathway:

$$O_2 + 2\,H^+ + 2\,e^- \rightarrow H_2O_2 \qquad (E^o = 0.70\ V) \qquad (1.26)$$

$$H_2O_2 + 2\,H^+ + 2\,e^- \rightarrow 2H_2O \qquad (E^o = 1.76\ V) \qquad (1.27)$$

The disproportionation of the peroxide molecule also leads to the formation of oxygen and water as follows:

$$H_2O_2 \rightarrow H_2O + \tfrac{1}{2}\,O_2 \qquad (1.28)$$

Alkaline Medium:

Four-electron pathway:

$$O_2 + 2H_2O + 4\,e^- \rightarrow 4\,OH^- \qquad (E^o = 0.40\ V) \qquad (1.29)$$

Two-electron pathway:

$$O_2 + H_2O + 2\,e^- \rightarrow OH^- + HO_2^- \qquad (E^o = -0.605\ V) \qquad (1.30)$$

$$HO_2^- + H_2O + 2\,e^- \rightarrow 3OH^- \qquad (1.31)$$

The decomposition of HO_2^- species also produces the OH^- and oxygen as follows:

$$HO_2^- \rightarrow OH^- + \tfrac{1}{2}\,O_2 \qquad (1.32)$$

The four-electron and two-electron pathways for ORR usually proceed through either associative or dissociative mechanism. The associative mechanism takes place through the adsorption of molecular O_2 on the catalyst surface and direct transfer of proton/electron occurs leading to the formation of OOH. In the next step, the intermediate OOH splits to form O and OH. However, in the case of the dissociative mechanism, the O-O bond gets break before the transfer of proton/electron followed by the formation of OH and then to H_2O.

Associative mechanism

$$Pt + O_2 \rightarrow Pt\text{-}O_2 \text{ ads} \quad (1.33)$$

$$Pt\text{-}O_{2\ ads} + H^+ + e^- \rightarrow Pt\text{-}O_2H_{\ ads} \quad (1.34)$$

$$Pt\text{-}O_2H_{ads} + H^+ + e^- \rightarrow H_2O + Pt\text{-}O_{\ ads} \quad (1.35)$$

$$Pt\text{-}O_{\ ads} + H^+ + e^- \rightarrow Pt\text{-}OH_{\ ads} \quad (1.36)$$

$$Pt\text{-}OH_{\ ads} + H^+ + e^- \rightarrow Pt + H_2O \quad (1.37)$$

Dissociative mechanism

$$Pt + ½\ O_2 \rightarrow Pt\text{-}O_{\ ads} \quad (1.38)$$

$$Pt\text{-}O_{\ ads} + H^+ + e^- \rightarrow Pt\text{-}OH \text{ ads} \quad (1.39)$$

$$Pt\text{-}OH_{\ ads} + H^+ + e^- \rightarrow Pt + H_2O \quad (1.40)$$

1.10.3a Electrocatalysts for ORR

The Pt is the best-known electrocatalyst for ORR in both alkaline and acidic media. Figure 1.11 shows the volcano plot constructed for ORR by analyzing the theoretical model of all the catalysts with the free energy of adsorption of oxygen (ΔE_0) as an activity parameter. Pt sits at the top of the volcano plot with an optimum ΔE_0 value and maximum exchange current density value. Other precious metals like Ir, Ru, Pd, etc. are lying near to Pt in the volcano plot. Compared to HER volcano plot, it is not easy to use ORR volcano plot, since it has multiple

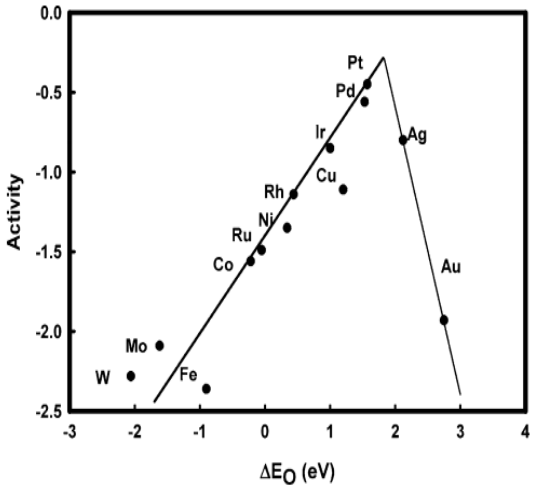

Figure 1.11 *Volcano plot constructed for oxygen reduction activity as a function of oxygen binding energy.*[63] *(Reprinted with permission, Copyright © 2004,* ***American Chemical Society****).*

electron transfer with more than one intermediate. The different intermediate possesses different thermodynamic energetics. The rate-limiting steps also vary from sample to sample based on their active sites. Most of the theoretical studies used ΔE_0 as an activity parameter along with the exchange current density in the y-axis. In a few cases, if the metal binds oxygen too strongly, the activity is limited by consecutive steps such as the electronic transition to intermediates such as OOH^* and O^*, etc. Some of the catalysts are suitable for O_2 bond breaking, some are for O^* adsorption and some are for electronic transfer to intermediate. An ideal catalyst should hold all these parameters together. Recently, more studies are emerging with projections of new intrinsic activity parameters for ORR catalysts such as the work function of the catalyst.

As per theoretical studies, it was found that Pt is the best known catalytic system for ORR. The *state-of-the-art* Pt catalyst itself possesses around 230 mV overpotential than that of the thermodynamic potential (1.23 V). There is a lot of research being done to improve the activity of Pt further to reduce the overpotential gap. Alloying of Pt with other transition metals such as Ni, Co, etc., is one of the best strategies to improve the Pt performance further. The incorporation of the transition metals into the Pt lattice changes the Pt 5d band vacancy by the electron transfer from the second metal leading to the decrease in the Pt-Pt interatomic distance. All these eventually help to improve the activity of the Pt system. Hence, the research on developing Pt alloy catalysts with transition metals has gained more attention recently.

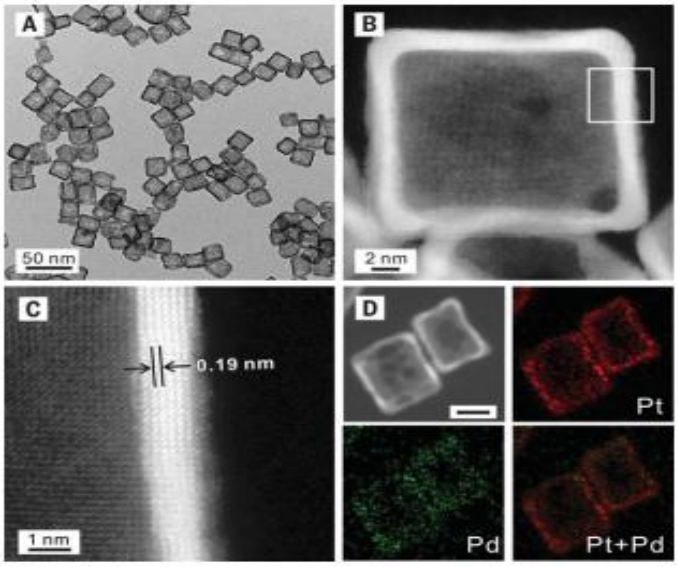

Figure 1.12 *The TEM and HAADF STEM images of Pt cubic nanocages prepared by using Pd nanocubes.*[64] *(Reprinted with permission, Copyright © 2015,* ***American Association for the Advancement of Science, License Number: 4870050992877****).*

Some well-known approaches exist to increase the performance of the Pt-based catalysts in PEMFCs. These include developing strategies to increase the number of the active sites, supporting Pt nanoparticles on a conducting support material such as carbon black, and increasing the intrinsic activity of the catalyst by adopting innovative approaches. The morphology tuning helps to improve the activity by exposing more active sites towards the reaction interphase. The shape-controlled Pt catalysts are a class of materials which helps to improve the active sites for ORR. To detect the ORR active plane in the Pt catalyst, the activity evaluation was carried out in different electrolytes with controlled exposing of the facets. The ORR activity follows the order of (110) > (111) > (100) facets in the case of single-crystalline Pt in a perchloric acid electrolyte. However, in an adsorbing electrolyte, the activity order is reshuffled and it follows the activity as (100) > (111) > (100). The above-mentioned studies motivate the synthesis of different Pt morphologies with better exposed active facets.

Xia *et al*. prepared Pt cubic and octahedral nanocages enclosed by the (100) and (111) facets.[64] They have used Pd nanoscale cubes and octahedra as the template materials for the synthesis. The nanocages were fabricated by depositing a few atomic layer thick Pt shell over the Pd core nanocrystals and, in the second step, the core Pd was etched away by keeping the Pt

outer shell. The electrochemical studies confirm that the as-prepared Pt nanocages are showing better mass activity and specific activity than the commercial Pt/C catalyst with improved stability. Sun *et al*. synthesized thin FePt and CoPt nanowires.[65] In the process, they have used metal carbonyl along with Pt acetylacetonate as a Pt precursor. They have simultaneously prepared Fe and Co alloy nanowire with Pt depending upon the metal carbonyl taken. The thicknesses of the nanowires were restricted to below 3 nm. However, the nanowire with a higher thickness (6.3 nm) formed after annealing was shown exceptional activity. This may be attributed to the formation of a thin layer of Pt skin over the nanowire by etching the Fe from the surface. Electrochemical analysis proved that these materials possess higher mass activity than the commercial Pt/C. The Pd-Pt bimetallic nanodendrites prepared by then Xia *et al*., have a dense array of Pt branches on Pd core.[66] The K_2PtCl_4 precursor was reduced by using L-ascorbic acid in the presence of Pd nanocrystal seeds in an aqueous solution. The Pd core helped to form the active facets in the Pt shell with a relatively large surface area. The Pd-Pt bimetallic nanodendrites have shown 2.5 times higher mass activity than that of the commercial Pt/C catalyst. Yan *et al*. synthesized supportless Pt nanotubes and Pt-Pd nanotubes as highly active catalysts for ORR.[67] The as prepared nanotubes have 50 nm diameter, 5-20 μm length and 4-7 nm wall thickness. The galvanic replacement of the polyol prepared Ag nanotube was adapted for the synthesis Pt nanotube. The Pt nanotube structure has an advantage of high surface area, high utilization, high activity, and long durability. Sun *et al*. reported high-temperature organic phase synthesized Pt nanocubes for ORR electrocatalysis.[68] Pt nanocubes were synthesized by the reduction of $Pt(acac)_2$ in the presence of oleic acid and oleyl amine and a trace amount of $Fe(CO)_5$. Self-assembly of these nanocubes results in a (100) textured array. The nanocubes on a carbon paper show enhanced catalysis toward oxygen reduction and their specific activity is over 2 times as high as that from the commercial Pt catalyst.

To expose more active Pt with improved activity, Pt nanoparticle deposited carbon support catalysts were introduced. These carbon support materials inherently have high electronic conductivity, large surface area, and chemical stability. However, there is a high chance of corrosion of these carbon support materials during the fuel cell operating conditions. This may have happened due to the weak interaction of Pt with the carbon surface. The carbon corrosion further causes the detachment of the deposited nanoparticles. Also, there is a chance of agglomeration of the Pt nanoparticles and the formation of large particles. The agglomeration

and leaching out of Pt nanoparticles cause the reduction of the active centers and result in activity loss. Hence, all these are pointing out that the stability of the support materials determines the overall stability of the Pt-decorated carbon catalysts. Compared to the amorphous carbon, graphitic carbon exhibits higher resistance to corrosion.

The alloying is one of the most important approaches for the enhancement of the Pt catalyst activity for ORR. The alloying facilitates the electronic transitions in the Pt surface during ORR. Also, alloying can decrease the oxygen adsorption energy on the outer Pt layer. The nanoclusters of the transition metals with Pt have electronic and morphological properties that mimic the Pt skin surface that can enhance ORR. One of the critical objectives in PEMFC technology is to improve and reduce Pt loading as the oxygen-reduction catalyst. Stamenkovic *et al*. prepared different bimetallic alloys of Pt_3M (M = Ni, Co, Fe, Ti, V) and their studies correlated the ORR activity and the surface electronic structures.[69] They have got a volcano plot with the Co alloy of Pt_3M at the top of the volcano, and the higher activity has been credited to the balance between the adsorption energies of the reactive intermediates and surface coverage. Electrocatalytic trends in ORR are established as a relation between the surface composition, specific activity, and the surface electronic structure of the Pt_3M (M = Ni, Co, Fe, V, Ti) surfaces.

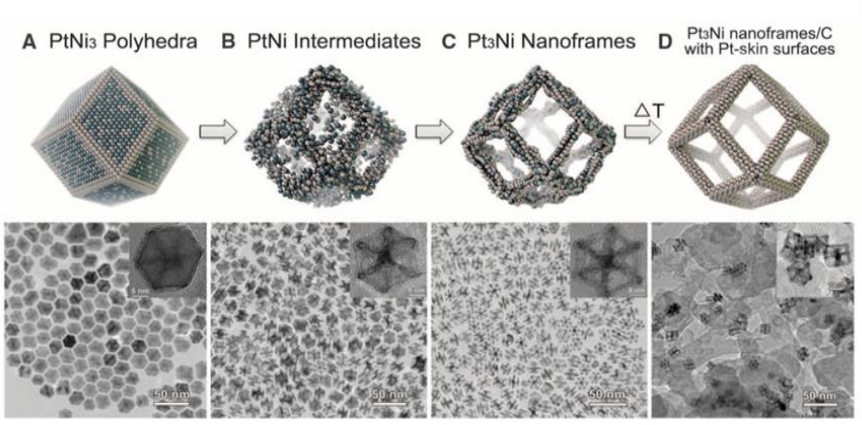

Figure 1.13 *Different stages of formation of Pt_3Ni nanoframes from $PtNi_3$ polyhedra are illustrated with corresponding TEM images.*[70] *(Reprinted with permission, Copyright © 2014,* ***American Association for the Advancement of Science, License Number: 4870051343341****).*

Pt-Ni is the most explored dual alloys in terms of the ORR activity. There are a lot of reports existing with various alloying compositions of Pt and Ni. Stamenkovic *et al*. prepared a novel class of Pt_3Ni catalyst with Pt-rich surface that showing high activity for ORR.[71] The prepared catalyst has extended single-crystal surfaces of $Pt_3Ni(111)$ with a Pt-rich outermost layer caused by the thermal annealing and restructuring in the near-surface region. These so-called Pt-skin structures showed a specific activity 10 times that of Pt(111) and 90 times that of the *state-of-the-art* Pt/C catalysts. In another work, they have synthesized high class active and durable catalyst by exploiting the structure evolution of Pt-Ni bimetallic nanocrystals.[70] The final three-dimensional Pt_3Ni catalyst was evolved as the outcome of the different stage of the morphological evolution. The $PtNi_3$ polyhedron was transformed into Pt_3Ni nanofarmes with three-dimensional molecular accessibility by interior erosion. The Pt edges in the $PtNi_3$ polyhedra have survived the erosion and sustained in the final Pt_3Ni nanoframes. The final Pt_3Ni nano framework material has the advantage of an open three-dimensional Pt-rich skin structure. With the higher exposed Pt rich sites, Pt_3Ni framework exhibits upgraded oxygen reduction reaction (ORR) activity. The Pt_3Ni nanoframe catalysts achieved a factor of 36 times enhancements in the mass activity and a factor of 22 times enhancement in the specific activity, respectively, compared to the *state-of-the-art* Pt catalyst. The most noticeable thing in this work is that the activity has remained unaltered even after 10000 durability cycles. As the next step of advancement in the field of ORR, the doping Pt_3Ni octahedra with transition metals was reported to further enhance their activities. Huang *et al*. reported the doping of Pt_3Ni with Mo, which opens on to improvement in the specific activity and mass activity by factors of 81 and 73, respectively, relative to the commercial Pt/C catalysts.[72] The computational studies provided the insight of the active sites, which states that the Mo concentrated on the surface vertex and edge sites in the presence of adsorbed oxygen and it strongly forms Mo-Pt and Mo-Ni bonds to stabilize both Pt and Ni atoms against dissolution. Even though the Mo-doped Pt_3Ni system outperformed the *state-of-the-art* catalysts, it still suffers the overpotential of 200 mV with the thermodynamic equilibrium potential. The research is still continuing in the direction to further reduce the overpotential gap.

1.10.3b Non-precious metal catalysts

The development of earth-abundant non-precious metal catalysts with low-cost and high-performance has gained attention due to the possibility of cost reduction. The non-precious metal catalysts such as metal oxides, nitrides, chalcogenides, carbide, etc. are reported so far for fuel cell applications. However, due to the low electrical conductivity of these classes of materials, their composites with various conducting carbon structures got extensive research interest. Most of the nonprecious metal-carbon composite catalysts are active under alkaline conditions. Only very few are active in acidic conditions. The major challenge associated with the development of non-precious catalysts for fuel cells is the fine-tuning of the catalyst material so that it can exhibit high activity in acidic medium. In acidic electrolytes, the carbon-supported transition-metal/nitrogen (MN_x/C, M = Co, Fe, Ni, *etc*.) compounds are found to be active and durable. The interactions between the transition metal, doped nitrogen, and the carbon support morphology together play a vital role in facilitating the ORR activity. The M-N-C based on Fe and Co has

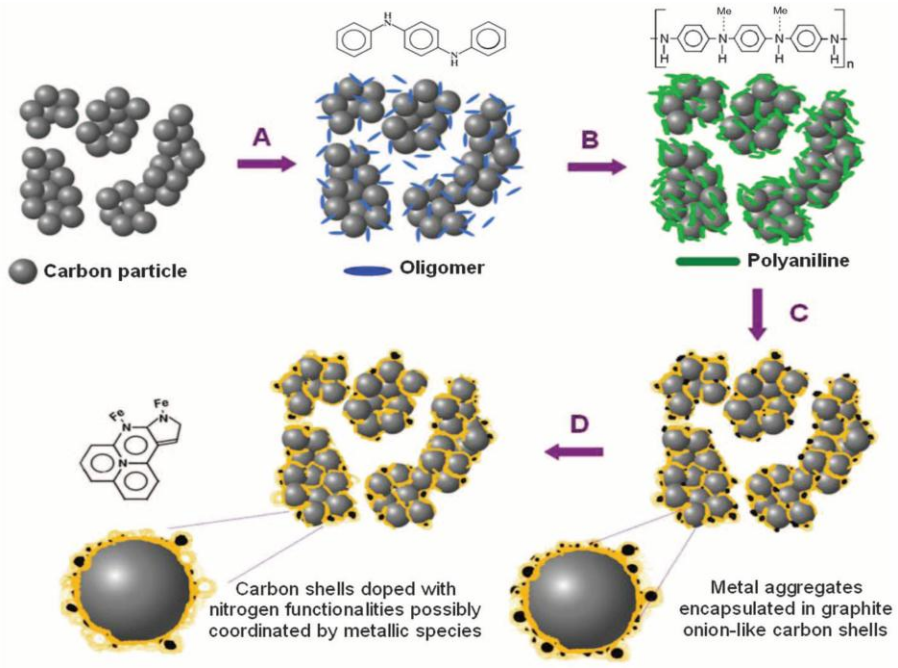

Figure 1.14 *Schematic illustration of synthesis of PANI-M-C catalysts prepared from high surface area carbon with mixing of aniline oligomers.*[73] *(Reprinted with permission, Copyright © 2011,* ***American Association for the Advancement of Science, License Number: 4870060032180****).*

demonstrated itself as a good candidate to replace the Pt/C catalyst in PEMFCs. Currently, the M-N-C catalysts are being prepared by many methods, which have shown excellent activity for ORR in acidic medium. Fe and Co are the most explored M-N-C catalyst systems due to their efficient oxygen binding properties. The high-temperature pyrolysis of MOF, which contains suitable metal atoms results in the formation of single-atom catalysts. Wang *et al*. recently prepared N-doped porous carbon catalyst with Fe and Co dual active sites (Fe, Co/NC), which was performing in par with the *state-of-the-art* Pt/C catalyst in acidic medium. [72] The above catalyst was applied in a single cell of PEMFC, which delivered a maximum power density of 0.98 W cm^{-2} at a back pressure of 0.2 MPa. Another way of the preparation of the M-N-C catalyst is the annealing of small organic molecules that contain N atoms along with a suitable metal salt. Wu *et al*. prepared different transition metal catalyst by interchanging the metal precursor and organic molecule. The metal precursor plays a key role in directing the morphology of the catalyst. The catalyst activity could be tuned by interchanging the small molecules and metal precursors. One of the most successful methods for the production of the M-N-C catalysts is the graphitization of the conducting polymer by high-temperature treatment. Zelenay *et al.* achieved success in the preparation of the M-N-C catalysts by using polyaniline as the source, which upon annealing with Fe and Co salt results in the formation of graphitic carbon containing M-N-C active sites. The PANI-FeCo-C catalyst showed high ORR activity in acidic medium with a 60 mV overpotential shift compared to the Pt/C catalyst at the half-wave potential region. Also, the above catalyst recorded a maximum power density of 550 mW cm^{-2} during single cell testing of PEMFC.

1.10.4 Oxygen Evolution Reaction (OER)

The oxygen evolution reaction (OER) is the key reaction in water electrolyzers, in which the oxidation of hydroxyl ions occurs at the anode to produces O_2. The OER has a thermodynamic potential of 1.23 V in both acidic and alkaline electrolytes. Similar to ORR, OER also proceeds through sluggish four electron mechanism which causes the higher overpotential and the operating potential shifts to more positive. In practice, the efficiency of water electrolysis is limited by large anodic overpotential of OER. Since the cathodic HER in the water electrolyzer is a two-electron reaction, its overpotential is less compared to OER. Thus, understanding, and optimizing the OER process is one of the grand challenges in water electrolyzer

commercialization. The high overpotential for OER hinders their widespread real-life application; hence, the overpotential should be minimum for the OER process. A better electrocatalyst could help to overcome the overpotential and provide higher efficiency for the system. Over the past few years, considerable research effort has been devoted to the design and synthesis of the OER electrocatalysts with the aim of achieving useful rates of active oxygen evolution at the lowest possible overpotential.

1.10.4a Mechanism of OER

Acidic media:[74]

$$M + H_2O \rightarrow M\text{-}OH + H^+ + e^- \quad (1.41)$$

$$M\text{-}OH \rightarrow M\text{-}O + H^+ + e^- \quad (1.42)$$

$$M\text{-}O + H_2O \rightarrow M\text{-}OOH + H^+ + e^- \quad (1.43)$$

$$M\text{-}OOH \rightarrow M\text{-}O_2 + H+ + e^- \quad (1.44)$$

$$M\text{-}O_2 \rightarrow O_2 + M \quad (1.45)$$

Alkaline media:[75]

$$M + OH^- \rightarrow M\text{-}OH + e^- \quad (1.46)$$

$$M\text{-}OH + OH^- \rightarrow H_2O + M\text{-}O + e^- \quad (1.47)$$

$$M\text{-}O + OH^- \rightarrow M\text{-}OOH + e^- \quad (1.48)$$

$$M\text{-}OOH + OH^- \rightarrow M\text{-}O_2 + H_2O + e– \quad (1.49)$$

$$M\text{-}O_2 \rightarrow O_2 + M \quad (1.50)$$

where, M is the active center.

1.10.4b Electrocatalysts for OER

The OER is the reversible reaction of the ORR process. In the case of both hydrogen oxidation and reduction reactions, Pt shows the best catalytic activity. Both HER and HOR are reversible

reactions involving the same steps. However, in the case of OER, it is the reversal reaction of what happens in ORR. As per the previous discussion, it is expected that Pt would be the best catalyst for OER, but this is not the reality. Pt suffers huge overpotential for OER than the other nonprecious metal catalysts.[76] Since, both OER and ORR involve multi-electron steps with higher overpotential, it is very difficult to observe a catalyst that performs well in both the directions. Also, there is a chance of surface oxidation of Pt during the course of ORR, which requires high positive potential. In the case of ORR, the molecular oxygen is the primary species, which gets adsorbed on the catalyst surface. However, in OER, the OH^- ions get adsorbed and converted to molecular oxygen as a result of a series of electron transfer processes.

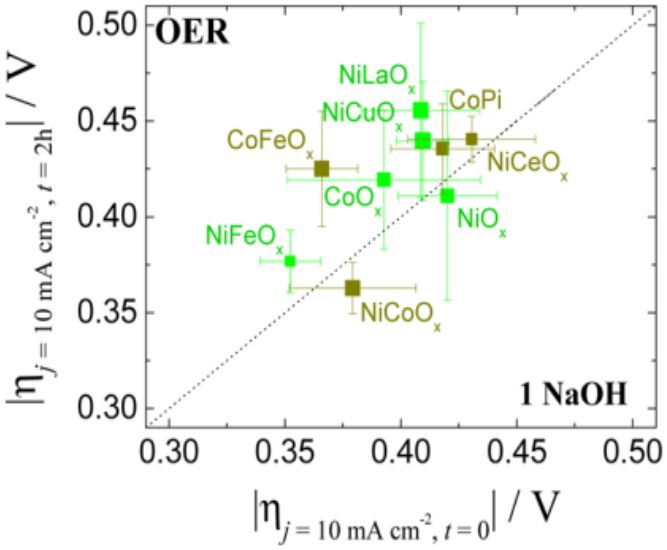

Figure 1.15 *The various metal oxide catalysts plotted on the basis of activity and stability for OER in 1M NaOH.[77] (Reprinted with permission, Copyright © 2013,* ***American Chemical Society****).*

In **Figure 1.15**, the volcano plot of OER is dominated by the transition metal oxides. The metal oxides with different crystal structures such as perovskite, spinel, rutile, etc., perform better for OER.[77-80] While constructing the volcano plot for OER, ΔG_O-ΔG_{OH} is used as the x-axis against the overpotential for 1 mA/cm^2 current density in the y-axis. The IrO_2 is the most active metal oxide catalyst for OER in acidic medium.[81] This activity is theoretically predicted, and it shows reasonable binding energies for the OER intermediate species. However, IrO_2 suffers large

overpotential, and it has shown low stability in a high oxidative environment. There are some reported combinations of IrO_2 with the other metal compounds that can help to reduce the overpotential with improved stability. The $IrO_x/SrIrO_3$ thin film catalyst is the one among them, and it has an overpotential of 270 mV along with enhanced stability.[82] The higher intrinsic activity of the catalyst is not achieved much realistically due to the surface area limitation of the thin-film morphology. These results point towards the need for structural modulation along with creation of the intrinsic active sites. Also, considering the scarcity and high cost of the precious metal catalysts such as IrO_2, RuO_2, the research focus is more attracted by nonprecious metal oxide compounds.

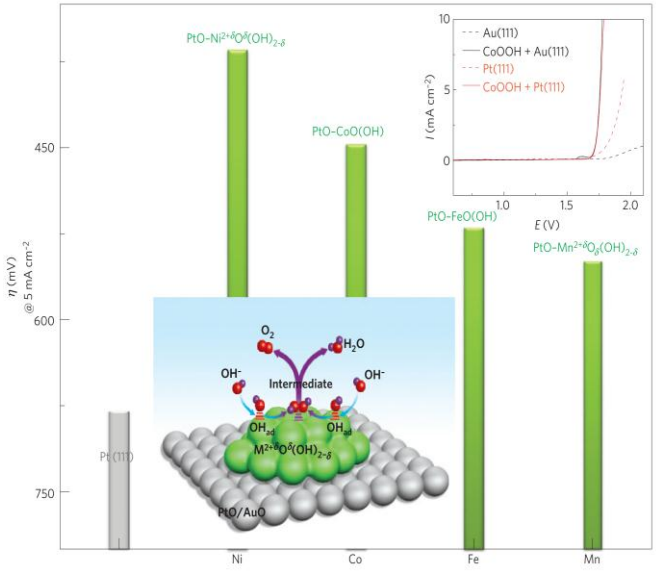

Figure 1.16 *The OER overpotential trends in the 3d transition elements, the elements are arranged with their oxophilicity.*[83] *(Reprinted with permission from* ***Springer Nature, License Number: 4870061287621****).*

Nickel oxides, cobalt oxides, and manganese oxides are the most studied class of nonprecious metal oxides for OER. Markovic *et al*. studied different 3d transition metal (Fe, Co, Ni and Mn) hydroxide and oxyhydroxides for hydrogen evolution and oxygen evolution reactions.[83] They have used OH_{ad}-M^+ interaction as the descriptor and calculated the activity trend for the prepared catalysts. It was found that the activity follows the order of Ni > Co > Fe > Mn for OER. While comparing the OER trend with the OH^- interaction, it was worthy to note that both have an inverse relationship. The identification of the catalyst trend with the activity

descriptor provides key insight for the material design with exposed active sites. Binary and ternary metal catalysts are also reported for OER with some significant activity. Among these catalysts, some of them surpasses the precious metal catalysts in the race of reduced overpotential for OER. Transition metal chalcogenides (TMC) are emerging as a new class materials for OER. The transition metal sulphides are oxidized by a so-called *in-situ* electrochemical oxidation tuning methodology to form nanoporous transition metal oxides for enhanced water oxidation. The chalcogenide-derived nanoporous oxides exhibit excellent electrocatalytic performance for water oxidation. Some of the OER electrocatalysts were found to be active for ORR also in alkaline media.[84] These bifunctional catalysts showing comparative activity for both OER and ORR are classified as a new class of materials in the water cyclic reactions.

Metal-free catalysts such as heteroatom doped carbon morphologies have recently got attention as a low-cost bifunctional catalyst for OER/ORR.[85] The heteroatom doping in the carbon matrix causes polarization in the carbon bonds and eventually results in improved conductivity. The doping creates active sites for the adsorption of the reactive intermediates. Mostly, the carbon atom near to the heteroatom acts as the active center for the binding of the reactive species. Also, the doping causes improved conductivity, which helps in enhanced electron transfer with the bonded intermediate species. As the next level of advancement in heteroatom engineering, co-doping of the carbon material has been demonstrated, which gives the synergistic effect for the better performance of the catalyst.

The extensive research is underway on the field of catalyst design for ORR and OER in acidic and basic media; still, there exists a gap between the experimental results and thermodynamic potential. One of the reasons for this activity losses is due to scaling relations between the reactive intermediates. The decoupling of the binding energies of individual species help to succeed in the issues related with higher overpotential. Also, the electrode-electrolyte interface is crucial for the performance of catalysts and their kinetics. Developing strategies to engineer a catalyst material around known scaling relations is just the first step in opening up opportunities to create near-ideal ORR/OER catalyst systems that would substantially increase the efficiency of a wide range of energy conversion devices.

1.11 Scope of the Present Research Work and Objectives of the Thesis

The electrochemical water cycle reactions are indispensable part of the commercialization of the electrochemical energy devices such as fuel cells, metal-air batteries, and water electrolyzers. The development of highly active catalysts with low cost is desirable for the advancement of the water cycle reactions and their applications in the energy devices. The morphology and distribution of the active centres have significant importance in deciding the performance of the electrocatalysts. The three-dimensional (3D) morphology of the catalysts will help to improve the mass transport to and fro from the catalyst surface. The rational designing of the active centers is essential to develop highly efficient catalysts. Among the different water cycle reactions, the oxygen reduction reaction (ORR) is the cornerstone of the electrochemical energy devices such as PEMFC and metal-air batteries. The sluggish kinetics of the reduction of molecular oxygen demands a highly active catalyst to overcome the kinetic barrier. In this context, precious metal catalysts such as Pt/C are widely used for ORR. However, the low stability of such catalysts, the inability of complete utilization of Pt at the reaction interphase and exorbitant cost hinder their widespread utilization for commercial applications.

The utilization of Pt is important to improve the efficiency of the system. Improving the electrode level performance of PEMFCs by enhancing the Pt utilization with improved durability in the *state-of-the-art* Pt catalyst is one of the focusing areas of research in PEMFCs. This requires strategies based on the engineering of the microstructure of the catalyst support for creating extended active "triple-phase boundary (TPB)" by using proton conducting ionomers. The Pt support structures also play vital roles in deciding the efficiency of the catalyst by providing necessary electronic support to the Pt nanoparticles. Also, due to the high cost of Pt, the development of non-precious metal catalysts is significant in the path of commercialization of PEMFCs. Heteroatom doped transition metal composites of carbon morphologies are potential candidates to replace the Pt/C systems in PEMFCs. In the case of rechargeable metal-air batteries, the air electrode requires a bifunctional catalyst that can facilitate both OER and ORR for its charging and discharging processes. Since, highly active ORR catalysts are inactive for OER and vice versa, the potential efficiency loss happens during the functioning of the metal-air batteries. The metal oxides are class of compounds, which are found to be active for both OER and ORR. However, the higher overpotential in those cases limits their further advancement. In

this scenario, the bimetallic oxide catalysts can contribute towards the bifunctional catalysis. Since mass diffusion is an important parameter in the air electrodes, the 3D array of the active centres can help to get higher efficiency for the system. The cathodic hydrogen evolution reaction (HER) of the water electrolyzer is an integral part of the water cycle reactions. Since its kinetics involves a two-electron transfer mechanism, the use of costly Pt catalyst is not mandatory to overcome its kinetic barrier. Carbon nitrides and hetero atom doped catalysts have the affinity of hydrogen adsorption, which can replace the *state-of-the-art* Pt catalysts.

The key objective of the present thesis is the development of 3D carbon morphologies and their surface modifications to enhance the kinetics of electrode reactions in electrochemical energy devices such as PEMFCs, metal-air batteries, and water electrolyzers. The melamine foam can be used as the template in combination with different carbon sources to create the 3D electrocatalysts. Simple and environmentally benign synthesis strategies need to be developed for the scalable production of the catalysts for commercial applications of the specific systems. The electrical conductivity and porosity of the catalysts required to be tuned along with the morphology to achieve better intrinsic activities. A systematic strategy has to be adopted to achieve improved performance with low overpotential as a replacement for the *state-of-the-art* electrocatalytic systems for real-life applications of PEMFCs, metal-air batteries and water electrolysers. Finally, the material level explorations need to be supplemented with system-level validation to understand the suitability of the adopted strategies and designed catalysts for real-life applications.

The specific objectives and work components considered for the preparation of the present thesis are as follows:

1) To develop a metal-free 3D structured electrocatalyst for HER application in acidic medium. Exploring the advantages of melamine foam as both the template for building the 3D structure and source of nitrogen for the uniform doping in the matrix. The 3D interconnected nitrogen doped graphene (CN_x@N-RGO) as the combination of the N-doped graphene and carbon nitride has to be prepared. DFT analysis of the CN_x@N-RGO to be performed to elaborate the mechanism of hydrogen evolution in the nonmetal catalytic systems.

2) Synthesis and comparison of the activity of Pt nanoparticles for ORR over three different carbon morphologies. The morphology of the supporting material and interaction of Pt nanoparticle with carbon support could decide the activity. A 3D morphology derived from melamine foam and graphene can help in exposing more Pt towards the reaction interphase. Along with it Pt catalysts based on Vulcan carbon (VC) and N-doped graphene (NRG) supports has to be prepared to compare the effect of support morphology on the ORR performance. Since the carbon support in one case has 3D structure, the *in situ* ionomer processing can be applied in this case for electrode fabrication to enhance the Pt utilization by forming an effective triple phase boundary. Finally, by utilizing the as-prepared electrode, demonstrate a single-cell of PEMFC by carefully evaluating and mapping the performance parameters.

3) Synthesis of a 3D structured non-precious metal catalyst for ORR application is another objective of this thesis. To increase the surface area of the catalyst, the wrapping of the graphitic carbon strategy can be adopted instead of hanging. The preparation of a 3D catalyst (3D-FePDC) from melamine foam and dopamine to get a highly active catalyst for ORR and construction of a single cell of a PEMFC with 3D-FePDC as the cathode catalyst and its activity analysis are the targeted work components.

4) Another objective considered here is the development of a 3D aligned $NiCo_2O_4$ growth pattern over CNT modified melamine sponge (NCS) prepared *via* an environmentally friendly and cost-effective method as a bifunctional catalyst for facilitating both ORR and OER in alkaline medium. This will be followed by the construction of a rechargeable Zn-air battery with NCS catalyst as an air electrode.

1.12 References

[1] https://www.oecd.org/greengrowth/greening-energy/49157219.pdf

[2] X. Zou, Y. Zhang, *Chem. Soc. Rev.*, **2015**, 44, 5148-5180

[3] W. Li, D. Xiong, X. Gao, L. Liu, *Chem. Commun*. **2019**, 55, 8744-8763.

[4] https://ourworldindata.org/energy

[5] Y. Gong, J. Wang, Y. Lin, Z. Yang, H. Pan and Z. Xu, *Appl. Surf. Sci.*, **2019**, 476, 600-607.

[6] P. P. Edwards, V. L. Kuznetsov, W. I. F. David and N. P. Brandon, *Energy Policy*, **2008**, **36**, 4356-4362.

[7] I. Stadler and M. Sterner, in *Urban Energy Transition (Second Edition)*, ed. P. Droege, Elsevier, 2018, DOI: https://doi.org/10.1016/B978-0-08-102074-6.00026-7, pp. 225-244.

[8] I. P. Jain, *Int. J. Hydrog. Energy*, **2009**, 34, 7368-7378.

[9] M. Ball and M. Wietschel, *Int. J. Hydrog. Energy*, **2009**, 34, 615-627.

[10] D. K. Liguras, D. I. Kondarides and X. E. Verykios, *Appl. Catal. B: Environ.*, **2003**, 43, 345-354.

[11] F. Si, C. Tang, Q. Gao, F. Peng, S. Zhang, Y. Fang and S. Yang, *J. Mater. Chem. A*, **2020**, 8, 3083-3096.

[12] J. Wang, W. Cui, Q. Liu, Z. Xing, A. M. Asiri and X. Sun, *Adv. Mater.*, **2016**, 28, 215-230.

[13] A. Boudghene Stambouli and E. Traversa, *Renew. Sust. Energ. Rev.*, **2002**, 6, 295-304.

[14] J.-S. Lee, S. Tai Kim, R. Cao, N.-S. Choi, M. Liu, K. T. Lee and J. Cho, *Adv. Energy Mater.*, **2011**, 1, 34-50.

[15] W. Kreuter and H. Hofmann, *Int. J. Hydrog. Energy*, **1998**, 23, 661-666.

[16] S. R. Kelly, X. Shi, S. Back, L. Vallez, S. Y. Park, S. Siahrostami, X. Zheng and J. K. Nørskov, *ACS Catal.*, **2019**, 9, 4593-4599.

[17] F. Cheng and J. Chen, *Chem. Soc. Rev.*, **2012**, 41, 2172-2192.

[18] https://en.wikipedia.org/wiki/William_Robert_Grove.

[19] https://www.nasa.gov/centers/glenn/technology/fuel_cells.html

[20] B. D. McNicol, D. A. J. Rand and K. R. Williams, *J. Power Sources*, **2001,** 100, 47-59.

[21] W. Reitz, *Mater. Manuf. Process.*, **2007**, 22, 789-789.

[22] A. A. Gewirth and M. S. Thorum, *Inorg. Chem.*, **2010**, 49, 3557-3566.

[23] J. R. Varcoe and R. C. T. Slade, *Fuel Cells*, **2005,** 5, 187-200.

[24] M. A. Hickner, H. Ghassemi, Y. S. Kim, B. R. Einsla and J. E. McGrath, *Chem. Rev.*, **2004**, 104, 4587-4612.

[25] W. A. Meulenberg, M. E. Ivanova, J. M. Serra and S. Roitsch, in *Advanced Membrane Science and Technology for Sustainable Energy and Environmental Applications*, eds. A. Basile and S. P. Nunes, Woodhead Publishing, 2011, DOI: https://doi.org/10.1533/9780857093790.4.541, pp. 541-567.

[26] Barbir F. (1995) Progress in PEM Fuel Cell Systems Development. In: Yürüm Y. (eds) Hydrogen Energy System. NATO ASI Series (Series E: Applied Sciences), vol 295. Springer, Dordrecht.

[27] F. Y. Cheng and J. Chen, *Chem. Soc. Rev.*, **2012**, 41, 2172.

[28] R. Cao, J. S. Lee, M. L. Liu and J. Cho, Adv. Energy Mater., **2012**, 2, 816.

[29] J. S. Lee, S. T. Kim, R. Cao, N. S. Choi, M. Liu, K. T. Lee and J. Cho, *Adv. Energy Mater.*, **2011**, 1, 34.

[30] V. R. Stamenkovic, D. Strmcnik, P. P. Lopes and N. M. Markovic, *Nat. Mater.*, **2017**, 16, 57-69.

[31] M. Carmo, D. L. Fritz, J. Mergel and D. Stolten, *Int. J. Hydrog. Energy*, **2013**, 38, 4901-4934.

[32] B. Conway and B. Tilak, *Electrochim. Acta*, **2002**, 47, 3571-3594.

[33] Y. Li, H. Wang, L. Xie, Y. Liang, G. Hong and H. Dai, *J. Am. Chem. Soc.*, **2011**, 133, 7296-7299.

[34] J. Greeley, T. F. Jaramillo, J. Bonde, I. Chorkendorff and J. K. Norskov, *Nat. Mater.*, **2006**, 5, 909-913.

[35] T. F. Jaramillo, *Science*, **2007**, 317, 100-102.

[36] S. Schuldiner, *J. Electrochem. Soc.*, **1959**, 106, 891-895.

[37] B. Cao, G. M. Veith, J. C. Neuefeind, R. R. Adzic and P. G. Khalifah, *J. Am. Chem. Soc.*, **2013**, 135, 19186-19192.

[38] H. Vrubel and X. Hu, *Angew. Chemie Int. Ed.*, **2012**, 51, 12703-12706.

[39] D. Voiry, H. Yamaguchi, J. Li, R. Silva, D. C. B. Alves, T. Fujita, M. Chen, T. Asefa, V. B. Shenoy, G. Eda and M. Chhowalla, *Nat. Mater.*, **2013**, 12, 850-855.

[40] W.-F. Chen, K. Sasaki, C. Ma, A. I. Frenkel, N. Marinkovic, J. T. Muckerman, Y. Zhu and R. R. Adzic, *Angew. Chemie Int. Ed.*, **2012**, 51, 6131-6135.

[41] D. Kong, J. J. Cha, H. Wang, H. R. Lee and Y. Cui, *Energy Environ. Sci.*, **2013**, 6, 3553-3558.

[42] Z. W. Seh, K. D. Fredrickson, B. Anasori, J. Kibsgaard, A. L. Strickler, M. R. Lukatskaya, Y. Gogotsi, T. F. Jaramillo and A. Vojvodic, *ACS Energy Lett.*, **2016**, 1, 589-594.

[43] J. K. Nørskov, T. Bligaard, A. Logadottir, J. R. Kitchin, J. G. Chen, S. Pandelov and U. Stimming, *J. Electrochem. Soc.*, **2005**, 152, J23-J26.

[44] E. J. Popczun, J. R. McKone, C. G. Read, A. J. Biacchi, A. M. Wiltrout, N. S. Lewis and R. E. Schaak, *J. Am. Chem. Soc.*, **2013**, 135, 9267-9270.

[45] M. R. Gennero de Chialvo and A. C. Chialvo, *J. Electroanal. Chem.*, **1998**, 448, 87-93.

[46] G. Schiller, R. Henne, P. Mohr and V. Peinecke, *Int. J. Hydrog. Energy*, **1998**, 23, 761-765.

[47] J. D. Benck, T. R. Hellstern, J. Kibsgaard, P. Chakthranont and T. F. Jaramillo, *ACS Catal.*, **2014**, 4, 3957-3971.

[48] L. Liao, J. Zhu, X. Bian, L. Zhu, M. D. Scanlon, H. H. Girault and B. Liu, *Adv. Funct. Mater.*, **2013**, 23, 5326-5333.

[49] Z. Chen, D. Cummins, B. N. Reinecke, E. Clark, M. K. Sunkara and T. F. Jaramillo, *Nano Lett.*, **2011**, 11, 4168-4175.

[50] D. Kong, H. Wang, J. J. Cha, M. Pasta, K. J. Koski, J. Yao and Y. Cui, *Nano Lett.*, **2013**, 13, 1341-1347.

[51] J. Kibsgaard, Z. Chen, B. N. Reinecke and T. F. Jaramillo, *Nat. Mater.*, **2012**, 11, 963-969.

[52] H. G. S. Casalongue, J. D. Benck, C. Tsai, R. K. B. Karlsson, S. Kaya, M. L. Ng, L. G. M. Pettersson, F. Abild-Pedersen, J. K. Nørskov, H. Ogasawara, T. F. Jaramillo and A. Nilsson, *J. Phys. Chem. C*, **2014**, 118, 29252-29259.

[53] D. Merki, H. Vrubel, L. Rovelli, S. Fierro and X. Hu, *Chem. Sci.*, **2012**, 3, 2515-2525.

[54] T. F. Jaramillo, J. Bonde, J. Zhang, B.-L. Ooi, K. Andersson, J. Ulstrup and I. Chorkendorff, *J. Phys. Chem. C*, **2008**, 112, 17492-17498.

[55] J. Kibsgaard, T. F. Jaramillo and F. Besenbacher, *Nat. Chem.*, **2014**, 6, 248-253.

[56] Y. Zhao, F. Zhao, X. Wang, C. Xu, Z. Zhang, G. Shi and L. Qu, *Angew. Chemie Int. Ed.*, **2014**, 53, 13934-13939.

[57] Y. Zheng, Y. Jiao, Y. Zhu, L. H. Li, Y. Han, Y. Chen, A. Du, M. Jaroniec and S. Z. Qiao, *Nat. Commun.*, **2014,** 5, 3783.

[58] Y. Ito, W. Cong, T. Fujita, Z. Tang and M. Chen, *Angew. Chemie Int. Ed.*, **2015**, 54, 2131-2136.

[59] Y. Zheng, Y. Jiao, L. H. Li, T. Xing, Y. Chen, M. Jaroniec and S. Z. Qiao, *ACS Nano*, **2014**, 8, 5290-5296.

[60] W. Cui, Q. Liu, N. Cheng, A. M. Asiri and X. Sun, *Chem. Commun.*, **2014**, 50, 9340-9342.

[61] J. Durst, *Energy Environ. Sci.*, **2014**, **7**, 2255-2260.

[62] K. J. P. Schouten, M. J. T. C. van der Niet and M. T. M. Koper, *Phys. Chem. Chem. Phys.*, **2010**, 12, 15217-15224.

[63] J. K. Nørskov, J. Rossmeisl, A. Logadottir, L. Lindqvist, J. R. Kitchin, T. Bligaard, H. Jónsson, *J. Phys. Chem. B*, **2004**, 108, 17886-17892

[64] L. Zhang, L. T. Roling, X. Wang, M. Vara, M. Chi, J. Liu, S.-I. Choi, J. Park, J. A. Herron, Z. Xie, M. Mavrikakis and Y. Xia, *Science*, **2015**, 349, 412-416.

[65] S. Guo, D. Li, H. Zhu, S. Zhang, N. M. Markovic, V. R. Stamenkovic and S. Sun, *Angew. Chemie Int. Ed.*, **2013**, 52, 3465-3468.

[66] B. Lim, M. Jiang, P. H. C. Camargo, E. C. Cho, J. Tao, X. Lu, Y. Zhu and Y. Xia, *Science*, **2009**, 324, 1302-1305.

[67] Z. Chen, M. Waje, W. Li and Y. Yan, *Angew. Chemie Int. Ed.*, **2007**, 46, 4060-4063.

[68] C. Wang, H. Daimon, Y. Lee, J. Kim and S. Sun, *J. Am. Chem. Soc.*, **2007**, 129, 6974-6975.

[69] V. R. Stamenkovic, B. S. Mun, M. Arenz, K. J. J. Mayrhofer, C. A. Lucas, G. Wang, P. N. Ross and N. M. Markovic, *Nat. Mater.*, **2007**, 6, 241.

[70] C. Chen, Y. Kang, Z. Huo, Z. Zhu, W. Huang, H. L. Xin, J. D. Snyder, D. Li, J. A. Herron, M. Mavrikakis, M. Chi, K. L. More, Y. Li, N. M. Markovic, G. A. Somorjai, P. Yang and V. R. Stamenkovic, *Science*, **2014**, 343, 1339-1343.

[71] V. R. Stamenkovic, B. Fowler, B. S. Mun, G. Wang, P. N. Ross, C. A. Lucas and N. M. Marković, *Science*, **2007**, 315, 493-497.

[72] X. Huang, Z. Zhao, L. Cao, Y. Chen, E. Zhu, Z. Lin, M. Li, A. Yan, A. Zettl, Y. M. Wang, X. Duan, T. Mueller and Y. Huang, *Science*, **2015**, 348, 1230-1234.

[73] G. Wu, K. L. More, C. M. Johnston and P. Zelenay, *Science*, **2011**, 332, 443-447.

[74] N.-T. Suen, S.-F. Hung, Q. Quan, N. Zhang, Y.-J. Xu and H. M. Chen, *Chem. Soc. Rev.*, **2017**, 46, 337-365.

[75] T. Reier, H. N. Nong, D. Teschner, R. Schlögl and P. Strasser, *Adv. Energy Mater.*, **2017**, 7, 1601275.

[76] T. Reier, M. Oezaslan and P. Strasser, *ACS Catal.*, **2012**, 2, 1765-1772.

[77] C. C. L. McCrory, S. Jung, J. C. Peters and T. F. Jaramillo, *J. Am. Chem. Soc.*, **2013**, 135, 16977-16987.

[78] J. Suntivich, K. J. May, H. Gasteiger, J. B. Goodenough and Y. Shao-horn, *Science*, **2011**, 334, 2010-2012.

[79] M. Risch, K. A. Stoerzinger, B. Han, T. Z. Regier, D. Peak, S. Y. Sayed, C. Wei, Z. Xu and Y. Shao-Horn, *J. Phys. Chem. C*, **2017**, 121, 17682-17692.

[80] Y. Liang, Y. Li, H. Wang, J. Zhou, J. Wang, T. Regier and H. Dai, *Nat. Mater.*, **2011**, 10, 780.

[81] Y. Lee, J. Suntivich, K. J. May, E. E. Perry and Y. Shao-Horn, *J. Phys. Chem. Lett.*, **2012**, 3, 399-404.

[82] L. C. Seitz, C. F. Dickens, K. Nishio, Y. Hikita, J. Montoya, A. Doyle, C. Kirk, A. Vojvodic, H. Y. Hwang, J. K. Norskov and T. F. Jaramillo, *Science*, **2016**, 353, 1011-1014.

[83] R. Subbaraman, D. Tripkovic, K.-C. Chang, D. Strmcnik, A. P. Paulikas, P. Hirunsit, M. Chan, J. Greeley, V. Stamenkovic and N. M. Markovic, *Nat. Mater.*, **2012**, 11, 550.

[84] S. Dresp, F. Luo, R. Schmack, S. Kühl, M. Gliech and P. Strasser, *Energy Environ. Sci.*, **2016**, 9, 2020-2024.

[85] J. Zhang, Z. Zhao, Z. Xia and L. Dai, *Nat. Nanotechnol.*, **2015**, 10, 444.

Chapter 2

Nitrogen-Doped Graphene with a Three-Dimensional Architecture Assisted by Carbon Nitride Tetrapods as an Efficient Metal-Free Electrocatalyst for Hydrogen Evolution

Current polymer membrane-based electrolyzers use Pt as a cathode catalyst for efficient reduction of water. The high cost of the Pt-based catalysts forces researchers to develop alternative electrocatalysts. Here, a simple strategy has been proposed to synthesize a metal-free electrocatalyst for the hydrogen evolution reaction (HER) by high-temperature annealing of graphene oxide-coated melamine foam. The prepared catalyst possesses both structural and functional advantages with its three-dimensional (3D) interconnected arms of carbon nitride (CN_x) backbone wrapped with nitrogen-doped graphene (N-RGO) sheets (CN_x@N-RGO). CN_x@N-RGO faces only a 193 mV overpotential to achieve a current density of 10 mA cm^{-2}, which is far superior to the previously reported Pt-free systems. Along with the high exchange current density of $34.7*10^{-6}$ A cm^{-2} and low Tafel slope of 54 mV dec^{-1}, CN_x@N-RGO follows a Volmer-Heyrovsky mechanism for HER. DFT calculations show that the synergy between CN_x and N-RGO facilitates good electrical coupling between the two moieties and provides optimal binding to H^+ ions on the catalyst that, in turn, results in efficient reduction of hydrogen ions.

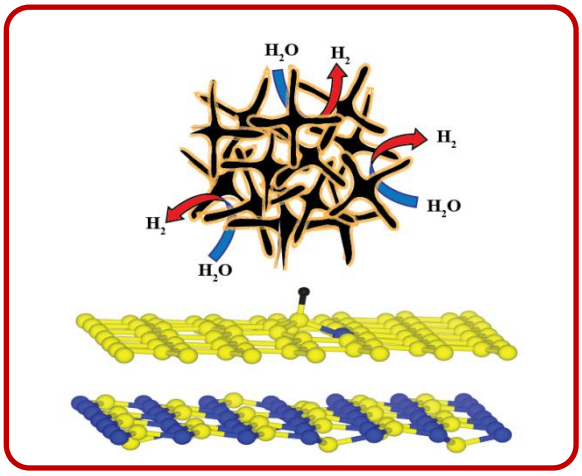

Content of this chapter is published in the following article:

ChemElectroChem, 2017, 4, 2643-2652

(https://chemistry-europe.onlinelibrary.wiley.com/doi/10.1002/celc.201700479**)**

Reproduced with permission from **John Wiley and Sons, License Number: 4871291437359**

2.1 Introduction

Hydrogen, a green fuel, is the next major contender of the world's energy needs to replace the fossil fuels.[1-3] Apart from the hydrocarbon cracking for the production of hydrogen, electrochemical reduction of water is an economically feasible and greener approach.[4-9] The cathodic hydrogen evolution reaction (HER) in proton exchange membrane (PEM) water electrolyzer requires an efficient electrocatalyst to attain a high current at low overpotential.[10] Platinum (Pt) is being considered as the most favourite HER catalyst in PEM electrolyzer considering its high exchange current density, low Tafel slope and extremely low free energy of hydrogen binding.[11-13] However, the high cost and scarcity of Pt urge researchers to search for an alternative catalyst for HER.[14] Large numbers of earth abundant transition metal catalysts are developed for HER to replace the state-of-the-art Pt catalysts. Of these, the non-noble metal catalysts based on Mo, W, Ni compounds, including their carbides, nitrides, sulphides, etc. have gained substantial space in the literature.[15-20] However, the inherent vulnerability to corrosion and passivation in acidic media impose limitations to opt these materials as the viable replacements for the proven Pt catalysts.[21] This triggers efforts into the search of active and durable carbon based metal-free systems for HER.

There has been an increasing thrust on developing metal-free electrocatalysts with different carbon morphologies and easily tunable molecular structure as cost-effective alternatives to the state-of-the-art HER catalysts. In this class, the electrocatalysts based on heteroatom-doped carbon and graphitic carbon nitrides (g-C_3N_4) are found to be promising towards HER.[22-25] Although they are excellent candidates considering the corrosion resistive nature, these materials suffer from high overpotential towards HER in comparison with Pt/C. On the other hand, even though the theoretical evidence highlights the key role played by the metal-H bond formation for enabling HER on the metallic catalyst surface, an insightful investigation unraveling the hydrogen evolution mechanism in the metal-free system is not available as of now. Hence, the present efforts for developing the metal-free catalysts for HER are generally not based on strategically building the desired active centres. In this scenario, the structural modifications and the spatial arrangement of the doped carbon morphologies are being practiced as the viable means to boost the HER activity of such metal-free electrocatalysts. By modifying the spatial arrangement of the doped carbon, one can improve the active

reaction centres and reactant/product distributions in the electrocatalyst.[26-28] Even though such structural and functional modifications are found to help reduce the overpotential for HER, significant breakthroughs in this direction are yet to be achieved.

In order to understand the existing challenges on the development of effective metal-free electrocatalysts for various applications, our research group has made advances by designing electrocatalysts in which the required features such as exposed active sites, open and interconnected channels for reactant distribution, and electrical conductivity are simultaneously established. We have recently reported an electrocatalyst consisting of interconnected tetrapods of CN_x acting as nano-hangers for nitrogen-doped graphene as a versatile catalyst for oxygen reduction reaction (ORR).[29] In our later studies, we have observed that same catalyst, which as such is less active towards HER, could be activated for hydrogen evolution application by affecting some changes in the synthesis protocol. This has been mainly accomplished by reducing the nitrogen-doped graphene layer thickness in the bilayer structure by simultaneously decreasing the graphene oxide (GO) concentration and controlling the adsorption of GO on the melamine sponge in the synthesis step. This study is also focused on to understand the nature of the active sites and their influence on the Gibbs free energy for the reaction by performing first-principles density functional theory (DFT) based calculations. Our experiments on HER have revealed that this catalyst possessing the integrated features works very well for this application with a substantially reduced overpotential in acidic condition. The catalyst, designated as CN_x@N-RGO, consists of the active sites for HER on nitrogen-doped reduced graphene oxide (N-RGO) layers, which are wrapped in the interconnected arms of the tetrapods of the carbon nitride (CN_x). CN_x@N-RGO retains a three-dimensional (3D) morphology, which is achieved by a simple dip coating strategy as illustrated in **Figure 2.1**. The spatial rearrangement of N-RGO on CN_x provides the high density of in-plane nitrogen coordinated active centers whereas the 3D macroporous morphology assists efficient reactant/product distribution. This controlled structure property interplay positions this metal-free system as a competitive electrocatalyst for HER in acidic condition with a substantially low overpotential of 193 mV to attain a current density of 10 mA cm^{-2}. To the best of our knowledge, this is the lowest overpotential reported for a non-metallic electrocatalyst for HER.

2.2 Experimental Section

2.2.1 Preparation of CN_x@N-RGO

For the preparation of CN_x@N-RGO, we have followed our own reported procedure, which is briefly illustrated here.[29] The melamine foam purchased from Global Nanotech-Mumbai, India, was used for the preparation of CN_x@N-RGO. The square pieces (1×1 cm^2) of melamine foam were dipped in the graphene oxide (GO) solution in water (2 mg ml^{-1}) for 5 min. to achieve complete absorption of GO by the foam. The GO-soaked melamine foam was then kept for drying under an IR lamp for 6 h. The dried melamine foam with adsorbed GO was annealed in an argon atmosphere at 900 ^oC for 3 h. This thermal annealing under inert atmosphere converts the foam into an interconnected network consisting of the tetrapods of CN_x bearing the nitrogen doped reduced graphene oxide (N-RGO) sheets (CN_x@N-RGO). Thermal decomposition of melamine expels nitrogen, which gets harvested by GO, leading to the formation of N-RGO. GO loading in the melamine foam was varied by changing the dipping number of the melamine foam in the GO solution.

2.2.2 Preparation of Nitrogen-Doped Graphene (N-RGO)

As a control sample, free-standing N-RGO was separately synthesized by annealing a mixture of GO with melamine powder followed by annealing at 900 ^oC for 3 h under argon atmosphere. Here, the melamine powder acts as the nitrogen precursor, which, unlike the melamine foam, decomposes completely without giving the residue of CN_x.

2.2.3 Synthesis of Graphene Oxide (GO)

GO was synthesized by improved Hummer's method. 3 g of graphite powder was grounded well with 18 g $KMnO_4$ to get fine powder. The above mixture was added slowly into a 9:1 mixture of concentrated H_2SO_4 and H_3PO_4 (400 ml) with constant stirring. The resultant dark green mixture was then kept in an oil bath at a temperature of 60 ^oC for 12 h with continuous stirring. The colour of the reaction mixture was changed to pink. The resulting solution was then diluted gradually and carefully with an excess of ice-cold distilled water containing 5 ml of H_2O_2. The colour of the mixture turned to bright yellow at this stage. The mixture was centrifuged and washed with excess of distilled water for a number of times until the pH of the solution becomes

higher than 3. The resultant brownish solution was then washed 3-4 times with ethanol. Finally, the viscous brownish solution was coagulated using diethyl ether and the product was filtered. The GO thus obtained was dried in a vacuum oven at a temperature of 60 ^{o}C. It is used as the starting material for further studies.

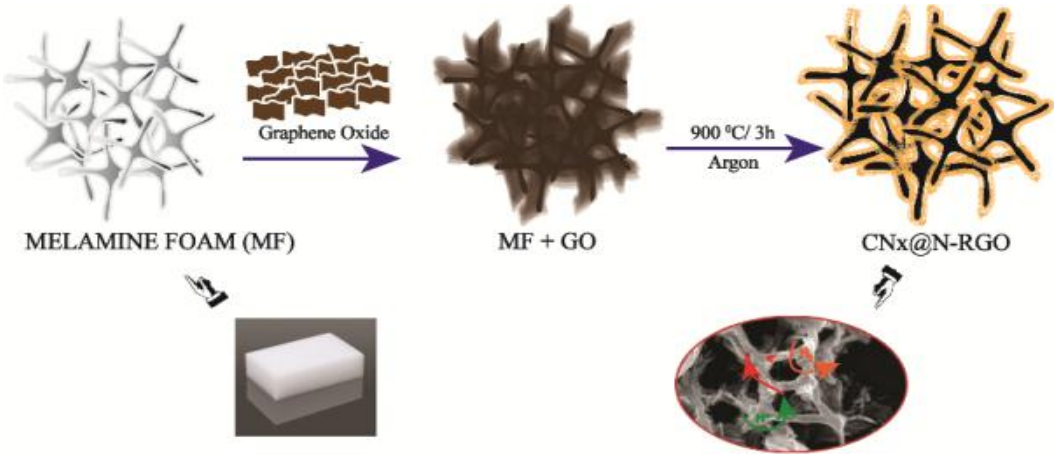

Figure 2.1 *A pictorial representation illustrating the preparation of the CN_x@N-RGO catalyst using melamine foam and graphene oxide (GO). Decomposition of the GO-soaked melamine foam generates interconnected tetrapods of graphitic carbon nitride (CN_x) with wrapped and specially separated layers of nitrogen-doped reduced graphene oxide (N-RGO).*

2.2.4 Computational Study

All the calculations were performed using Quantum ESPRESSO software, a plane wave based implementation of density functional theory,[30] to solve the spin polarized KohnSham equations. The electronic exchange and correlation potential is described by the generalized gradient approximation (GGA) based parameterization of Perdew-Burke-Ernzerhof (PBE).[31] The van der Waals interactions, that are usually not included in conventional DFT functional, are incorporated using semi-empirical Grimme's scheme to better describe the non-bonding interaction between the graphitic carbon nitride (g-CN) and graphene (Gr).[32] Ultrasoft pseudo potentials were used to describe the electron-ion interactions.[33] A plane wave basis set was used with kinetic energy cut-off 35 Ry, and charge density cut-off 300 Ry. To model nitrogen doping, we have considered a (6×6) supercell. The Brillouin-zone integrations were done with a 6x6x1 Monkhorst-Pack (MP) k-point mesh.[34] In order to minimize the spurious interactions between the periodic images, we have used a vacuum of at least 15 Å.

2.2.4a Calculation of N defect formation energies:

The formation energy of the N doped systems was calculated using the following equation,

$$E_{form} = E_{CNx@N-RGO} - E_{CNx@RGO} - \frac{n}{2}E_{N_2} + m\,E_{C_{Gr}} \quad (2.1),$$

where, $E_{CNx@N-RGO}$ is the total energy of the N doped system, $E_{CNx@RGO}$ is the total energy of the undoped system, $E_{C_{Gr}}$ is the energy of the graphene per C atom, *n* is the number of the N atoms doped, E_{N_2} is the total energy of the gas phase nitrogen molecule, *m* is the number of the C atoms removed from CN_x-RGO to form the N doped system.

2.2.4b Charge transfer calculations:

The charge transfer ($\Delta\rho(r)$) is given by:

$$\Delta\rho(r) = \rho(r)_{bl} - \rho(r)_{l1} - \rho(r)_{l2}, \quad (2.2)$$

where, $\rho(r)_{bl}$, $\rho(r)_{l1}$, and $\rho(r)_{l2}$ are the charge density of the bilayer (CN_x@RGO or CN_x@N-RGO), layer 1 (CN_x) and layer 2 (RGO or N-RGO), respectively. The charge density of the later two is calculated in the same geometry as that in the bilayer.

2.2.4c Calculation of H adsorption energy and change in Gibbs free energy due to H adsorption:

The H adsorption energy (ΔE_{H*}) was calculated as,

$$\Delta E_{H*} = E_{s+nH} - E_s - \frac{n}{2}E_{H_2} \quad (2.3)$$

where, E_{s+nH} is the total energy of the bilayer with the hydrogen adsorbed on it, E_s is the total energy of the clean bilayer, $E_{H_2}$is the total energy of the gas phase hydrogen molecule and *n* is the number of hydrogen atoms adsorbed. $E_{H_2}$was calculated by taking a H_2 molecule in a cubic-cell having dimensions of 15 Å. The H-H bond length is obtained to be 0.75 Å with a binding energy of -4.52 eV. The calculated values are in good agreement with the experimental values of 0.74 Å and -4.52 eV. The change in the Gibbs free energy for the hydrogen absorbed state, that is the second step in the HER pathway, was corrected for change in entropy and zero point energy as,

$$\Delta G_{H*} = \Delta E_{H*} + \Delta E_{ZPE*} - T\Delta S_H \quad (2.4)$$

where, $\Delta E_{ZPE*}$is the difference in the zero-point energy between the adsorbed hydrogen and hydrogen in the gas phase, T is the temperature and ΔS_H is the entropy difference between the adsorbed state and the gas phase. As the contribution from the vibrational entropy of H in the adsorbed state is negligibly small, the entropy of hydrogen adsorption is $\Delta S_H = -\frac{1}{2}S_{H_2}$, where S_{H_2} is the entropy of H_2 in the gas phase at the standard conditions. Then, the Gibbs free energy with the overall corrections is given by$\Delta G_{H*} = \Delta E_{H*} + 0.24$ eV[2].

2.2.5 Material characterization

High-resolution transmission electron microscopic (HR-TEM) images were recorded by operating an FEI Technai G2 T20 instrument at 300 kV. A Quanta 200 3D FEI instrument was used to record the scanning electron microscopic (SEM) images. Raman analysis was performed with the help of a LabRam spectrometer (HJY, France) equipped with a laser wavelength of 632 nm whereas the X-ray diffraction (XRD) patterns were recorded on the PANalytical instrument using Cu Kα radiation (λ=1.54 Å) by operating at a scanning rate of 2^o min^{-1} and a step size of 0.02^o in 2θ. The surface investigation on the coordinated states of the moieties was mainly performed with the help of a VG Micro Tech ESCA 300^o X-ray photoelectron spectroscopy (XPS) at a pressure of $>1\times10^{-9}$ Torr (pass energy 50 eV, electron take-off angle 60^o, and the overall resolution ~0.1 eV). The surface area and pore size distribution of the sample were investigated using a Quantachrome Quandrasorb automatic volumetric measurement system. The instrument was operated at 77 K using ultra-pure nitrogen gas.

2.2.6 Electrochemical characterization

A set of electrochemical methodologies was adopted for performing the electrochemical measurements and a Biologic electrochemical workstation (VMP3) was used for this purpose. The measurements were performed using a conventional three-electrode setup by using 0.5 M H_2SO_4 as the electrolyte, a glassy carbon rotating disc electrode coated with the catalyst (Pine Instruments Inc.) as the working electrode and $Hg/HgSO_4$ as the reference electrode. The electrode potential measured using the $Hg/HgSO_4$ electrode was normalized for hydrogen electrode (RHE), for which the following equation was used:

($E_{RHE} = E_{Hg/HgSO4} + 0.650 + 0.059$ pH (2.5)

To prevent any possible Pt contamination during the measurements, a graphite rod, instead of a Pt rod, was used as the counter electrode. 10 mg of the catalyst in 2 ml of 2:3 mixture of isopropyl alcohol and water was sonicated for 1 h to prepare the catalyst ink. 10 µl from this ink was drop cast on the glassy carbon electrode, followed by drying under an IR lamp. Subsequently, 1 µl of 0.01 wt. % Nafion solution in ethanol was applied on the catalyst, which acts as a binder as well as an ionomer. The final working electrode formed at this stage has a catalyst loading of 250 µg cm^{-2}. By following the same protocol, another electrode was prepared by coating the commercial 40 wt. % Pt/C from Johnson Mattey (Alpha Acessar) for comparative purpose

2.3 Result and Discussion

High-temperature annealing of the GO-soaked melamine foam in the presence of an inert gas (Argon) produces CN_x@N-RGO. This has been attained by the decomposition of melamine to CN_x (*i.e.*, the graphitic carbon nitride) with a concomitant reduction of GO to RGO and doping of the expelled nitrogen from melamine on RGO to form N-RGO.[35, 36] The high-temperature annealing of melamine foam in the inert atmosphere leads to the carbonization of the sponge material. The chemical structure of melamine foam consists of formaldehyde-melamine-sodium bisulphite copolymer. The melamine is a rich source of nitrogen which is being used as a nitrogen precursor in many chemical reactions. Since melamine sponge contains a high amount of nitrogen content, during carbonization at high temperature, it forms carbon nitride with chemical formula CN_x. It is neither forming an exact graphitic carbon nitride of formula C_3N_4 and nor graphitic carbon. Here, CN_x attains an interconnected tetrapod-like scaffold for N-RGO, which not only prevents restacking of the N-RGO layers but the morphology also ensures a 3D network with enhanced exposed surface area and accessible pores. Thus, through this transformation, the CN_x@N-RGO electrocatalyst attains a high density of inplane nitrogen and efficient reactant/product distribution through the 3D micropores. With these structural and functional features, an essential requirement needed for an electrocatalyst for an application like HER is fulfilled.

2.3.1 SEM analysis

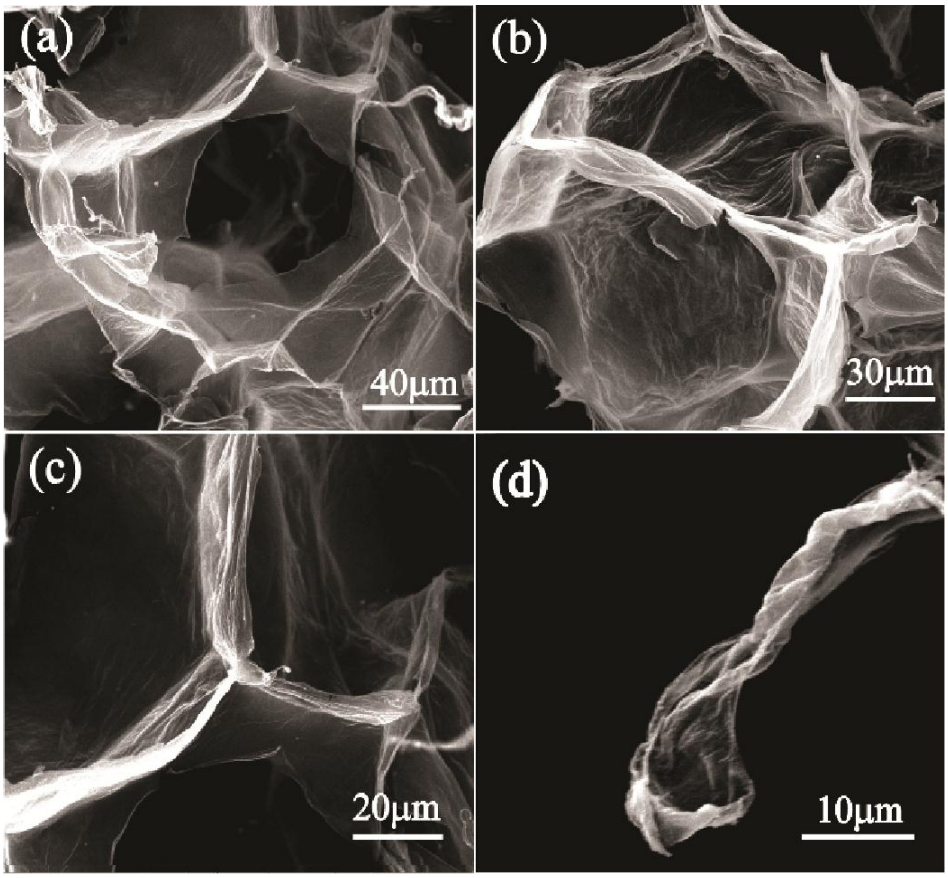

Figure 2.2 *(a, b) SEM images representing an interconnected 3D network of CN_x@N-RGO at different magnifications; c) the tetrapod structure of CN_x@N-RGO; d) the single arm of the tetrapod of CN_x@N-RGO, showing the wrapping of the arm by the N-RGO sheet.*

The SEM images of the CN_x@N-RGO as presented in **Figure 2.2a to d** clearly depicts the 3-D interconnected macroporous framework structure of the system, where the N-RGO layers are found to be spread-out on the CN_x backbone and give a "tent-like" morphology. Thin layer of the graphene sheets over the CN_x tetrapods with the eventual formation of the well interconnected porous and accessible morphology is clearly evident from the set of the SEM images presented in the figure. The length of each arm of the tetrapod structure is in the range of 10-30 μm with a width of 0.4-1 μm range. **Figure 2.3a** represents the SEM image of bare CN_x formed by annealing the melamine foam without incorporating GO. The CN_x tetrapods in this case are found to be less interconnected due to crumbling, presumably happened due to the thermal stress induced during the annealing process. However, a comparison of the morphology

of the bare CN_x with its N-RGO loaded counterpart indicates that the RGO layer on the CN_x backbone favorably assists the system to attain the 3D interconnected morphology. This 3D architecture is expected to improve efficient mass distribution throughout the structure. Along with this, the high temperature reduced NRGO provides better electrical conductivity and aerophobic nature to the N-RGO wrapped structure.[37, 38]

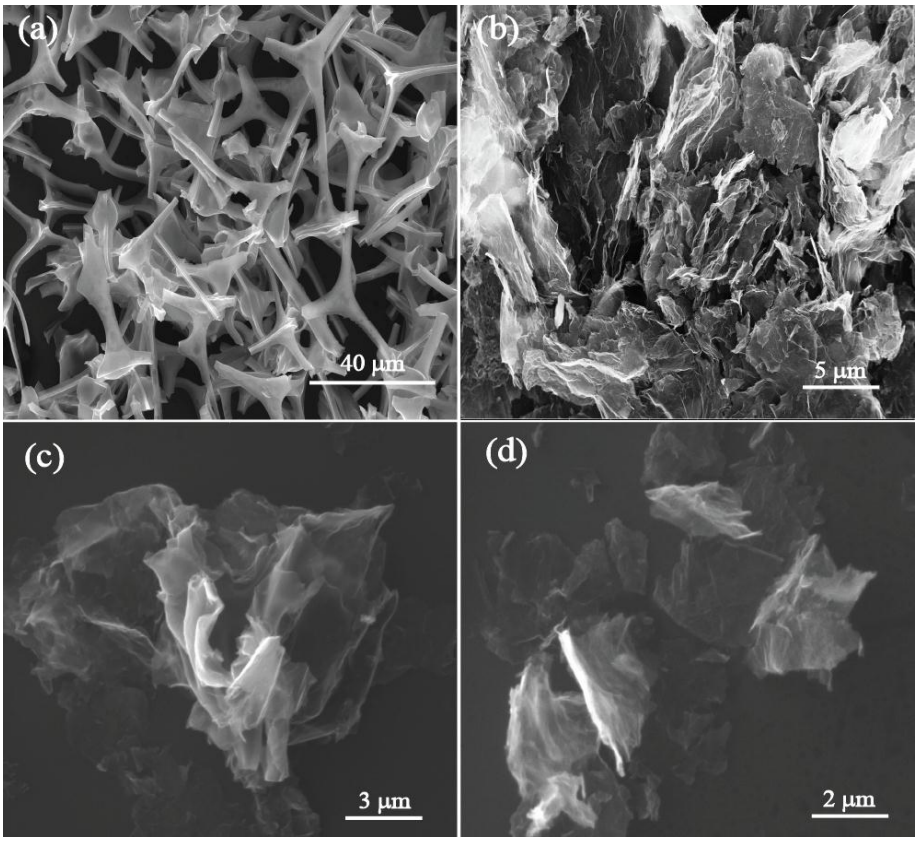

Figure 2.3 *(a) SEM image of the annealed melamine foam (CN_x) without GO, which clearly shows the tetrapod structure of the unwrapped CN_x, (b) SEM image representing the stacked structure of N-RGO prepared directly from GO and the nitrogen precursor, (c and d) SEM images of CN_x@N-RGO synthesized by dipping melamine foam in the GO solution for 6 times.*

The role of the CN_x scaffold in establishing the unique layer-separated distribution of N-RGO can be visualized from the SEM image of N-RGO presented in **Figure 2.3b**, which was prepared directly from GO and melamine powder as the nitrogen precursor. Unlike its CN_x based counterpart, the N-RGO layers in this material are stacked together, suffering from the inherent

issues like poor exposure and accessibility of the active sites. The morphology of the "tent-like" structure also strongly depends on the number of dipping of the melamine foam in the GO solution.[29] The increased content of N-RGO collapses the 3D morphology of CN_x@N-RGO with an eventual formation of a sheet-like structure (**Figure 2.3c and d**).

2.3.2 TEM analysis

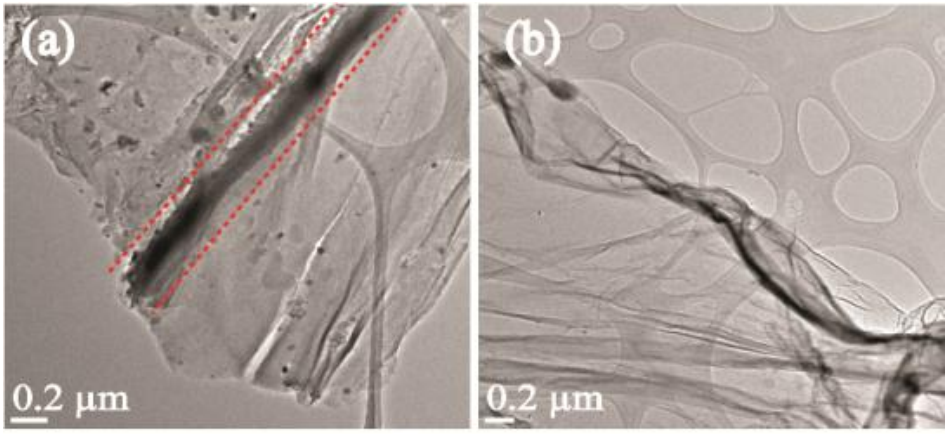

Figure 2.4 *(a) and (b) TEM images of CN_x@N-RGO, indicating a portion of the arm of CN_x (indicated with red outlines) roofed by a thin layer of N-RGO.*

The transmission electron microscopic (TEM) image of CN_x@N-RGO (**Figure 2.4a**) depicts the presence of a thin layer of N-RGO resting on the top of the arm of the CN_x tetrapod, which is represented with a red outline in the figure. A more selective imaging recorded at the edge of CN_x@N-RGO clearly shows the typical transparent nature of the few-layer N-RGO (**Figure 2.4b**). Thus, the process adopted here ensured a layer-separated distribution of N-RGO, helping the system to expose maximum of its active sites readily available for the reactants during its application for HER. This gets further benefited from the enhanced reactant distribution possible in the system due to its interconnected 3D microporous structure. Thus, the presence of well-designed channels for the reactant distribution and exposed active sites in the close proximity along the channel surface make the system more adaptable for tackling the reaction, which includes adsorption and subsequent reduction of hydrogen ions. In conjunction with this, the aerophobic nature of the N-RGO is expected to assist quick removal of the produced gases, making the active center readily available for a fresh round of reaction again.

2.3.3 Raman and XRD analysis

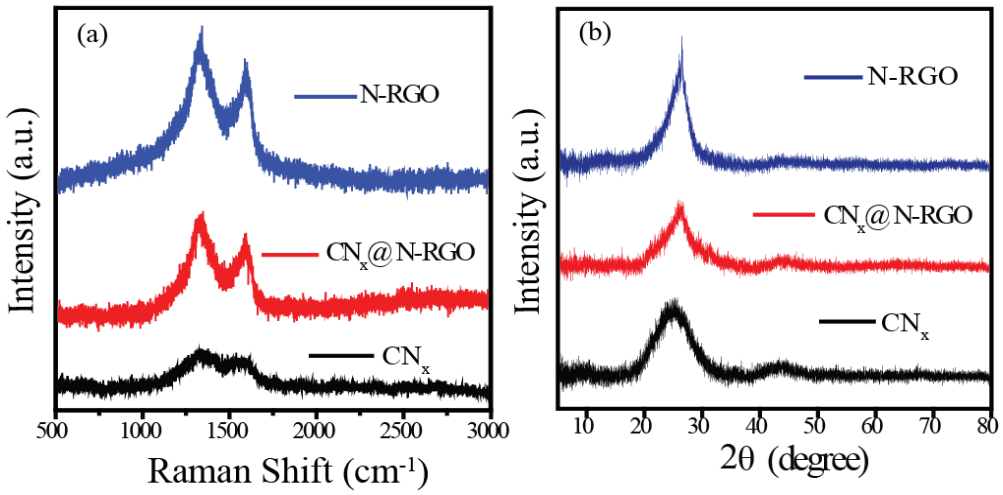

Figure 2.5 *(a) Raman spectra and (b) XRD profiles of CN_x@N-RGO, CN_x and NRGO.*

Raman spectra give confirmation on the defects created due to nitrogen doping in the sp^2 lattice of RGO by high temperature synthesis process (**Figure 2.5a**). The spectrum corresponding to CN_x@N-RGO shows the G-band and D-band at 1596 cm^{-1} and 1332 cm^{-1}, respectively. The G-band position in this case is found to be shifted to the positive side by 15 cm^{-1} with respect to the pure graphite, indicating the presence of defects in the system.[39] However, in the case of CN_x, due to the lack of sp^2 carbon sites, a downshift in the G-band (1569 cm^{-1}) position is observed. On the other hand, N-RGO, *i.e.*, the sample that does not contain CN_x, shows the G-band frequency lower by 5 cm^{-1} (1591 cm^{-1}) compared to CN_x@N-RGO. This small difference in the G-band frequency between these samples is caused by the thin layer coating of the N-RGO sheets over CN_x. Also, it should be noted that compared to the graphitic G-band (1581 cm^{-1}), both N-RGO and CN_x@N-RGO display a blue shift in the G-band frequency, which accounts that the nitrogen dopants in both the cases are of n-type.[40] Still, compared to CN_x@N-RGO and CN_x, the G-band frequency of N-RGO is found to be closer to that of graphite. It is known that if the graphene layer thickness is more, its frequency will tend to be more negative and meet the G-band frequency of N-RGO.[36-38] Along with the peak position, the intensity ratio (I_D/I_G ratio) of the defective band (I_D) to graphitic band (I_G) also gives useful information on the chemical modification occurred in the carbon lattice of the material. The estimated I_D/I_G ratios of CN_x, N-RGO, and CN_x@N-RGO are 1.05, 1.10, 1.12, respectively. The higher I_D/I_G ratio of all the

materials is pointing towards the defective sites created on them during the high-temperature annealing process. The XRD analysis of CN_x, N-RGO, and CN_x@N-RGO shows a well-defined peak at a 2θ value of 26°, which is attributed to the graphitic (002) plane (**Figure 2.5b**). [39] Along with the main intense peak at 26°, it is showing a small peak at 44°, corresponding to the (110) plain of the graphitic carbon. The nature of this peak is found to be slightly broad in the case of CN_x, whereas, it appeared to be sharper in the case of N-RGO. The semi-broad nature of the peak of CN_x@N-RGO is possibly due to the thin layer covering of the N-RGO sheets on the CN_x tetrapods.

2.3.4 Surface area analysis

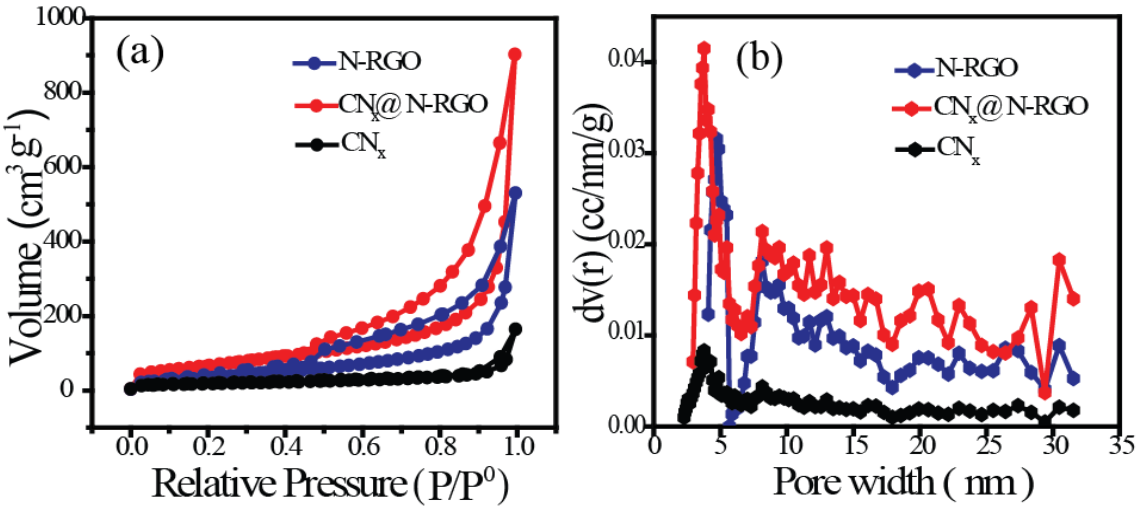

Figure 2.6 *(a) BET isotherms and (b) pore-size distribution profiles of CN_x@N-RGO, N-RGO and CN_x.*

The Brunauer-Emmett-Teller (BET) surface area of CN_x@N-RGO, measured from the nitrogen adsorption-desorption analysis is 256 $m^2 g^{-1}$ (**Figure 2.6a**). We note that this is almost double compared to that of N-RGO (136 $m^2 g^{-1}$) and about five times that of CN_x (61 $m^2 g^{-1}$). The N_2 adsorption isotherm presented in **Figure 2.6a** displays the typical Type-IV characteristic in the relative pressure (P/P^0) values between 0.40 to 0.95.[40] Along with the higher surface area, CN_x@N-RGO displays a wide range of pores with a size distribution in the range of 3–30 nm (**Figure 2.6b**), where the predominant distribution is found to be with a size range of 3–5 nm. This structural modulation incurred by the system by ensuring high surface area and porosity

through the inter-connected network architecture helps the system to make the active reaction sites easily accessible and reactant distribution seamless.

2.3.5 XPS Analysis

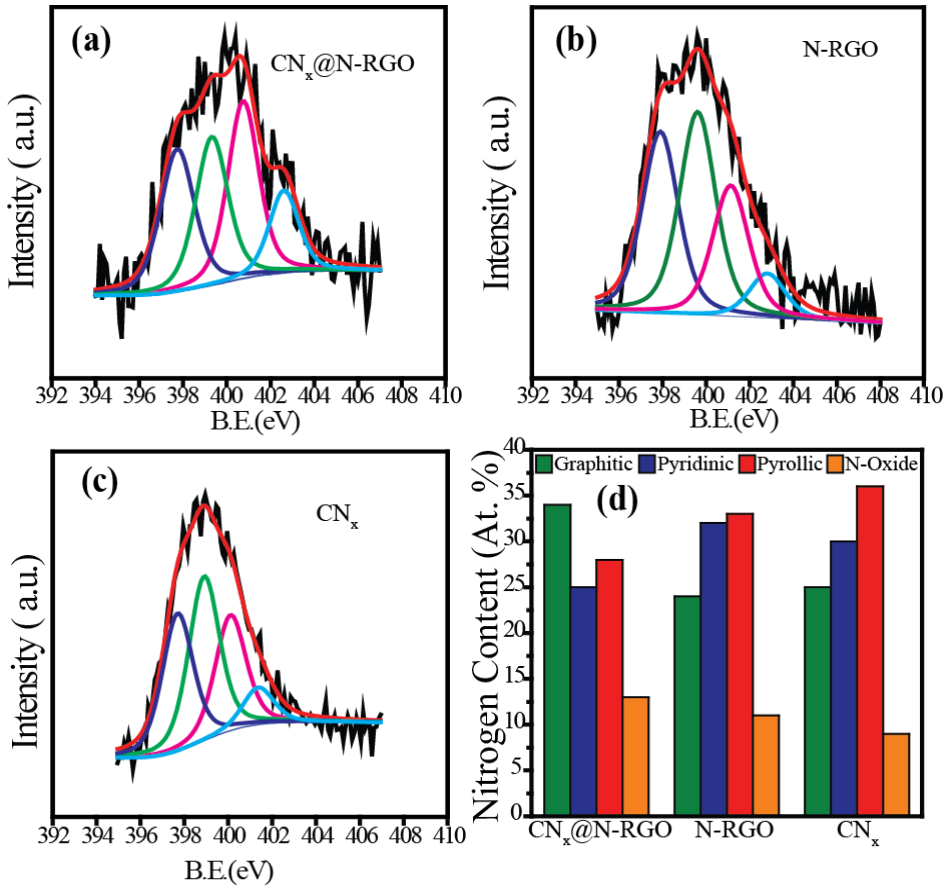

Figure 2.7 *Deconvoluted N1s XPS spectra of (a) CN_x@N-RGO, (b) N-RGO, and (c) CN_x. The bar diagram presented in (d) shows the different types of nitrogens and their atomic weight percentage as detected in the three catalysts.*

The chemical composition of CN_x@N-RGO, CN_x, and N-RGO was investigated using X-ray photoelectron spectroscopy (XPS). The XPS analysis reveals the presence of C, O, N and S in CN_x@N-RGO and CN_x. The presence of S in these two samples is expected to be originated from the melamine foam. On the other hand, XPS spectrum does not show the presence of S in N-RGO as it was prepared by using melamine powder in place of the foam. The N contents in the samples are quantified from the spectral data and the corresponding values are in the order of N-RGO (3.0 wt. %) > CN_x@N-RGO (2.8 wt. %) > CN_x (2.5 wt. %) (**Table 2.1**).

Table 2.1 *Chemical composition of CN_x@N-RGO, CN_x and N-RGO, indicating the weight percentage and atomic percentage of the different moieties present in the systems.*

Material	Carbon		Nitrogen		Oxygen		Sulphur	
	Wt. %	**At. %**	**Wt. %**	**At. %**	**Wt. %**	**At. %**	**Wt. %**	**At. %**
CN_x@N-RGO	82.0	85.6	2.8	2.5	15.0	11.7	0.2	0.08
CN_x	72.5	77.6	3.0	2.8	24.0	19.3	1.0	0.4
N-RGO	82.5	86.0	2.5	2.2	15.0	11.8	0	0

The N1s spectra of all the samples are deconvoluted to understand the different types of the nitrogen coordinations existing in the carbon matrix; the corresponding spectra are presented in **Figure 2.7a to c**. All the three samples show four different types of nitrogen coordinations with the binding energies of 397.4 (pyridinic), 399.5 (pyrrolic), 401.0 (graphitic) and 402.5 eV (pyridinic-N-oxide).[46, 47] From the quantified values presented in **Figure 2.7d**, it can be inferred that among the three catalysts, CN_x@N-RGO possesses 34 At. % of the graphitic nitrogen compared to N-RGO (24 At. %) and CN_x (25 At. %). Similarly, the pyridinic nitrogen content is in the order of N-RGO (32 At. %) > CN_x (30 At. %) > CN_x@N-RGO (25 At. %). Density Functional Theory (DFT) studies show that the graphitic and pyridinic nitrogens are playing an important role for adsorption of H* on the catalyst and its subsequent desorption (discussed in detail in a later section).[48] The overall high percentile of the graphitic and pyridinic nitrogens in CN_x@N-RGO thus generates more active reaction centres compared to N-RGO and CN_x. This gives a favourable edge for CN_x@N-RGO to perform better as an electrocatalyst for the reduction of water.

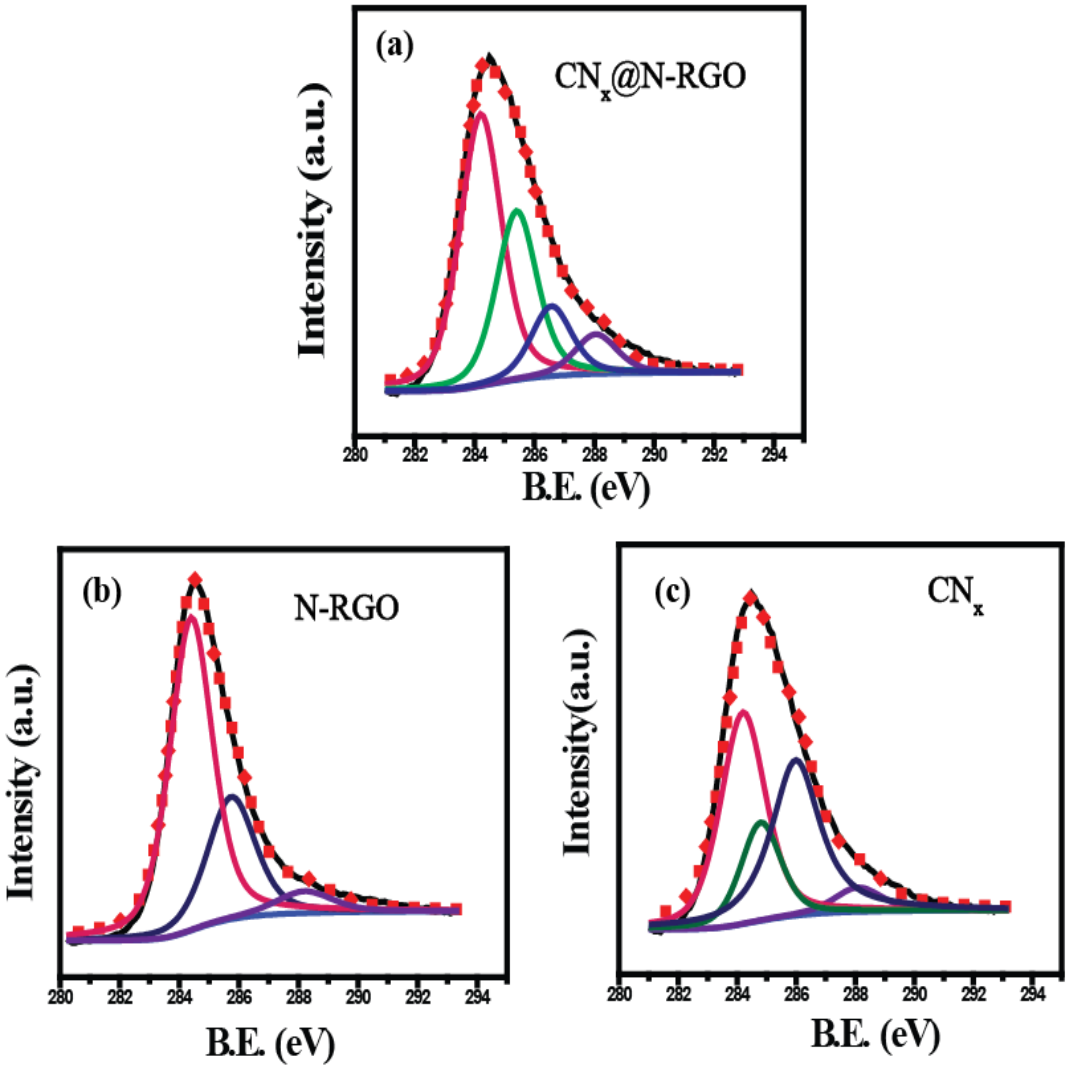

Figure 2.8 *Deconvoluted C1s XPS spectra of (a) CN_x@N-RGO, (b) N-RGO and (c) CN_x.*

Deconvoluted C1s spectra (**Figure 2.8a to c**) of CN_x@N-RGO show four distinct peaks corresponding to the binding energies of 284.24 (C=C), 285.38 (C–N), 286.58 (C–O), and 288.05 eV (C=O). The relatively intense peak at 284.24 eV stands out as valid evidence on the improved graphitization accomplished by the system. Also, comparing the peak intensities corresponding to the C=C bond in the three morphologies, it is found that N-RGO shows more intense peak followed by CN_x@N-RGO and CN_x. This trend follows the order of graphitization in the three structures and is in line with the XRD and Raman results.

2.3.6 Electrochemical analysis

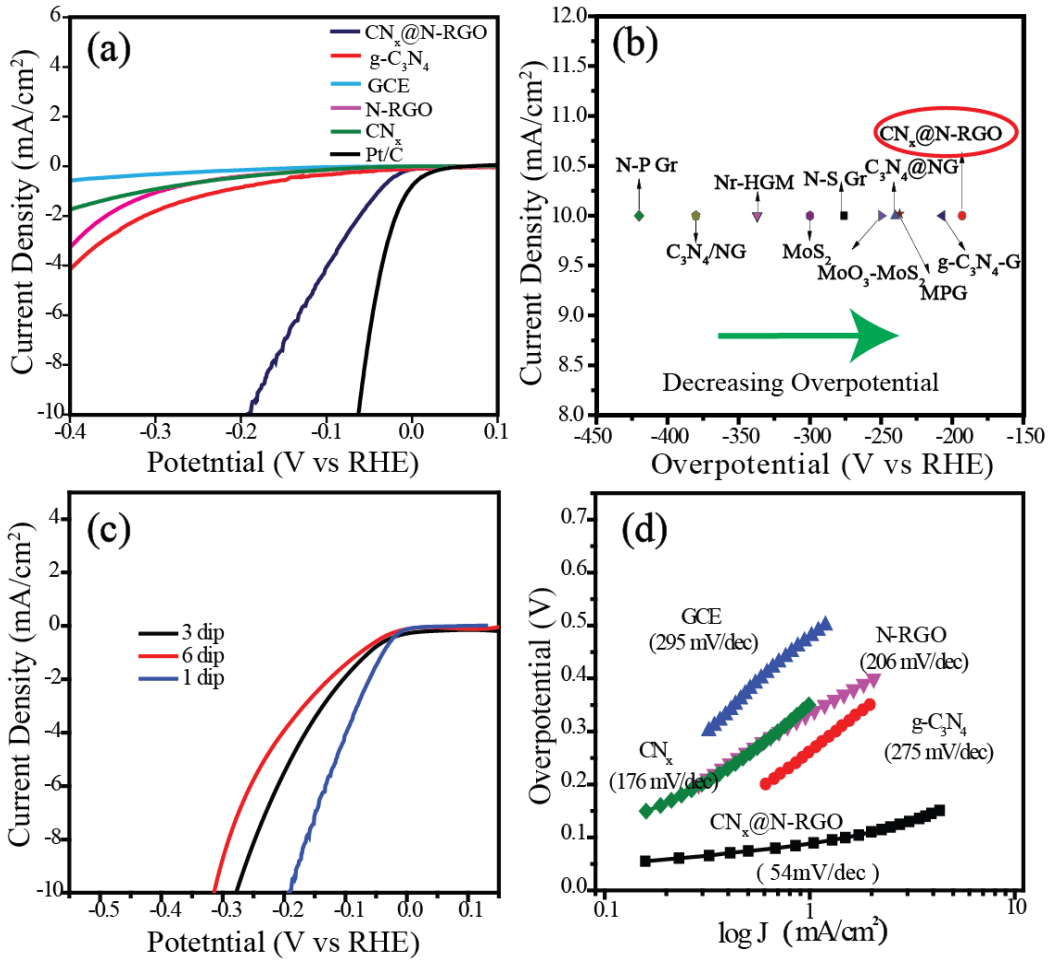

Figure 2.9 *(a) HER polarization curves of the different catalyst materials recorded in 0.5 M H_2SO_4 electrolyte at a scan rate of 10 mV s^{-1}, (b) comparison of the overpotential of CN_x@N-RGO with the reported catalysts at a current density of 10 mA cm^{-2}, (c) LSV of CN_x@N-RGO with different dip coating number of the melamine foam in the GO solution in 0.5M H_2SO_4 electrolyte at a scan rate of 10 mV s^{-1} and (d) Tafel plots of all the catalysts,*

The HER activity of CN_x@N-RGO was studied in nitrogen saturated 0.5 M H_2SO_4. For comparison purpose, the HER activities of N-RGO, g-C_3N_4, CN_x, Pt/C, and the bare glassy carbon electrode (GCE) were also investigated under the similar experimental conditions. CN_x@N-RGO displays an onset potential of 40 mV and a current density of 10 mA cm^{-2} could be achieved at a potential of 193 mV (**Figure 2.9a**). However, both CN_x and N-RGO require

more than 400 mV overpotential to reach the current density of 10 mA cm^{-2}. The difference in the overpotential in the above two cases (*i. e*., 193 and 400 mV) clearly depicts the importance of the architectural benefit achieved in CN_x@N-RGO. Here, the structural parameters and functional modulations incurred by the synergistic interactions between the participating components CN_x and N-RGO in CN_x@N-RGO are playing pivotal roles in redefining the activity characteristics. CN_x@N-RGO shows a performance which is even higher than that of the best reported non-metal system, *viz*, g-C_3N_4 nano ribbons on the graphene sheet. Whereas the reported one shows an overpotential value of 209 mV to attain the benchmark current density of 10 mA cm^{-2}, CN_x@N-RGO meets this target at a substantially reduced overpotential of 193 mV. **Figure 2.9b** shows the reported HER overpotential values at a current density of 10 mA cm^{-2} for some of the best-known electrocatalysts in comparison with CN_x@N-RGO. Among the candidates, CN_x@N-RGO can be seen as a prominent system having the lowest overpotential for HER, claiming a niche space as a practical electrocatalyst for the reduction of water.[22-25, 49-52]

Further, the layer thickness of the N-RGO sheets on CN_x is also varied and tested for HER (**Figure 2.9c**). An increase in the layer thickness beyond a threshold level is found to be adversely affecting the HER activity. It indicates that with an increase in the N-RGO layers, the benefit from the synergistic effect between N-RGO and CN_x diminishes and also the number of the active sites located on N-RGO becomes less exposed. The Tafel slope of CN_x@N-RGO is 54 mV dec^{-1}, which is comparable to Pt/C (40 mV dec^{-1}). The other carbon catalysts such as CN_x, N-RGO, g-C_3N_4 have the Tafel slope values of 176, 206 and 275 mV dec^{-1}, respectively (**Figure 2.9d**). This low Tafel slope value of CN_x@N-RGO suggested the Volmer-Heyrovsky mechanism for HER.[53] The exchange current density (J_0) of CN_x@N-RGO, which was calculated by extrapolating the Tafel slope, is estimated to be 34.7 mA cm^{-2}; this value is higher than that reported on some of the metal-free and metal based catalysts (**Table 2.2**).

Normally, the Tafel slope helps to elucidate the kinetics of HER.[54] Tafel slopes for discharge, desorption and recombination steps theoretically have values of 118.0, 39.0 and 29.5 mV dec^{-1}, respectively.[55,56] At a lower overpotential, desorption or recombination is the rate determining step. While going to higher overpotential, the hydrogen adsorption on the catalyst surface approaches saturation and the initial discharge step becomes the rate determining.[57] The Gibbs free energy (ΔG_{H^*}) for the absorption also depends on the rate determining step.[58, 13] If

Table 2.2 *A comparison of the activities of the electrocatalysts reported in the literature and the in-house catalyst based on key performance indicators.*

Catalyst	**Tafel slop (mV/dec)**	**Jo (μA/ cm^2)**	**Cdl (mF/cm^2)**	**Overpotential @ J=10 $mAcm^{-2}$ (mV)**	**Reference**
MoS_2/Graphene	42	3	10.4	~	[57]
N-S-500	81	8.4	-	276	[25]
g-C_3N_4nanoribbon-G	54	39.8	13	209	[23]
C_3N_4@NG	51.5	0.35	5	240	[22]
C_3N_4/NG	67	0.025	1.4	380	[22]
MoO_3–MoS_2 nanowire	50~60	0.08	2.2	~ 250	[49]
N-P G-1	91	0.24	10.6	420	[24]
CN_x@N-RGO	54	34.7	11	193	This work

ΔG_{H^*} is positive, the H-adsorption step will be the rate determining step, whereas, a negative value indicates the involvement of the H desorption step as the rate determining step.[13] Adsorption of H atom on the catalyst surface plays a vital role in the HER activity. On the metal surface, the metal-H bond should be loosely bounded to enable the effective desorption of the hydrogen gas, whereas, in the case of a nonmetal system, it is still a matter of discussion.[4, 59] The free energy for hydrogen adsorption is also an important parameter for determining the activity of an electrocatalyst for the hydrogen evolution.[53]

The mechanism of HER can be represented through the following equations: [54, 55]

1. Primary discharge step (Volmer reaction)

$$H_3O^+ + 1e^- \longrightarrow H_{ads} + H_2O$$

2. Electrochemical desorption step (Heyrovsky reaction)

$$H_{ads} + H_3O + 1e^- \longrightarrow H_2 + H_2O$$

3. Recombination Step (Tafel reaction)

$$H_{ads} + H_{ads} \longrightarrow H_2$$

In the Volmer reaction pathway (Step 1), the protons from the electrolyte get adsorbed at the catalyst surface. In the next step, the process can advance through either electrochemical conversion (Step 2) or chemical conversion (Step 3) of the adsorbed hydrogen into molecular hydrogen.[55] Chemical conversion is through the recombination step in which two adsorbed H-atoms combine to form an H_2 molecule (Tafel Reaction). The electrochemical reduction is occurring through a desorption step in which the adsorbed H* accepts a proton from the electrolyte and gets converted to H_2 molecule (Heyrovsky reaction). The Tafel slope value of 54 $mVdec^{-1}$ in CN_x@N-RGO proposes the Volmer-Heyrovsky mechanism of hydrogen evolution reaction. [55] The protons from the electrolytic solution get adsorbed on the active carbon centers

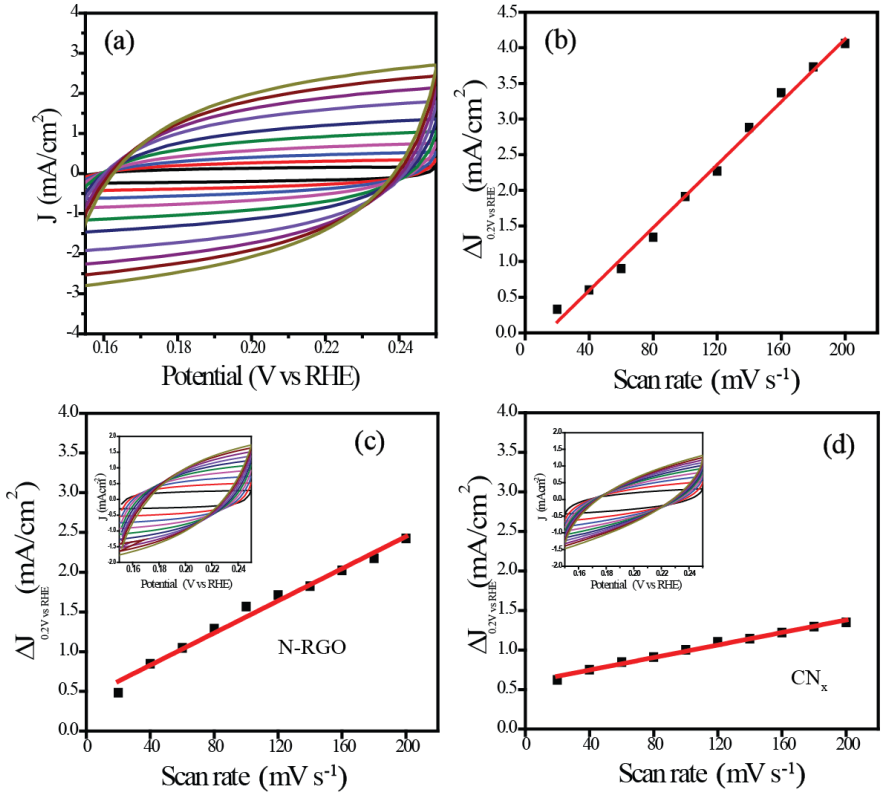

Figure 2.10 *(a) CV profiles of CN_x@N-RGO in the region of 0.15-0.25 V vs. RHE, (b) C_{dl} measurement of CN_x@N-RGO, linear fitting of the current density differences of the catalyst vs scan rate along with the CV profiles of (c) N-RGO and (d) CN_x.*

in the first step, which subsequently get reduced into H_2 gas by the electrochemical desorption method. During this process, the N-doped graphene layer facilitates the electron transfer for the reduction of the adsorbed protons. Also, the Heyrovsky reaction is the rate limiting step for HER in CN_x@N-RGO since its Tafel slope value is close to the theoretical value.[55]

The electrochemical double layer capacitance (C_{dl}) is indirectly helping to estimate the effective surface area of CN_x@N-RGO by calculating the charge transfer between the solid-liquid interfaces.[60] Cyclic voltammetry (CV) was performed at various scan rates (20, 40, 60, 80 mV s^{-1}, etc.) in a potential range of 0.15–0.25 V, where, the pure double layer capacitance is visible. The C_{dl} is calculated by plotting ΔJ (Ja-Jc) at 0.2 V vs. RHE against the scan rate, where, Ja is the anodic current density and Jc is the cathodic current density (**Figure 2.10a and b**). The slope of the straight line obtained from the above plot is twice the value of C_{dl}. The calculated C_{dl} of CN_x@N-RGO is 11 mF cm^{-2}. This value is higher than that obtained for the many reported systems in the literature (Table 2.2), indicating that the electro active surface area of CN_x@N-RGO is greater and, thus, more reactive sites are available for the reduction of water. The C_{dl} values of N-RGO (4.5 mF cm^{-2}) and CN_x (1.9 mF cm^{-2}) are also calculated along with CN_x@N-RGO and the values are found to be lower than that of CN_x@N-RGO (**Figure 2.10c and d**).

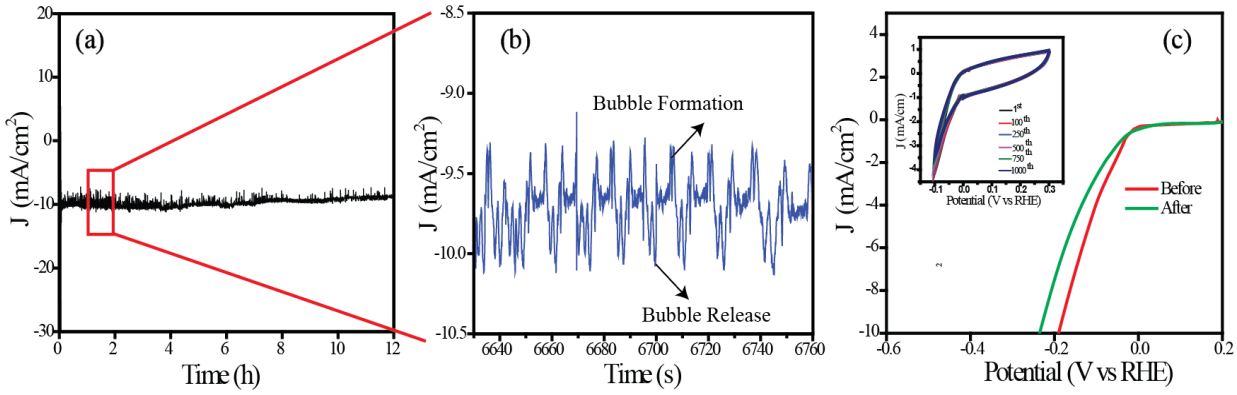

Figure 2.11 *(a) Chronoamperogram obtained for CN_x@N-RGO at a current density of 10 mA cm^{-2}, (b) an enlarged view of the chronoamperogram presented in (a) indicating the bubble formation and its release during the measurement and (c) Linear Sweep Voltammograms of CN_x@N-RGO taken before and after the cycling stability study at a scan rate of 10 mV s^{-1} in 0.5 M H_2SO_4. The inset is showing the cyclic voltammograms corresponding to the cycling stability.*

The durability assessment of the CN_x@N-RGO catalyst has been carried out through chronoamperometry in nitrogen saturated 0.5 M H_2SO_4 at a current density of 10 mA cm^{-2}. It could be deduced from the chronoamperogram of CN_x@N-RGO presented in **Figure 2.11a** that, even after a 12 h continuous run, the system suffered only 10% loss in the reduction activity. This degradation in the activity may be ascribed to the hindering of some active sites by the bubbles generated in the process, which are evident from **Figure 2.11b**. Further, stability of the catalysts was also evaluated through cycling study. The catalyst was forced to degradation by potential cycling in the onset region (-0.1 V to 0.3 V vs RHE) for 1000 cycles in N_2 saturated 0.5 M H_2SO_4 electrolyte. After 1000 continues cycles, the onset potential remained unaltered and the overpotential is changed by a small difference of 36 mV (**Figure 2.11c**).

2.3.7 Computational Study

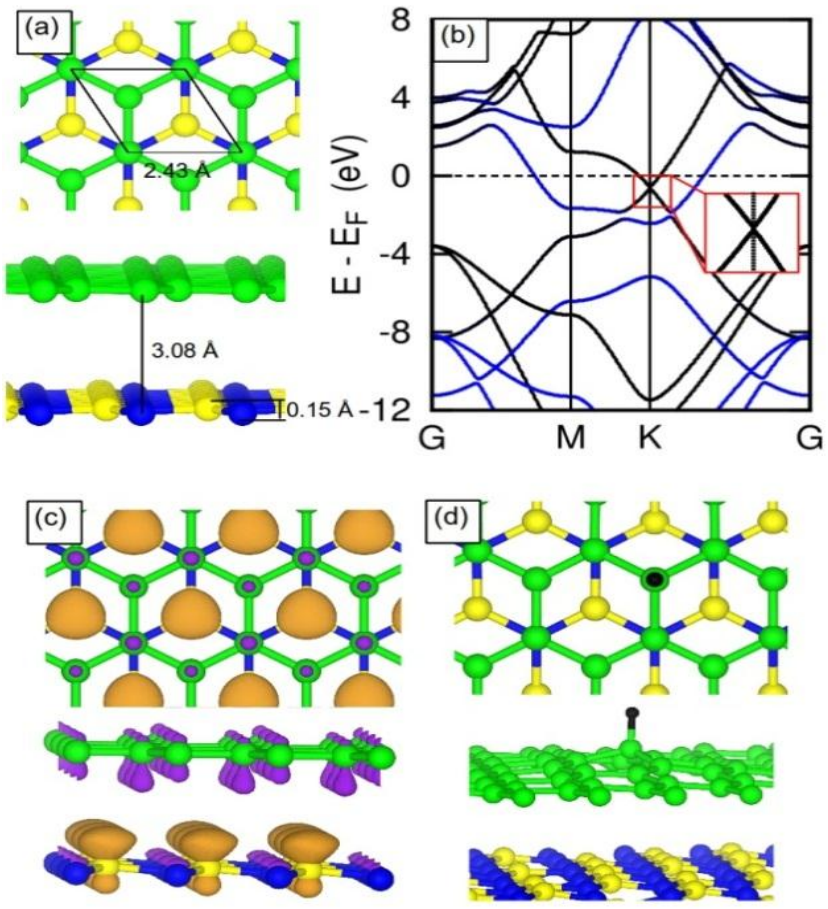

Figure 2.12 *(a) Structure of the model catalyst used to represent CN_x@RGO. The top and bottom panels show the top and side views, respectively. Also shown are the lattice parameter, interplanar distance, and buckling in the CN layer. (b) Band structure along high-symmetry directions of the Brillouin zone for the model catalyst. Blue indicates contributions to the bands from the CN layer, whereas black indicates the contribution from the graphene sheet. (c) Iso surfaces of charge density differences, showing charge transfer from CN to graphene. The iso value is 0.007 $e^-/Å^3$. In this figure and subsequent figures, magenta (brown) denotes charge accumulation (depletion). (d) Most stable hydrogen adsorption configuration on the catalyst. In this figure and subsequent figures, green spheres represent C atoms in the graphene sheet, yellow spheres represent C atoms in CN, blue spheres represent N atoms in CN, and the black sphere represents the H atom adsorbed on the graphene surface.*

In order to obtain a microscopic insight into why CN_x@N-RGO acts as the best transition metal-free catalyst, we have performed DFT based calculations. The complex CN_x@RGO was modeled with a bilayer of graphene (RGO) and carbon-nitride (CN). The N rich CN_x in the experiments is modeled with CN where C:N is 1:1. Further RGO is modeled with a graphene sheet. Hence we neglect the effect of O based functional groups that are typically present in RGO. The top (upper panel) and the side views (lower panel) of the relaxed geometry of the bilayer is shown in **Figure 2.12a**. Of the two in equivalent C atoms in the graphene sheet, one of them is on top of the N atoms of CN while the other one is at the center of the hexagon. The surface unit cell has a lattice parameter of about 2.43 Å while the inter planar separation between the two layers is about 3.08 Å suggesting that the interaction between the two layers is primarily through van der Waals attraction. Additionally, we observe a buckling of about 0.15 Å in the CN sheet. The band structure of the bilayer shown in **Figure 2.12b** shows that the electronic nature of the individual components is preserved except that there is a charge transfer (about 2.28×10^{17} e^-/m^2, as obtained from Löwd in charge analysis) from CN to graphene. This results in graphene's Dirac cone being shifted by about 0.8 eV below the Fermi energy. This is further corroborated by the charge density difference of (please refer to Equation 2.2 in section 2.2.4b for details of how the charge density difference is calculated) iso surface shown in **Figure 2.12c**. Thus, the CN sheet is positively charged while the RGO sheet is negatively charged thereby forming a built in electric field directed from CN to RGO that might facilitate rapid electron transfer from the electrode.

Followed by these encouraging results, we proceeded to study the thermodynamics of H adsorption on the bilayer. Since experimental evidences show that RGO/N-RGO is exposed (**Figure 2.2**), we have considered H adsorption only on the RGO/N-RGO sheet of the undoped and N-doped bilayer. Our calculations show that binding of H (**Figure 2.12d**) is highly endothermic on CN_x@RGO with a binding energy lying between 1.14 and 1.19 eV depending on which C atom the H is adsorbed. This gives a $|\Delta GH^*| \approx 1.40$ eV that is much larger than the ideal value of 0.00 eV for an efficient catalyst. This shows that though rapid electron transfer from electrode may be facilitated in this complex due to the electrical coupling between CN and graphene, the thermodynamics is definitely not favoured, suggesting that N doping plays a crucial role in providing the ideal binding energy of H to these sheets. Therefore, we proceed towards understanding how N doping in RGO of CN_x@RGO alters the electronic properties of the catalyst and thereby facilitates HER. To do so, we have considered only graphitic and pyridinic N doping in the graphene sheet of the bilayer. Since we are using an infinite sheet and there are no O based functional groups in the model undoped catalyst, we are neglecting the pyrolic N and N-oxide dopings that were also found in the experiments. For the graphitic N, there are two possible configurations: (a) the C atom of graphene on top of N atom of CN is replaced with a N atom (Gr1) and (b) the C atom occupying the hollow site of the hexagon in CN is replaced with N (Gr2). We find that the formation energies for graphitic N formation for both the configurations are similar (0.78 eV for Gr1 and 0.81 eV for Gr2). Pyridinic N doping can be modeled by creating a C vacancy in the graphene sheet of the bilayer and replacing one of the three C atoms around the vacancy with N atom. Now since there are two in equivalent C atoms that can be removed to create a vacancy, we have considered two configurations: (a) where the C atom on top of N in CN is removed and the C atom on top of the hollow site is replaced with N (Pr1) and (b) vice-versa of (a) (Pr2). The formation energies of these two configurations are also very similar (4.26 and 4.39 eV for Pr1 and Pr2 respectively). However, in contrast with the graphitic N, the formation energies of pyridinic N are much higher suggesting that the concentration of graphitic N in these samples is larger. We note that these results are consistent with the experimental findings (**Figure 2.7d**). Moreover, similar to that of the undoped system, we find that there is a charge transfer from CN to the N-doped graphene sheet suggesting that in presence of doped N the electrical coupling between the two moieties is still retained. However, compared to the undoped system, the amount of charge transfer from CN_x to RGO depends on

the type of N present in the doped one. While for the graphitic N we find that there is a reduction in the amount of charge transfer (~ 1.42×10^{17} e^-/m^2) compared to the undoped one, for the pyridinic N there is a significant enhancement in the amount of charge transfer (4.37×10^{17} e^-/m^2 for Pr1 and 3.67×10^{17} e^-/m^2 for Pr2).

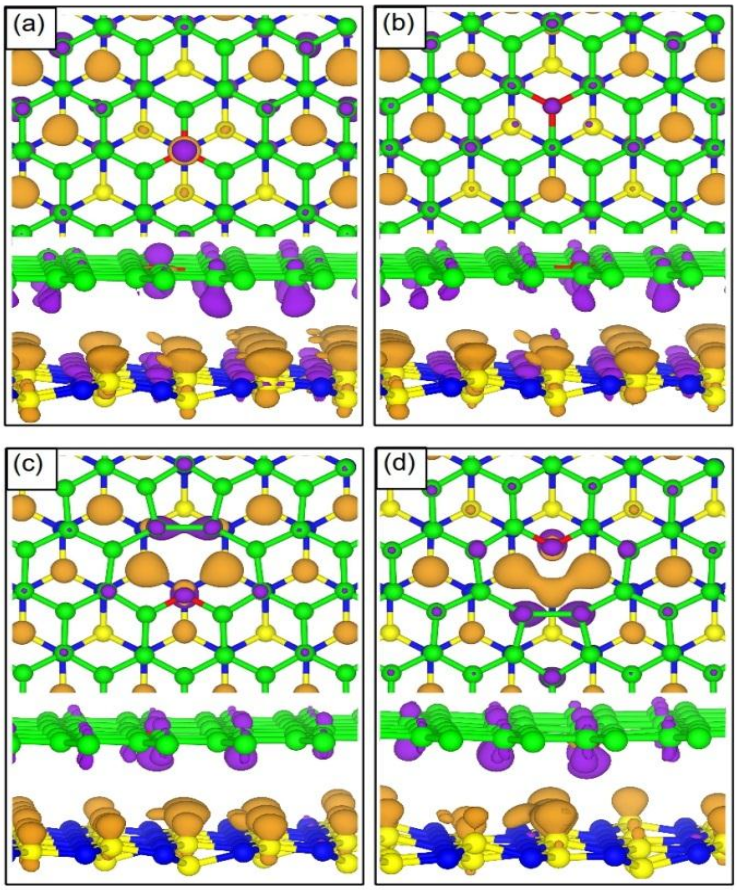

Figure 2.13 *Isosurfaces of charge density differences showing charge transfer from CN to graphene in presence of N doping in the graphene sheet for GrN-1 (a), GrN-2 (b), PrN-1 (c) and PrN-2 (d). The doped N atom is denoted by red sphere. The isovalues for (a), (b), (c) and (d) are 0.003 and 0.007* $e^-/Å^3$.

Figure 2.13 shows the charge transfer for the four cases. Nevertheless, unlike the undoped system where the excess charge is more or less uniformly distributed on the graphene sheet, the excess charge in the doped ones is localized primarily on the N atom and C atoms

around the defect resulting in a charge in homogeneity in N-RGO of CN_x@N-RGO. We note that our computational results are in accordance with the XPS data. **Figure 2.7 and 2.8** give the deconvoluted N1s and C1s spectra respectively for the chemically different C and N atoms in CN_x@N-RGO, CN_x and RGO. Compared to that of RGO, in CN_x@N-RGO, we find that the peaks shift towards the low binding energy side suggesting gain of electrons. Even the relative differences in the shift (that correlates with the amount of charge transfer) for the chemically different C and N atoms follow trends similar to what has been observed in the charge transfer calculations. For example, the calculations predict that the amount of charge transfer in case of the pyridinic N is more than that of the graphitic N. In the N1s XPS spectra, we find that the shift in the peak positions of the pyridinic-N (about 0.52 eV) is almost six times more compared to that of the graphitic-N (about 0.09 eV). This shows that our relatively simple model can capture correctly the effects of N doping in the actual catalyst.

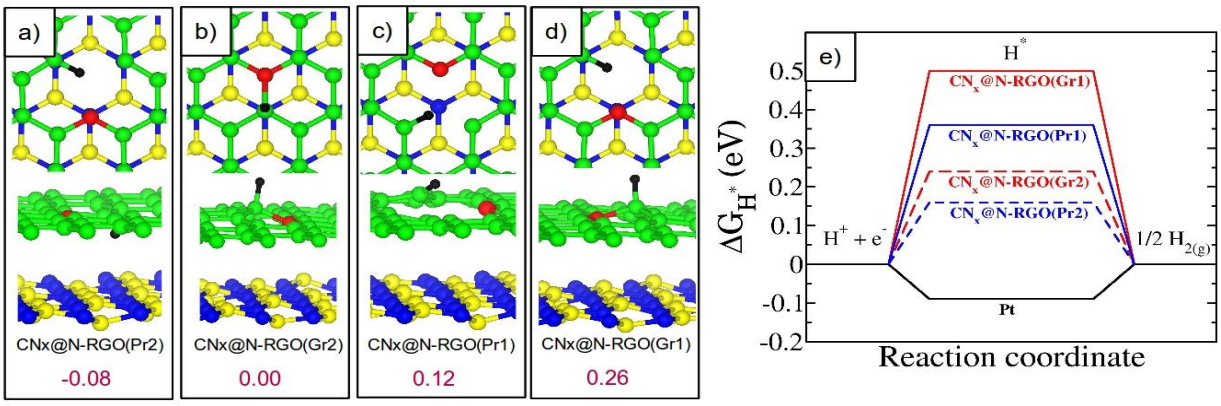

Figure 2.14 *(a), (b), (c) and (d) show the most stable configurations of H adsorbed on Pr2, Gr2, Pr1 and Gr1 respectively. For each case the H binding energies (in eV) are given below. (e) Free energy diagram of HER on the four N-doped configurations in* CN_x*@N-RGO.*

To understand how the charge in homogeneity affects the binding of the H to the catalyst and thereby HER, we have computed the adsorption energy of hydrogen on the above defect rather than on the N atom itself. The lowest energy configurations of H bound to these four types of N-doped systems are given in **Figure 2.14a-d**. We find that only for Pr2, the H binding is slightly exothermic while for all the other cases it is slightly endothermic. The endothermicity is

much less compared to that in the undoped system. This suggests that Pr2 can show efficient HER activity. We describe the overall HER pathway with a three-state diagram consisting of (i) an initial state of H^+ + e-, (ii) an intermediate state where H is adsorbed on the catalyst (H*), and (3) a final state where 1/2 H_2 is generated. [13, 58, 61] The Gibbs free energy profile for this pathway is shown in **Figure 2.14e**. Among the various N-doped catalysts considered in this study, we find that the pyridinic-N doping in CN_x@N-RGO (Pr2) has the smallest $|\Delta G_{H^*}|$ value of 0.16 eV. This value is comparable to that of -0.09 eV in Pt that is till date the most efficient catalyst available in the market. Moreover, for the graphitic N doping (Gr2), the $|\Delta G_{H^*}|$ value is 0.24 eV. This suggests that both types of N doping might be favourable for HER. Hence, our calculations show that the enhanced catalytic activity towards HER reaction in CN_x@N-RGO is due to the synergistic effects of (a) the interlayer charge transfer between CN_x and RGO and (b) inhomogeneity of the charge redistribution in the RGO sheet induced by N-doping. While the former provides electrical coupling between CN_x and N-RGO that induces fast electron transfer from electrode, the later provides optimal thermodynamic stability to the H^+ ions so that they can adsorb on the catalyst and easily converted to H_2.

2.4. Conclusions

Here, a simple approach is adopted to synthesise a three-dimensional nanostructure (CN_x@N-RGO) consisting of the nitrogen doped graphene (N-RGO) layers distributed on the interconnected arms of carbon nitride (CN_x) tetrapods, which acts as an efficient catalyst for the electrochemical hydrogen evolution reaction (HER). The desired morphology of CN_x@N-RGO is obtained by thermal annealing of graphene oxide (GO) coated melamine foam. The melamine foam acts both as the nitrogen source and structure directing material for CN_x@N-RGO. The SEM and TEM images of the catalyst prove the formation of the 3D architecture with the CN_x backbone covered with the N-RGO sheets. The thickness of the N-RGO layer on CN_x increases with the dipping number of the melamine foam in the GO solution. Nitrogen doping in the 3D architecture is analysed using XRD, Raman, and XPS methods. The higher surface area and mesoporous structure with the inter-connected network help to improve the mass transport of the reactants on the catalyst surface. CN_x@N-RGO shows better electrocatalytic activity towards HER in acidic medium. It requires only 193 mV overpotential to reach the current density of 10 mA cm^{-2} with a high exchange current density (34.7 μA cm^{-2}) and low Tafel slope value (54 mV

dec^{-1}). DFT calculations show that the synergy between CN_x and N-RGO facilitates good electrical coupling between the two moieties and provide optimal binding to H^+ ions on the catalyst that results in a more efficient HER activity compared to the individual ones. Durability analysis of CN_x@N-RGO shows the HER activity remains more or less unaltered even after 12 h at a current density of 10 mA cm^{-2}. With high HER activity and electrochemical stability, the metal-free CN_x@N-RGO catalyst stands out as a low-cost active material for PEM electrolyzer cathode.

2.5. References

[1] J. A. Turner, *Science*, **2004**, 305, 972-974.

[2] M. S. Dresselhaus and I. L. Thomas, *Nature*, **2001**, 414, 332-337.

[3] T. R. Cook, D. K. Dogutan, S. Y. Reece, Y. Surendranath, T. S. Teets and D. G. Nocera, *Chem. Rev.*, **2010**, 110, 6474-6502.

[4] M. G. Walter, E. L. Warren, J. R. McKone, S. W. Boettcher, Q. Mi, E. A. Santori and N. S. Lewis, *Chem. Rev.*, **2010**, 110, 6446-6473.

[5] J. Kibsgaard and T. F. Jaramillo, *Angew. Chem. Int. Ed.*, **2014**, 53, 14433-14437.

[6] J. R. Rostrup-Nielsen, *Cat. Rev.*, **2004**, 46, 247-270.

[7] C. G. Morales-Guio, L.-A. Stern and X. Hu, *Chem. Soc. Rev.*, **2014**, 43, 6555-6569.

[8] Y. Zheng, Y. Jiao, M. Jaroniec and S. Z. Qiao, *Angew. Chem. Int. Ed.*, **2015**, 54, 52-65.

[9] Y. Jiao, Y. Zheng, M. Jaroniec and S. Z. Qiao, *Chem. Soc. Rev.*, **2015**, 44, 2060-2086.

[10] M. Carmo, D. L. Fritz, J. Mergel and D. Stolten, *Int. J. Hydrogen Energy*, **2013**, 38, 4901-4934.

[11] S. Schuldiner, *J. Electrochem. Soc.*, **1959**, 106, 891-895.

[12] B. E. Conway and B. V. Tilak, *Electrochim. Acta*, **2002**, 47, 3571-3594.

[13] J. Greeley, T. F. Jaramillo, J. Bonde, I. Chorkendorff and J. K. Norskov, *Nat. Mater*, **2006**, 5, 909-913.

[14] S. Trasatti, in *Advances in Electrochemical Science and Engineering*, Wiley-VCH Verlag GmbH, 2008, DOI: 10.1002/9783527616763.ch1, pp. 1-85.

[15] T. F. Jaramillo, K. P. Jørgensen, J. Bonde, J. H. Nielsen, S. Horch and I. Chorkendorff, *Science*, **2007**, 317, 100-102.

[16] B. Cao, G. M. Veith, J. C. Neuefeind, R. R. Adzic and P. G. Khalifah, *J. Am. Chem. Soc.*, **2013**, 135, 19186-19192.

[17] H. Vrubel and X. Hu, *Angew. Chem. Int. Ed.*, **2012**, 51, 12703-12706.

[18] D. Voiry, H. Yamaguchi, J. Li, R. Silva, D. C. B. Alves, T. Fujita, M. Chen, T. Asefa, V. B. Shenoy, G. Eda and M. Chhowalla, *Nat. Mater*, **2013**, 12, 850-855.

[19] W.-F. Chen, K. Sasaki, C. Ma, A. I. Frenkel, N. Marinkovic, J. T. Muckerman, Y. Zhu and R. R. Adzic, *Angew. Chem. Int. Ed.*, **2012**, 51, 6131-6135.

[20] D. Kong, J. J. Cha, H. Wang, H. R. Lee and Y. Cui, *Energy Environ. Sci.*, **2013**, 6, 3553-3558.

[21] E. J. Popczun, J. R. McKone, C. G. Read, A. J. Biacchi, A. M. Wiltrout, N. S. Lewis and R. E. Schaak, *J. Am. Chem. Soc.*, **2013**, 135, 9267-9270.

[22] Y. Zheng, Y. Jiao, Y. Zhu, L. H. Li, Y. Han, Y. Chen, A. Du, M. Jaroniec and S. Z. Qiao, *Nat. Commun.*, **2014**, 5.

[23] Y. Zhao, F. Zhao, X. Wang, C. Xu, Z. Zhang, G. Shi and L. Qu, *Angew. Chem. Int. Ed.*, **2014**, 53, 13934-13939.

[24] Y. Zheng, Y. Jiao, L. H. Li, T. Xing, Y. Chen, M. Jaroniec and S. Z. Qiao, *ACS Nano*, **2014**, 8, 5290-5296.

[25] Y. Ito, W. Cong, T. Fujita, Z. Tang and M. Chen, *Angew. Chem. Int. Ed.*, **2015**, 54, 2131-2136.

[26] W. He, Y. Wang, C. Jiang and L. Lu, *Chem. Soc. Rev.*, **2016**, 45, 2396-2409.

[27] W. He, C. Jiang, J. Wang and L. Lu, *Angew. Chem. Int. Ed.*, **2014**, 53, 9503-9507.

[28] H.-W. Liang, W. Wei, Z.-S. Wu, X. Feng and K. Müllen, *J. Am. Chem. Soc.*, **2013**, 135, 16002-16005.

[29] S. M. Unni, R. Illathvalappil, P. K. Gangadharan, S. N. Bhange and S. Kurungot, *Chem. Commun.*, **2014**, 50, 13769-13772.

[30] G. Paolo, B. Stefano, B. Nicola, C. Matteo, C. Roberto, C. Carlo, C. Davide, L. C. Guido, C. Matteo, D. Ismaila, C. Andrea Dal, G. Stefano de, F. Stefano, F. Guido, G. Ralph, G. Uwe, G. Christos, K. Anton, L. Michele, M.-S. Layla, M. Nicola, M. Francesco, M. Riccardo, P. Stefano, P. Alfredo, P. Lorenzo, S. Carlo, S. Sandro, S. Gabriele, P. S. Ari, S. Alexander, U. Paolo and M. W. Renata, *J. Phys.: Condens. Matter*, **2009**, 21, 395502.

[31] J. P. Perdew, K. Burke and M. Ernzerhof, *Phys. Rev. Lett.*, **1997**, 78, 1396-1396.

[32] S. Grimme, *J. Comput. Chem.*, **2004**, 25, 1463-1473.

[33] D. Vanderbilt, *Phys. Rev. B*, **1990**, 41, 7892-7895.

[34] H. J. Monkhorst and J. D. Pack, *Phys. Rev. B*, **1976**, 13, 5188-5192.

[35] M. Kodama, J. Yamashita, Y. Soneda, H. Hatori and K. Kamegawa, *Carbon*, **2007**, 45, 1105-1107.

[36] Z.-H. Sheng, L. Shao, J.-J. Chen, W.-J. Bao, F.-B. Wang and X.-H. Xia, *ACS Nano*, **2011**, 5, 4350-4358.

[37] K. Akbar, J. H. Kim, Z. Lee, M. Kim, Y. Yi, S.-H. Chun, *NPG Asia Mater.*, **2017**, *9*, e378.

[38] X. Li, H. Wang, J. T. Robinson, H. Sanchez, G. Diankov and H. Dai, *J. Am. Chem. Soc.*, **2009**, 131, 15939-15944.

[39] A. Das, S. Pisana, B. Chakraborty, S. Piscanec, S. K. Saha, U. V. Waghmare, K. S. Novoselov, H. R. Krishnamurthy, A. K. Geim, A. C. Ferrari and A. K. Sood, *Nat. Nano*, **2008**, 3, 210-215.

[40] Z. Zafar, Z. H. Ni, X. Wu, Z. X. Shi, H. Y. Nan, J. Bai and L. T. Sun, *Carbon*, **2013**, 61, 57-62.

[41] H. Zhou, F. Yu, H. Yang, C. Qiu, M. Chen, L. Hu, Y. Guo, H. Yang, C. Gu and L. Sun, *Chem. Commun.*, **2011**, 47, 9408-9410.

[42] I. Childres, L. A. Jauregui, W. Park, H. Cao and Y. P. Chen, *New developments in photon and materials research*, **2013**, 1.

[43] A. Gupta, G. Chen, P. Joshi, S. Tadigadapa and Eklund, *Nano Lett.*, 2006, 6, 2667-2673.

[44] C. Hu, X. Zhai, L. Liu, Y. Zhao, L. Jiang and L. Qu, *Sci. Rep.*, **2013**, 3, 2065.

[45] K. S. W. Sing, D. H. Everett, R. A. W. Haul, L. Moscou, R. A. Pierotti, J. Rouquerol and T. Siemieniewska, in *Handbook of Heterogeneous Catalysis*, Wiley-VCH Verlag GmbH & Co. KGaA, 2008, DOI: 10.1002/9783527610044.hetcat0065.

[46] S. Kundu, T. C. Nagaiah, W. Xia, Y. Wang, S. V. Dommele, J. H. Bitter, M. Santa, G. Grundmeier, M. Bron, W. Schuhmann, M. Muhler, *J. Phys. Chem. C* **2009**, *113*, 14302-14310

[47] P. H. Matter, L. Zhang, U. S. Ozkan, *J. Catal.* **2006**, *239*, 83-96

[48] E. Skúlason, V. Tripkovic, M. E. Björketun, S. Gudmundsdóttir, G. Karlberg, J. Rossmeisl, T. Bligaard, H. Jónsson and J. K. Nørskov, *J. Phys. Chem. C*, **2010**, 114, 18182-18197.

[49] Y. Zheng, Y. Jiao, Y. Zhu, L. H. Li, Y. Han, Y. Chen, A. Du, M. Jaroniec and S. Z. Qiao, *Nat. Commun.*, **2014**, 5, 3783.

[50] J.-M. Ge, B. Zhang, L.-B. Lv, H.-H. Wang, T.-N. Ye, X. Wei, J. Su, K.-X. Wang, X.-H. Li and J.-S. Chen, *Nano Energy*, **2015**, 15, 567-575.

[51] Z. Chen, D. Cummins, B. N. Reinecke, E. Clark, M. K. Sunkara and T. F. Jaramillo, *Nano Lett.*, 2011, 11, 4168-4175.

[52] X. Huang, Y. Zhao, Z. Ao and G. Wang, *Sci. Rep.*, **2014**, 4, 7557.

[53] E. Gileadi, *Physical electrochemistry: fundamentals, techniques and applications*, **2011**.

[54] N. Pentland, J. O. M. Bockris and E. Sheldon, *J. Electrochem. Soc.*, **1957**, 104, 182-194.

[55] B. Conway and B. Tilak, *Electrochim. Acta*, **2002**, 47, 3571-3594.

[56] Y. Li, H. Wang, L. Xie, Y. Liang, G. Hong and H. Dai, *J. Am. Chem. Soc.*, **2011**, 133, 7296-7299.

[57] A. Lasia, in *Handbook of Fuel Cells*, John Wiley & Sons, Ltd, 2010, DOI: 10.1002/9780470974001.f204033.

[58] J. K. Nørskov, T. Bligaard, A. Logadottir, J. R. Kitchin, J. G. Chen, S. Pandelov and U. Stimming, *J. Electrochem. Soc.*, **2005**, 152, J23-J26.

[59] L. Liao, J. Zhu, X. Bian, L. Zhu, M. D. Scanlon, H. H. Girault and B. Liu, *Adv. Funct. Mater.*, **2013**, 23, 5326-5333.

[60] M. A. Lukowski, A. S. Daniel, F. Meng, A. Forticaux, L. Li and S. Jin, *J. Am. Chem. Soc.*, **2013**, 135, 10274-10277.

[61] J. K. Norskov, T. Bligaard, J. Rossmeisl and C. H. Christensen, *Nat. Chem.*, **2009**, 1, 37-46.

Chapter 3

Platinum nanoparticle-decorated three-dimensional graphene with *in situ* formed ionomer interface as an active cathode for high-temperature polymer electrolyte membrane fuel cell

For improving the performance of platinum (Pt) electrocatalysts in polymer electrolyte membrane fuel cells (PEMFCs), it is important to enhance the Pt utilisation level in the catalyst systems. The work covered in this chapter focuses on the development of a high performing electrocatalyst (Pt/3DNG) for PEMFC applications by using nitrogen-doped three-dimensional graphene (3DNG) as the support material and an *in situ* grafted active "triple-phase boundary" to more precisely control the formation of the proton conducting ionomer interface at the active sites. Considering the 3D morphology of the system, during the electrode fabrication for realistic single-cell evaluation, the concept of *in situ* generation of the proton conducting-ionomer based "active triple-phase boundary" is introduced, which can potentially replace the conventional method of using Nafion ionomer for the electrode preparation. The monomers owing to their small-size can access the pores and inner regions of the 3DNG support, which on UV-curing, undergo polymerization and transform into an ionomer with the extended interfacial network into the nano regimes of 3DNG. Single cell evaluation of the membrane electrode assembly (MEA) in a high-temperature polymer electrolyte membrane fuel cell (HT-PEMFC) by using phosphoric acid doped polybenzimidazole membrane displayed competency of the present strategy.

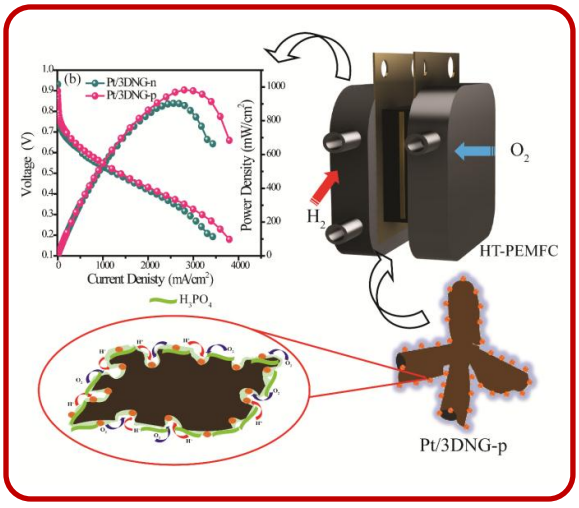

Content of this chapter is published in the following article:

Adv. Sustain. Syst., 2021, 5, 2000125

(https://onlinelibrary.wiley.com/doi/10.1002/adsu.202000125)

3. 1 Introduction

The advancement of the materialization of the hydrogen economy depends on the viability of the commercialization of the fuel cells. Fuel cells endowed with renewable hydrogen feedstock could contribute to the carbon-free energy economy by the conversion of the chemical energy into electrical energy and heat.[1-3] Among the different fuel cell systems, polymer electrolyte membrane fuel cells (PEMFCs) gained attention due to their low working temperature, high power output, and scalability of the system according to the demand.[4-6] However, several hurdles are needed to be overcome prior to the commercialization of PEMFCs. [7, 8] The electrocatalysts at the cathode require particular attention to overcome the present issues related to high overpotential, exorbitant cost, and low durability.[9-11] The cathode catalyst contributes more towards the underlying cost since the oxygen reduction reaction (ORR) in the cathode is the more energy-intensive process than the hydrogen oxidation reaction (HOR) in the anode.[12, 13] Substantial attempts are being made towards the development of PEMFC catalysts to get better activity with a reduced amount of the state-of-the-art Pt catalyst loading and high durability.[14, 15] A strategy for lowering the Pt-loading and improving the Pt-utilization in the catalyst based on a carbon support with retarded corrosion rate is required for realizing cost-effective PEMFC assemblies for practical applications.[16, 17] Also, such possible advancements in the electrocatalyst designing must be complemented with efficient process protocols for electrode fabrication in order to effectively translate the qualified performance characteristics in a single electrode to the system level in a single cell mode.

Improving the electrode level performance of PEMFCs by enhancing the Pt utilization in the state-of-the-art Pt catalyst is one of the focusing areas of research.[18, 19] This requires strategies based on engineering of the microstructure of the catalyst support for creating extended active “triple-phase boundary (TPB)” based on proton conducting ionomers. Even though Pt is the frontline for the reaction sites, the Pt support structures also play vital roles in deciding the efficiency of the catalyst by providing necessary electronic support to the Pt nanoparticles.[20-23] However, the Pt nanoparticles anchored over the carbon support should have to maintain the appropriate TPB, which ensures the interface between the Pt surface, ionomer and the reacting gases.[24, 25] Usually, the spherical graphitic carbon has been used as the support material for dispersing Pt nanoparticles in the commercial PEMFC catalysts.[26] However, the 2D morphology of these materials leads to underutilization of Pt after mixing the catalyst with an

ionomer like Nafion, which is the widely used process for creating TPB. The TPB formation is non-uniform in these types of electrodes, which is primarily caused by the improper coverage of the highly viscous and high molecular weight ionomer over the 2D support morphology. In such cases, TPB is not expected to be extended to the inner cavities and micro regime of the carbon support where the Pt particles are likely to reside. Nafion has several other drawbacks such as its high synthesis cost because of the complex fluorine chemistry, and requirement of high humidity with a low-temperature range for its operation.[27, 28] During the fuel cell operation, the perfluoro sulphonic acid ionomers are prone to degrade to form HF and other radicals, causing Pt dissolution from the electrode surface.[29] Also, the SO_3^- groups in the Nafion side-chains cause the poisoning of the Pt surface during the fuel cell operation.[30, 31] All these significantly reduce the Pt utilization with eventual reduction in the mass activity of the Pt catalyst.

The existing drawbacks in the fuel cell catalysts can be overcome to a significant extent by the introduction of three-dimensional (3D) carbon supports and *in situ* generated polymer ionomer interface from pre-admitted ionomer moieties rather than directly applying a high molecular weight ionomer in the system. In this context, we decided to explore these two requirements of structurally and functionally fine tuning the electrode characteristics by developing an ORR catalyst possessing adequate structured features complemented with a better process for creating the TPB. This resulted into the development of a high performing electrocatalyst (Pt/3DNG) by using nitrogen-doped three-dimensional graphene (3DNG) as the support material and *in situ* grafted TPB to more precisely control the formation of the proton conducting ionomer interface at the active sites. The *in situ* generation of the TPB has been conceived through ultraviolet (UV)-light assisted free-radical polymerization leading to the formation of ionomer from the constituent monomers (acrylate and allyl ether-based monomers).[32-34] This concerted effort led to significantly enhanced performance characteristics in the material level and also during its electrode level exploration in a single cell mode of high-temperature PEMFC (HT-PEMFC). Unlike low-temperature PEMFC (LT-PEMFC) which mainly uses Nafion as the ionomer in the electrode to build TPB, the HT-PEMFC requires immobilized H_3PO_4 ideally in a uniformly distributed polymer matrix around the active Pt particles. The proposed 3D architecting of the catalyst support matrix and *in situ* polymerization in the presence of the acid medium help to create the indented TPB with immobilized H_3PO_4 moieties.

3.2 Experimental Section

3.2.1 Synthesis of 3DNG

We have followed our previous synthesis protocol for the preparation of 3DNG, which is briefly explained here.[35] In a typical synthesis, commercially purchased melamine foam was dipped in the graphene oxide (GO) solution in water (4 mg/ml) followed by drying under an IR lamp. The number of dipping was optimised as three times to get a uniform coating of the graphene oxide layer over the melamine foam. The wholly dried GO-melamine foam was then annealed at 900 ^{o}C for 3 h in an argon atmosphere. The annealed product has a bilayer structure with carbon nitride backbone, which is wrapped by a reduced graphene layer (3DNG). The carbon nitride in 3DNG is derived from the melamine foam whereas the graphene layer wrapping over it is achieved from the GO dipping.

3.2.2 Synthesis of Pt/3DNG

90 ml of ethylene glycol and 60 ml of H_2O were mixed well in a beaker. After uniform mixing, the whole solution was made into two portions of 60 ml and 90 ml of each. 40 mg of 3DNG was dispersed in 60 ml portion of the solution with continues stirring for 3 h. 26.5 mg of H_2PtCl_6 was dissolved in the remaining 90 ml solution. This solution was then added slowly to the 3DNG dispersion by using a burette. After the complete addition, the resultant solution was kept under stirring for overnight. It was then heated at 140 ^{o}C for 8 h. The solution mixture was then filtered and washed with DI water and dried at 120 ^{o}C in a vacuum oven to get the final Pt/3DNG catalyst.

3.2.3 Synthesis of NRG

The NRG was synthesized by annealing the mixture of GO flakes and melamine powder in the ratio of 3:2 in a tubular furnace at 900 ^{o}C for 3 h in an argon atmosphere.

3.2.4 Synthesis of Pt/VC & Pt/NRG

The Pt/VC and Pt/NRG were prepared by polyol method as mentioned for Pt/3DNG. Instead of 3DNG, here Vulcan carbon and NRG were used as support material for platinum dispersion.

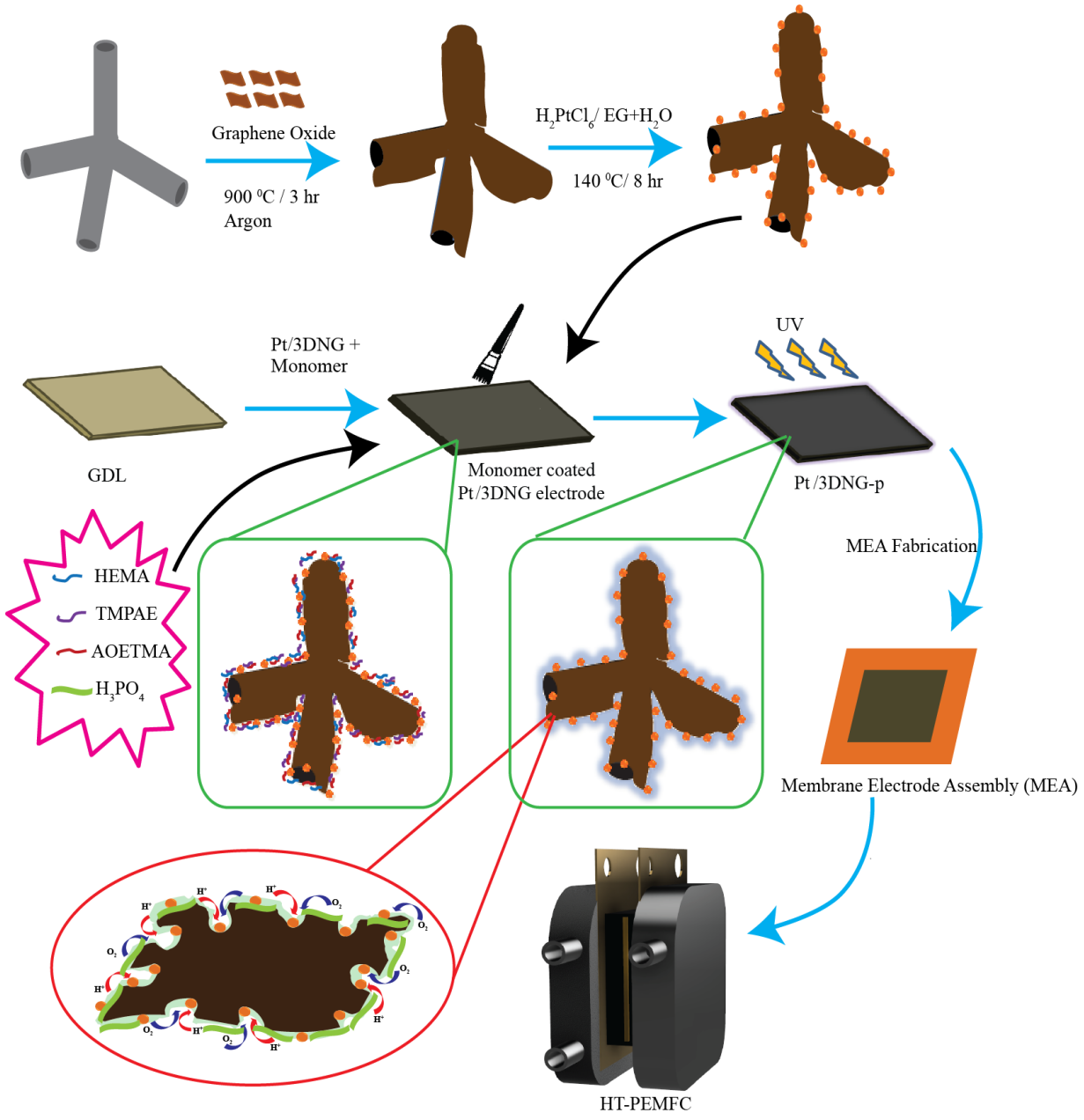

Figure 3.1 *Schematic presentation of the synthesis of the Pt/3DNG electrocatalyst and stepwise fabrication of the single cell of the high-temperature proton exchange membrane fuel cell (HT-PEMFC) by using Pt/3DNG as the cathode catalyst.*

3.2.5 Preparation of the Cathode

The precursor solution for the *in situ* generation of the ionomer was prepared by mixing a fixed volume of the monomers *viz*., hydroxyethyl methacrylate (HEMA), trimethylolpropane allyl ether (TMPAE), and [2-(acryloyloxy) ethyl] trimethyl ammonium chloride (AOETMA) solution (80 wt. % in H_2O) in a fixed ratio (the volume ratio of the monomers is HEMA:TMPAE: AOETMA = 1:1:2) and 30% (v/v) of concentrated H_3PO_4 (15.1 M/88 wt. % aqueous solution of H_3PO_4). An additional 5 µl of the UV-initiator, 2-hydroxy-2-methylpropiophenone (HMPP) was also added. In a typical procedure, 287.5 µl each of HEMA and TMPAE, 575 µl and 450 µl each of AOETMA and H_3PO_4 were used (total volume of the precursor solution is 1505 µl including the volume of HMPP). The solution was appropriately subjected to vortex stirring for an hour and was added to the Pt catalyst slurry (prepared in isopropyl alcohol) by maintaining the monomer:carbon ratio (by weight) of 0.40 (m/c = 0.4). Thus prepared catalytic slurry was again thoroughly bath sonicated for 10 minutes. The catalyst-ink was then coated over the GDL with a fine brush gently and unidirectional; after each layer coating, the GDL was kept on the hot plate at 40 ^oC for the evaporation of the IPA and proper drying. The process was repeated until the whole ink was coated. Thus coated GDL electrode was later placed in a UV chamber (the laboratory-grade UV chamber used for the polymerization contained eight fluorescent lamps in a metallic chamber (Model: OSRAM L BL UVA 15 W/78)) for polymerization followed by heating at 125 ^oC for overnight.

3.2.6 Doping of PBI membrane

For the doping of the PBI AP membrane, 4 cm x 4 cm PBI membrane was cut. The uncured membrane was then immersed in 85 wt. % of phosphoric acid at 100 ^oC for 3 h. The cured PBI membrane was kept in an air-conditioned room for 48 h. After that, it was preserved under an N_2 atmosphere for further use.

3.2.7 Preparation of Anode

For the anode, the catalytic slurry with a Nafion:carbon weight ratio of 0.40 (n/c = 0.40) was prepared by adding 125 mg of Pt/C (40%), which was wetted with 2 ml of deionized water, and 10 ml of IPA was added. The mixture was adequately mixed by a probe sonicator for 10 min. and coated over the 3.5 cm x 3.5 cm GDL using a fine brush, unidirectional by keeping the

coated GDL over the hot plate at 40^{o}C after each coating. The catalytic slurry was coated entirely, and the electrode was kept in the oven at 125^{o}C for overnight.

3.2.8 Membrane Electrode Assembly (MEA) preparation

For the MEA preparation, we have adopted our own developed protocol.[36] The catalyst coated cathode and anode (3.5 cm × 3.5 cm in size) were sandwiched with a H_3PO_4 pretreated polybenzimidazole (PBI) membrane in the center. The active area of the MEA was fixed as 9 cm^2. Before sandwiching the electrodes, a fine layer of H_3PO_4 was coated on the electrodes by using the brush. Thus prepared MEA was hot-pressed for 10 min. at 130^{o}C under the load of 1 metric ton. The prepared MEA was assembled in a standard test fixture (Fuel Cell Technologies, Inc., USA) by applying a torque of 3 Nm. The fixture was then connected to a fuel cell test - station (Fuel Cell Technologies, Inc., USA) for final fuel cell studies.

3.2.9 Material characterization

The scanning electron microscopic (FESEM) images were recorded in a Nova Nano SEM 450 instrument. A FEI Technai G2 T20 instrument which was operated at 200 k eV, was used to obtain the transmission electron microscopic (TEM) images. X-ray diffraction (XRD) studies were conducted using a PANalytical instrument using Cu Kα (λ=1.54 Å) radiation by operating at a scanning rate of 5^{o} min^{-1}. Raman analysis was performed with the help of a LabRam spectrometer (HJY, France) equipped with a laser wavelength of 632 nm. The surface investigation of the catalyst was performed with the help of a VG Micro Tech ESCA 300^{0} X-ray photoelectron spectroscopy (XPS) at a pressure of >1×10^{-9} Torr. The surface area and pore size distribution of the sample were investigated using a Quantachrome Quandrasorb automatic volumetric measurement system. The instrument was operated at 77 K using ultra-pure nitrogen gas.

3.2.10 Electrochemical characterization

A set of electrochemical methodologies was adopted for performing the electrochemical measurements and a Biologic electrochemical workstation (VMP3) was used for this purpose. The measurements were performed using a conventional three-electrode setup by using 0.1 M $HClO_4$ as the electrolyte, a glassy carbon rotating disc electrode coated with the catalyst (Pine

Instruments Inc.) as the working electrode and Ag/AgCl as the reference electrode. The electrode potential measured using the Ag/AgCl electrode was normalized for hydrogen electrode (RHE), for which the following equation was used:

$E_{RHE} = E_{Ag/AgCl} + 0.196 + 0.059\ pH$ (3.1)

10 mg of the catalyst in 2 ml of 2:3 mixture of isopropyl alcohol and water was sonicated for 1 h to prepare the catalyst ink. 10 µl from this ink was drop cast on the glassy carbon electrode, followed by drying under an IR lamp. Subsequently, 1 µl of 0.01 wt. % Nafion solution in ethanol was applied to the catalyst, which acts as a binder as well as an ionomer. The following equations were used to derive the electrochemical activity parameters of the catalysts.

$$\text{ECSA } (m^2\ g_{Pt}^{-1}) = \frac{Q_{H-adsorption}\ (mC)}{0.210\ (mC\ cm^{-2}) * L_{Pt}\ (mg)} \quad (3.2)$$

$Q_{H\text{-}adsorption}$ = Charge for hydrogen underpotential adsorption.

L = Pt loading

$$rf = \frac{A_{real}}{A\ geo} = \frac{Q_{H-adsorption}\ (mC)}{0.210\ (mC\ cm^{-2}) * 0.196\ cm^2} \quad (3.3)$$

rf = roughness factor

A_{real} = Surface area of Pt measured from CV

A_{geo} = Area of the working electrode

The kinetic current i_k can be calculated by Equation 3.4, where i_o is the observed current at E = 0.850 V and i_d is the limiting current that can be directly obtained from the ORR curve.

$$i_k = \frac{i_d * i_o}{i_d - i_o} \quad (3.4)$$

Mass activity $MA = \frac{i_k * r_f}{L_{Pt}}$ (3.5)

Specific activity $SA = \frac{i_k}{A_{real}}$ (3.6)

3.3 Result and Discussion

The annealing of the GO soaked melamine foam creates a bilayer architecture having carbon nitride backbone with nitrogen-doped graphene sheet hanged over it. During the annealing at high temperature, the melamine foam carbonizes in an inert atmosphere to form tetrapods of non-stoichiometric carbon nitride (CN_x) with concomitant release of some amount of nitrogen. This expelled nitrogen will be partially harvested by the graphene sheets formed by the thermal reduction of the GO wrapped over the CN_x tetrapods (3DNG). Thus, apart from acting as a mechanical support, melamine foam serves as a nitrogen precursor, which helps to achieve the nitrogen doping in the graphene layer to form 3DNG.

3.3.1 SEM analysis

The SEM and TEM images presented in **Figure 3.2a** and **b** display the morphological features of 3DNG, where the interconnected 3D architecture of the system is evident. The arms of the interconnected tetrapod structures are found to be having a length of around 20 μm and width of around 1 μm. The bilayer 3D carbon morphology was used further as the carbon support for the anchoring of the Pt nanoparticles through the polyol method as detailed in the experimental section. The 3D architecture of the system is found to be retained even after the Pt dispersion process, which is confirmed from the SEM and TEM images of Pt/3DNG presented in **Figure 3.2c** and **d**. **Figure 3.2d** shows the low magnification TEM image focused on the sheet-like morphology of the graphene layer residing over the carbon nitride support material. The image depicts the uniformly embedded Pt nanoparticles on the graphene layer. Since the graphene layers where the Pt nanoparticles dispersed are hanged over the tetrapods of the CN_x structure, the system ensures spatial separation of the graphene layers by effectively preventing the interlayer stacking.[37] Further, a high magnification image presented in **Figure 3.2e** at 10 nm scale bar validates the uniform distribution of the Pt nanoparticles without indication of any observable agglomeration. Another image recorded at 5 nm scale (**Figure 3.2f**) confirms the spherical nature of the Pt nanoparticles with size in the range of 2 to 4 nm. Also, the TEM line profile identified a d-spacing value of 0.221 nm, corresponding to the Pt (111) plane (inset **Figure 3.2f**).[38] This confirms the exposure of the ORR active 111 planes of Pt in Pt/3DNG.

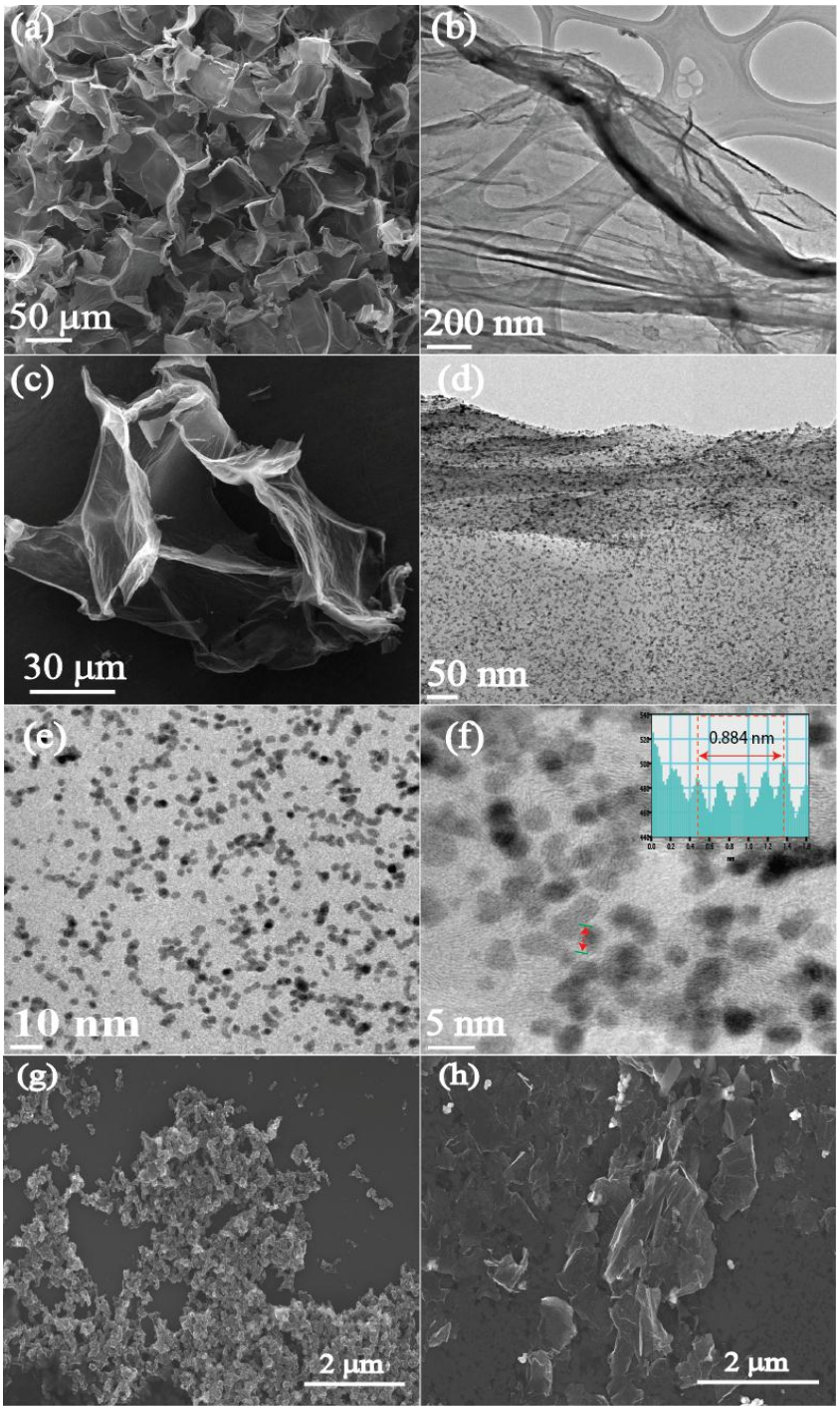

Figure 3.2 *(a) The SEM image of the 3DNG system showing the interconnected network structure, (b) the TEM image of 3DNG showing the sheet like graphene layer, (c) the SEM image of Pt/3DNG and (d, e and f) the TEM images of Pt/3DNG catalyst recorded at different magnifications, inset of Figure (f) is the line profile of the Pt nanoparticles, (g) FESEM image of Pt/VC and (h) FESEM image of Pt/NRG.*

For the comparison purpose, Pt/VC and Pt/NRG were prepared as control samples and the FESEM images of the corresponding samples are presented in **Figure 3.2g and h**. A comparison with respect to the morphological features and Pt dispersion characteristics between the control samples and Pt/3DNG clearly portrays the advantages acquired by the later system due to its more exposed and accessible nature of the active sites. From our previous studies, it was observed that a thin wrapping of the graphene layer on the CN_x tetrapod reduces the electronic conductivity of the support material whereas a higher thickness beyond a threshold level affects its preferred 3D-interconnected morphology.[35, 37] In an electrode level requirement for realistic system level application of PEMFC, it is important to ensure that the system meets the key features like the accessibility of the Pt nanoparticles, distribution of the reactants within the electrode matrix and dissipation of the product water during the course of the reaction. The morphological investigation as detailed here provides strong evidence that Pt/3DNG meets these key requisites.

3.3.2 Raman and XRD analysis

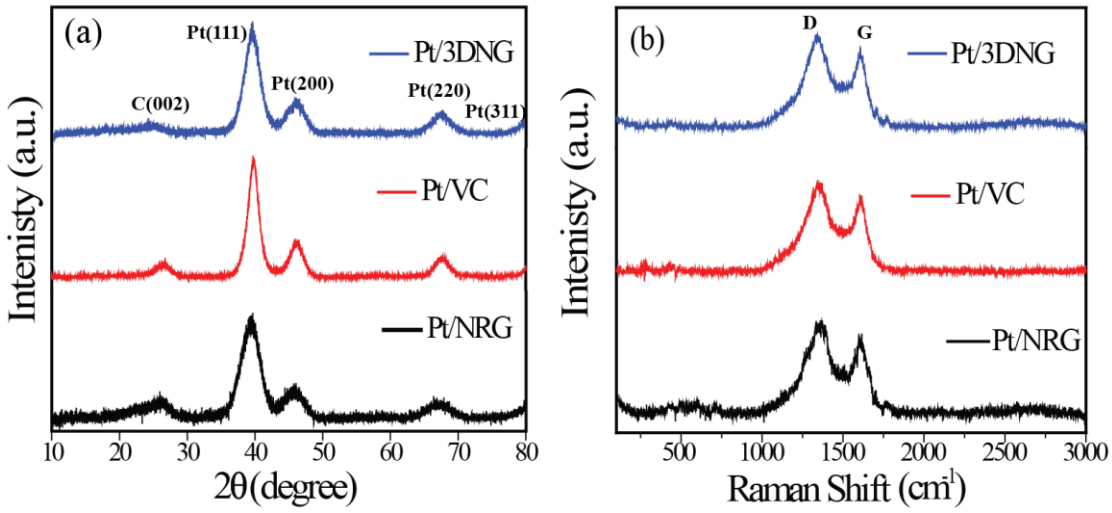

Figure 3.3 *(a) XRD profiles and (b) Raman spectra of Pt/3DNG, Pt/VC and Pt/NRG.*

The powder X-ray diffraction (XRD) pattern of Pt/3DNG is compared with that of Pt/NRG and Pt/VC in **Figure 3.3a**. All the three samples show the same peak positions corresponding to the Pt nanoparticles and the carbon support materials. The peaks at the 2θ values of 39.6° (111), 45.4° (200) and 68.1° (220) are attributed to the different planes of Pt (JCPDS: 87-0647). The

XRD spectra confirm the existence of the face centred cubic crystal lattice of Pt nanoparticles in the crystalline state. Since all the support materials compared here are conducting carbons but with distinct morphological differences, all are showing the same peaks corresponding to carbon (2θ values of 26.3^{o}) without any visible shift in the position of the peaks. **Figure 3.3b** shows the comparative Raman spectra of all the catalysts. Even though the frequencies of the G and D bands of all the catalysts have similar Raman shift value, the catalysts differ with respect to the intensity ratio of the D and G bands. The G and D bands appear at 1590 and 1334 cm^{-1}, respectively. Here, the G band represents the graphitic content and the peaks originate from the zone-centre E_{2g} mode, whereas the D band represents the peak assigned to the A_{1g} zone-edge phonon induced by the disorder in the graphite lattice.[39] Hence, the G band denotes the sp^2 carbons in the hexagonal framework of the carbon and the D band corresponds to the defective sp^3 carbons formed in the sp^2 carbon lattice.

3.3.3 Surface area analysis

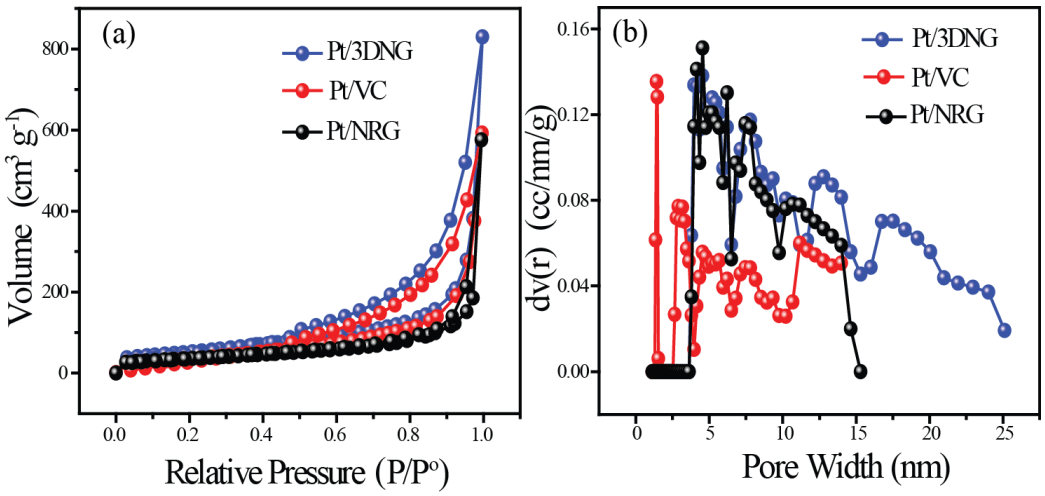

Figure 3.4 *(a) BET isotherms and (b) pore-size distribution profiles of Pt/3DNG, Pt/VC and Pt/NRG.*

The Brunauer-Emmett-Teller (BET) surface area of all the samples was measured from the nitrogen adsorption-desorption analysis. **Figure 3.4a** shows the N_2 adsorption isotherms of all the samples, which follow a typical Type II characteristic in the relative pressure region of (P/P^0) 0.40 to 0.95. The surface area values of all the catalysts are in the following order: Pt/3DNG (186 m^2 g^{-1}) > Pt/VC (154 m^2 g^{-1}) > Pt/NRG (127 m^2 g^{-1}). It is interesting to note that even

though Vulcan carbon displays higher surface area than graphene in general, when graphene is distributed across the CN_x framework in Pt/3DNG, the system acquires a surface area which is the highest among the three systems. Along with the higher surface area, all the catalysts have a wide range of pore width in the mesoporous region (**Figure 3.4b**). However, it is evident from **Figure 3.4b** that, among all the three systems, Pt/3DNG has the highest overall pore volume in the mesopores region, which is a favourable morphological modulation considering the end application of the system in the electrodes of PEMFC.

3.3.4 XPS Analysis

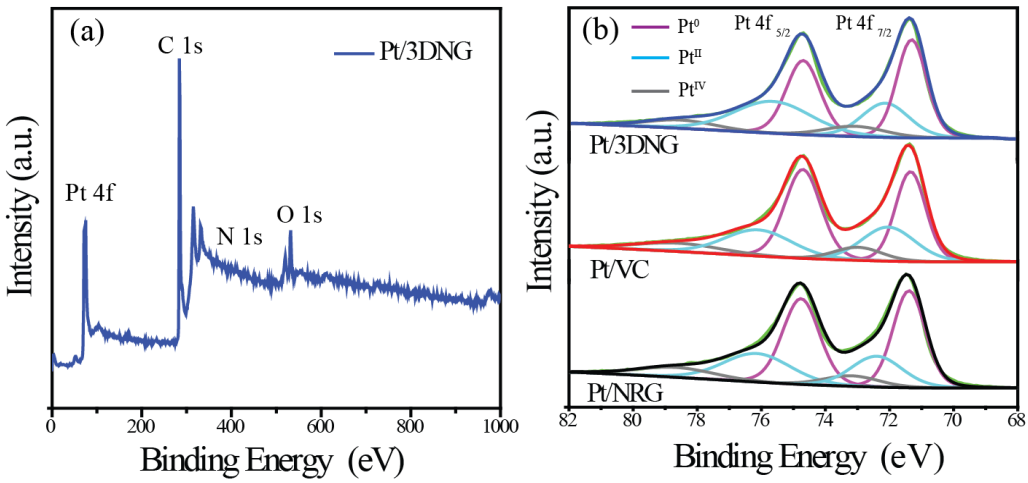

Figure 3.5 *(a) XPS survey spectrum of Pt/3DNG catalyst. (b) Comparative XPS profiles of Pt/3DNG, Pt/ VC and Pt/NRG.*

Further insightful information on the nature and state of the catalytic systems could be gained with the help of the X-ray photoelectron spectroscopy (XPS) analysis. The survey spectrum of Pt/3DNG presented in **Figure 3.5a** displays four distinct peaks at ~70.0, ~284.1, ~400.1 and ~532.1 eV corresponding to the presence of Pt, C, N and O, respectively. Furthermore, to investigate the possible interaction between the Pt nanoparticles and the support morphologies, high-resolution XPS signals of Pt 4f and N 1s were deconvoluted into the corresponding components, as presented in **Figure 3.5b** and **Figure 3.6**. The Pt 4f XPS spectra of all the samples show the two typical peaks at high and low binding energy values respectively corresponding to Pt $4f_{5/2}$ and Pt $4f_{7/2}$. The Pt 4f signals can be deconvoluted into three doublets which can be assigned to the Pt^0 state (magenta line), Pt^{2+} state (cyan line), and Pt^{4+} state (ash

line).[40] The doublets with low binding energies such as 71.5 and 74.9 eV are corresponding to the metallic Pt particles Pt^0. The doublets with the higher binding energies in the deconvoluted spectrum can be assigned to the surface oxidized Pt species Pt^{4+}.[41] The electron deficient and atomically dispersed Pt particles formed as Pt^{2+} in the graphene surface is also detected in XPS.[42, 43] The DFT calculation reveals that the formation of such electron-deficient metal species may occur due to the interaction of metals with nitrogen atoms at the N doped carbon surface.[44] By comparing the XPS peaks of all the catalysts, it could be seen that the binding energies for both Pt $4f_{5/2}$ and $4f_{7/2}$ peaks in Pt-3DNG and Pt/NRG are shifted positively by ~0.22 and ~0.14 eV relative to Pt/VC. This shift in the binding energy could be ascribed to the electronic interaction between the embedded Pt nanoparticles and the surface nitrogen atoms,

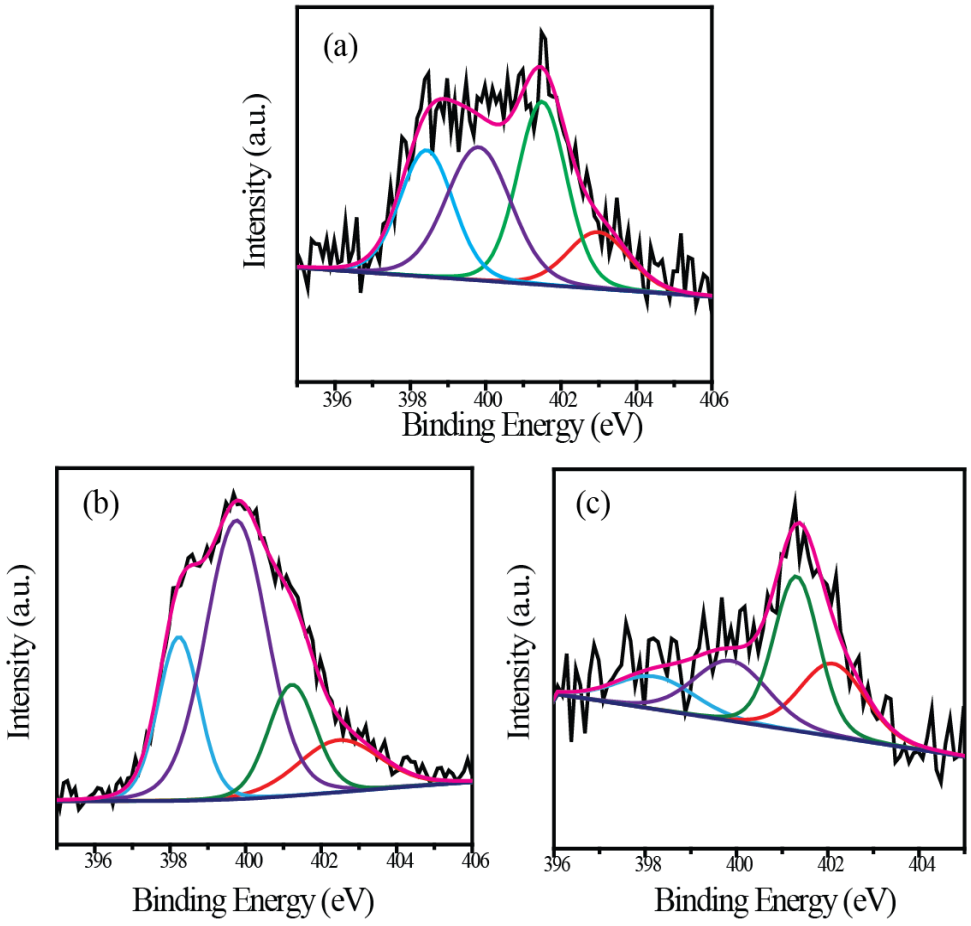

Figure 3.6 *Deconvoluted N 1s spectra of (a) Pt/3DNG, (b) Pt/NRG and (c) Pt/VC.*

which was corroborated by the shift of the N 1s peak in Pt/3DNG toward a lower binding energy value compared with the reported N doped systems.[45] The interaction of the N and Pt further could be confirmed from the analysis of the N 1s spectra. This reveals the presence of four different types of N such as pyridinic (398.3 eV), pyrrolic (399.6 eV), graphitic (401.4 eV) and N-oxide (402.9). The electronic interaction between the Pt nanoparticles and the N-doped graphene layer would alter the electronic structures of the surface atoms in the Pt nanoparticles and, thus facilitates the adsorption/desorption of the oxygen species present on their surface, which would contribute towards improved stability and catalytic activity of Pt/3DNG.

3.3.5. Thermogravimetric analysis

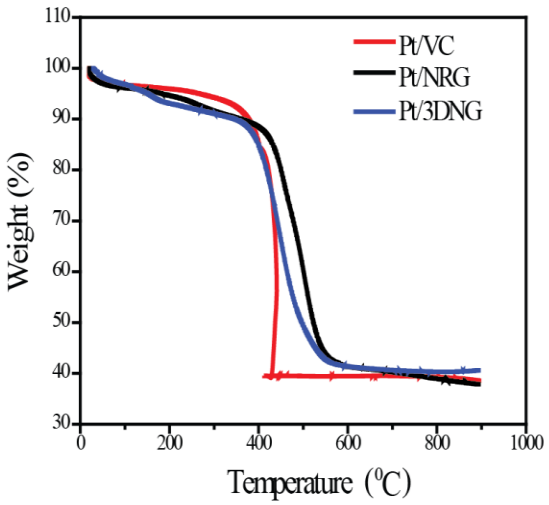

Figure 3.7 *TGA profiles of Pt/3DNG, Pt/VC and Pt/NRG catalysts recorded in an oxygen atmosphere.*

TGA profiles of all the samples were recorded in the oxygen atmosphere at a heating rate of 10^{o}C per minute and the corresponding plots are presented in **Figure 3.7**. All the three catalysts show an initial degradation of 10 wt. % up to 400 ^{o}C which is due to the removal of the adsorbed moisture. This is followed by a major weight loss in the range of 400 to 600 ^{o}C resulted due to the oxidation of carbon. After 600 ^{o}C, the TGA profile of Pt/3DNG shows a flat portion with a residue content of 40 wt. % corresponding to the overall Pt loading in the system. In a similar way, the other two systems also display a Pt loading of 40 wt. %. It should be noted that the 40 wt. % loading on carbon is generally maintained in the state-of-the-art Pt/C catalysts for PEMFC

applications. The high Pt loading has the advantage that the required Pt loading in the electrode (1 mg cm^{-2}) can be achieved by maintaining the electrode thickness within the acceptable range to prevent the system from the issues of mass transfer and ohmic drop. It should be noted that the required 40 wt. % Pt on Pt/3DNG could be attained all the while by restricting the size of the Pt nanoparticles in 2-5 nm and without any indication of particle agglomeration, as evident from the TEM studies.

3.3.6 Electrochemical analysis

Electrochemical evaluation of the catalysts was first performed using cyclic voltammetry (CV) in 0.1 M $HClO_4$ with Ag/AgCl as the reference electrode and graphite rod as the counter electrode. **Figure 3.8a** shows the comparative cyclic voltammograms of Pt/3DNG, Pt/VC and Pt/NRG in N_2 saturated 0.1 M $HClO_4$ electrolyte at a scan rate of 50 mV s^{-1}. The CV profiles show the typical Pt feature comprising of the potential regions corresponding to hydrogen adsorption-desorption, oxygen adsorption-desorption and non-faradaic capacitance. The electrochemically active surface area (ECSA) of all the samples was calculated from the hydrogen desorption using **Equation 3.1**. The ECSA value of Pt/3DNG is calculated to be 62.4 m^2 g^{-1}, which is higher than that of Pt/VC (56.7 m^2 g^{-1}) and Pt/NRG (51.3 m^2 g^{-1}). This high ECSA of Pt/3DNG could be originated from the features like better exposure and uniform size distribution the Pt nanoparticles as well as the more accessible textural characteristics of the catalyst. **Figure 3.8b** shows the linear sweep voltammograms (LSVs) corresponding to oxygen reduction reaction (ORR) recorded at 1600 rpm of the working electrode in oxygen saturated 0.1 M $HClO_4$.

Pt/3DNG (0.991 V) recorded the highest onset potential among the three catalysts, followed by Pt/VC (0.979 V) and Pt/NRG (0.968 V). However, this difference in the onset potential becomes more dominant in the half-wave potential ($E_{1/2}$) region, which is a very important parameter in judging how well the catalyst can facilitate ORR under the more realistic perspective of the current dragging condition. The $E_{1/2}$ value recorded for Pt/3DNG (0.846 V) is substantially higher than that of Pt/C (0.817 V) and Pt/3DNG (0.795 V), and this significant advantage in the case of Pt/3DNG is originated mainly from its structural features. Under the current dragging condition, a system which can offer improved reactant distribution and active site accessibility fares better and Pt/3DNG thus outperforms the other systems in terms of $E_{1/2}$ due to its unique structural features.

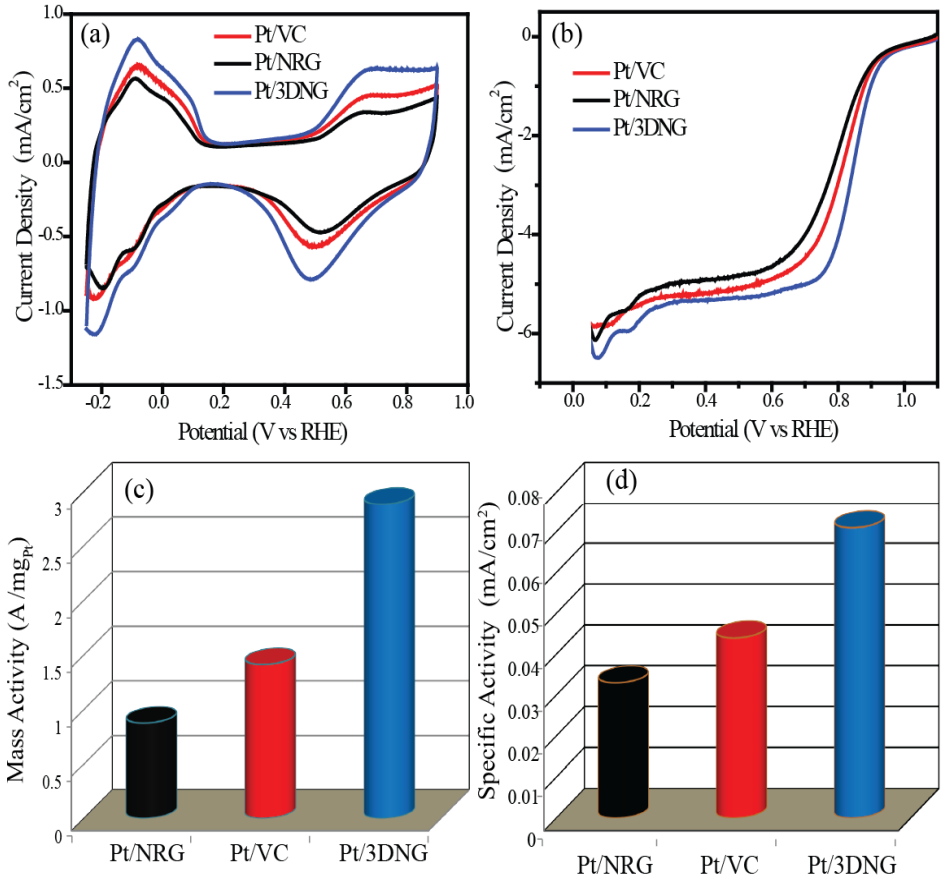

Figure 3.8 *(a) The CV profiles of all the catalysts in 0.1 M $HClO_4$ recorded at a scan rate of 50 mV s^{-1}, (b) LSVs recorded for all the catalysts in 0.1M $HClO_4$ at an electrode rotation speed of 1600 rpm, (c & d) specific activity and mass activity plots of all the catalysts measured at 0.850 V vs RHE.*

The mass activity and specific activity of all the catalysts were calculated at the kinetic region (0.850 V *vs* RHE) by using **Equation 3.5** and **3.6**. The mass activity follows the trend: Pt/3DNG (2.88 A mg^{-1}_{Pt}) > Pt/VC (1.41 A mg^{-1}_{Pt}) > Pt/NRG (0.88 A mg^{-1}_{Pt}) (**Figure 3.8c**). The specific activity also follows the same trend of Pt/3DNG (0.071 mA cm^{-2}) > Pt/VC (0.044 mA cm^{-2}) > Pt/NRG (0.033 mA cm^{-2}) (**Figure 3.8d**). As in the case of the $E_{1/2}$ values, the differences in the mass activity and specific activity value of the three catalysts also point towards the important role played by the support morphology in imparting the required activity and performance characteristics to the Pt-based systems under the standard working environments.

Pt/3DNG with its 3D aligned morphology and exposed Pt active sites becomes a more dynamic system compared to its counterpart systems which have inherent limitations imposed by the support morphologies.

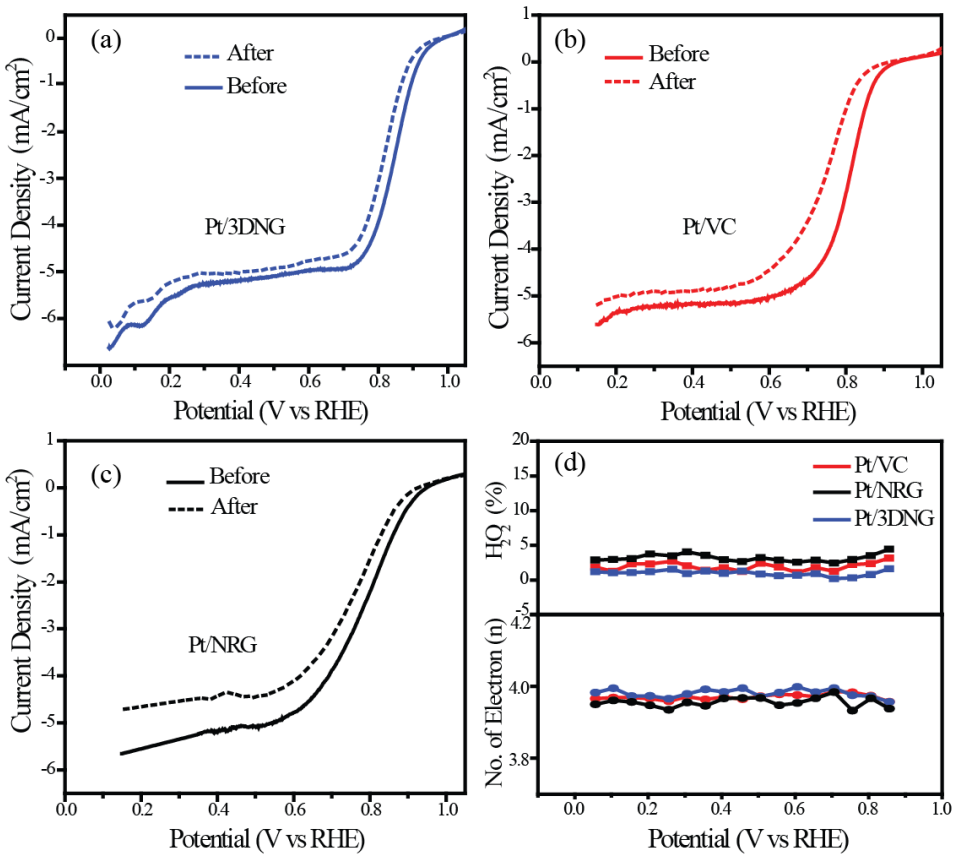

Figure 3.9 *(a) LSVs of (a) Pt/3DNG,(b) Pt/VC and (c) Pt/NRG catalysts recorded before and after the 5000 ADT cycles; (d) the amount of H_2O_2 calculated for Pt/3DNG as a function of the electrode potential (above) and the number of electron transfer for ORR calculated from the RRDE analysis (below).*

It is important in an electrochemical perspective that the catalyst possesses structural integrity and active site retainment during the course of the reaction lasting for several hours. To investigate this, an accelerated durability test (ADT) was performed in the oxygen reduction region by cycling the potential between 0.60 to 1.0 V for 5000 cycles with continues oxygen purging. The LSVs recorded in the case of Pt/3DNG before and after ADT are compared in **Figure 3.9a**, which display only 23 mV shift in the $E_{1/2}$ value subsequent to ADT. This value is significantly low compared to that obtained in the case of Pt/VC (60 mV) and Pt/NRG (41 mV)

(**Figure 3.9b and c**). The controlled buckling of the nitrogen-doped graphene layer and unsaturation help 3DNG to strongly bind the Pt nanoparticles. At the same time, the aligned and layer-separated dispersion of the NG sheets along the CN_x tetrapod prevents gradual restacking of the NG layers. A controlled interplay of these beneficial factors helps Pt/3DNG to survive better under the ADT conditions. On the other hand, VC in Pt/VC is prone to high carbon corrosion whereas NRG in Pt/NRG is susceptible for restacking of the catalyst layers. Hence, these two systems show a greater rate of fall in $E_{1/2}$ during the course of ADT.

To gain more quantitative information on the ORR kinetics, rotating ring-disc electrode (RRDE) analysis was performed and estimated the number of electrons involved and the quantity of the H_2O_2 intermediate formed during the reaction. These results are presented in **Figure 3.9d**. All the three catalysts recorded the electron transfer number very close to the desired value of 4.0, indicating the reaction kinetics favouring the formation of H_2O. This is substantiated with the significantly low amount of H_2O_2 (< 4 %). Being Pt as the active site in all the three cases, the kinetic behaviour is as expected. At the same time, due to the presence of multiple components in the substrate matrix like CN_x and N-doped graphene in the case of Pt/3DNG, it is important to rule out the possibilities of any significant contributions by the parasitic 2-electron transfer reaction triggered by the functional groups and heteroatoms present in the system. The RRDE data obtained in the present case rule out all such possibilities.

Followed by the promising single electrode results obtained in the case of Pt/3DNG towards ORR, a realistic system level validation has been performed by testing a single cell of a high-temperature PEMFC (HT-PEMFC). Unlike its low-temperature counterpart (LT-PEMFC), which is mainly based on Nafion as the proton-conducting membrane, the HT-PEMFC (based on H_3PO_4 doped polybenzimidazole (PBI) membrane) possesses more electrode level challenges. The factors like the presence of free H_3PO_4, the high operating temperature in the range of 150-170^oC and high rate of carbon corrosion demand new types of electrodes which can better take care of the issues related to mass transfer, catalyst utilization and stability. Due to the advantageous features as understood from the previous discussions, the Pt/3DNG based electrode is expected to be a better contender for the HT-PEMFC application.

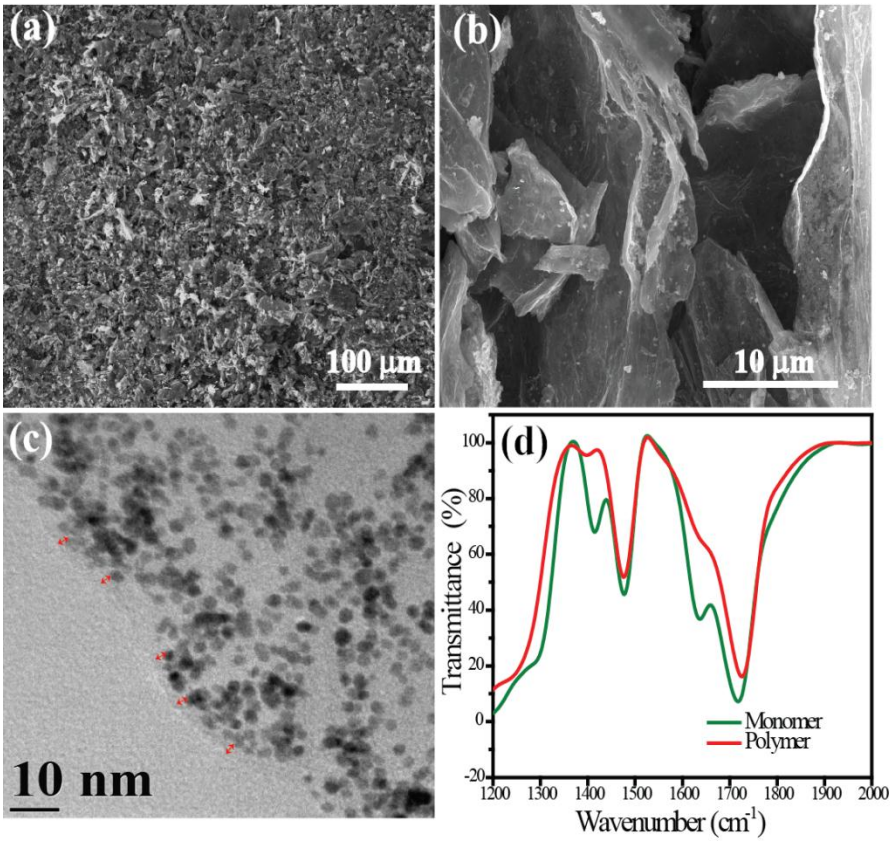

Figure 3.10 *(a) and (b) ESEM images of the Pt/3DNG-p electrode surface recorded at different magnifications; (c) the TEM images depicting the "triple-phase boundary" of the Pt/3DNG-p; (d) FTIR spectra of the Pt/3DNG-p electrode before and after UV polymerization.*

The membrane electrode assembly (MEA) was prepared by sandwiching the H_3PO_4 doped PBI membrane in between the Pt/3DNG coated gas diffusion layer (GDL) as the cathode and commercial Pt/C coated GDL as the anode. Due to the peculiar morphology of Pt/3DNG, we have avoided the conventional methods adopted for creating the active ionomer interface (known as the "triple-phase boundary") considering the fact that the polymeric solid electrolytes or binders cannot infiltrate into the interstitial space created by the CN_x tetrapods due to the size mismatch. Instead, we have adopted UV-light induced free-radical polymerization for the *in situ* generation of a fluorine-free ionomer to act as a medium to entrap H_3PO_4 and thereby to create a well-extended ionically conductive interface around the dispersed Pt nanoparticles. The monomers for the *in situ* polymerization were judiciously chosen considering our previous

works, in which the *in situ* polymerization in combination with H_3PO_4 is reported to possess ionic conductivity in the order of 10^{-1} to 10^{-2} S cm^{-1}.[33, 46] The electrode was fabricated by following two simple steps as shown in **Figure 3.1**. In the first step, the Pt/3DNG catalyst was mixed with the monomer mixture consisting of hydroxyethyl methacrylate (HEMA), trimethylolpropane allyl ether (TMPAE), and [2-(acryloyloxy) ethyl] trimethyl ammonium chloride (AOETMA) and H_3PO_4, and dispersed well with the help of bath sonication to get uniform spread of the ionomer mix over the catalyst surface. The as prepared catalyst slurry was then uniformly brush coated over a GDL. In the next step, the electrode was kept under a UV source for triggering *in situ* polymerization of the monomers by concomitantly entrapping the H_3PO_4 moieties to form the ionomer interface. In this way, the *in situ* polymerization helps to achieve well extended and uniformly distributed active "triple-phase boundary" in the electrode matrix by effectively controlling the pore blocking. This reduces the Knudsen resistance and improves the mass flow through the ionomer surface.[47] The ratio of the monomer to carbon (m/c) was optimized by trial and error method and an m/c ratio of 0.40 was found to be the optimum value. The electrodes were then hot-pressed with the H_3PO_4 doped PBI membrane to form the final MEA of 9 cm^2 active area. The ESEM images of the brush coated Pt/3DNG electrode possessing the *in situ* polymer ionomer interface (Pt/3DNG-p) recorded at two different magnifications are given in **Figure 3.10a** and **b**. The high magnification ESEM image of the surface of the Pt/3DNG-p cathode shows that that the 3D architecture of the catalyst morphology is well maintained during the electrode fabrication. Thus, the electrode holds the active channels for reactant distribution and product dissipation, which conveys the purpose of developing the *in situ* polymerization strategy for achieving the active "triple-phase boundary". The TEM image of the Pt/3DNG-p electrode shown in **Figure 3.10c** clearly shows the presence of the thin and uniform coating of the ionomer layer formed over the electrode surface. Nearly 4 nm thick ionomer layer is found to be uniformly spread over the catalyst layer. The comparative FT-IR data presented in **Figure 3.10d** confirms polymerization under the UV irradiation conditions. The peak present at 1413 cm^{-1} in the case of the monomer, which corresponds to the CH bending vibration in the $-CH_2$ groups, and the C=C stretching (non-conjugated) peaks at 1635 cm^{-1} are found to be disappeared after the polymerization.

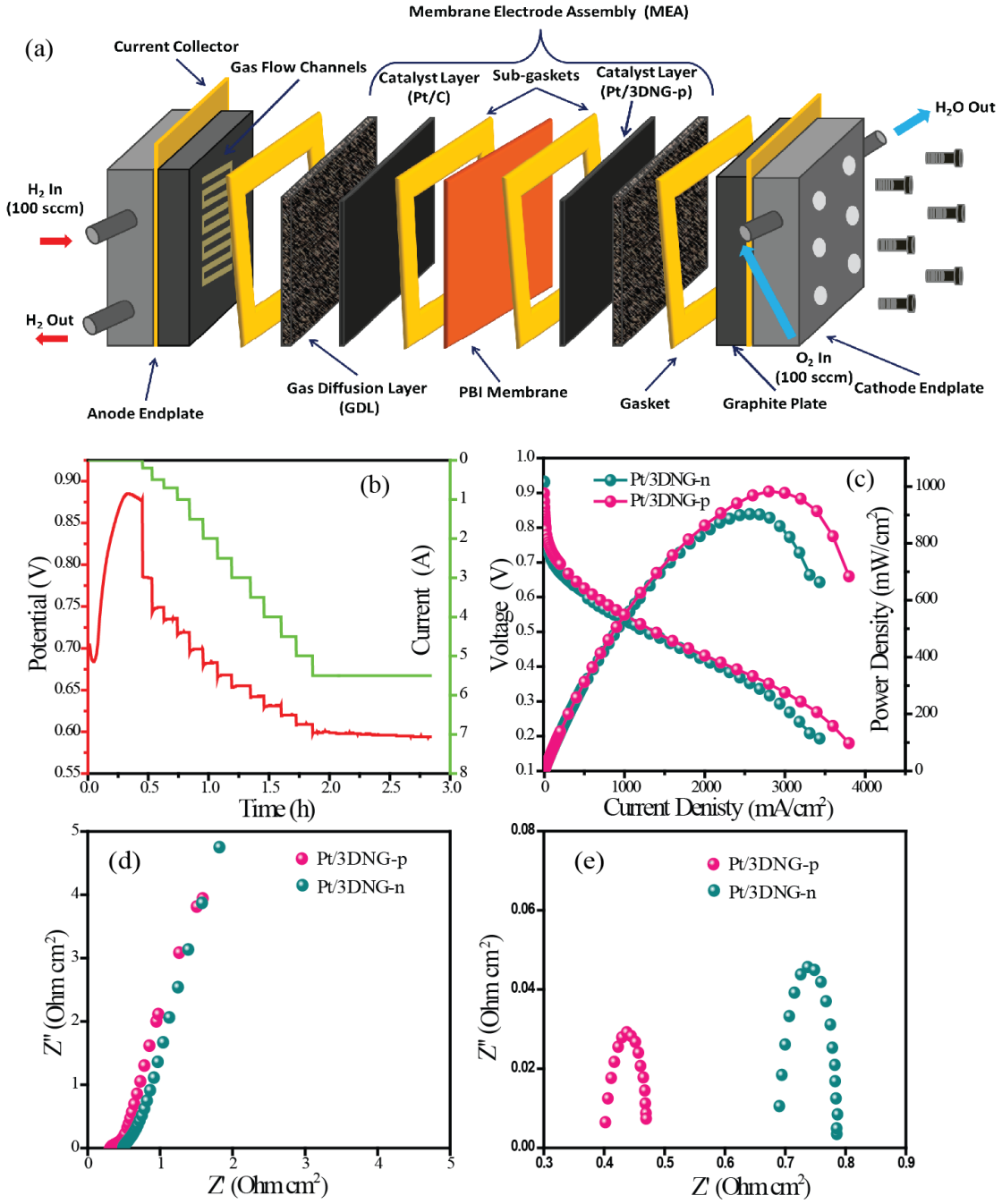

Figure 3.11 *(a) Schematic illustration representing the components and assembling of a single cell of HT-PEMFC, (b) conditioning plot for the MEA based on the Pt/3DNG-p cathode, (c) comparative I-V polarization plots recorded during the single cell evaluation of the MEAs with the Pt/3DNG-p and Pt/3DNG-n cathodes; Nyquist plots recorded during the single cell evaluation of the MEAs at (d) open circuit potential and (e) at 0.60 V.*

The single cell testing (9 cm^2 active area) of the MEAs was performed under H_2-O_2 feed conditions at an operating temperature of 160 ^oC by maintaining the anode and cathode gas flow rates as 100 sccm and 100 sccm, respectively. **Figure 3.11a** represents the test assembly representing how the MEA is configured in the cell. Prior to the current (I) – voltage (V) polarization studies, the MEA was conditioned by stepwise dragging of small current with simultaneous increase of temperature up to 160 ^oC and till the cell voltage reaches up to 0.60 V (**Figure 3.11b**). **Figure 3.11c** shows the comparative I-V polarization plots recorded during the single cell evaluation of the MEA based on the Pt/3DNG-p cathode and another MEA consisting of the cathode prepared by following the standard protocol by using Nafion as the ionomer (Pt/3DNG-n). In both cases, the same commercial Pt/C JM catalyst based electrodes with Nafion ionomer binder were used as the anode. It can be readily seen that, both the MEAs display well featured polarization plots covering the entire window of activation, ohmic and mass transfer regions. However, a close look at the polarization plots reveals that the MEA based on the Pt/3DNG-p cathode slightly outperforms the counterpart system based on the Pt/3DNG-n cathode. The magnitude of the performance increases with the current density, which leads to a significant difference in terms of the maximum power density displayed by the two systems. The maximum power density displayed by the Pt/3DNG-p and Pt/3DNG-n systems is 982 and 860 mW cm^{-2}, respectively. This notable difference is expected to be originated from the ability of the in-house system to address the mass transfer requirements of the system in a better way, particularly under the high current dragging conditions, due to its favourable morphological features. Also, it should be noted that, even at 0.60 V, which is considered as one of the standard operating potential regions of a PEMFC, the Pt/3DNG-p system with 0.650 A cm^{-2} as its achievable current density outperforms the Pt/3DNG-n system which delivered a current density of only 0.533 A cm^{-2}.

More insightful information on the MEA characteristics, particularly to understand the activity modulation achieved through the adopted *in situ* polymerization strategy, has been gained by performing *in situ* electrochemical impedance spectroscopic (EIS) analysis. The corresponding data are presented in **Figure 3.11d** and **e**. The high frequency intercept of the Nyquist plot recorded under H_2/O_2 flow at the open circuit voltage (OCV) represents the proton conductivity values originated from the membrane, which are found to be 0.016 and 0.010 S cm^{-1} for the MEAs based on Pt/3DNG-p and Pt/3DNG-n, respectively (**Figure 3.11d**). To

understand the EIS characteristics under the dynamic condition of the MEA, Nyquist plots were recorded for both the MEAs at the standard operating condition of 0.60 V, and the corresponding plots are presented in **Figure 3.11e**. It should be noted that, the current dragging corresponds to 0.60 V will lead to sluggishness in the electrode processes, which will lead to more charge transfer limitations in the cathode side. Hence, a cathode with a uniform and extended ionomer/catalyst interface will be in a better position to tackle the charge transfer resistance (CTR). CTR can be calculated from the diameter of the semi-circular loop of the Nyquist plots and the measured values are 0.007 and 0.010 Ω, respectively for the systems based on Pt/3DNG-p and Pt/3DNG-n. The significantly low CTR while maintaining high proton conductivity in the case of the Pt/3DNG-p based MEA reflects the better ability of the system to tackle the electrode kinetics at the cathode. Thus, the EIS data stands out as a strong proof on the efficiency of the *in situ* polymerization strategy adopted for building the ionic interface within the electrode matrix in a controlled way. The charge transfer resistance reflects the Knudsen resistance behaviour of the MEAs. Since Pt/3DNG-p has a uniform ionomer-catalyst interface which could be achieved from the controlled *in situ* polymerization of the pre-admitted monomer moieties, favourable kinetic modulation could be achieved in this case. Along with this, the texture of the electrode which ensured exposure of the active sites and accessibility by the reactants through the interconnected CN_x tetrapod support morphology also played a critical role in achieving the reduced EIS value. Thus, altogether, the MEA derived from the Pt/3DNG based catalyst and *in situ* derived ionomer-catalyst interface acquired the desirable activity characteristics during the realistic system level validation of a single cell of PEMFC.

3.4. Conclusions

A high performing electrocatalyst (Pt/3DNG) for HT-PEMFC applications by using nitrogen-doped three-dimensional graphene (3DNG) as the support material and *in situ* grafted active "triple-phase boundary" could be prepared. While the 3D architecture of the catalyst provided advantages in terms of more exposure of the active sites and mass transfer, the *in situ* creation of the active "triple-phase boundary" helped to improve the overall catalyst utilization by reducing the electrode charge transfer resistance (CTR). The half-cell study of the catalyst performed in acidic electrolyte recorded an $E_{1/2}$ value of 0.846 V for Pt/3DNG, which is higher than that of other catalysts such as Pt/VC (0.817 V) and Pt/NRG (0.795 V). In a similar way, Pt/3DNG

recorded higher ECSA value (62.4 m^2 g^{-1}) compared to that of the Pt/VC (56.7 m^2 g^{-1}) and Pt/NRG (51.3 m^2 g^{-1}) catalysts. Also, the high intrinsic activity of the catalyst could be verified in terms of mass activity and specific activity. The strong interaction of the Pt nanoparticles with the anchoring sites on the N-doped graphene helped Pt/3DNG to achieve better durability and structural integrity during ORR. The single cell of a HT-PEMFC system based on the Pt/3DNG catalyst and *in situ* generated ionomer interface (Pt/3DNG-p) provided a peak power density of 982 mW cm^{-2}, outperforming a similar system based on the electrode based on the conventional Nafion ionomer interface (Pt/3DNG-n). The in-house MEA also benefited in terms of a low CTR of 0.007 Ω value, inferring to favourable kinetic modulation achieved by the system in this case. Thus the single-cell performance data of HT-PEMFC displayed competency of the present strategy as a promising way to tackle the issues related to catalyst utilization, durability and mass transfer. This finally reflected in terms of notable system level performance enhancement in the I-V polarization plot both in the operating potential (close to 0.60 V) and high current density (prone to mass transfer issues) regions. This justifies the logic of designing the new catalyst morphology and protocol of electrode fabrication involving generation of the ionomer interface from pre-admitted monomers through the *in situ* polymerization strategy.

3.5. References

[1] R. F. Service, *Science*, **2002**, 296, 1222-1224.

[2] B. C. H. Steele and A. Heinzel, *Nature*, **2001**, 414, 345-352.

[3] M. K. Debe, *Nature*, ***2012***, 486, 43-51.

[4] H. A. Gasteiger, S. S. Kocha, B. Sompalli and F. T. Wagner, *Appl. Catal. B*, **2005**, 56, 9-35.

[5] W. Smith, *J. Power Sources*, **2000**, 86, 74-83.

[6] L. Carrette, K. A. Friedrich and U. Stimming, *Fuel Cells*, **2001**, 1, 5-39.

[7] F. T. Wagner, B. Lakshmanan and M. F. Mathias, *J. Phys. Chem Lett.*, **2010**, 1, 2204-2219.

[8] H. A. Gasteiger and N. M. Marković, *Science*, **2009**, 324, 48-49.

[9] J. Wu and H. Yang, *Acc. Chem. Res.*, **2013**, 46, 1848-1857.

[10] M. Shao, Q. Chang, J.-P. Dodelet and R. Chenitz, *Chem. Rev.*, **2016**, 116, 3594-3657.

[11] A. Rabis, P. Rodriguez and T. J. Schmidt, *ACS Catal.*, **2012**, 2, 864-890.

[12] A. Morozan, B. Jousselme and S. Palacin, *Energy Environ. Sci.*, **2011**, 4, 1238-1254.

[13] J. K. Nørskov, J. Rossmeisl, A. Logadottir, L. Lindqvist, J. R. Kitchin, T. Bligaard and H. Jónsson, *J. Phys. Chem. B*, **2004**, 108, 17886-17892.

[14] A. Kulkarni, S. Siahrostami, A. Patel and J. K. Nørskov, *Chem. Rev.*, **2018**, 118, 2302-2312.

[15] J. Greeley, I. E. L. Stephens, A. S. Bondarenko, T. P. Johansson, H. A. Hansen, T. F. Jaramillo, J. Rossmeisl, I. Chorkendorff and J. K. Nørskov, *Nat. Chem.*, **2009**, 1, 552-556.

[16] Y.-J. Wang, D. P. Wilkinson and J. Zhang, *Chem. Rev.*, **2011**, 111, 7625-7651.

[17] R. Borup, J. Meyers, B. Pivovar, Y. S. Kim, R. Mukundan, N. Garland, D. Myers, M. Wilson, F. Garzon, D. Wood, P. Zelenay, K. More, K. Stroh, T. Zawodzinski, J. Boncella, J. E. McGrath, M. Inaba, K. Miyatake, M. Hori, K. Ota, Z. Ogumi, S. Miyata, A. Nishikata, Z. Siroma, Y. Uchimoto, K. Yasuda, K.-i. Kimijima and N. Iwashita, *Chem. Rev.*, **2007**, 107, 3904-3951.

[18] X. Cheng, B. Yi, M. Han, J. Zhang, Y. Qiao and J. Yu, *J. Power Sources*, **1999**, 79, 75-81.

[19] M. S. Wilson and S. Gottesfeld, *J. Electrochem. Soc.*, **1992**, 139, L28-L30.

[20] X. Wang, Y. Orikasa and Y. Uchimoto, *ACS Catal.*, **2016**, 6, 4195-4198.

[21] Y. Luo and N. Alonso-Vante, *Electrochim. Acta*, **2015**, 179, 108-118.

[22] K. K. Karuppanan, Appu V. Raghu, M. K. Panthalingal, V. Thiruvenkatam, K. P and B. Pullithadathil, *Sustain. Energy & Fuels*, **2019**, 3, 996-1011.

[23] K. K. Karuppanan, Appu V. Raghu, M. K. Panthalingal, S. Ramanathan, T. Kumaresan and B. Pullithadathil, *J. Mater. Chem. A*, **2018**, 6, 12768-12781.

[24] R. O'Hayre, D. M. Barnett and F. B. Prinz, *J. Electrochem. Soc.*, **2005**, 152, A439-A444.

[25] R. O'Hayre and F. B. Prinz, *J. Electrochem. Soc.*, **2004**, 151, A756-A762.

[26] Y.-C. Park, H. Tokiwa, K. Kakinuma, M. Watanabe and M. Uchida, *J. Power Sources*, **2016**, 315, 179-191.

[27] Q. Li, R. He, J. O. Jensen and N. J. Bjerrum, *Chem. Mater.*, **2003**, 15, 4896-4915.

[28] M. A. Hickner, H. Ghassemi, Y. S. Kim, B. R. Einsla and J. E. McGrath, *Chem. Rev.*, **2004**, 104, 4587-4612.

[29] T. H. Yu, Y. Sha, W.-G. Liu, B. V. Merinov, P. Shirvanian and W. A. Goddard, *J. Am. Chem. Soc.*, **2011**, 133, 19857-19863.

[30] K. Shinozaki, Y. Morimoto, B. S. Pivovar and S. S. Kocha, *J. Power Sources*, **2016**, 325, 745-751.

[31] A. Ohma, K. Fushinobu and K. Okazaki, *Electrochim. Acta*, **2010**, 55, 8829-8838.

[32] V. Vijayakumar, B. Anothumakkool, A. Torris A. T, S. B. Nair, M. V. Badiger and S. Kurungot, *J. Mater. Chem. A*, **2017**, 5, 8461-8476.

[33] B. Anothumakkool, A. Torris A. T, S. Veeliyath, V. Vijayakumar, M. V. Badiger and S. Kurungot, *ACS Appl. Mater. Interfaces*, **2016**, 8, 1233-1241.

[34] R. Soni, V. Vijayakumar and S. Kurungot, *ACS Appl. Nano Mater.*, **2018**, 1, 4576-4586.

[35] P. K. Gangadharan, S. M. Unni, N. Kumar, P. Ghosh and S. Kurungot, *ChemElectroChem*, **2017**, 4, 2643-2652.

[36] US Pat., US 20160315343A1, 2016.

[37] S. M. Unni, R. Illathvalappil, P. K. Gangadharan, S. N. Bhange and S. Kurungot, *Chem. Commun.*, **2014**, 50, 13769-13772.

[38] P. Xu, L. Dong, M. Neek-Amal, M. L. Ackerman, J. Yu, S. D. Barber, J. K. Schoelz, D. Qi, F. Xu, P. M. Thibado and F. M. Peeters, *ACS Nano*, **2014**, 8, 2697-2703.

[39] R. J. Nemanich and S. A. Solin, *Phys. Rev. B*, **1979**, 20, 392-401.

[40] X. Tong, J. Zhang, G. Zhang, Q. Wei, R. Chenitz, J. P. Claverie and S. Sun, *Chem. Mater.*, **2017**, 29, 9579-9587.

[41] L. K. Ono, B. Yuan, H. Heinrich and B. R. Cuenya, *J. Phys. Chem. C*, **2010**, 114, 22119-22133.

[42] E. I. Vovk, A. V. Kalinkin, M. Y. Smirnov, I. O. Klembovskii and V. I. Bukhtiyarov, *J. Phys. Chem. C*, **2017**, 121, 17297-17304.

[43] Y.-T. Kim, K. Ohshima, K. Higashimine, T. Uruga, M. Takata, H. Suematsu and T. Mitani, *Angew. Chemie Int. Ed.*, **2006**, 45, 407-411.

[44] D. A. Bulushev, M. Zacharska, A. S. Lisitsyn, O. Y. Podyacheva, F. S. Hage, Q. M. Ramasse, U. Bangert and L. G. Bulusheva, *ACS Catal.*, **2016**, 6, 3442-3451.

[45] S. M. Unni, S. Devulapally, N. Karjule and S. Kurungot, *J. Mater. Chem.*, **2012**, 22, 23506-23513.

[46] V. Vijayakumar, M. Ghosh, A. Torris A. T, N. C. M. K, S. B. Nair, M. V. Badiger and S. Kurungot, *ACS Sustain. Chem. & Eng.*, **2018**, 6, 12630-12640.

[47] S. Ott, A. Orfanidi, H. Schmies, B. Anke, H. N. Nong, J. Hübner, U. Gernert, M. Gliech, M. Lerch and P. Strasser, *Nat. Mater.*, **2020**, 19, 77-85.

Chapter 4

Three-Dimensionally Interconnected Graphitic Carbon Enriched with Iron Carbide Core-Shell Particles as a Highly Active Electrocatalyst for Oxygen Reduction Reaction in Acidic and Alkaline Media

Recent advancements on the development of non-precious electrocatalysts with iron (Fe) incorporated active centres have generated confidence on meeting the goal of realizing cost-effective proton exchange membrane fuel cells (PEMFCs). However, most of these catalysts that emerged as a substitution for the platinum supported on carbon (Pt/C) catalysts in oxygen reduction reaction (ORR) are active under basic conditions and their feasibility in PEMFCs remains as a challenge. In this scenario, this work reports the synthesis of a platinum-free (Pt-free) oxygen reduction electrocatalyst prepared by the annealing of polydopamine grown melamine foam. The prepared catalyst has a three-dimensional (3D) interconnected bilayer network structure possessing the carbon nitride backbone wrapped by graphitic carbon layer bearing iron carbides and nitrides as the active centres (3D-FePDC). Whereas the ORR performance of 3D-FePDC closely matches that of the commercial Pt/C in the basic medium, it displays only a low overpotential value of 60 mV under acidic conditions compared to its Pt counterpart. Testing of a PEMFC in a single cell mode by using 3D-FePDC as the cathode catalyst and Nafion membrane delivered a maximum power density of 278 mW cm^{-2}, which is a promising value expected from a system based on non-precious metal cathode. Ultimately, as a cost-effective catalyst that can effectively perform irrespective of the pH conditions, 3D-FePDC offers significant prospects in the areas like fuel cells and metal-air batteries which work in acidic and/or basic conditions.

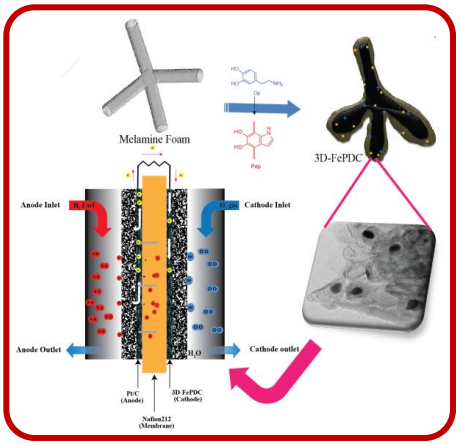

Content of this chapter is published in the following article:

ACS Appl. Mater. Interfaces, 2021, 13, 8147-8158

(https://pubs.acs.org/doi/10.1021/acsami.0c18036)

4.1 Introduction

In the past few years, fuel cells gained significant attention in the field of sustainable development as a clean, efficient, and viable energy conversion technology.[1-4] The four-electron (4e) reduction of molecular oxygen, a vital but sluggish process, is the bottleneck in the operation of the fuel cell cathodes.[5-7] The development of electrocatalysts to overcome the challenges associated with oxygen reduction reaction (ORR) is an inevitable part of electrochemical research dealing with fuel cells.[8,9] Precious metal platinum (Pt) and its alloys have been widely used as the active catalysts to overcome the kinetic barriers of ORR.[10-12] However, their high cost, inadequacy, and limited durability hinder their widespread applications.[13] Therefore, the development of alternative earth-abundant non-precious metal catalysts with low-cost and high-performance has triggered extensive research interest.[14-16] Since the oxides, nitrides, and chalcogenides of the non-precious metals suffer from the issues of low electrical conductivity and stability in acidic medium, their composites with a wide variety of carbon morphologies have gained more research attention.[17-21] However, only a few types of materials such as carbon-supported transition-metal/nitrogen (MN_x/C, M = Co, Fe, Ni, *etc*.) compounds and metal-free nitrogen-doped carbon are found to be active and durable towards ORR in acidic conditions.[22,23] It is generally endorsed that the interactions between the transition metals, doped nitrogen, and carbon support (the morphology of the carbon support is also important) in the composite materials play a key role in facilitating ORR.[24] These catalysts are often derived by annealing processes, which usually involve a suitable metal precursor (metal-organic framework, metal salts, etc.) and conducting polymer or small organic molecules. [14, 25]

Among the non-precious metal catalysts for ORR, the iron (Fe) compounds gained prime attention due to their high activity and stability in harsh conditions. Different iron-based carbon composites such as iron carbides, iron nitrides, and iron-containing single atomic catalysts are reported recently for ORR irrespective of the reaction medium involved.[26-28] The iron-impregnated nitrogen-doped carbon (Fe-N-C) sites are considered to be one of the best catalytic sites among these systems.[29] However, recent research has demonstrated that iron carbide-based electrocatalysts displayed significantly enhanced electrocatalytic activity and stability in highly corrosive acidic condition.[30-32] Most of the iron carbide catalysts are found to possess a core-

shell structure with Fe_3C core embedded inside a shell made of graphitic carbon in which the Fe_3C activates the graphitic layer towards ORR. Also, the thin layer graphitic shell protects the metal core centre from leaching out in the harsh reaction conditions. In most cases, the Fe_3C core-shell particles are not exposed towards the periphery of the carbon support, which causes reduced activity due to the limited utilization of the active centres. In such situations, the Fe_3C particles arranged in a three-dimensional (3D) carbon support morphology can help with the enhancement of the overall activity of the catalyst by exposing more active centres. Despite recent progress in the Fe_3C core-shell electrocatalysts for ORR, the design and synthesis of the Fe_3C incorporated architectures that offer a high surface area for the improved fast mass transport and the exposure of a high density of active sites for effective electrocatalysis still remain a challenge.

In this work, to tackle the existing complexities confronting in the catalyst development, we attempt the synthesis of an electrocatalyst based on Fe_3C core-shells embedded within nitrogen-doped three-dimensional graphitic carbon (3D-FePDC). The development of the electrocatalyst with the iron carbide active centres aligned over 3D carbon morphology could overcome the existing issues related to the mass transport and low active material utilization in the Fe_3C catalysts. It is also envisaged that the structural and functional tuning could bring this material close to the *state-of-the-art* Pt/C systems leading to improved ORR performance in commercial fuel cells. Here, polydopamine, an organic polymeric material, is *in situ* grown in presence of an iron precursor over the melamine foam, which upon annealing leads to the formation of the Fe_3C core-shell particles incorporated within the framework of the 3D graphitic carbon. In the first step of this process, the slow self-polymerization of dopamine in air atmosphere helps the full encasement of the melamine foam along with the iron precursor. During the annealing step, the melamine-derived carbon nitride tetrapods evolve as the backbone structure, which is wrapped with the nitrogen-doped graphitic carbon derived from the polydopamine anchored with the Fe_3C core-shell particles. The nitrogen doping in the catalyst system arose from the melamine foam and dopamine sources that help to create more active centres by coordinating with the N with Fe centres apart from the iron carbide alone. The collective adaptation of dual doping (N and Fe) achieved in the system along with the morphological advantages assists to acquire high intrinsic activity for ORR in acidic and alkaline media. Ultimately, this work provides an approach that is simple but with high potential for the

mass production of N-doped 3D graphitic carbon enriched with iron carbide. The features of the catalyst are recorded with high ORR performance in both alkaline and acidic media, especially in a real-life PEMFC assembly.

4.2 Experimental Section

4.2.1 Synthesis of 3D-FePDC

In a typical experiment, 30 mg of dopamine hydrochloride and 1 mM of $FeCl_3$ were dissolved in 10 mL bicarbonate buffer (pH = 8.5). Commercially available melamine foam slices were soaked in the solution and stirred for 24 h. The melamine foam impregnated with $FeCl_3$ and polydopamine was dried under an IR lamp for overnight and then annealed in Ar atmosphere for 3 h at 900 ^{o}C with a heating rate of 5 °C min^{-1}. Further, the carbonized material was acid washed with 2 M H_2SO_4 at 60° C for 1 h to remove the impurities. It was then washed with DI water for three times and dried for further use. The obtained material is hereafter called as 3D-FePDC. For the preparation of 2D-FePDC, the same protocol was followed without the use of the melamine foam. Two other control samples, designated as 3D-PDC and 2D-PDC, were also prepared by omitting iron precursor from the above protocols. The melamine foam was used in the preparation of 3D-PDC, whereas, it was omitted while preparing 2D-PDC.

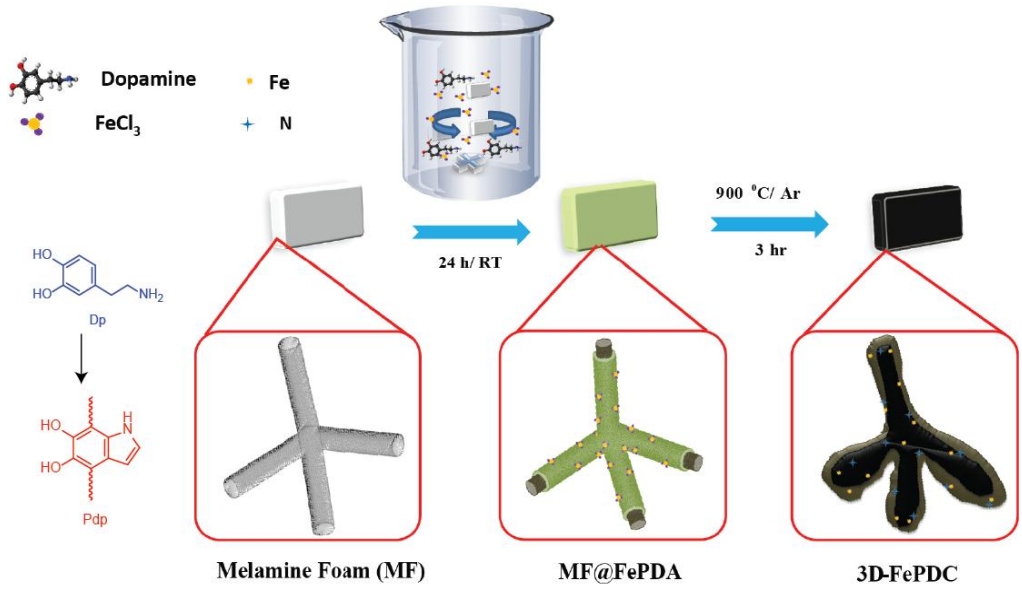

Figure 4.1 *Schematic representation of the synthesis of the 3D-FePDC electrocatalyst.*

4.2.2 Fabrication of Membrane Electrode Assembly (MEA)

The MEA for fuel cell testing was prepared by sandwiching a piece of pre-treated Nafion 212 membrane in between the Pt/C anode and 3D-FeDC cathode.[33] The conventional brush coating of the catalytic slurry over the gas diffusion layer (GDL) was employed for the preparation of the electrodes. The catalytic slurry for brush coating was prepared by dispersing the catalyst powder (3D-FePDC for cathode and Pt/C 40% for anode) in isopropyl alcohol by using a probe sonicator. 20 wt. % Nafion (in iso-propyl alcohol and water, Du-Point USA) was added in the mixture in order to function as the ionomer as well as the binder. The ionomer to catalyst ratio (i/c) was fixed as 0.40 for both the 3D-FePDC and Pt/C electrodes. The non-Pt cathode (3D-FePDC) was prepared with a catalyst loading of 2.0 mg cm^{-2} and the anode was prepared with the standard Pt/C catalyst by maintaining a Pt loading of 0.50 mg cm^{-2}. The MEA was prepared by hot-pressing the electrodes by keeping a Nafion membrane in between the electrodes. The temperature of the hot-press was maintained as 130 ^{o}C and applied the load of 1-0 metric ton for 1 min. The as prepared MEA with the active area of 4 cm^2 (2 cm x 2 cm) was assembled in a standard single-cell fixture (Fuel Cell Technologies, Inc., USA) by applying a torque of 3 Nm. The fixture was then attached to a fuel cell test station (Fuel Cell Technologies, Inc., USA) for the cell analysis.

4.2.3 Material characterization

The scanning electron microscope (SEM) analysis of the samples was carried out on a Quanta and Nova SEM 450. A Tecnai-T 20 transmission electron microscope (TEM) operated at an acceleration voltage of 200 kV was used for the analysis of the morphology of the synthesized materials. The surface area and pore size distribution analyses were carried out on a Quantachrome Quadrasorb automatic volumetric instrument. XRD analysis was performed on a Rigaku SmartLab diffractometer with Cu Ka radiation (λ = 1.54 Å) at a scan rate of 5^{o} min^{-1}. Raman study was performed using an HR 800 Raman spectrometer (Jobin Yvon, Horiba, France) by using 632 nm wavelength laser. A VG Microtech Multilab ESCA 3000 spectrometer was used for the X-ray photoelectron spectroscopic (XPS) surface investigation of the catalysts. For electrochemical characterization, a Bio-logic VMP-3 PG Stat was employed for performing the cyclic voltammetry and linear sweep voltammetry. The Pine Research Instruments rotating disk electrode (RDE) and rotating ring disk electrode (RRDE) setup connected to a potentiostat

were used to perform the RDE and RRDE analyses of the catalyst. The number electron transfer (n) during the oxygen reduction reaction and the amount of intermediate formation of H_2O_2 were calculated using the following equations from the RRDE data:

$$n = \frac{4\, I_d}{(I_d + I_r/\mathrm{N})} \qquad (4.1)$$

$$H_2O_2\,\% = \frac{200\, I_r/\mathrm{N}}{(I_d + I_r/\mathrm{N})} \qquad (4.2)$$

where, I_r, I_d, and N are the ring current, disc current and collection efficiency (0.37), respectively.

4.3 Result and Discussion

The synthesis of the iron coordinated 3D nitrogen-doped bilayer graphitic carbon (3D-FePDC) is illustrated in **Figure 4.1**. The synthesis consists of two steps, in which the polydopamine with the iron precursor was anchored over the melamine foam in the first step, which was annealed at 900 ^{o}C for 3 h in the next step. The dopamine solution maintained a pH of 8.5 in the bisulphate buffer, which assists the slow polymerization in the presence of air. The annealing of the polydopamine anchored melamine foam creates a bilayer structure consisting of carbon nitride backbone wrapped by the nitrogen-doped graphitic carbon layer. During the annealing, the melamine foam itself converts to carbon nitride and polydopamine grew over it transferred to the N-doped graphitic carbon. The amine groups in the dopamine and melamine foam donate nitrogen, which gets equally distributed over the graphitic carbon along with iron coordination. Here, melamine foam acts as a template to form the 3D morphology as well as a nitrogen source

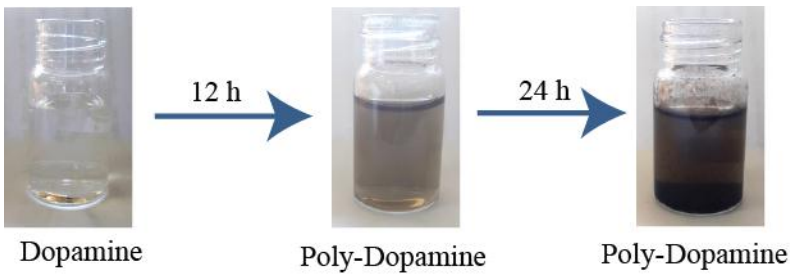

Figure 4.2 *Optical image representing the dopamine polymerization at different time intervals.*

for the doping. However, the nitrogen-doped graphene layer formed over the tetrapods is embedded with Fe_3C and other iron-based coordination sites from dopamine and the metal precursor. The Fe_3C particles could be originated from the reduction of the iron precursor by carbon during the high-temperature annealing process. If a sufficient amount of iron precursor is present in the system, it would aggregate and form metallic iron which further reacts with the carbon atoms to form the Fe_3C particles encapsulated by the graphitic carbon during the course of the annealing.[34] The optical image given in **Figure 4.2** shows the different stages of auto self-polymerization of dopamine in the presence of air atmosphere. It is visible that the colourless solution changes to pale dark colour after 12 h. However, the presence of any settled particles was not observed after the 12 h of the reaction time. It indicates the incomplete polymerization of dopamine within the time period. After 24 h of the reaction time, it could be observed that the solution changes to dark colour with settled black particles at the bottom of the glass vessel. The black particles correspond to the polydopamine lumps formed and settled down during the polymerization.

4.3.1 FT-IR Analysis

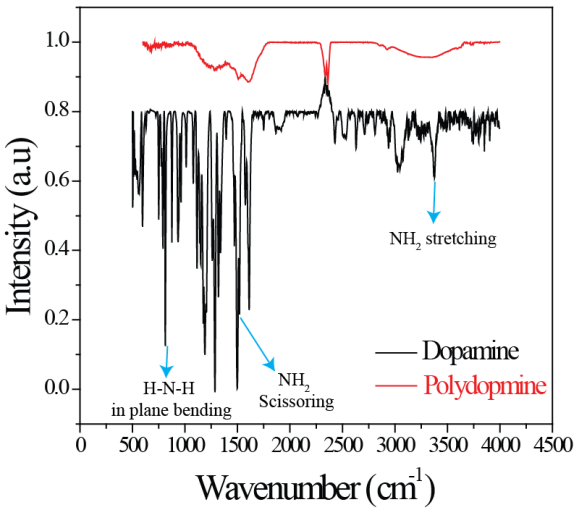

Figure 4.3 *FT-IR spectra of dopamine and polydopamine.*

Further, the polymerization of dopamine and its mechanism were confirmed with the help of FT-IR spectra. In **Figure 4.3**, the FT-IR spectra of dopamine and polydopamine were compared. The bands appeared at 878 and 1601 cm^{-1} are attributable to the in-plane bending of the H–N–H

group in the dopamine.[35] However, few weak bands have appeared at the same position in the polydopamine spectrum. One of the characteristic peaks of the dopamine molecule appeared at 1519 cm^{-1} corresponds to the NH_2 scissoring of the primary amine. Also, one of the two bands for the NH_2 stretching (3347 and 3237 cm^{-1}) has disappeared in polydopamine because a transformation occurs form the primary amine to the secondary amine during the polymerization of dopamine.[36] In contrast, the FT-IR spectrum of polydopamine recorded a large and broad peak at 3600–3200 cm^{-1}, indicates the presence of hydroxyl groups. Unlike in the FT-IR spectrum of the dopamine molecule, the peaks corresponding to the -NH_2 and N–H stretching were absent in the spectrum of the polymerized dopamine molecule. More notably, the characteristic peaks of the indole and indoline structures at 1613 and 1519 cm^{-1} were observed in the polydopamine spectrum.[37] All these observations indicate the structural evolution and polymerization mechanisms of dopamine *via* intramolecular cyclization reaction of the dopamine.

4.3.2 SEM analysis

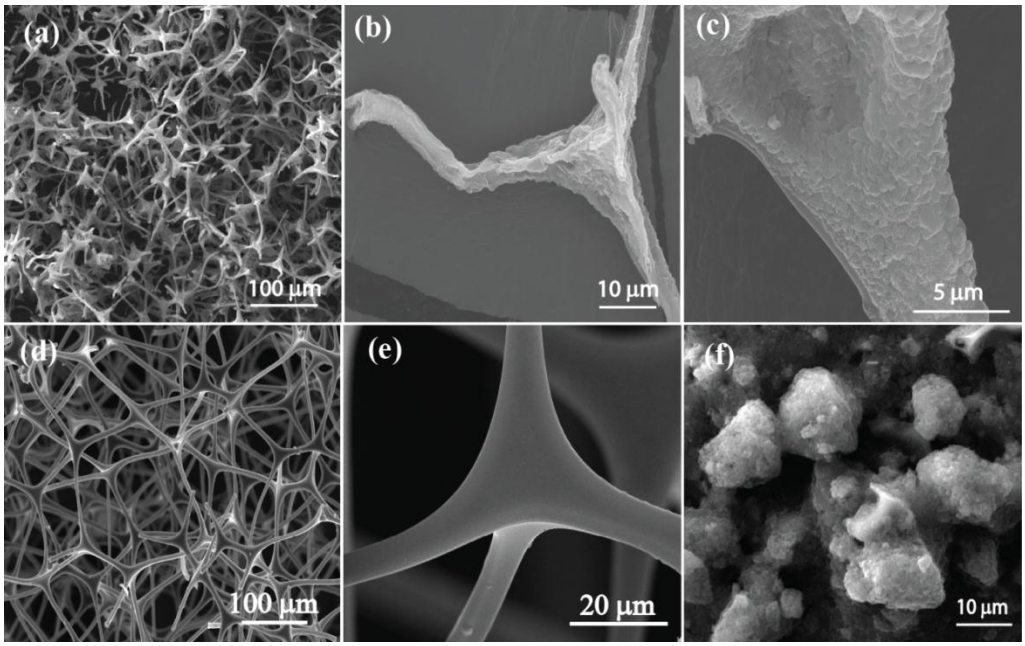

Figure 4.4 *(a), (b) and (c) The FESEM images of 3D-FePDC recorded at different magnifications, (d) and (e) the FESEM images of the bare melamine foam recorded at different magnifications and (f) the FESEM image of 2D-FePDC catalyst prepared without using the melamine foam.*

Figures 4.4a to **c** show the FESEM images of 3D-FePDC taken at different magnifications. The low magnification image shown in **Figure 4.4a** depicts the interconnected network architecture of the 3D-FePDC catalyst. Since the melamine foam is used as the template during the synthesis, it helps to form a 3D morphology without any crumbling in the structure. The graphitic carbon layer formed over the carbon nitride tightly wrapped over it, which helps to retain the structure without any destruction in the 3D morphology. The evaluation of a cross-section of one arm of 3D-FePDC appears like a bilayer structure with the carbon nitride core formed from the melamine foam counterpart completely wrapped by the graphitic carbon shell by dopamine. A close inspection on the surface of the melamine foam in **Figure 4.4d** and **e** helps to differentiate the graphitic carbon layer formed from dopamine in the case of 3D-FePDC. Also, thermal stress generated during the high-temperature annealing causes wrinkling in the structure of 3D-FePDC than that of the perfect spherical edges in the melamine foam. Further, for the comparison of the influence of the morphology on the performance of the catalyst, the 2D-FePDC catalyst also was prepared using the same protocol, but without employing the melamine foam. 2D-FePDC forms two-dimensional (2D) lumps like structure without definite geometry in the absence of the melamine foam template (**Figure 4.4f**).

4.3.3 TEM analysis

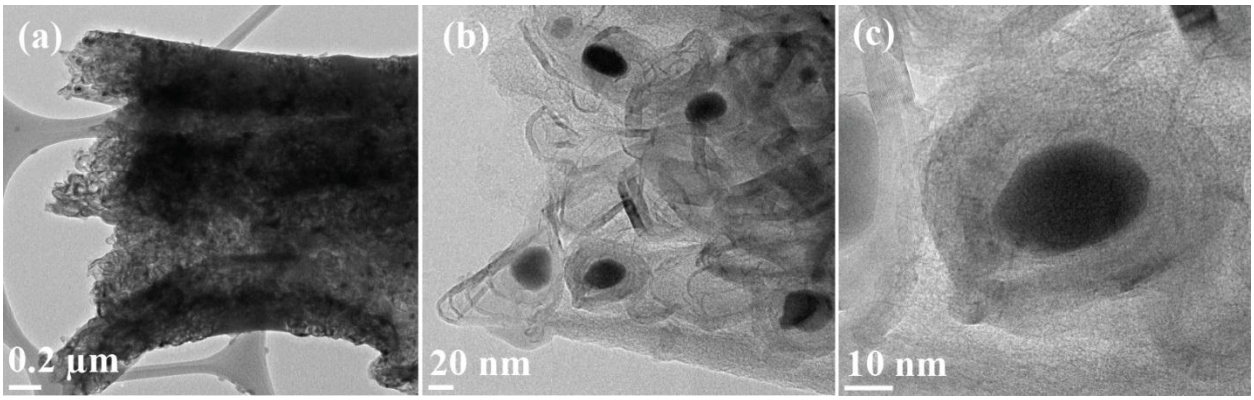

Figure 4.5 *Images (a), (b) and (c) are the TEM images of 3D-FePDC recorded at different scale bars.*

Further, TEM images were taken to get insightful information about the outer carbon layer of 3D-FePDC. The low magnification TEM image shown in **Figure 4.5a** depicts the formation of the graphitic carbon layer over the carbon nitride tetrapods. The complete surface wrapping of

the graphitic carbon layer over the carbon nitride tetrapod is ensured by the TEM image. The high magnification image displayed in **Figure 4.5b** shows the iron carbide particles encapsulated inside the carbon shell. The iron carbide core-shell is better viewed in a high magnification TEM image presented in **Figure 4.5c**. The size of the particles calculated from the TEM image was found to be 10 nm.

4.3.4 XPS analysis

Further, the nature and surface composition of the catalyst was analysed by X-ray photoelectron spectroscopy (XPS). **Figure 4.6a** shows the XPS survey spectra of 3D-FePDC. It exhibits four spikes at ~399.9, ~532.7, ~285.1 and ~712.9 eV corresponding to the presence of N, O, C, Fe, respectively. **Figure 4.6b** shows the deconvoluted Fe 2p XPS of 3D-FePDC, which consist of two major peaks attribute to the existence of Fe $2p_{3/2}$ (711.1 eV) and Fe $2p_{1/2}$ (725.4 eV), corresponding to the lower and higher binding energies, respectively. The Fe $2p_{3/2}$ and Fe $2p_{1/2}$ signals could be further deconvoluted to two pair of doublets analogous to Fe^{3+} and Fe^{2+} with a pair of satellite peaks.[38] The existence of the variable oxidation states confirms the presence of the different iron moieties in the system. The iron content detected from XPS is nearly 0.13 %. XPS being a surface technique, the low iron content detected could be due to the encapsulation of the metal carbide particles within the graphitized carbon layer, which shields the incident photons.[38]

Further, the C 1s spectrum of 3D-FePDC is deconvoluted to get an insight into the several carbon interactions presented on the catalyst surface (**Figure 4.6c**). A low intense peak positioned at 283.8 eV is attributed to the metal carbide interaction. Apart from the metal carbide peak, four distinct peaks corresponding to the binding energies of 284.6 (C=C), 285.7 (C-N), 287.4 (C-O), and 290.1 eV (C=O) were identified in the deconvoluted C 1s spectra of 3D-FePDC.[39] The relatively higher intense peak appeared at 284.6 eV corresponds to the C=C bond, which corroborates the high degree of graphitization in the system. Along with the iron moieties, the kinds of nitrogen present in the catalyst and their quantity have a significant influence on the performance of the catalyst for ORR. The deconvoluted N 1s spectrum of 3D-FePDC identified the presence of pyridinic (398.2 eV), pyrrolic (399.5 eV), graphitic (400.7 eV) and oxide (403.5 eV) forms of nitrogen (**Figure 4.6d**).[40] Along with these common nitrogen

peaks which are observable in the nitrogen-doped carbon systems, a peak observed at the binding energy of 397.4 eV in the deconvoluted N 1s spectrum confirms the

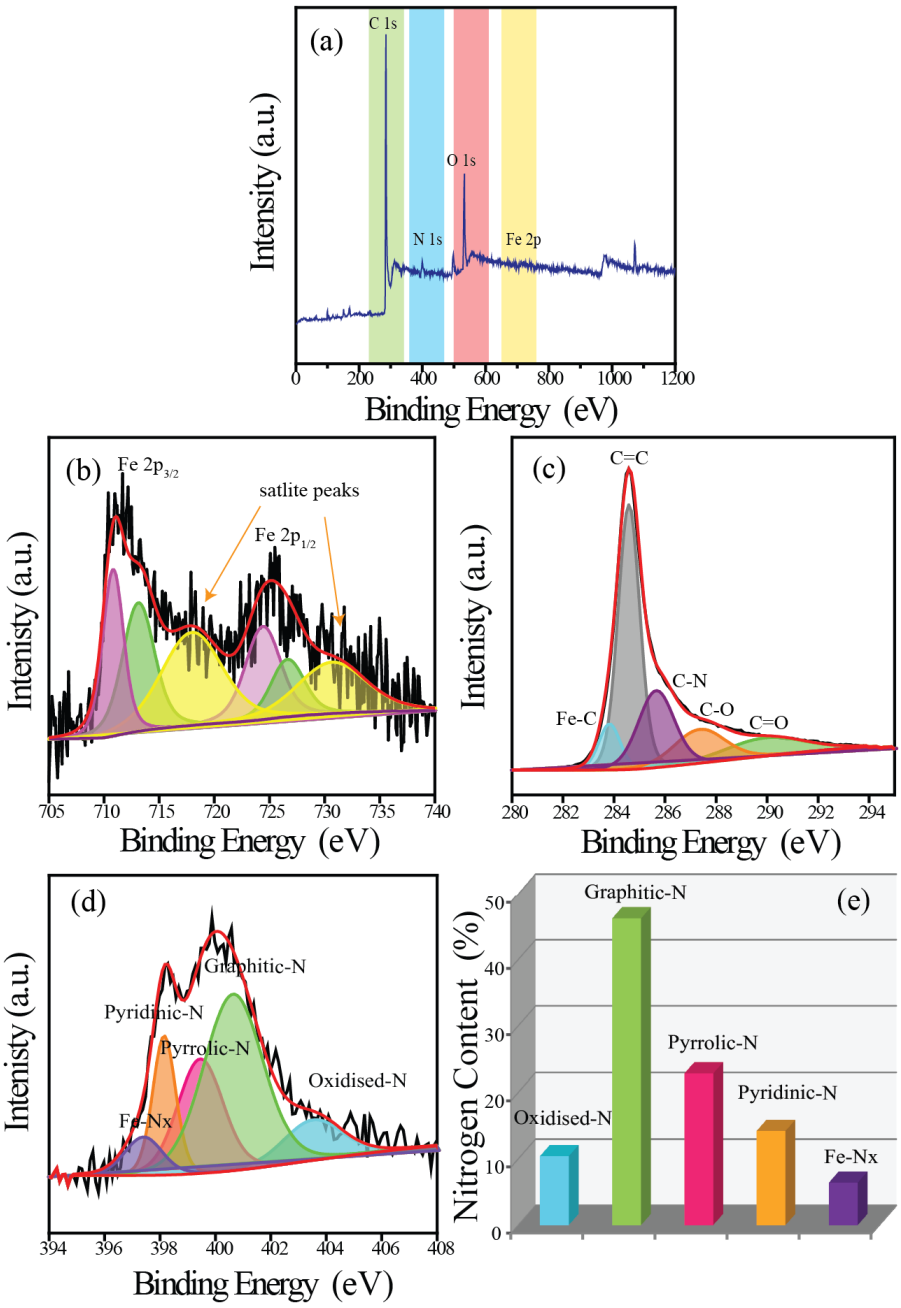

Figure 4.6 *(a) XPS survey spectrum of 3D-FePDC depicts the presence of N, Fe, O and C, deconvoluted (b) Fe 2p, (c) C 1s and (d) N 1s XPS spectra of 3D-FePDC, (e) representation of the different types of nitrogen and their atomic weight percentage as detected in the N 1s spectrum of 3D-FePDC.*

existence of iron nitride.[41] Also, it is worth note that the pyridinic nitrogen and pyrrolic nitrogen atoms contain lone pair of electrons which can coordinate with the Fe to form the Fe-N_x active site.[42] The high density of the pyridinic and pyrrolic nitrogen creates a favourable environment for the formation of the Fe-N_x active sites.[43] This confirms that the Fe-N_x moiety, one of the eminent ORR active sites, is present in the 3D-FePDC system in addition to the Fe_3C active centers, which also contribute to ORR.

The number of the different nitrogen species presented in 3D-FePDC is quantified and tabulated in the form of a bar diagram (**Figure 4.6e**). More amount of the graphitic nitrogen, which is known for its ORR activity, has been detected in the XPS spectrum of 3D-FePDC. Since the graphitic nitrogen helps to get non-uniform electron distribution in the carbon matrix with shortening of the C-N bond, it leads to the improvement of the catalytic activity of the carbon.[44] Therefore, a co-action of the graphitic and pyridinic nitrogen together with the iron coordinated active sites help the 3D-FePDC catalyst system to achieve better ORR activity.[45, 46] Along with the high density of the active centers, their uniform distribution on the catalyst surface is crucial in achieving high performance for ORR. These factors reflect on the performance indicative parameters in the working conditions.

4.3.5 Surface area analysis

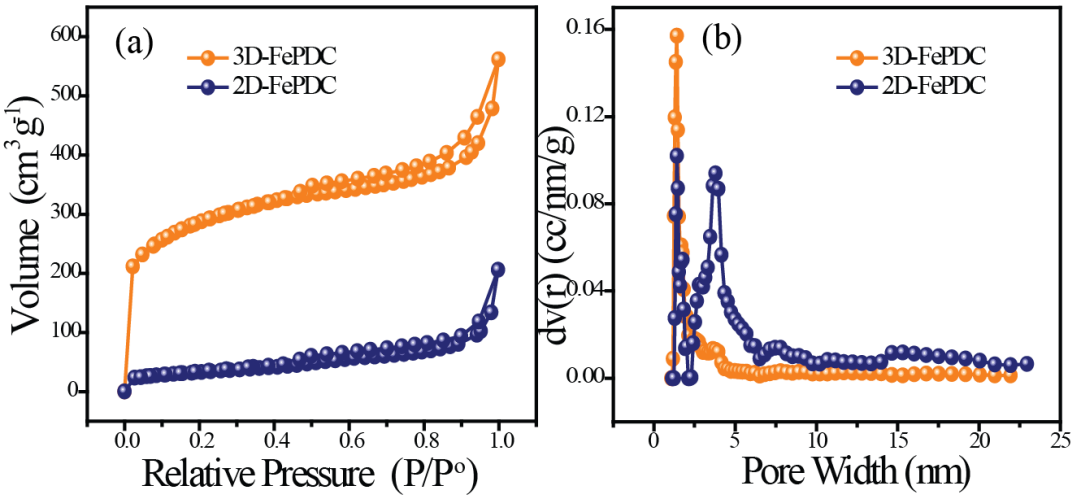

Figure 4.7 *(a) BET isotherms and (d) pore-size distribution profiles of 3D-FePDC and 2D-FePDC.*

The Brunauer-Emmett-Teller (BET) surface area of 3D-FePDC and 2D-FePDC catalysts was measured from the nitrogen adsorption-desorption analysis (**Figure 4.7a**). 2D-FePDC displays a surface area of 117.8 m^2 g^{-1}. Since it forms lumps like particle structure, its surface area is limited. On the other hand, 3D-FePDC recorded a five times higher surface area of 1027.8 m^2 g^{-1} compared to 2D-FePDC. The melamine foam used in the 3D-FePDC helped to attain the nine-fold improvement in the surface area of the system. While using the melamine foam as a template, it helps to grow the polymerized dopamine over it, resulting into the formation of a 3D interconnected network structure. Also, the 24 h reaction time ensures the complete wrapping over the melamine foam. The obtained surface area is higher than that of the other melamine foam based catalysts reported elsewhere.[47] In these reports, the materials are mostly characterized by their interconnected tent-like morphology by the combination of the melamine foam tetrapods and graphene sheets. However, in the current work, the transition from hanging to wrapping by using the melamine foam as a template with a combination of the graphitic carbon layer helped to achieve a huge enlargement in the surface area. Besides, the dopamine coating over the melamine foam helps to prevent the crumbling of the structure during the annealing of the sample to get the graphitized catalyst. The thickness control of the outer shell layer of the graphitic carbon derived from the polydopamine helped to attain high surface area. The pore-size profiles of both the catalysts are depicted in **Figure 4.7b**. 3D-FePDC shows the high density of pores with a diameter below 2 nm and this reflects the microporous nature of the catalyst. However, the 2D-FePDC has pores in the range of 2-6 nm, implying the mesoporous nature of the system. This indicates that the melamine foam assisted the growth of the dopamine results in the change in porosity from mesoporous to microporous.

4.3.6 Raman Analysis

Raman spectra recorded for 3D-FePDC and 2D-FePDC do not show any characteristic vibrations corresponding to the Fe_3C and FeN_x moieties which are usually observed below 1000 cm^{-1} (**Figure 4.8**). This may be due to the low concentration of the iron in the catalyst and also the iron particles are encapsulated inside the graphitic carbon shell.[48] However, both the catalysts show the well-defined peaks corresponding to the graphitic and defective bands of the graphitic carbon. The sharp Raman peaks are attributed to the graphitization of the polydopamine by the annealing method. The G and D bands of both the catalysts appeared at 1330 and 1594 cm^{-1},

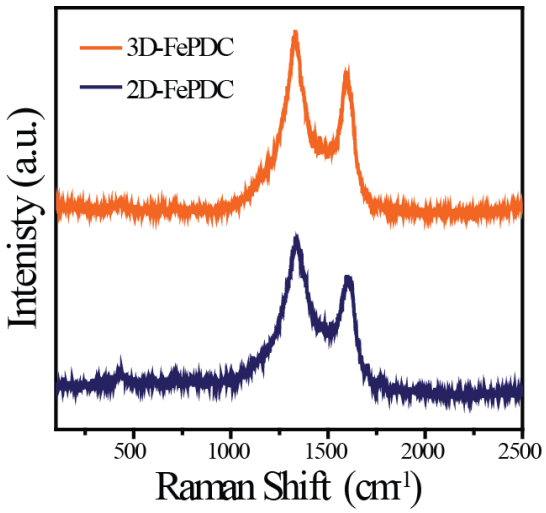

Figure 4.8 *Raman spectra of 3D-FePDC and 2D-FePDC.*

respectively, with a difference in the intensity ratio. The D band is attributed to the structural defects on the graphitic plane and the G band, which is common in all graphitic structure, corresponds to the E_{2g} vibration mode present in the graphitic carbon. The intensity ratio of the D and G band (I_D/I_G) was calculated to get information about the defects created on the catalysts. 2D-FePDC shows a high value I_D/I_G ratio of 1.1 compared to 1.07 of 3D-FePDC. Since 2D-FePDC originated from the randomly formed polydopamine, it is expected that the system shows a higher degree of defects in the matrix.

4.3.7 XRD Analysis

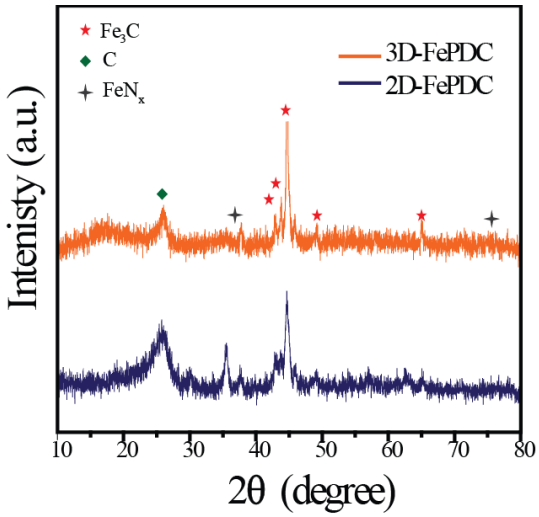

Figure 4.9 *XRD profiles of 3D-FePDC and 2D-FePDC.*

The X-ray diffraction (XRD) profiles recorded for 3D-FePDC and 2D-FePDC presented in **Figure 4.9** indicate the graphitization of the carbon derived from the polydopamine polymer matrix. In **Figure 4.9**, both the samples show a broad peak at a 2θ value of ~ 26.1^{o} corresponding to the (002) graphitic plane of the carbon. Apart from the graphitic carbon peak, sharp diffraction peaks are observed for both the catalysts. It is noticed that both 3D-FePDC and 2D-FePDC display similar peaks since both have difference only in their morphology. The major peaks are matching to the 2θ values of Fe_3C (37.6°, 43.6°, 46.0, 49.2 and 54.3°) (JCPDS file no. 892867).[49] Apart from Fe_3C, the XRD spectrum of 3D-FePDC shows the peaks corresponding to Fe-N (36.10°, 76.30°). No peaks corresponding to metallic iron were detected in the XRD, suggesting that the acid washing removes the inactive and unstable iron species. The presence of Fe-N and Fe_3C phases in 3D-FePDC is expected to provide the system with better active sites for assisting ORR in acidic medium.

4.3.8 Thermogravimetric analysis

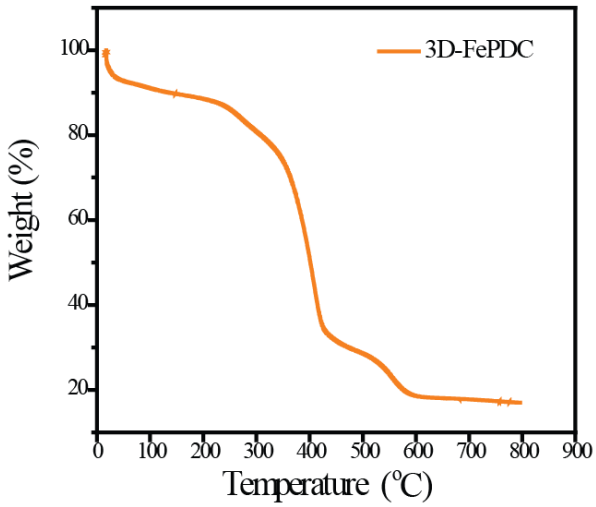

Figure 4.10 *TGA profile of 3D-FePDC recorded in O_2 atmosphere.*

The metal content in 3D-FePDC is calculated by thermogravimetric analysis in O_2 atmosphere (**Figure 4.10**). The thermogram shows initial weight decrease up to 100 °C, which is due to the loss of the adsorbed moisture. The final weight residue found at 800 ^{o}C is attributed to the metal content, which is found to be 16 %.

4.3.9 Electrochemical analysis

The rotating disc electrode (RDE) and rotating ring disc electrode (RRDE) techniques were employed to evaluate the oxygen reduction reaction (ORR) activity of the PDC catalysts in oxygen saturated 0.5 M H_2SO_4. For exploring the contribution of iron on creating the active centres for ORR, the catalysts without the iron precursor also were prepared using the same experimental conditions (2D-PDC and 3D-PDC). A glassy carbon electrode modified with the catalyst was used as the working electrode; a graphite rod and $Hg/HgSO_4$ were employed as the counter and reference electrodes, respectively, in a standard thee-electrode setup. **Figure 4.11a** shows the linear sweep voltammograms (LSVs) measured at a scan rate of 10 mV s^{-1} with an electrode rotation speed of 1600 rpm. For the assessment of the performance of the catalyst, the activity is compared with the *state of the art* 40 wt. % Pt/C catalyst. The 3D-FePDC catalyst exhibits an onset potential of 0.93 V (0.99 V for Pt/C) and a half-wave potential ($E_{1/2}$) of 0.71 V (0.80 V for Pt/C) *vs*. RHE, which are more positive than that of the control samples. The ORR onset potentials measured for 2D-FePDC, 3D-PDC and 2D-PDC are 0.89, 0.86 and 0.84 V *vs* RHE, respectively.

The highest oxygen reduction potential recorded for 3D-FePDC indicates its superior ORR activity compared to its other counterparts. 3D-FePDC records an overpotential gap of 60 mV in the onset potential and 90 mV in the $E_{1/2}$ regions compared to the commercial Pt/C (40 wt. %). However, this small potential gap with the *state of the art* Pt/C catalyst illustrates that 3D-FePDC is superior to some of the recently reported non-Pt ORR catalysts in acidic environment.[23, 50-53] The almost comparable onset potential recorded in the case of the 3D-FePDC:2D-FePDC and 3D-PDC:2D-PDC pairs point out similar intrinsic activity and active centre densities possessed by the systems. However, the molecular oxygen reduction current density at lower potential (limiting region) is higher for the 3D counterparts compared to the 2D counterparts. Also, the onset potential gap is observed between the iron coordinated and iron-free catalysts. The iron-free counterparts show considerable difference in ORR activity compared to other catalysts, which emphasizes the necessity of the incorporation of the Fe active centres to enable the system more facile towards ORR under acidic conditions. The huge activity differences between 2D-PDC and 3D-FePDC might be the reason of many simultaneously acting

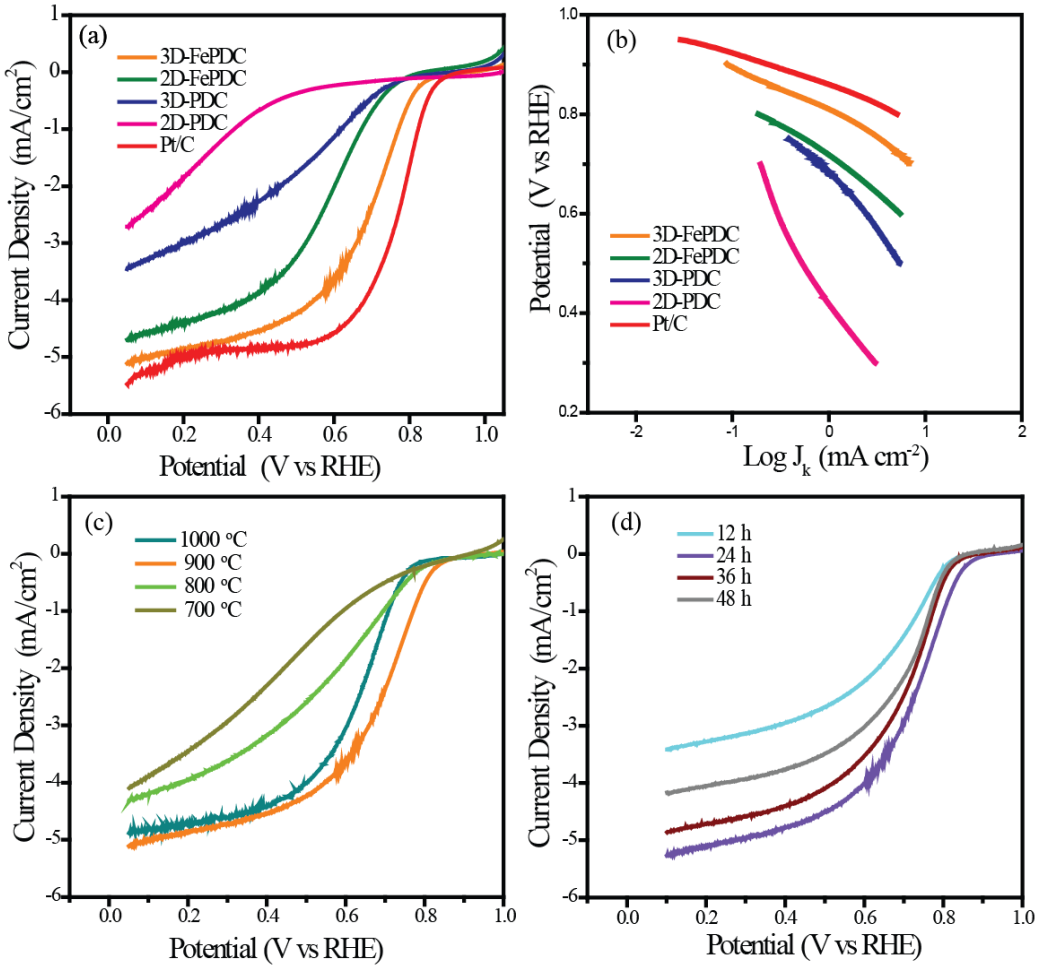

Figure 4.11 *(a) The comparative LSVs of all the catalysts recorded in oxygen saturated 0.5 M H_2SO_4 at an electrode rotation rate of 1600 rpm; (b) Tafel plot comparison of all the catalysts; LSVs of 3D-FePDC catalyst prepared, (c) at different annealing temperature and (d) at different time duration; the plots were recorded at an electrode rotation rate of 1600 rpm at 10 mV s^{-1} scan rate in oxygen saturated 0.5 M H_2SO_4.*

features such as high density of active sites, better reactant accessibility to the catalytic sites, and increase in the inherent electrical conductivity by the structural and morphological modifications. These observations depict the importance of the morphological tuning along with the structural modification. Compared to the onset potential, the $E_{1/2}$ gap is higher in the 3D and 2D counterparts, which indicates the mass transfer advantages of the 3D structures having interconnected network morphology.

Even though it is easy to get equal performance for the non-precious metal-based catalysts with that of the *state-of-the-art* Pt/C catalyst in basic media, it is hard to get the same in acidic conditions. In 3D-FePDC, the XPS analysis shows the presence of Fe, N and S along with C. These elements are discovered as the key factors which bring in the ORR activity in the case of the non-precious metal electrocatalysts. As an indispensable quantitative performance indicator to compare the intrinsic activity kinetics of the electrocatalysts, the Tafel slope analysis was performed and the corresponding plots are given in **Figure 4.11b**. Comparable Tafel slope values of 3D-FePDC (91 mV dec^{-1}) and Pt/C (72 mV dec^{-1}) indicate that the dioxygen reduction mechanism is similar in both the cases. A low Tafel slope value observed in both the cases indicates faster reaction kinetics with efficient active sites towards ORR. On the other hand, the control samples are recorded with higher Tafel slope values (above 120 mV dec^{-1}), specifying less facile reaction kinetics for ORR.

The impact of graphitization on the activity of the catalyst is evaluated by comparing the performance of 3D-FePDC prepared at the different annealing temperature. **Figure 4.11c** shows the LSVs of 3D-FePDC prepared at the different annealing temperatures. Among the different temperatures, the 900 ^{o}C is found to be optimum for generating the most active reaction centres. The activity follows the order of 900 > 1000 > 800 > 700 ^{o}C. As expected, at lower temperatures such as 700 and 800 ^{o}C, the catalysts display low activity due to the low degree of graphitization. The improvement in the activity observed at high temperature is attributed to the formation of more carbides from the F-N-C and Fe particles along with enhanced graphitization. Also, how the thickness of the graphitic carbon layer influences the performance has been analyzed by preparing the catalysts at different polymerization time (**Figure 4.11d**). It was realized that the reaction duration of 24 h for dopamine polymerization is the optimum time required for the formation of the ideal combination of the graphitic carbon layer with the Fe_3C incorporation. The higher reaction times such as 36 and 48 h are found to exhibit lower ORR activity compared to the sample prepared at 24 h of the reaction. However, at 12 h, the activity was lowest among all and this points out the incomplete wrapping of the graphitic carbon layer over the carbon nitride tetrapods.

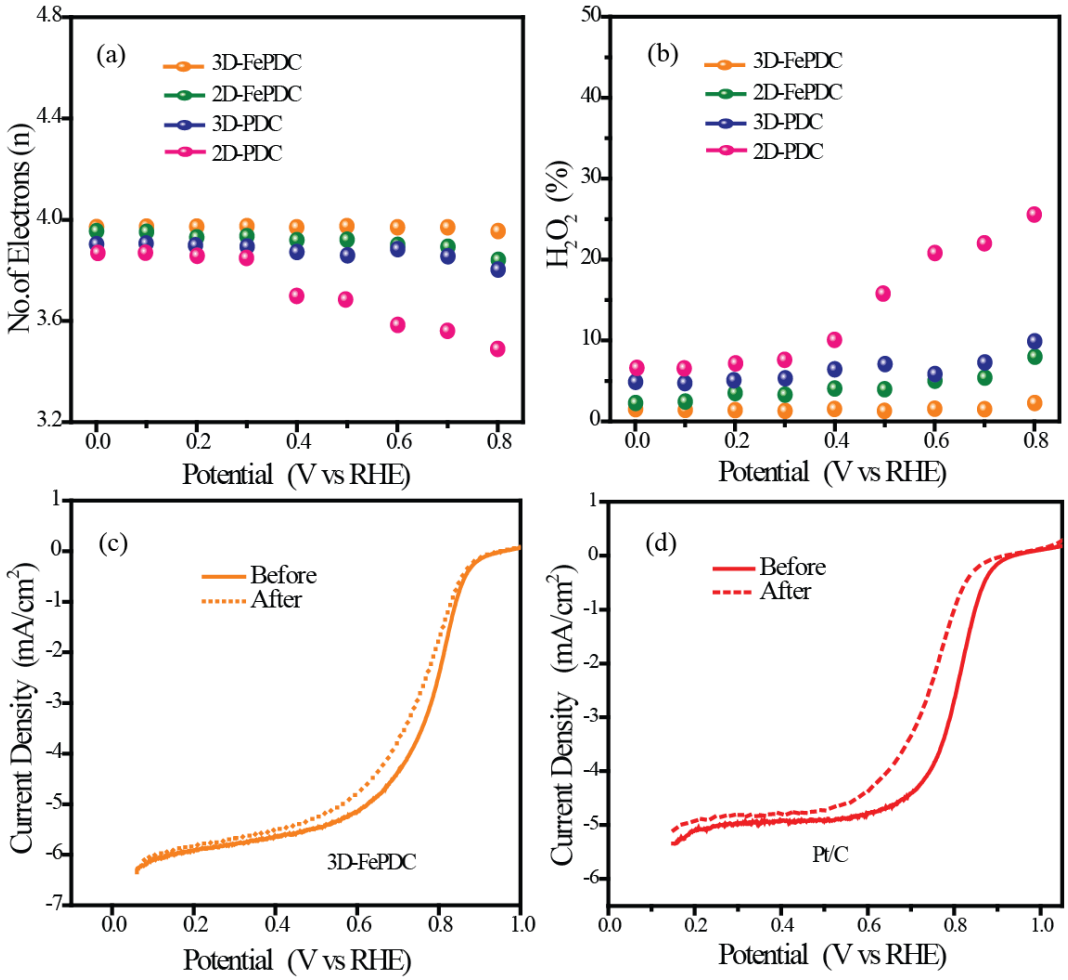

Figure 4.12 *(a) The electron transfer number (n) for ORR calculated from the RRDE analysis; (b) amount of H_2O_2 generated during ORR calculated as a function of the electrode potential; LSV comparison of (c) 3D-FePDC and (d) Pt/C before and after ADT in 0.5 M H_2SO_4 recorded at a scan rate of 10 mV s^{-1} and an electrode rotation speed of 1600 rpm.*

Followed by the intrinsic activity assessment of the catalysts, RRDE analysis was performed to get more insightful information on the reaction kinetics over the catalysts. The RRDE voltammograms were performed in oxygen saturated 0.5 M H_2SO_4 at a scan rate of 10 mV s^{-1} and the electrode rotation rate of 1600 rpm. The percentage of H_2O_2 generated and the number electron (n) transferred during the reaction were derived from the RRDE output by using **Equation 4.1** and **4.2**. The number of electrons obtained are 3.97, 3.92, 3.88 and 3.71, respectively, for 3D-FePDC, 2D-FePDC, 3D-PDC and 2D-PDC (**Figure 4.12a**). The 3D-FePDC

recorded the highest value among all the catalysts, which is close to 4, indicates that it follows the theoretically predicted reaction pathway for oxygen reduction. Further, quantifying the amount of H_2O_2 generated by the parasitic side reaction confirms the result obtained in the number of electron calculation. All the catalysts show less than 10 % peroxide formation at the lower reaction potential (**Figure 4.12b**). However, in the case of the less ORR active 2D-PDC, the peroxide formation shows an increment beyond 10 % at higher potentials. The reduction of molecular oxygen to hydroxyl ion through the theoretically predicted reaction pathway is further substantiated by the RRDE analysis. Since 3D-FePDC possesses the advantage of the interconnected network structure with Fe induced active sites, this eventually leads to the active mass transport to drive the facile reduction of dioxygen through high kinetic rate. The noticeable difference between 3D-FePDC and the least active 2D-FePDC in the kinetic analysis stipulates the role of the structure and morphology modification to accommodate ORR.

Along with the activity of the catalyst, stability is also of supreme importance for ensuring the real-life application of the catalyst in the fuel cell. In 3D-FePDC, the active sites created by the iron moieties other than the iron carbides are randomly dispersed over the graphitic carbon outer layer, which may be susceptible for the degradation during the operation. Hence, the durability of 3D-FePDC in the acidic environment has been evaluated by accelerated durability test (ADT). The ADT of 3D-FePDC has been carried out by performing 5000 potential cycles by sweeping the potential in the window of 1.0 to 0.60 V *vs* RHE at a scan rate of 100 mV s^{-1} in oxygen-enriched 0.5 M H_2SO_4. The durability of 3D-FePDC is validated by measuring the changes in the halfwave potential ($E_{1/2}$) sustained subsequent to the corrosive ADT. Since ADT causes the degradation of the carbon surface along with the dopants and metal centres, it is used as an ideal tool for the ratification of the electrochemical stability of the carbon catalysts. The LSV curves recorded for 3D-FePDC before and after ADT are presented in **Figure 4.12c**. 3D-FePDC suffers only 23 mV shift in $E_{1/2}$ without facing any change in the onset potential. However, the ADT performed for the commercial Pt/C at the same electrochemical environment resulted into 60 mV retardation in $E_{1/2}$ with 15 mV negative shift in the onset region (**Figure 4.12d**). The large gap detected in the case of Pt/C may be attributed to the agglomeration and detachment of the Pt nanoparticles form the carbon support. 3D-FePDC tolerated the harsh acidic condition with a lower rate of performance loss due to its strong structural integrity.

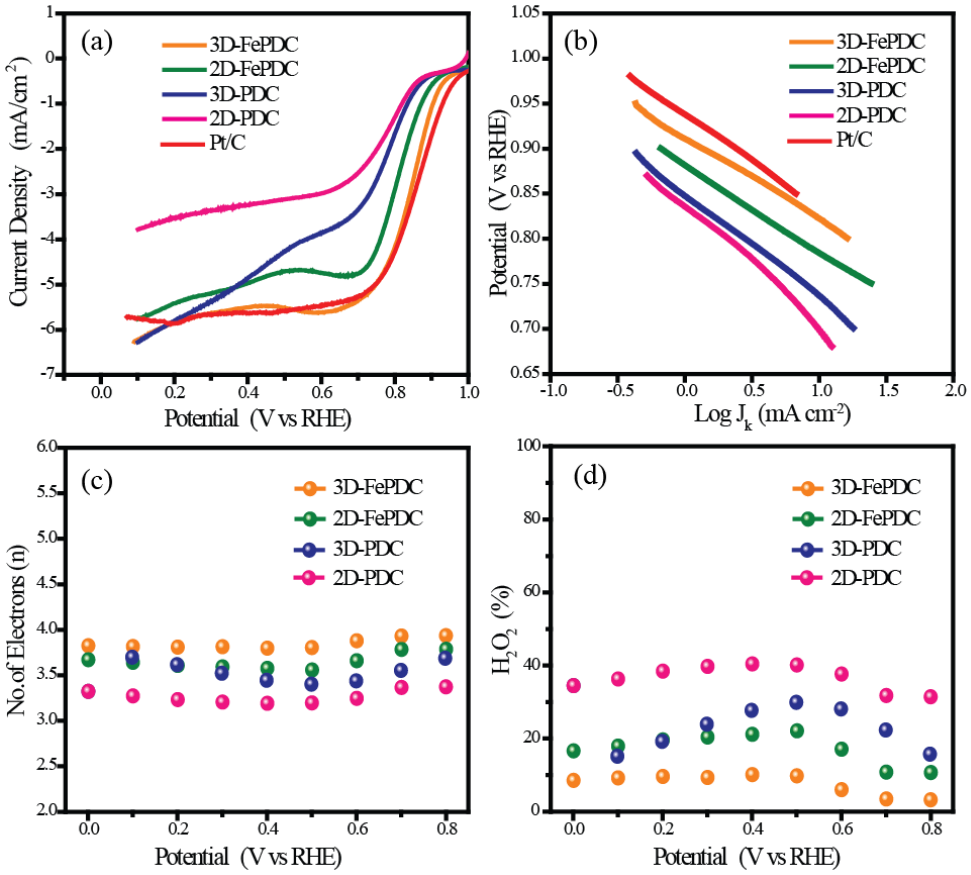

Figure 4.13 *(a) LSVs recorded for all the catalysts in 0.1 M KOH at an electrode rotation rate of 1600 rpm, (b) Tafel plots comparison of all the catalysts, (c) the number of electron transfer for ORR calculated from the RRDE analysis and (d) the amount of H_2O_2 calculated as a function of the electrode potential.*

The electrochemical activity and reaction kinetics of the catalysts are also probed in the basic medium. **Figure 4.13a** shows the LSV curve of all the catalysts in 0.1 M KOH recorded at a scan rate of 10 mV s^{-1}. It is worth mentioning that all the catalysts performed well in basic condition compared to that in acidic. In the case of the onset potential and $E_{1/2}$ values, a notable positive shift is visible in the basic medium compared to that of acid. Among all the catalysts, 3D-FePDC recorded an overlapping performance with the *state of the art* 40 wt. % Pt/C catalyst. The 3D-FePDC (0.978 V) shows only 22 mV gap with Pt/C (1.0 V) in the onset region, which diminishes to 9 mV in the $E_{1/2}$ region (0.842 V for 3D-FePDC and 0.851 V for Pt/C). The distinctive interconnected bilayer structure having the iron-induced active sites at the graphitic

carbon layer helps 3D-FePDC to achieve remarkable performance in the basic medium. Since the graphitic carbon layer contains mixed compounds of iron, it is expected to deliver higher performance in basic medium. Also, the 3D morphological advantage of the catalyst helps in facilitating mass transport with its more exposed and accessible active sites. However, the ORR trends of the other controlled samples in the basic medium are found to be similar to that in the acidic medium. Even the less active 2D-PDC catalyst could manage to decline the onset potential gap from 150 to 100 mV with Pt/C in the basic medium compared to that of the acidic medium. Thus, the ORR performance in the acidic and basic media corroborates that 3D-FePDC is a potential contender which can replace the precious metal based catalysts in PEMFCs irrespective of the nature of membrane used.

The higher activity of the catalysts in the basic medium further elucidated by comparing the Tafel slops obtained (**Figure 4.13b**). A similar Tafel slope of Pt/C (77 mV dec^{-1}) and 3D-FePDC (81 mV dec^{-1}) indicates an analogous mechanism for the dioxygen reduction reaction in basic medium. All the other catalysts also have shown low Tafel slope values for ORR in the basic medium compared to their corresponding values in the acidic environment. Further, the kinetics of the catalysts in the basic medium was analysed by RRDE analysis. The 3D-FePDC shown better kinetic features with respect to the number of electron transfer for the ORR process and the quantity of the intermediate H_2O_2 formed in the basic medium (**Figure 4.13c and d**). 3D-FePDC has recorded a yield lesser than 10 % for H_2O_2 with an 'n' value close to 4. However, all the other catalysts exhibited a yield above 10 % in the basic medium, which was lesser in the acidic medium. Thus, a key finding from the RRDE analysis is that the basic medium favours more H_2O_2 intermediate formation during ORR.

Since 3D-FePDC shows higher activity and stability for ORR under more challenging acidic condition, system-level validation of the catalyst is performed by fabricating a single cell of proton exchange membrane fuel cell (PEMFC) with the membrane electrode assembly (MEA) made up of 3D-FePDC cathode. The MEA with an active area of 4 cm^2 was prepared by using 3D-FePDC cathode (2.0 mg cm^{-2}) and Pt/C (0.50 mg cm^{-2}) anode. An MEA prepared based on Pt/C (0.50 mg cm^{-2}) as both the anode and cathode was used as the reference for the comparison purpose. The MEAs were prepared by sandwiching a Nafion 212 (DuPont, USA) proton-conducting membrane between the electrodes. **Figure 4.14b** depicts the comparative I-V

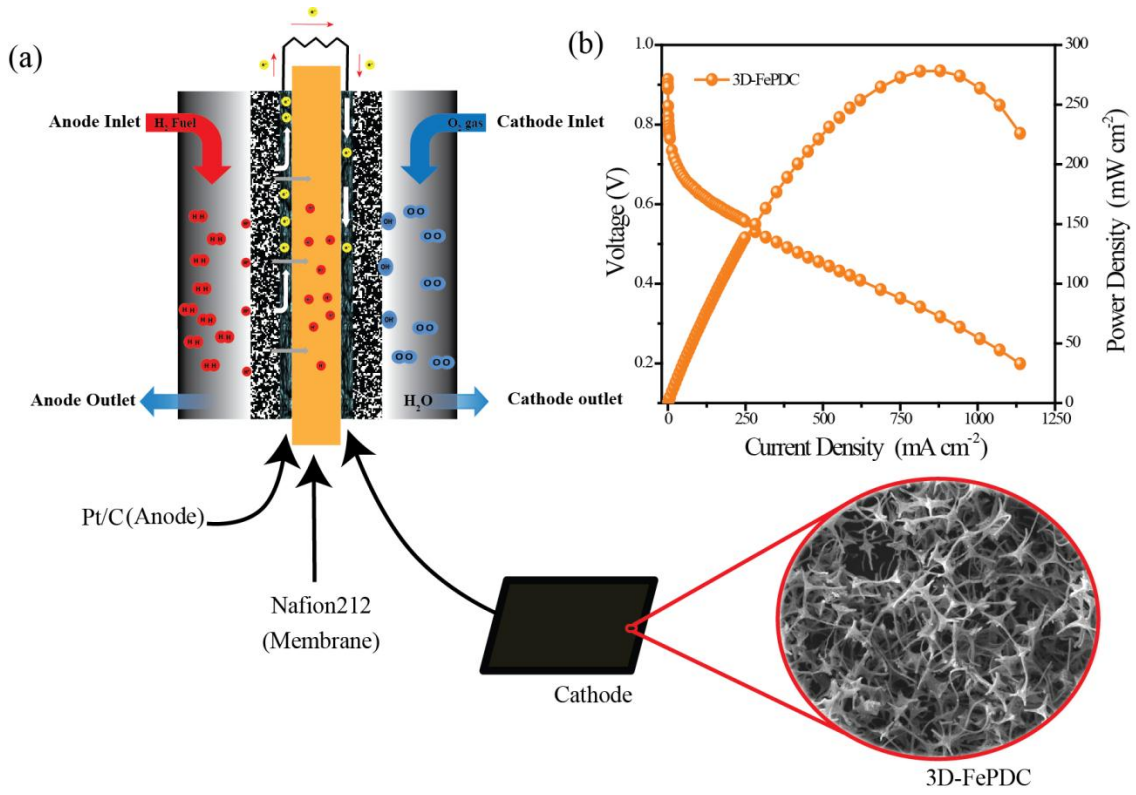

Figure 4.14 *(a) Schematic representation of the proton exchange membrane fuel cell (PEMFC) and (b) comparison of the single-cell polarization plots of the MEAs fabricated by using 3D-FePDC and Pt/C as the cathode catalysts in H_2-O_2 condition.*

polarization plots obtained for the MEAs based on 3D-FePDC and Pt/C as the cathodes. The 3D-FePDC and Pt/C based MEAs display the open-circuit voltage (OCV) of 0.89 and 0.95 V, respectively. The onset potentials recorded for the 3D-FePDC and Pt/C systems are lower than that obtained in the half cell mode. The polarization curves of both the MEAs display well-featured I-V plots consisting of activation, ohmic and mass transfer regions. The 3D-FePDC MEA recorded a maximum power density of 278 mW cm^{-2} without aid of back-pressure. However, in the same situation, the *state-of-the-art* Pt/C based MEA recorded a higher power density of 686 mW cm^{-2}. Also, the performance of the MEAs was evaluated in practical working conditions such as 0.60 V, which is important in a real-life application perspective. The 3D-FePDC and Pt/C cathode based MEAs delivered current densities of 150 and 340 mA cm^{-2}, respectively, at 0.60 V. The performance of the in-house MEA is comparatively lower than that based on Pt/C; however, considering the other non-precious metal catalysts reported for PEMFC cathode under acidic conditions, the current performance is encouraging.

4.4. Conclusions

Nitrogen-doped iron coordinated three-dimensional (3D) interconnected bilayer graphitic carbon possessing high surface area and accessible active sites (3D-FePDC) could be prepared from polydopamine and melamine foam through high-temperature annealing under an inert atmosphere. The melamine foam used as the template helped to grow the polydopamine over it, which on annealing with the iron precursor forms the iron carbide core-shell structure with dual doping of nitrogen. The 3D architecture of the catalyst provided morphological advantages in terms of more exposure of the active sites and mass transfer. On the other hand, the sites created by the iron coordination and N-doping displayed high activity towards electrochemical oxygen reduction reaction (ORR). 3D-FePDC displayed exceptional ORR activity with appreciably low overpotential in both acidic and basic electrolyte conditions compared to the other control samples prepared by compromising the morphological and structural modifications inherited in 3D-FePDC. 3D-FePDC shows high ORR activity in acidic medium, which shows an overpotential of 60 mV compared to that of the *state-of-the-art* 40 wt. % Pt/C. However, in the basic medium, this catalyst displays an overlapping performance with the Pt/C catalyst. Therefore, 3D-FePDC, a non-precious catalyst, could fulfil the need for an ORR catalyst with better performance in two furthest pH environments. The single-cell analysis by employing 3D-FePDC in the cathode of the low-temperature proton exchange membrane fuel cell (PEMFC) recorded a maximum power density of 278 mW cm^{-2} with a characteristic current-voltage polarization feature. The 3D morphology of the catalyst supplemented with the iron and nitrogen induced active sites thus turns out to be a promising non-Pt electrocatalyst for PEMFC application under realistic testing conditions.

4.5 References

[1] B. C. H. Steele and A. Heinzel, *Nature*, **2001**, 414, 345-352.

[2] M. K. Debe, *Nature*, **2012**, 486, 43-51.

[3] H. A. Gasteiger and N. M. Marković, *Science*, **2009**, 324, 48-49.

[4] M. Winter and R. J. Brodd, *Chem. Rev.*, **2004**, 104, 4245-4270.

[5] Y. Nie, L. Li and Z. Wei, *Chem. Soc. Rev.*, **2015**, 44, 2168-2201.

[6] F. Jaouen, E. Proietti, M. Lefèvre, R. Chenitz, J.-P. Dodelet, G. Wu, H. T. Chung, C. M. Johnston and P. Zelenay, *Energy Environ. Sci.*, **2011**, 4, 114-130.

[7] G.-F. Wei, Y.-H. Fang and Z.-P. Liu, *J. Phys. Chem. C*, **2012**, 116, 12696-12705.

[8] Y. Jiao, Y. Zheng, M. Jaroniec and S. Z. Qiao, *Chem. Soc. Rev.*, **2015**, 44, 2060-2086.

[9] M. Shao, Q. Chang, J.-P. Dodelet and R. Chenitz, *Chem. Rev.*, **2016**, 116, 3594-3657.

[10] A. Chen and P. Holt-Hindle, *Chem. Rev.*, **2010**, 110, 3767-3804.

[11] D. Banham and S. Ye, *ACS Energy Lett.*, **2017**, 2, 629-638.

[12] J. Wu and H. Yang, *Acc. Chem. Res.*, **2013**, 46, 1848-1857.

[13] G. Wu and P. Zelenay, *Acc. Chem. Res.*, **2013**, 46, 1878-1889.

[14] G. Wu, K. L. More, C. M. Johnston and P. Zelenay, *Science*, **2011**, 332, 443-447.

[15] Z. Chen, D. Higgins, A. Yu, L. Zhang and J. Zhang, *Energy Environ. Sci.*, **2011**, 4, 3167-3192.

[16] R. Bashyam and P. Zelenay, *Nature*, **2006**, 443, 63-66.

[17] A. Ishihara, Y. Ohgi, K. Matsuzawa, S. Mitsushima and K.-i. Ota, *Electrochim. Acta*, **2010**, 55, 8005-8012.

[18] Z.-S. Wu, S. Yang, Y. Sun, K. Parvez, X. Feng and K. Müllen, *J. Am. Chem. Soc.*, **2012**, 134, 9082-9085.

[19] F. Cheng, Y. Su, J. Liang, Z. Tao and J. Chen, *Chem. Mater.*, **2010**, 22, 898-905.

[20] T. Sun, Y. Jiang, Q. Wu, L. Du, Z. Zhang, L. Yang, X. Wang and Z. Hu, *Catal. Sci. Technol.*, **2017**, 7, 51-55.

[21] J. Yu, G. Chen, J. Sunarso, Y. Zhu, R. Ran, Z. Zhu, W. Zhou and Z. Shao, *Adv. Sci.*, **2016**, 3, 1600060.

[22] J. Shui, M. Wang, F. Du and L. Dai, *Sci. Adv.*, **2015**, 1, e1400129.

[23] S. N. Bhange, S. M. Unni and S. Kurungot, *J. Mater. Chem. A*, **2016**, 4, 6014-6020.

[24] M. Lefèvre, E. Proietti, F. Jaouen and J.-P. Dodelet, *Science*, **2009**, 324, 71-74.

[25] Z.-Y. Wu, S.-L. Xu, Q.-Q. Yan, Z.-Q. Chen, Y.-W. Ding, C. Li, H.-W. Liang and S.-H. Yu, *Sci. Adv.*, **2018**, 4, eaat0788.

[26] H. Tan, Y. Li, J. Kim, T. Takei, Z. Wang, X. Xu, J. Wang, Y. Bando, Y.-M. Kang, J. Tang and Y. Yamauchi, *Adv. Sci.*, **2018**, 5, 1800120.

[27] L. Yang, D. Cheng, H. Xu, X. Zeng, X. Wan, J. Shui, Z. Xiang and D. Cao, *Proc. Natl. Acad. Sci. USA*, **2018**, 115, 6626-6631.

[28] H. Zhang, S. Hwang, M. Wang, Z. Feng, S. Karakalos, L. Luo, Z. Qiao, X. Xie, C. Wang, D. Su, Y. Shao and G. Wu, *J. Am. Chem. Soc.*, **2017**, 139, 14143-14149.

[29] S. N. Bhange, S. M. Unni and S. Kurungot, *ACS Appl. Energy Mater.*, **2018**, 1, 368-376.

[30] Y. Hu, J. O. Jensen, W. Zhang, L. N. Cleemann, W. Xing, N. J. Bjerrum and Q. Li, *Angew. Chemie Int. Ed.*, **2014**, 53, 3675-3679.

[31] M. Xiao, J. Zhu, L. Feng, C. Liu and W. Xing, *Adv. Mater.*, **2015**, 27, 2521-2527.

[32] W. Yang, X. Liu, X. Yue, J. Jia and S. Guo, *J. Am. Chem. Soc.*, **2015**, 137, 1436-1439.

[33] S. M. Unni, R. Illathvalappil, S. N. Bhange, H. Puthenpediakkal and S. Kurungot, *ACS Appl. Mater. Interfaces*, **2015**, 7, 24256-24264.

[34] Z. He, J.-L. Maurice, A. Gohier, C. S. Lee, D. Pribat and C. S. Cojocaru, *Chem. Mater.*, **2011**, 23, 5379-5387.

[35] S. Pande, S. Jana, A. K. Sinha, S. Sarkar, M. Basu, M. Pradhan, A. Pal, J. Chowdhury and T. Pal, *J. Phys. Chem. C*, **2009**, 113, 6989-7002.

[36] C.-C. Ho and S.-J. Ding, *J. Mater. Sci.: Mater. Med.*, **2013**, 24, 2381-2390.

[37] D. R. Dreyer, D. J. Miller, B. D. Freeman, D. R. Paul and C. W. Bielawski, *Langmuir*, **2012**, 28, 6428-6435.

[38] T.-N. Tran, M. Y. Song, K. P. Singh, D.-S. Yang and J.-S. Yu, *J. Mater. Chem. A*, **2016**, 4, 8645-8657.

[39] Z. Wang, Y. Dong, H. Li, Z. Zhao, H. Bin Wu, C. Hao, S. Liu, J. Qiu and X. W. Lou, *Nat. Commun.*, **2014**, 5, 5002.

[40] J. R. Pels, F. Kapteijn, J. A. Moulijn, Q. Zhu and K. M. Thomas, *Carbon*, **1995**, 33, 1641-1653.

[41] X. Wang, W. T. Zheng, H. W. Tian, S. S. Yu, W. Xu, S. H. Meng, X. D. He, J. C. Han, C. Q. Sun and B. K. Tay, *Appl. Surf. Sci.*, **2003**, 220, 30-39.

[42] Y. Mao, H. Duan, B. Xu, L. Zhang, Y. Hu, C. Zhao, Z. Wang, L. Chen and Y. Yang, *Energy Environ. Sci.*, **2012**, 5, 7950-7955.

[43] L. Lin, Q. Zhu and A.-W. Xu, *J. Am. Chem. Soc.*, **2014**, 136, 11027-11033.

[44] H. Kim, K. Lee, S. I. Woo and Y. Jung, *Phys. Chem. Chem. Phys.*, **2011**, 13, 17505-17510.

[45] H.-W. Liang, W. Wei, Z.-S. Wu, X. Feng and K. Müllen, *J. Am. Chem. Soc.*, **2013**, 135, 16002-16005.

[46] Y. Li, W. Zhou, H. Wang, L. Xie, Y. Liang, F. Wei, J.-C. Idrobo, S. J. Pennycook and H. Dai, *Nat. Nanotechnol.*, **2012**, 7, 394-400.

[47] S. M. Unni, R. Illathvalappil, P. K. Gangadharan, S. N. Bhange and S. Kurungot, *Chem. Commun.*, **2014**, 50, 13769-13772.

[48] C. Rémazeilles, M. Saheb, D. Neff, E. Guilminot, K. Tran, J.-A. Bourdoiseau, R. Sabot, M. Jeannin, H. Matthiesen, P. Dillmann and P. Refait, *J. Raman Spectrosc.*, **2010**, 41, 1425-1433.

[49] Z. Wen, S. Ci, F. Zhang, X. Feng, S. Cui, S. Mao, S. Luo, Z. He and J. Chen, *Adv. Mater.*, **2012**, 24, 1399-1404.

[50] G. Wu, C. M. Johnston, N. H. Mack, K. Artyushkova, M. Ferrandon, M. Nelson, J. S. Lezama-Pacheco, S. D. Conradson, K. L. More, D. J. Myers and P. Zelenay, *J. Mater. Chem.*, **2011**, 21, 11392-11405.

[51] J. Shi, X. Zhou, P. Xu, J. Qiao, Z. Chen and Y. Liu, *Electrochim. Acta*, **2014**, 145, 259-269.

[52] M.-Q. Wang, W.-H. Yang, H.-H. Wang, C. Chen, Z.-Y. Zhou and S.-G. Sun, *ACS Catal.*, **2014**, 4, 3928-3936.

[53] D. Susac, L. Zhu, M. Teo, A. Sode, K. C. Wong, P. C. Wong, R. R. Parsons, D. Bizzotto, K. A. R. Mitchell and S. A. Campbell, *J. Phys. Chem. C*, **2007**, 111, 18715-18723.

Chapter 5

$NiCo_2O_4$ Nanoarray on CNT Sponge: A Bifunctional Oxygen Electrode Material for Rechargeable Zn–air Batteries

Ni- and Co-based materials have of late gained prominence over conventional noble metal-based ones as catalysts for energy devices. Here, a high performance catalyst which can facilitate both the oxygen evolution reaction (OER) and oxygen reduction reaction (ORR) was developed by anchoring a $NiCo_2O_4$ nanowire array on a carbon nanotube sponge (NCS). The three-dimensional morphology of NCS ensured efficient transport of the reactants and products on the catalyst surface, thereby improving the activity of the material. The prepared catalyst showed remarkable OER activity, requiring an overpotential of 280 mV, which is comparable to that of the noble-metal catalysts. In addition to the noteworthy OER performance, the catalyst performed well with respect to ORR. The total oxygen electrode activity overpotential of the catalyst was found to be 0.83 V, which is lower than that of commercial electrodes such as Pt/C and RuO_2. A rechargeable Zn–air battery constructed with NCS had an open circuit voltage of 1.42 V, a maximum power density of 160 mW cm^2, and an energy density of 706 W h kg^{-1}. NCS exhibited bifunctional electrocatalytic activity and high stability for both the OER and ORR, proving to be a good replacement for the noble metal electrodes in rechargeable metal–air batteries.

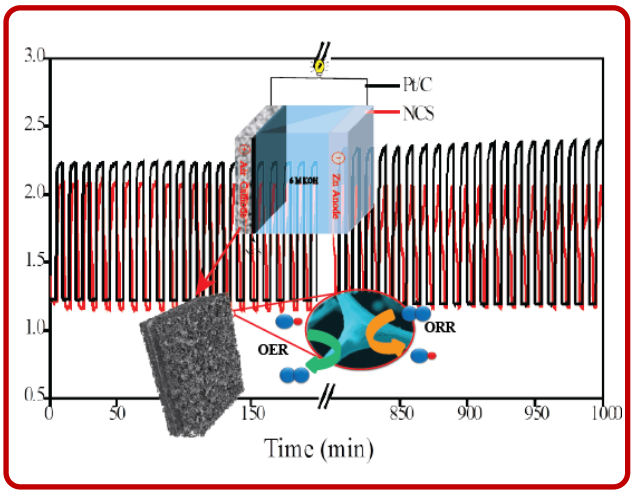

Content of this chapter is published in the following article:

Nanoscale Adv., **2019**, **1**, **3243-3251**

(https://pubs.rsc.org/en/content/articlelanding/2019/na/c9na00311h#!divAbstract)

5. 1 Introduction

The adverse effects of the continued use of fossil fuels urge the scientific world towards the practice of green and renewable energy technologies. The suitable application of metal-air batteries,[1, 2] fuel cells,[3] and water electrolysers[4-6] will have the potential to substitute conventional energy systems. All these energy systems involve two primary reactions, namely, the formation and dissociation of water.[7, 8] Among the different energy systems, Zn-air batteries are set apart by their high energy density.[9, 10] The battery uses Zn, which is an environmentally benign, earth-abundant metal, and the system has higher theoretical energy density than Li-ion batteries.[11-13] However, the high overpotential due to the sluggish kinetics of the multistep ORR/OER precludes the effective commercialization of rechargeable Zn-air batteries.[14,15] Noble metals such as Pt and RuO_2 are the foremost contenders when considering catalyst systems for rechargeable Zn-air batteries.[16] Despite precious metal catalysts being more active for the ORR/OER, their commercial use is limited by their high cost, scarcity, and poor durability.[17,18] Moreover, these catalysts cannot perform satisfactorily in both ORR and OER simultaneously. Substantial and inexpensive generation of energy requires the replacement of the conventional noble metal catalysts with alternatives that can overcome these disadvantages.

Recently, more efforts have been dedicated to developing alternatives for noble metal-based catalysts in oxygen reactions. Non-precious metal oxides, perovskites, and metal–organic frameworks have been reported as bifunctional catalysts for the ORR/OER.[19-27] Among the various non-precious metal catalysts, Co_3O_4 spinel, which shows high activity in alkaline media for both ORR and OER, has been well studied. Especially, the incorporation of Ni in the Co_3O_4 spinel matrix further improves the electrical conductivity with the generation of more active sites.[28] Among the various non-noble metal-based catalysts, Ni- and Co-based mixed oxides with the spinel structure have shown significant activity for both OER and ORR.[29,30] The advantages of a mixed-valence metal oxide over a single metal oxide for electrocatalysis are well studied in $NiCo_2O_4$. The cost of this type of transition metal compound is significantly lower than that of noble metals for large-scale energy storage. Nanostructuring in $NiCo_2O_4$ is a crucial step in the field of metal oxide research. Despite its impressive electrocatalytic performance, $NiCo_2O_4$ required extensive tuning of its morphology to expose more sites for electrocatalysis.[31,32] The anchoring of $NiCo_2O_4$ on a carbon support with an appropriate three-

dimensional alignment can overcome the pertinent issues related to the activity and stability of $NiCo_2O_4$ towards OER and ORR.

Herein, we achieved the anchoring of $NiCo_2O_4$ on a carbon nanotube sponge-based three-dimensional architecture, for increasing the availability of catalytic sites in $NiCo_2O_4$ and improving the mass transport. The synthesis of the $NiCo_2O_4$-CNT sponge (NCS) catalyst is a two-step process, involving the conversion of melamine sponge (MS) to carbon nanotube coated sponge (CS) in the first step, followed by the anchoring of $NiCo_2O_4$ on it by a solvothermal treatment in the second step. Such a three-dimensional structure possesses easily accessible active sites and high conductivity and it allows fast reactant/product transport. Along with high OER performance, NCS shows reasonable ORR activity in basic media. A realistic validation of the bifunctional aspect of the catalyst could be done by demonstrating a rechargeable Zn-air battery system composed of the electrode derived from the present catalyst. In terms of both activity and stability, the present system is found to outperform its counterparts based on the state-of-the-art precious metal catalysts.

5.2 Experimental Section

5.2.1 Synthesis of CS

500 mg of sodium dodecyl benzene sulphonate was dispersed in 50 ml DI water using bath sonication for 30 min. 75 mg of CNT was added to this solution followed by bath sonication for 30 min. and probe sonication for 10 min. The melamine sponge (MS) was soaked in the CNT solution and kept for one hour for complete absorption after which it was dried under an IR lamp; the process was repeated until the CNT solution was completely absorbed. The thus-formed material is designated CS.

5.2.2 Synthesis of NCS

80 ml each of ethanol and DI water were mixed well in a beaker. Urea (2.8 g), along with 2.32 g $Co(NO_3)_2.6H_2O$ and 1.16 g $Ni(NO_3)_2.6H_2O$ was added to the water-ethanol mixture and stirred well for about 1 h. The solution mixture was transferred to a Teflon-lined autoclave. CS was added to the autoclave and heated at 100 ^oC for 8 h. After the reaction, it was removed from the

autoclave, washed with ethanol and heated in a tubular furnace at about 350 ^{o}C for 2 h to form the final NCS catalyst.

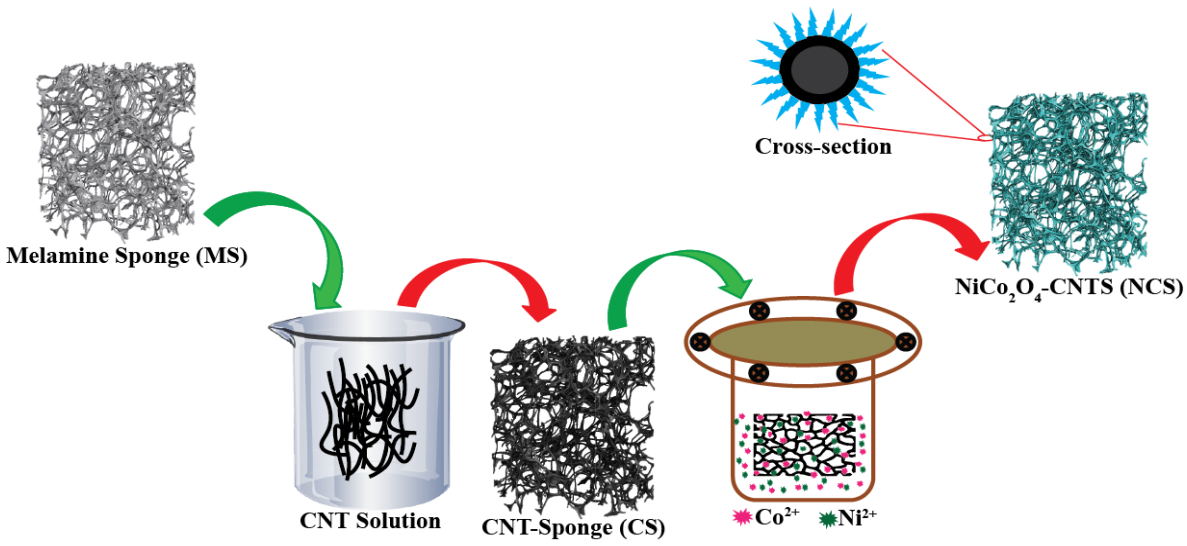

Figure 5.1. *Schematic illustration of the NCS synthesis which depicts the stepwise transformation occurring in the melamine sponge precursor leading to the synthesis of NCS.*

5.2.3 Material characterization

SEM analysis was carried out using a Zeiss DSM 950 instrument. Transmission electron microscopy (TEM) images were obtained using an FEI Technai G2 T20 instrument at an operation voltage of 200 kV. A PANalytical instrument was operated using Cu Kα radiation (l ¼ 1.54 Å) at a scanning rate of 2^{o} min^{-1} and a step size of 0.02^{o} in 2θ to acquire the X-ray diffraction spectra. XPS studies were carried out on a VG Micro Tech ESCA 3000 with a Mg Kα X-ray source. TGA was carried out on an SDTQ600 TG-DTA analyser in an oxygen environment with a 10^{o}C min^{-1} temperature ramp. A Quantachrome Quadrasorb automatic volumetric measurement instrument operated at 77 K using ultra-pure nitrogen gas was used for the BET surface area and pore size distribution analysis.

5.2.4 Electrochemical characterization

All the electrochemical studies were conducted on a Biologic electrochemical workstation (VMP3) by using a conventional three-electrode setup. A GC rotating disc electrode coated with

the catalyst (Pine Instruments Inc.) was used as the working electrode. A graphite rod as the counter electrode and Hg/HgO as the reference electrode with 1M KOH electrolyte were used for electrochemical studies. The obtained current was converted into current density *via* dividing it by the geometrical surface area of the working electrode. Also, the applied potentials were normalized with respect to RHE. The catalyst ink was prepared by dispersing 10 mg of the catalyst in 2 ml of a 2:3 mixture of isopropyl alcohol and water with the help of sonication. 10 ml of the catalyst slurry was dropcast on the GC electrode surface and dried under an IR lamp. Subsequently, 1 ml of 0.01 wt. % fumion solution in ethanol was applied to the catalyst, which acts as a binder as well as an ionomer. Standard commercial catalysts (Pt/C and RuO_2/C) for activity comparison were prepared by following the same protocol.

The number of electron transfer (n), percentage of hydrogen peroxide production (% H_2O_2) during ORR and faradaic efficiency during OER were calculated from rotating ring disc electrode (RRDE) analysis by using the following equations:

$$n = \frac{4\, I_d}{(I_d + I_r/\mathrm{N})} \qquad (5.1)$$

$$H_2O_2\,\% = \frac{200\, I_r/\mathrm{N}}{(I_d + I_r/\mathrm{N})} \qquad (5.2)$$

$$Faradaic\ Efficiency\ (\varepsilon) = \frac{2*\mathrm{Ir}}{Id*N} \qquad (5.3)$$

where, I_d is the disc current, I_r is the ring current, and N is the collection efficiency of the Pt ring (0.37).

5.2.5. Zn-air battery testing

For rechargeable Zn-air battery cells, a two-electrode configuration was used by pairing the NCS loaded carbon paper electrode (cathode) having an active area of 1 cm^2 with a Zn foil of the same area (Alfa Aesar) in 20 ml of 6M KOH. The cathode (air electrode) was fabricated with a catalyst loading of 1 mg cm^{-2} over the GDL. Oxygen was continuously purged to the cell while testing the battery.

5.3. Result and Discussion

NCS was prepared by a simple two-step process. The synthesis procedure for NCS is illustrated in **Figure 5.1** Briefly, in the first step, commercially available inert MS was coated with a layer of CNT (CS) by dipping MS in CNT slurry that contained sodium dodecyl benzene sulphonate as a binder. The modification of MS as CS helps to induce electrical conductivity in the polymer template material. Usually, a high-temperature annealing process is required to generate conductivity in melamine foam by converting it into carbon nitride (CN_x).[33] On the other hand, the MS to CS modification by the dip coating method mentioned above helps to achieve conductivity at room temperature without the need for extra energy and without imparting morphological alterations to the sponge structure. In the next step, $NiCo_2O_4$ nanowire was grown on CS by hydrothermal treatment with Ni and Co precursors in a 1:2 ethanol-water mixture in the presence of thiourea. After hydrothermal treatment, the sponge was heated at 350 ^oC in the presence of air for complete conversion of the precursor into metal oxide.

5.3.1 SEM and TEM analysis

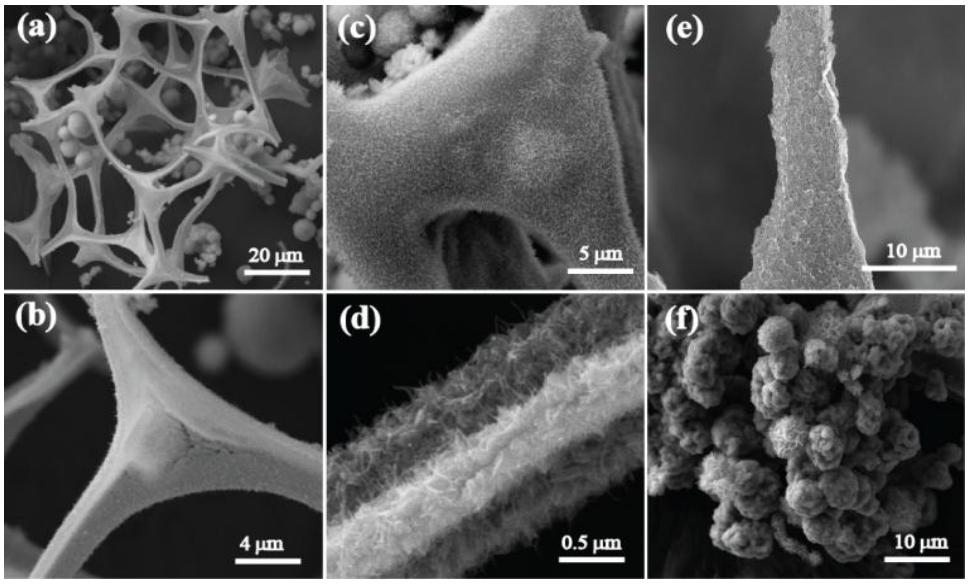

Figure 5.2 *(a) and (b) are the low magnification FESEM images of NCS showing the interconnected three-dimensional network, (c) and (d) are the high magnification FESEM images presenting the nanoarray of $NiCo_2O_4$ over the CS surface, (e) the FESEM image of the CS surface and (f) FESEM image of the $NiCo_2O_4$ flower bundle structure formed in the reaction with CN_x.*

Figure 5.2a to d show the field emission scanning electron microscopy (FESEM) images of NCS recorded at different magnifications. The low magnification image in **Figure 5.2a** shows the three-dimensional interconnected morphology of the as-prepared NCS. In the NCS structure, melamine foam acts as a backbone, which helps in the formation of the three-dimensional morphology. **Figure 5.2c** and **d** depict the $NiCo_2O_4$ nanowire array over the CS surface. The as-formed NCS has an attractive morphology for electrocatalysis with its three-dimensional interconnected tetrapod structure, which will enhance the active passage of the reactant and products through the catalyst surface. The size of these interconnected tetrapod structures is in micrometres, with a typical length of ~20 μm and width of 1-10 μm. For comparison, images of CS are also given in **Figure 5.2e.** From **Figure 5.2e**, we can observe that the CNT completely covers the arms of the melamine sponge. The annealing of melamine foam in an inert atmosphere forms the CN_x tetrapod structure that has low electronic conductivity. To elucidate the role of CS in the anchoring of $NiCo_2O_4$ over its surface, the above reaction was carried out with CN_x instead of CS. However, under the same reaction conditions, $NiCo_2O_4$ formed a flower-like morphology (NMS) which was separated from the backbone structure implying that there was no interaction with CN_x and $NiCo_2O_4$. Instead of forming a nanoarray, the $NiCo_2O_4$ growth had a distinct flower-like morphology (**Figure5.2f**). In **Figure 5.2c**, it is visible that $NiCo_2O_4$ grown on the CS surface has complete coverage of the structure. The conducting CNT-wrapped sponge surface helped the formation and growth of the $NiCo_2O_4$. **Figure 5.2d** shows the magnified images of $NiCo_2O_4$-CNT, which are very helpful for a detailed understanding of the morphology. The $NiCo_2O_4$ nanowires grow vertically on the CNT surface.

Figure 5.3a shows the scanning electron microscopy (SEM) image of the section selected for NCS to perform the elemental mapping of the different elements present on its surface and the corresponding images are shown from **Figure 5.3b-d**. From the SEM images, it is evident that Ni, Co and O are distributed uniformly on the NCS surface. **Figure 5.3e** and **f** show the transmission electron microscopy (TEM) images of NCS recorded at different magnifications. The TEM images help to reveal the interconnected $NiCo_2O_4$ nanowire array over the CS surface. It can be observed from the TEM images that the $NiCo_2O_4$ and CNTs have different aspect ratios and are evidently separated from each other. Both the $NiCo_2O_4$ nanoarray and CNTs have the same width around 15-20 nm, from each other. However, the length of the

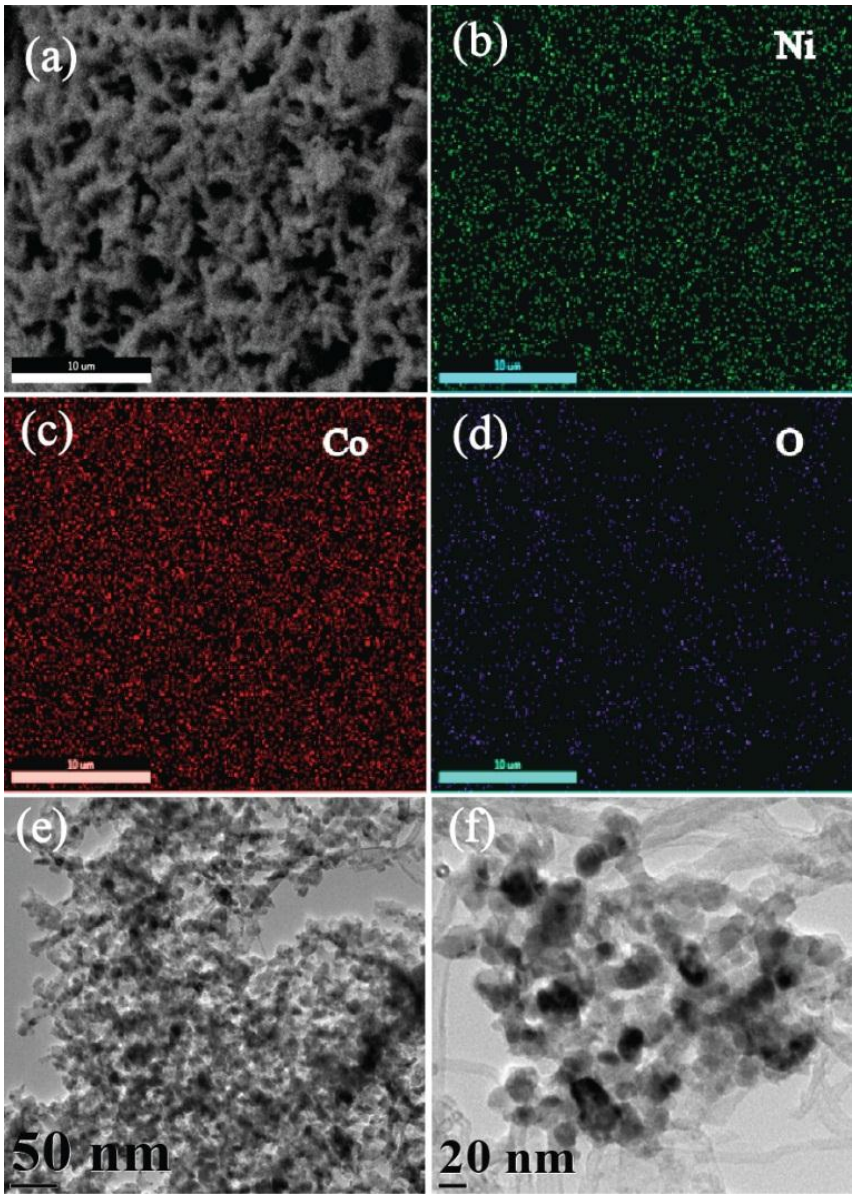

Figure 5.3. *(a) The SEM image of NCS; (b), (c), and (d) are the corresponding Ni, Co, and O elemental mappings showing the uniform distribution of the elements; (e) and (f) are the TEM images of NCS at different magnifications.*

nanoarray is restricted to below 100 nm, which is much lower than that of the CNTs. This significant difference in the aspect ratio clearly separates them in the TEM analysis. Also, in **Figure 5.3f**, it is observable that CNTs are lying behind the $NiCo_2O_4$ nanoarray.

5.3.2 XRD analysis

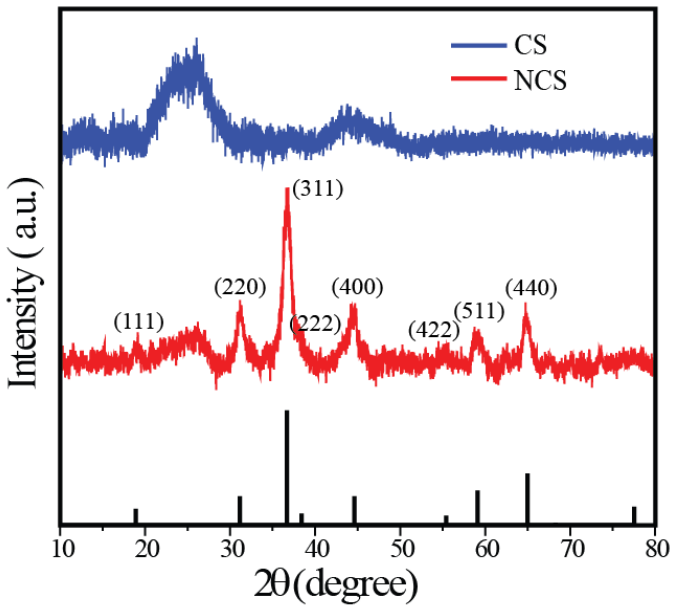

Figure 5.4. *XRD profiles of NCS and CS.*

The X-ray diffraction (XRD) patterns of NCS and CS are shown in **Figure 5.4** The crystal structure of $NiCo_2O_4$ in NCS has been investigated by powder XRD, and the characteristic spectrum is well indexed to the $NiCo_2O_4$ spinel structure (JCPDS Card No. 20-0781). The broad peak observed at a 2θ value of 26^o (200 plane) in the NCS spectrum arose from the CNT, while all the other high intensity peaks were related to the $NiCo_2O_4$ crystal structure. Compared to the C peak, $NiCo_2O_4$ peaks are sharper and more intense. $NiCo_2O_4$ shows characteristic peaks at the 2θ values of 18.9, 31.15, 36.7, 44.62, 59.1, and 64.98^o, which correspond to the (111), (220), (311), (400), (511), and (440) planes, respectively. No other impure peaks such as those for NiO or $Ni(OH)_2$ could be observed, indicating the complete formation of $NiCo_2O_4$. The $NiCo_2O_4$ in NCS has an inverse spinel crystal structure in which Co^{3+} occupies the tetrahedral sites, while Co^{3+} and Ni^{2+} occupy the octahedral sites. Since $NiCo_2O_4$ contains the same cation with different valencies, it displays higher electrical conductivity than the monometallic oxides of Ni and Co.[34,35]

5.3.3 XPS Analysis

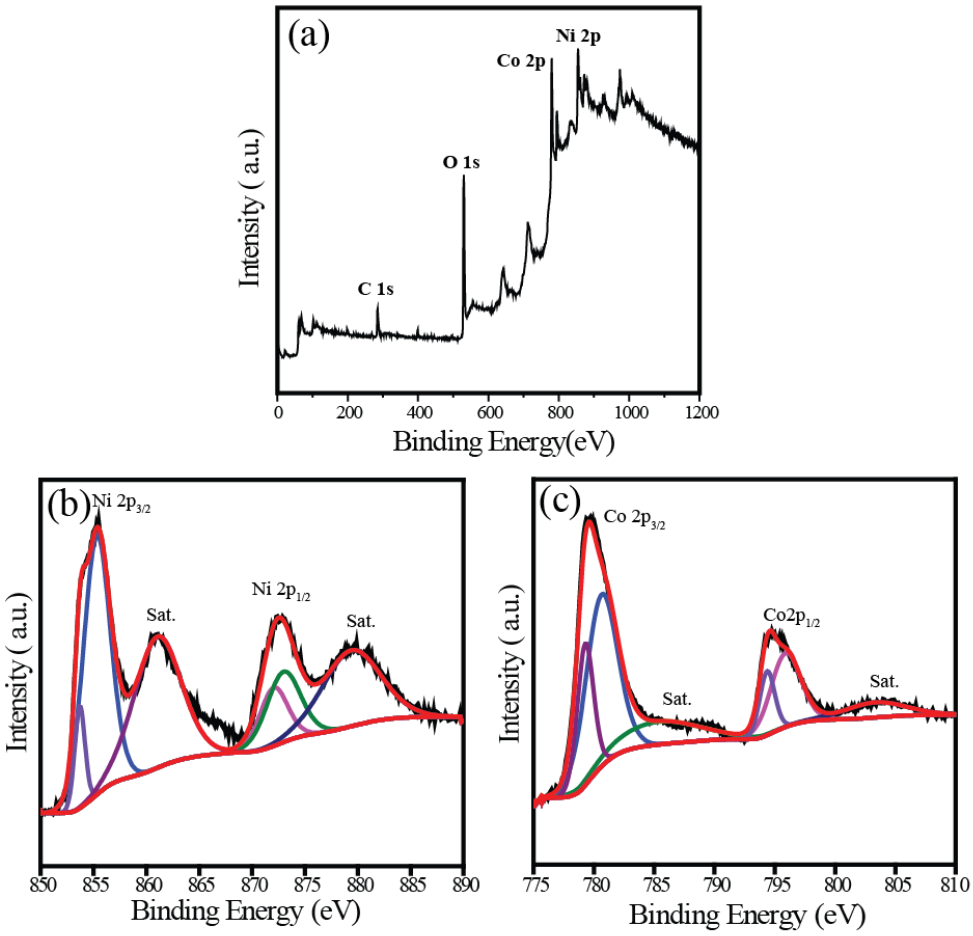

Figure 5.5. *(a) XPS survey spectrum representing the elements in NCS; (b) and (c) the deconvoluted Ni 2p and Co 2p XPS spectra of NCS.*

The surface composition and elemental analysis of NCS is further investigated using X-ray photoelectron spectroscopy (XPS). The full-scan survey spectrum in **Figure 5.5a** demonstrates the presence of Ni, Co, O, and C in NCS. The high-resolution Ni 2p spectrum is shown in **Figure 5.5b**, which consists of two spin-orbit doublets characteristic of Ni^{2+} and Ni^{3+} along with two shakeup satellite peaks. The peaks at 853.7 and 872.1 eV are indexed to Ni^{2+}, while those at 855.4 and 873.1 eV can be assigned to Ni^{3+}. Two shakeup satellite peaks appear at the positions 860.9 and 879.5 eV, respectively. Similarly, the Co 2p XPS spectrum was also deconvoluted to two spin-orbit doublets with shakeup satellite peaks. The binding energies at 780.7 and 795.9 eV are ascribed to Co^{2+}, and the binding energies at 779.3 and 794.4 eV are attributed to Co^{3+}.

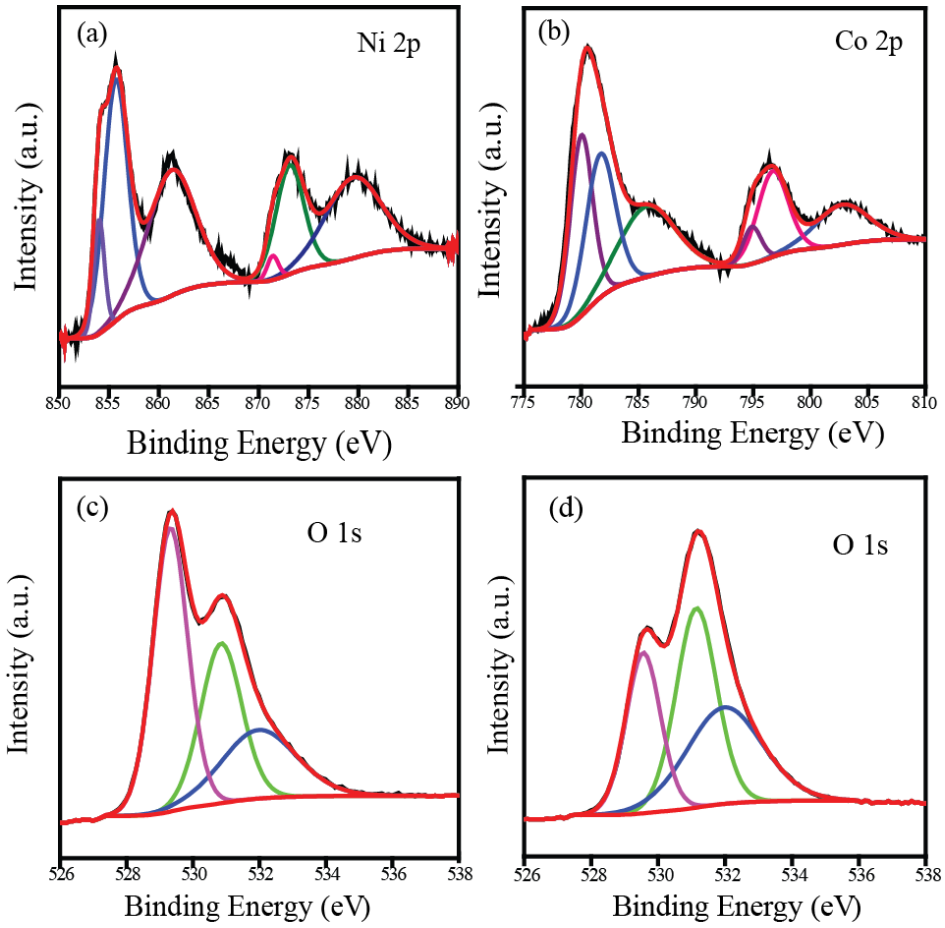

Figure 5.6. *Ni 2p (a) and Co 2p (b) XPS spectra of NMS; O 1s XPS spectra of (c) NCS and (d) NMS.*

To gain insight into the role of CS in the $NiCo_2O_4$-nanowire growth, XPS analysis of NMS was performed (**Figure 5.6a** and **b**). The Ni 2p and Co 2p XPS spectra of NCS exhibit a negative shift in the binding energy compared to NMS. The interaction between the C layer and metal oxide is responsible for this shift in the binding energy. This lightens the role of the CNT sponge platform in the growth of the $NiCo_2O_4$ nanowire. Furthermore, the metal oxide-C interaction is confirmed by the O 1s spectra comparison of both NCS and NMS (**Figure 5.6c** and **d**). The deconvoluted O 1s spectrum of NMS contained a 26% M–O–M peak at 529.4 eV, while it increases to 45% in the case of NCS. The higher percentage in NCS justifies the assumption of metal oxide interaction with the CNT layer.

5.3.4. TGA and Surface area analysis

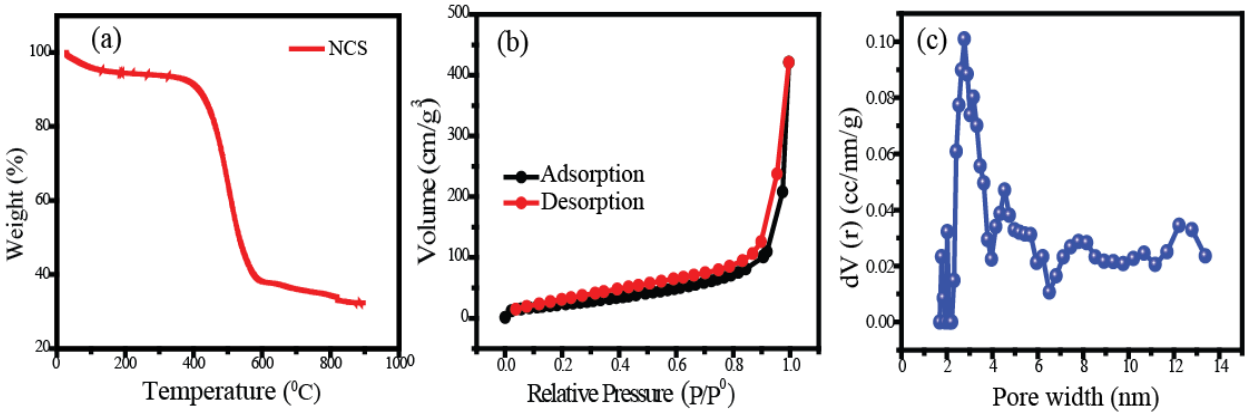

Figure 5.7. *(a) TGA profile of NCS in O_2 atmosphere; (b) and (c) BET adsorption isotherm and pore-size distribution profile of NCS.*

The thermogravimetric analysis (TGA) of NCS was carried out in an oxygen atmosphere. **Figure 5.7a** shows the typical TGA curve of the metal oxide-supported carbon morphology. In the TGA profile, the initial losses up to a temperature of 400 ^{o}C were due to the removal of adsorbed moisture from the catalyst surface. After this initial region of the temperature profile, a sudden weight loss is observed in the temperature range of 400-550 ^{0}C owing to the burning (oxidation) of the carbonaceous components of the catalyst. Above 850 ^{o}C, the metal oxide residue alone remains and the total $NiCo_2O_4$ content in the NCS as obtained from TGA is 40%. The Brunauer-Emmett-Teller (BET) surface area and pore volume of NCS were also calculated from the nitrogen adsorption-desorption studies (**Figure 5.7b and c**). The BET surface area is found to be 86 m^2 g^{-1}. The adsorption isotherm shows Type II features in the relative pressure range from 0.4 to 0.9. Along with the larger surface area, NCS is mesoporous with pore sizes ranging from 3 to 20 nm. The interconnected architecture with the mesoporous metal oxide anchored on a surface that has a large area enhances the reactant-product transport and thus improves the electrocatalytic activity.

5.3.5 Electrochemical analysis

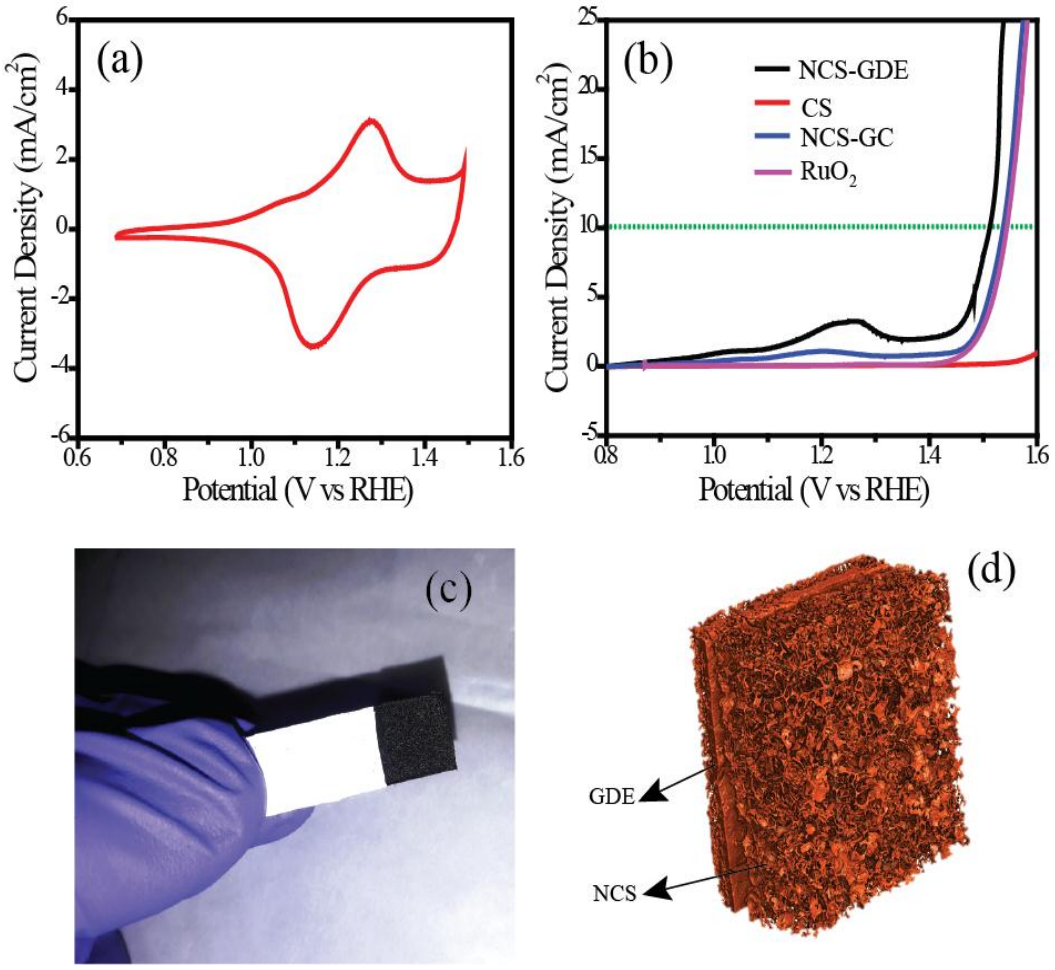

Figure 5.8. *(a) Cyclic voltammogram of NCS in N_2-saturated 1M KOH; (b OER polarization curves of the different catalysts recorded in 1M KOH electrolyte at a scan rate of 10 mV s^{-1}; (c) optical image of the three dimensional electrode prepared by pasting the NCS over GDE; (d) tomography image of the NCS electrode material.*

Electrocatalytic activity of NCS was analyzed using cyclic voltammetry (CV) in a conventional three-electrode electrochemical cell in 1M KOH with Hg/HgO as the reference electrode and a graphite rod as the counter electrode. All the experimental results pertaining to the OER on the catalysts are reported as current density *vs* iR-corrected applied potential (V *vs* RHE). **Figure**

5.8a shows the CV plot of NCS in 1M KOH solution. It has three potential regions: the non-faradaic double layer region, Ni redox couple region, and oxygen evolution region. Furthermore, for a detailed study of the OER, we performed linear sweep voltammetry (LSV). In **Figure 5.8b**, the NCS coated glassy carbon (NCS-GC) electrode has an onset potential of 1.48 V, and it reaches the benchmark current density of 10 mA cm^{-2} at the potential of 1.53 V. While evaluating the overpotential, it was found that NCS has a 300 mV overpotential, which is lower than that of the commercial electrode catalysts based on IrO_2 and RuO_2. For exploring the advantages of the three-dimensional interconnected electrode and for mimicking a real cell electrode, the same experiments were repeated by replacing the NCS-GC electrode with an NCS pasted gas diffusion electrode (NCS-GDE) (**Figure 5.8c** and **d**). The three-dimensional morphology of NCS is better retained on the NCS-GDE electrode than on the NCS-GC electrode, and this augments the reactant and product gas distribution through the catalyst surface. The advantage of this morphology is well reflected in the oxygen evolution performance of the material as well. The overpotential for NCS-GC is reduced from 300 to 280 mV by using a NCS-GDE. For a comparative evaluation of the performance of the NCS-coated electrode for the OER, state-of-the-art RuO_2 and CS electrodes were also studied under the same reaction conditions. It was observed that CS does not exhibit any visible activity for the OER; however, RuO_2 required an overpotential of 310 mV to attain the current density of 10 mA cm^{-2}.

The CV was performed in the double-layer region with different scan rates ranging from 20 to 200 mV s^{-1}, revealing a linear trend in the increment of anodic and cathodic current with the scan rate. Furthermore, the anodic and cathodic currents at a potential of 0.06 V are plotted against the scan rate; the slope of the straight line is indicative of the double layer capacitance **(Figure 5.9)**. The obtained electro-active area is higher than that of some recently reported OER catalysts. The slopes of NCS-GDE, NCS-GC, RuO_2 and CS electrodes were found to be 31.1×10^{-4} μF cm^{-2}, 5.36×10^{-4} μF cm^{-2}, 3.84×10^{-4} μF cm^{-2}, and 3.03×10^{-4} μF cm^{-2}, respectively. The considerable difference in the electroactive surface area of the NCS-GDE electrode compared to the other catalysts indicates the importance of the three-dimensional interconnected surfaces for electrocatalysis. This higher electroactive surface area provides a higher density of active sites.

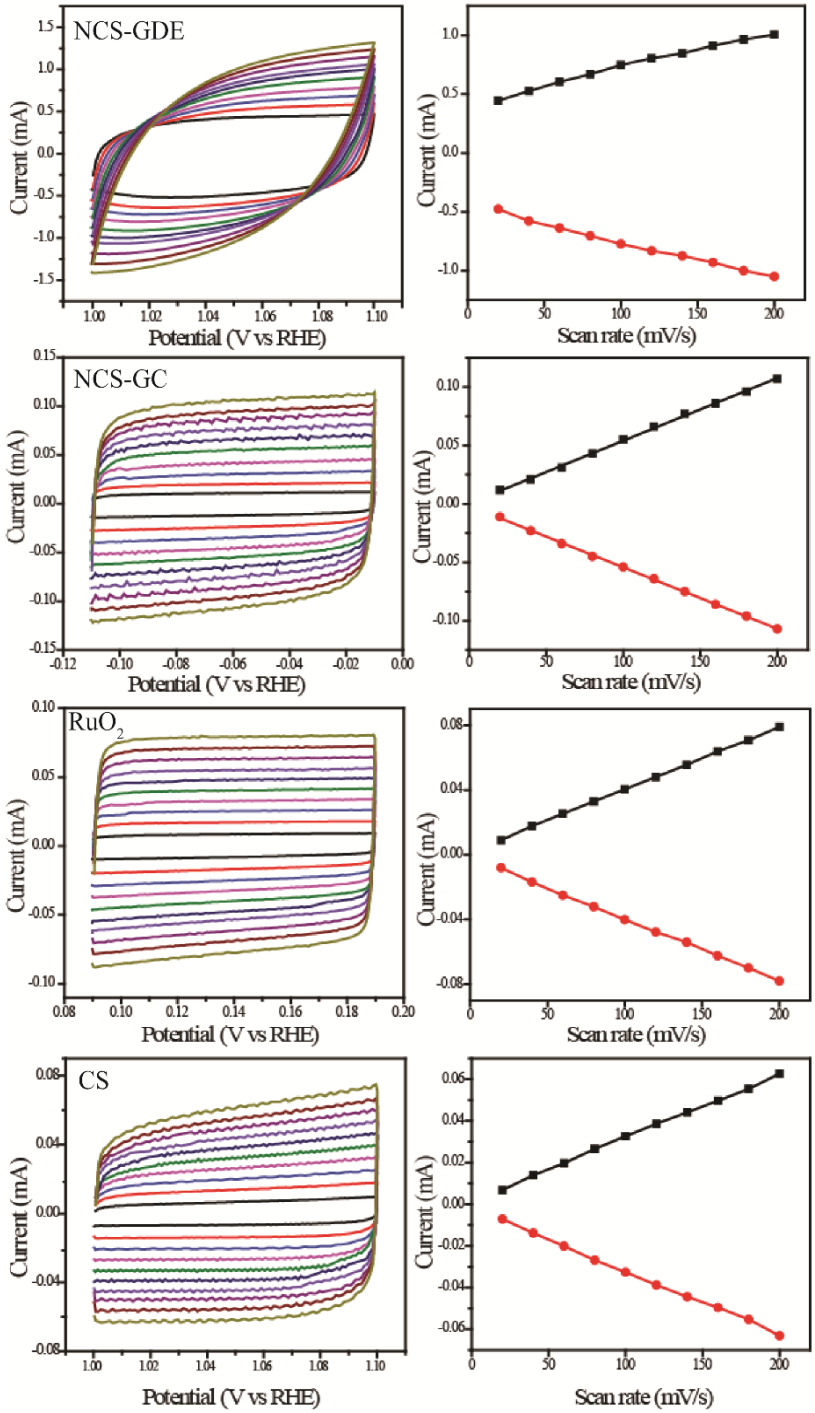

Figure 5.9 *Linear fitting of the current density differences of the catalyst vs scan rate along with the CV profiles of NCS-GDE, NCS-GC, RuO_2 and CS.*

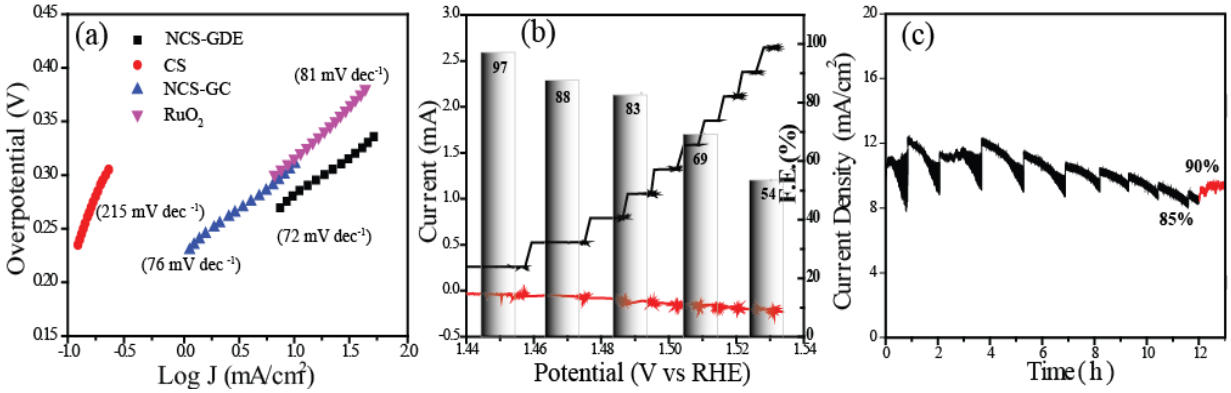

Figure 5.10 *(a)Tafel plots of the different catalysts recorded in 1M KOH electrolyte at a scan rate of 10 mV* s^{-1}*; (b) RRDE analysis of NCS showing the applied disc current, obtained ring current, and faradaic efficiency at different applied current steps; (c) chronoamperogram obtained for NCS at a potential of 1.51 V.*

The Tafel plots given in **Figure 5.10a** exhibit a lower Tafel slope of 72 mV dec^{-1} for NCS-GDE compared to that of NCS-GC (76 mV dec^{-1}) and CS (215 mV dec^{-1}), suggesting the more favorable kinetics of the NCS material towards the OER. This Tafel slope value is lower than that of the reference RuO_2 (81 mV dec^{-1}) catalyst. The faradaic efficiency (ε) of the NCS catalyst is determined by using the rotating ring-disk electrode (RRDE) technique in 1M KOH in an N_2-saturated atmosphere. During the RRDE measurement, oxygen evolved at the disk electrode, and was collected and reduced at the Pt-ring electrode with a corresponding current response. The faradaic efficiency (ε) was calculated from RRDE data using **Equation 5.3**. **Figure 5.10b** shows the plots of the faradaic efficiency obtained against the applied disk current, with the corresponding disk and ring currents and detected potential. Approximately 97% faradaic efficiency was obtained at an applied current density of 1 mA cm^{-2}. This indicates the oxygen generation at the disc and the corresponding reduction at the Pt-ring. While incrementing the applied current density from 1 mA cm^{-2} to 10 mA cm^{-2}, it was found that faradaic efficiency decreased. The faradaic efficiency at 10 mA cm^{-2} reached a low value of 54%. The gradual decrease in the faradaic efficiency with the applied current density is due to the inefficiency of the Pt-ring in collecting all the evolved oxygen. The faradaic efficiency obtained at 1 mA cm^{-2} is considered as the actual value since this current density is sufficient to produce a substantial amount of oxygen. Finally, the higher faradaic efficiency obtained confirms the OER on the disk

electrode surface instead of other side reactions. After evaluating the oxygen evolution performance of NCS, the stability of the catalyst was measured by the chronoamperometric technique (**Figure 5.10c**). We applied a potential of 1.51 V (overpotential of 280 mV) and performed continuous analysis for 12 h. After 12 h, the current density decreased to 8.5 mA cm^{-2} from the initial value of 10 mA cm^{-2}. The 85% retention in the activity of the material observed after 12 h is pointing out the high stability of the catalyst. Due to the bubble formation and removal during the OER, a zig-zagging behaviour was observed during chronoamperometry. During bubble formation, active sites are blocked by these bubbles from further reaction, and this decreases the current. The accumulated bubbles release abruptly, causing an increase in current. After 12 h of operation, the electrode was taken out and dried to remove the gasses from the surface, and chronoamperometry was restarted resulting in an increase in the current density up to 9 mA cm^{-2}. This shows that the 5% decrease in activity can be attributed to the gas bubbles. This experiment ascertains the durability of the catalyst for real-life applications.

Along with the OER activity, the ORR activity of the catalyst was also analyzed. While preparing the slurry for ORR activity analysis, we added carbon black (Vulcan Carbon XC-72) to prevent the distortion of the structure and promote restacking to ensure that the catalyst surfaces are well exposed.[36,37] **Figure 5.11a** shows the cyclic voltammogram of NCS in O_2- and N_2-saturated electrolytes. The characteristic oxygen reduction peak starting at 0.92 V was observed in the O_2-saturated atmosphere but not in the N_2-saturated electrolyte, thus confirming the high ORR activity of the catalyst. We conducted LSV measurements of NCS with different ratios of VC ranging from 10 to 40% of the NCS to identify the optimum combination. For comparison, the ORR activity of the commercially available Pt/C was also measured under the same experimental conditions (**Figure 5.11b**). The onset potential of the Pt/C was observed as 1.0 V *vs* RHE. However, all the NCS samples had onset potentials in the range of 0.920 V. The catalyst with 20% VC (NCS-VC20) was found to give the best performance among all the NCS samples. NCS-VC20 has an onset potential value of 0.920 V and $E_{1/2}$ value of 0.75 V. Even though the value of its potential is slightly lower than that of Pt/C, NCS-VC20 has a higher limiting current compared to the Pt system. This points towards the availability of more number of accessible and exposed active centers in the system, presumably achieved through the 3D interconnected and distributed structure of the catalyst.

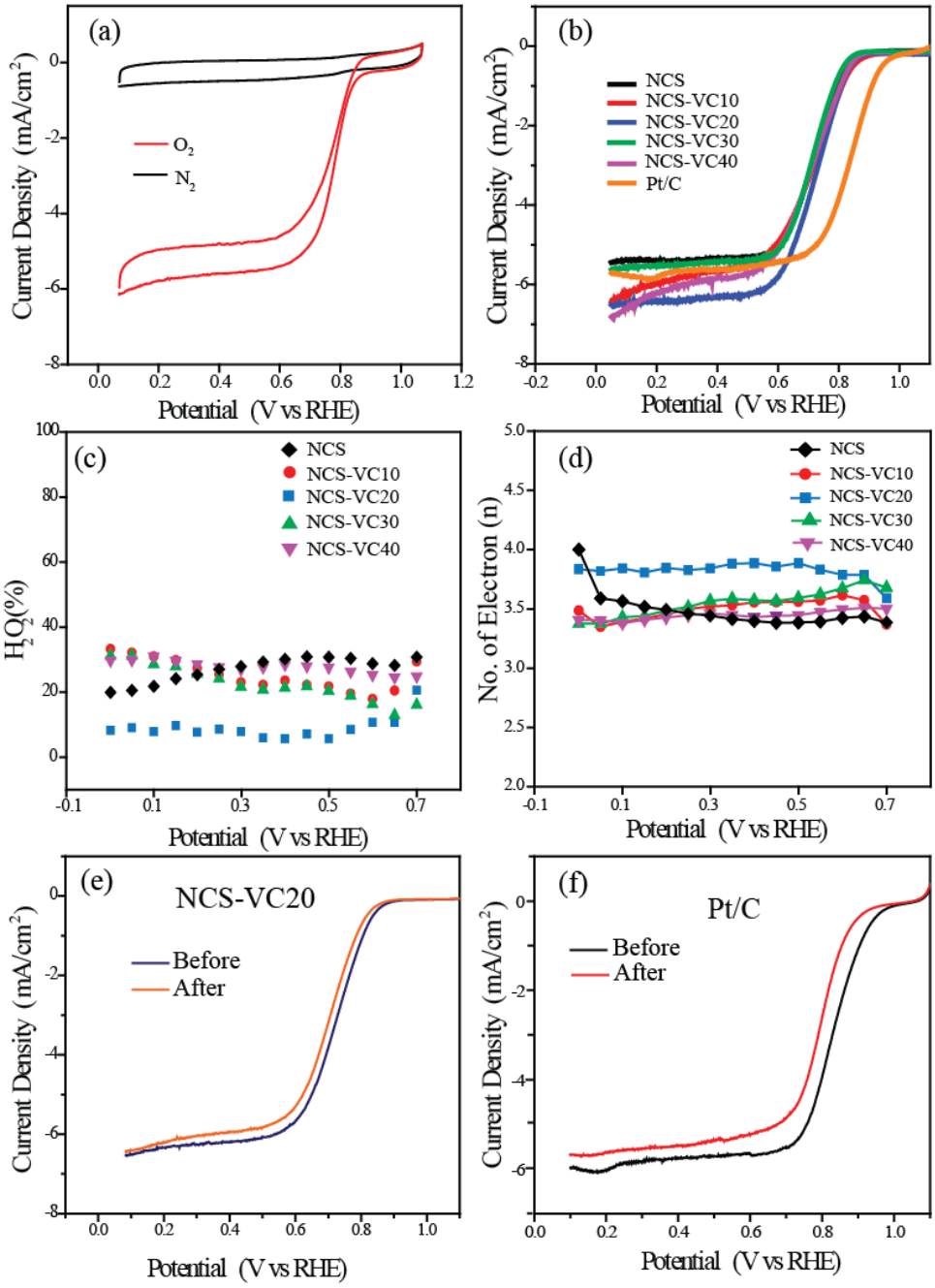

Figure 5.11 *(a) Cyclic voltammogram of NCS in O_2- and N_2-saturated 0.1 M KOH, (b) linear sweep voltammograms (LSVs) recorded for all the catalysts in 0.1M KOH at an electrode rotation speed of 1600 rpm, (c) the number of electron transfer of oxygen reduction reaction calculated as a function of the electrode potential from RRDE, (d) the amount of H_2O_2 calculated as a function of the electrode potential from RRDE and LSVs of (e) NCS and (f) recorded before and after ADT.*

RRDE analysis was performed for evaluating the ORR kinetics of the different NCS samples. The number of electrons involved in the oxygen reduction process and the quantity of the H_2O_2 intermediate formed during the reaction were calculated from the RRDE data. The number of electrons involved was found to be in the range from 3.4 to 3.8, indicating the predominance of the theoretical four-electron pathway corresponding to the formation of H_2O as the end product to the reduction process. NCS-VC20, which showed the best performance, displays an electron transfer number of 3.8, the closest value to 4 among all the samples (**Figure 5.11c**). The formation of intermediate H_2O_2 was also measured using the RRDE study. Among the different samples, NCS-VC20 catalyst is detected with less than 10% of H_2O_2, whereas, the other samples generated H_2O_2 in the range of 20 to 34% (**Figure 5.11d**). The increase in the H_2O_2 percentage is an indicative on the low preferred ORR kinetics on the catalyst surface. Stability of the NCS for ORR was evaluated by cycling the potential in the kinetic region for 5000 cycles. After 5000 cycles, it was found that NCS displays only 20 mV shift in $E_{1/2}$ compared to a 35 mV shift displayed for the Pt/C catalyst under the same conditions (**Figure 5.11e & Figure 5.11f**).

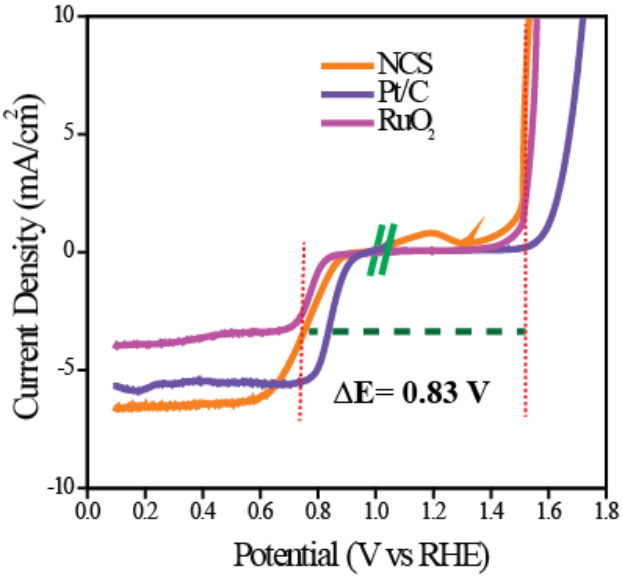

Figure 5.12. *The plot representing the bifunctional catalytic activities of NCS toward ORR and OER.*

The oxygen electrode activity (OEA) of the NCS catalyst for the bifunctional catalysis was calculated by combining the LSV plots of ORR and OER. The catalyst with the minimum potential difference (ΔE) for ORR and OER is found to be the ideal catalyst for the oxygen electrode. The OEA can be measured by subtracting the OER potential at a current density of 10 mV cm^{-2} from the $E_{1/2}$ potential of ORR. The OEA of the NCS calculated from **Figure 5.12** is found to be 0.83 V. It is lower than that of the commercial catalyst coated electrodes such as Pt/C (0.92 V) and RuO_2 (0.87 V). These studies suggest that NCS, with its promising bifunctional activity, has the potential to replace the traditional precious metal catalyst systems.

Finally, as a realistic system level validation to understand the bifunctional characteristics of the NCS catalyst, a rechargeable Zn-air battery (ZAB) was fabricated using NCS coated GDE as the cathode, Zn foil as the anode and 6M KOH as the electrolyte (**Figure 5.13a**). For comparison, a similar system constructed with the commercial Pt/C coated GDE was used as the air electrode and analysed in the same conditions. In the Zn-air battery, OER and ORR are taking place at the air electrode in the course of charging and discharging processes, respectively. In the discharging process, the oxygen supplied at the air cathode undergoes reduction to form hydroxyl ions. As generated hydroxyl ions diffuse towards the anode side of the battery and reacts with the Zn ions, which are generated by the anodic oxidation of the Zn electrode, and to produce the intermediate zincate ($Zn(OH)_4^{2-}$) ions. The as formed intermediate further decomposed into zinc oxide (ZnO) at supersaturated concentration. During the charging of the battery, the process at the respective electrodes undergo reverse reaction, *i.e.*, OER will occur at the air electrode interface with the release of oxygen, and the generated ZnO gets redeposited from the electrolyte at the anode. The reaction mechanisms of the charging and discharging processes are summarized as follows:

Discharge:

Air electrode:

$$O_2 + 2H_2O + 4e^- \rightarrow 4OH^-$$

Zinc electrode:

$$Zn + 4OH^- \rightarrow Zn(OH)_4^{2-} + 2e^-$$

$Zn(OH)_4^{2-} \rightarrow ZnO + H_2O + 2OH^-$

Recharge:

Air electrode:

$4OH^- \rightarrow O_2 + 2H_2O + 4e^-$

Zinc electrode:

$ZnO + H_2O + 2OH^- \rightarrow Zn(OH)_4^{2-}$

$Zn(OH)_4^{2-} + 2e^- \rightarrow Zn + 4OH^-$

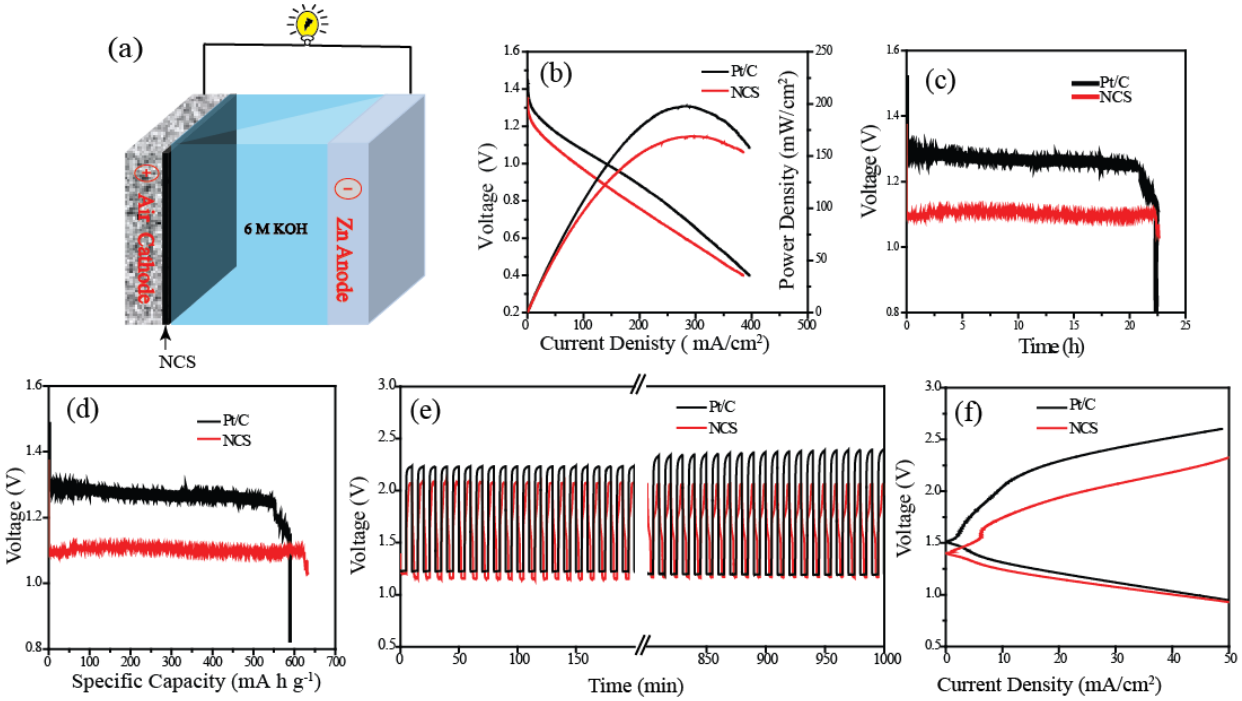

Figure 5.13 *(a) Schematic structure of the Zn-air battery, (b) I-V polarization curves of the battery by using NCS and Pt/C as the cathode materials, (c) typical discharge curves of the Zn-air battery under continuous discharge until complete consumption of Zn,* (d) *galvanostatic discharge curves of Zn-air batteries with NCS and Pt/C as the cathodes until complete consumption of Zn anode. (e) charge-discharge cycles performed at a current density of 10 mA/cm^2 and (e) charging and discharging polarization (i-v) plots of the rechargeable Zn-air battery.*

The Zn-air battery has a theoretical open circuit voltage (OCV) of 1.65 V based on the above reaction mechanisms. However, the OCVs of the real cells are normally slightly lower, mainly due to overpotential associated with the air electrode. In the present case, the OCVs measured for the Zn-air batteries fabricated with NCS and Pt/C are observed to be 1.42 and 1.46 V, respectively. The discharge current-voltage (I-V) polarization plots of the systems obtained by the primary battery mode are shown in **Figure 5.13b**. Maximum power densities of 160 and 200 mW cm^{-2} respectively are obtained for the systems based on the NCS and Pt/C cathodes, indicating that the newly developed Pt-free system can be a potential candidate for fabricating a cost-effective ZAB system. The rechargeable Zn-air battery made with NCS was very robust. To explore the robustness of the battery, we conducted galvanostatic discharging of the systems based on NCS and Pt/C as the air electrodes (**Figure 5.13c**). No apparent voltage drop was observed for 22 h during the discharge process, suggesting the higher ORR stability of NCS. The final drop in the continuous discharging occurred due to the complete consumption of the Zn foil. Also, we found that mechanical recharging by replacing the Zn anode could regenerate the battery with the same cathode material at the same potential for a long duration. The specific capacity normalized to the mass of the consumed Zn was calculated to be 636 mA h g^{-1} for the NCS and 587 for the Pt/C based systems (**Figure 5.13d**). The energy density calculated from the capacity was 706 W h kg^{-1} and 686 W h kg^{-1} for the NCS and Pt/C systems, respectively. Further, the ZAB performance evaluation was conducted in the rechargeable mode. The reversing of the primary reaction requires high overpotential, which is almost higher than 2 V. The higher overpotential comes from the sluggish kinetics of the air electrode and dendrite formation at the Zn anode. The three-dimensional interconnected porous NCS can overcome the activation loss in the air electrode. **Figure 5.13e** shows the typical charge-discharge cycling stability test of the ZAB recorded at a high current density of 10 mA cm^{-2}. The NCS exhibits an initial charge-discharge voltage gap of 0.89 V which is lower than that of Pt/C (0.96 V). After a long run of 1000 min at a rate of 10 min per cycles, the same charge-discharge potential gap is observed to be maintained for NCS. However, In the case of the Pt/C based system, the potential gap increases and reaches 1.18 V. The continues oxidation-reduction reactions during the course of the charge-discharge cycle can trigger corrosion of the catalyst in the air electrodes. Initial charging of the Pt/C electrode requires 2.21 V, which increases to 2.37 V after 1000 cycles of the charge-discharge. High potential required for the charging initiates the carbon corrosion with

concomitant platinum leaching. However, the NCS catalyst is appeared to be sustained in the corrosive environment without any noticeable change in the charge-discharge potential in course of the process cycles. Further, **Figure 5.13f** shows the charge-discharge polarization of the rechargeable Zn-air battery. The NCS system exhibits a lower charge-discharge potential gap of 0.78 V at a current density of 20 mA cm^{-2} compared to the Pt/C based system (1.06 V). This low overpotential gap of the in-house system compared to the system based on the expensive Pt/C electrode points towards the feasibility of developing cost-effective Zn-Battery for realistic applications by using the NCS catalyst as the air electrode.

5.4. Conclusions

In this work, we have developed an innovative method for the production of an active electrocatalyst which can facilitate both oxygen evolution and oxygen reduction reactions (OER and ORR, respectively). A low-priced melamine sponge (MS) was used as the template material for the preparation of the three-dimensional interconnected electrocatalyst material (NCS). The NCS catalyst possesses a 3-D morphology with a carbon-nanotube coated melamine foam base and a $NiCo_2O_4$ nanoarray over it. The CNT wrapping on MS gives electric conductivity to the template for further the anchoring of $NiCo_2O_4$ nanoarray. The role of CNT layer for growing of $NiCo_2O_4$ nanoarray was uncovered by FESEM analysis. TEM analysis identified the two distinct CNT and $NiCo_2O_4$ phases in NCS. The interconnected macroporous morphology exposes more active sites and also enables the efficient reactant-product transport on the catalyst surface. Since the catalyst showed bifunctional electrocatalytic activity for OER and ORR in alkaline medium, its total Oxygen Electrode Activity was found to be higher than the state-of-the-art commercial catalyst systems. The NCS catalyst exhibited better performance in rechargeable Zn-air batteries. From this study, it seems possible that the newly developed catalyst can replace commercial RuO_2 for OER and Pt/C for ORR with a single catalyst material for oxygen electrode applications such as in a rechargeable battery. The low-cost material with a simple synthetic protocol, albeit with higher activity and stability, is an ideal replacement for state-of-the art systems.

5.5 References

[1] D. Larcher and J. M. Tarascon, *Nat. Chem.*, **2014**, 7, 19.

[2] Z.-L. Wang, D. Xu, J.-J. Xu and X.-B. Zhang, *Chem. Soc. Rev.*, **2014**, 43, 7746-7786.

[3] B. C. Steele and A. Heinzel, *Nature*, **2001**, 414, 345-352.

[4] J. A. Turner, *Science*, **1999**, 285, 687-689.

[5] N. Armaroli and V. Balzani, *Angew. Chemie Int. Ed.*, **2007**, 46, 52-66.

[6] S. Park, Y. Shao, J. Liu and Y. Wang, *Energy Environ. Sci.*, **2012**, 5, 9331-9344.

[7] V. R. Stamenkovic, D. Strmcnik, P. P. Lopes and N. M. Markovic, *Nat. Mater.*, **2016**, 16, 57.

[8] N. M. Markovic, *Nat. Mater.*, **2013**, 12, 101-102.

[9] Y. Li and H. Dai, *Chem. Soc. Rev.*, **2014**, 43, 5257-5275.

[10] P. Gu, M. Zheng, Q. Zhao, X. Xiao, H. Xue and H. Pang, *J. Mater. Chem. A*, **2017**, 5, 7651-7666.

[11] V. Neburchilov, H. Wang, J. J. Martin and W. Qu, *J. Power Sources*, **2010**, 195, 1271-1291.

[12] G. Girishkumar, B. McCloskey, A. C. Luntz, S. Swanson and W. Wilcke, *J. Phys. Chem. Lette.*, **2010**, 1, 2193-2203.

[13] J. S. Lee, S. T. Kim, R. Cao, N. S. Choi, M. Liu, K. T. Lee and J. Cho, *Adv. Energy Mater.*, **2011**, 1, 2-2.

[14] Y. Gorlin and T. F. Jaramillo, *J. Am. Chem. Soc.*, **2010**, 132, 13612-13614.

[15] D. U. Lee, J. Y. Choi, K. Feng, H. W. Park and Z. Chen, *Adv. Energy Mater.*, **2014**, 4, 1301389.

[16] W. T. Hong, *Energy Environ. Sci.*, **2015**, 8, 1404-1427.

[17] F. Cheng and J. Chen, *Chem. Soc. Rev.*, **2012**, 41, 2172-2192.

[18] Q. Liu, Y. Wang, L. Dai and J. Yao, *Adv. Mater.*, **2016**, 28, 3000-3006.

[19] J. Masa, W. Xia, I. Sinev, A. Zhao, Z. Sun, S. Grützke, P. Weide, M. Muhler and W. Schuhmann, *Angew. Chemie Int. Ed.*, 2014, 53, 8508-8512.

[20] M. Jahan, Z. Liu and K. P. Loh, *Adv. Funct. Mater.*, **2013**, 23, 5363-5372.

[21] J. I. Jung, H. Y. Jeong, J. S. Lee, M. G. Kim and J. Cho, *Angew. Chem.*, **2014**, 126, 4670-4674.

[22] C. Jin, X. Cao, L. Zhang, C. Zhang and R. Yang, *J. Power Sources*, **2013**, 241, 225-230.

[23] J.-I. Jung, M. Risch, S. Park, M. G. Kim, G. Nam, H.-Y. Jeong, Y. Shao-Horn and J. Cho, *Energy Environ. Sci.*, **2016**, 9, 176-183.

[24] B. Y. Xia, Y. Yan, N. Li, H. B. Wu, X. W. Lou and X. Wang, *Nat. Energy*, **2016**, 1, 15006.

[25] S. Gadipelli, T. Zhao, S. A. Shevlin and Z. Guo, *Energy Environ. Sci.*, **2016**, 9, 1661-1667.

[26] C. Zhang, M. Antonietti and T. P. Fellinger, *Adv. Funct. Mater.*, **2014**, 24, 7655-7665.

[27] X. Liu, M. Park, M. G. Kim, S. Gupta, G. Wu and J. Cho, *Angew. Chemie Int. Ed.*, **2015**, 54, 9654-9658.

[28] H. B. Wu, H. Pang and X. W. Lou, *Energy Environ. Sci.*, **2013**, 6, 3619-3626.

[29] C. Jin, F. Lu, X. Cao, Z. Yang and R. Yang, *J. Mater. Chem. A*, **2013**, 1, 12170-12177.

[30] D. U. Lee, B. J. Kim and Z. Chen, *J. Mater. Chem. A*, **2013,** 1, 4754-4762.

[31] S. Chen and S.-Z. Qiao, *ACS Nano*, **2013,** 7, 10190-10196.

[32] H. Hu, B. Guan, B. Xia and X. W. Lou, *J. Am. Chem. Soc.*, **2015,** 137, 5590-5595.

[33] P. K. Gangadharan, S. M. Unni, N. Kumar, P. Ghosh and S. Kurungot, *ChemElectroChem*, **2017,** 4, 2643-2652.

[34] L. Hu, L. Wu, M. Liao, X. Hu and X. Fang, *Adv. Funct. Mater.*, **2012**, 22, 998-1004.

[35] M. N. Iliev, P. Silwal, B. Loukya, R. Datta, D. H. Kim, N. D. Todorov, N. Pachauri and A. Gupta, *J. Appl. Phys.*, **2013**, 114, 033514.

[36] V. Kashyap, S. K. Singh and S. Kurungot, *ACS Appl. Mater. Interfaces*, **2016**, 8, 20730-20740.

[37] Y. Ma, H. Wang, S. Ji, J. Goh, H. Feng and R. Wang, *Electrochim. Acta*, **2014**, 133, 391-398.

Chapter 6

Summary

This chapter provides an overall outline and conclusion of the research works as explained in the previous chapters focused on the development of the three-dimensional (3D) catalysts for the electrochemical water cycle reactions. Electrochemical energy devices such as polymer electrolyte membrane fuel cells (PEMFCs), metal-air batteries, and water electrolyzers extensively contribute towards energy sustainability. However, the widespread commercialization prospects of the electrochemical energy devices are hindered by the practical complexities related to the catalyst development. Significant efforts are required to overcome the limitations associated with the existing catalysts. In the path of the catalyst development for the water cycle reactions, the morphology of the catalyst is an important performance deciding parameter along with its chemical structure since effective mass diffusion is essential for the organized functioning of the catalyst. Apart from the desired morphology, a good catalyst should have the essential criteria such as efficient active centers for the adsorption of the reaction species, high electronic conductivity which enables the electron transfer through the catalyst, and the structural integrity to withstand the harsh reaction conditions. Also, the catalyst materials should be cost-effective for improving the commercialization prospects in developing cost competitive electrochemical energy devices. In this regard, the development of the 3D carbon

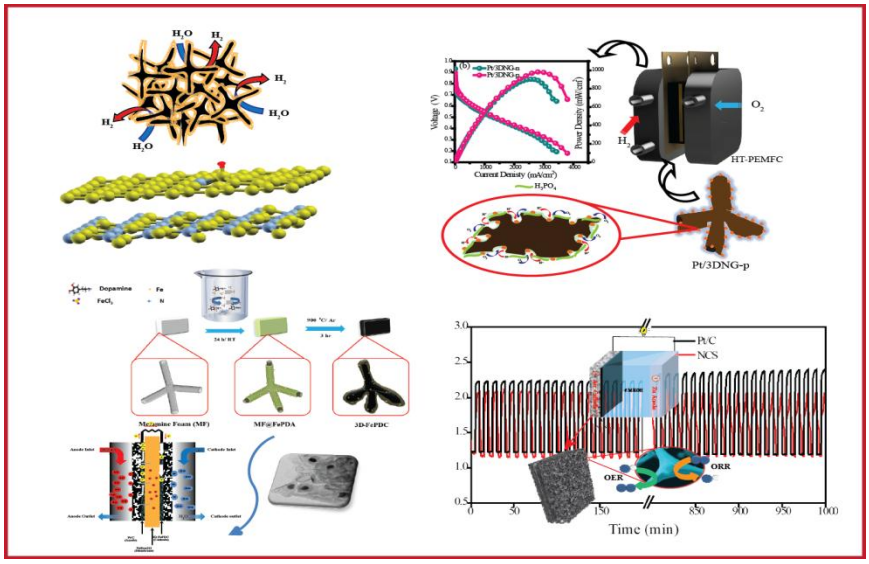

morphologies consisting of graphene and graphitic carbon are playing a vital role. A systematic literature survey was conducted, and efficient synthetic protocols were designed for the development of the catalysts which can offer high activity and low-cost. The prepared catalysts have the potential to replace the *state-of-the-art* electrocatalytic systems. The desired morphologies of the catalysts are opted without compromising the electrical conductivity and active surface area. This has been helpful in accomplishing enhanced performance towards the water cycle reactions. The synthesized materials achieved higher electrocatalytic activity by lowering the overpotential associated with the system. Also, the catalysts showed high durability in the reaction conditions which is essential for the long run. The improved performance of the catalyst is analogous to the morphological and structural fine-tuning of the system. The following sections summarize the important findings and conclusions of the various activities performed in realizing the aforementioned targeted goals. Along with the summary of the thesis, a discussion on the future prospects of the thesis work in the development of the electrochemical energy devices is included at the end of this chapter.

The major accomplishments of the thesis work are summarized below:

Nitrogen-Doped Graphene with Three-Dimensional Architecture Assisted by Carbon Nitride Tetrapods as an Efficient Metal-Free Electrocatalyst for Hydrogen Evolution

This work explains a new strategy to achieve higher hydrogen evolution activity in acidic media by a metal-free system. A simple approach is adopted to synthesize a three-dimensional (3D) nanostructure (CN_x@N-RGO) consisting of the nitrogen-doped graphene (N-RGO) layers distributed on the interconnected arms of the carbon nitride (CN_x) tetrapods, which acts as an efficient catalyst for the electrochemical hydrogen evolution reaction (HER). The metal-free catalyst has very low overpotential for HER, which is lower than that reported for the other metal-free catalysts and some metal-based catalysts. To understand the nature and activity of the active sites in the present system, DFT calculation was performed to support the experimental observations. The key aspects of the work are listed below:

- The synthesis of the catalyst involves simple two-step processes. The melamine foam acts both as a nitrogen source for doping the graphene layer and template for the construction of the 3D interconnected framework structure. The bilayer structure consists

of nitrogen-doped graphene hanged on the carbon nitride backbone. The 3D morphology with interconnected channels improves the reactant product distribution in the catalyst system.

- CN_x@N-RGO shows hydrogen evolution activity in acidic medium with a low overpotential of 193 mV @ 10 mA cm^{-2}, which is an outstanding value compared to the recent reports on the non-metal systems. The interconnected bilayer morphology of the synthesized catalyst provides more active reaction center density and wrapping of the CN_x tetrapod by N-RGO helps to achieve good electrical conductivity and electrochemical stability.
- The interconnected framework of the N-RGO-wrapped CN_x tetrapod structure ensures active passage of the reactant and product gasses within the system. The different types of the nitrogen formed during the synthesis help in creating the active sites for proton binding for HER. Consequently, this bilayer structure helps for proton capture and subsequent reduction into the hydrogen gas.
- CN_x@N-RGO requires a very low overpotential of 193 mV to attain the benchmark current density of 10 mA cm^2. As per our knowledge, the lowest overpotential for HER in the metal-free catalytic systems is attained for CN_x@N-RGO, and this value is also comparable to that reported on some conventional metal catalysts as well.
- CN_x@N-RGO has good intrinsic properties like the high electrochemical surface area and high exchange current density. The hydrogen evolution mechanism in CN_x@N-RGO was evaluated by Tafel slope calculation and it was found that the Volmer-Heyrovsky pathway is responsible for the reduction of the proton to hydrogen.
- The interaction of the moieties in the bilayer structure and the importance of the different types of nitrogen formed in the graphene matrix were evaluated through DFT calculation. The calculation revealed low Gibbs free energy of adsorption (0.16 eV) of the proton in CN_x@N-RGO, which is closer to the commercial Pt catalyst (0.09 eV).

***In situ* preparation of ionomer as a tool for triple-phase boundary enhancement in 3D graphene supported Pt catalyst**

This work deals with the development of a 3D support morphology for anchoring of Pt nanoparticles. The developed catalyst in combination with an *in situ* ionomer preparation

strategy helps in enhancing the active material utilization when used as the cathode in a high-temperature PEM fuel cell (HT-PEMFC). An interconnected network of the nitrogen-doped 3D graphene (3DNG), which was prepared by using melamine as a template, was used as the support morphology for anchoring of the Pt nanoparticles (Pt/3DNG). The Pt/3DNG catalyst shows high intrinsic activity for oxygen reduction reaction (ORR) in acidic medium. The electrode prepared with Pt/3DNG catalyst with the newly adopted *in situ* ionomer preparation strategy outperformed the conventional ionomer-based membrane electrode assembly (MEA) in the real-cell application. The noticeable features of the work are listed below:

- The catalyst development involves simple two-step processes. The 3D interconnected framework graphene (3DNG) was synthesized by using melamine foam as the template. The anchoring of the Pt nanoparticles over 3DNG was achieved in the next step by the polyol method. The significance of the support morphology on the performance of the catalyst was evaluated by a comparative study with two other catalysts which are prepared by using N-doped graphene (Pt/NRG) and Vulcan carbon (Pt/VC) as the support material.
- Pt/3DNG shows higher ORR activity in acidic environment with a halfwave potential ($E_{1/2}$) of 0.846 V *vs* RHE, which is substantially higher than that of Pt/VC (0.817 V) and Pt/NRG (0.795 V). Also, due to better exposure and uniform distribution of the Pt nanoparticles, Pt/3DNG recorded higher ECSA value (62.4 $m^2\ g^{-1}$) than that of Pt/VC (56.7 $m^2\ g^{-1}$) and Pt/NRG (51.3 $m^2\ g^{-1}$).
- The existing issues related to the stability of the catalysts such as carbon corrosion and leaching out of Pt from the substrate surface could overcome by the use of the 3DNG support. The Pt/3DNG survived the accelerated durability test (ADT) with a low negative shift of 23 mV in $E_{1/2}$ after 5000 cycles due to a controlled interplay of the morphological parameters. On the other hand, VC in Pt/VC is prone to high carbon corrosion, whereas NRG in Pt/NRG is susceptible to restacking of the catalyst layers. Hence, these two systems show a greater rate of fall in $E_{1/2}$ during the course of ADT.
- Pt/3DNG with its 3D aligned morphology and exposed Pt active sites becomes a more dynamic system compared to its counterpart systems which have inherent limitations imposed by the support morphologies. The high intrinsic activity is acquired by the morphological advantage of the support structure, which could give features like better

exposure and uniform size distribution of the Pt nanoparticles as well as the more exposed and accessible nature of the active sites. Also, Pt/3DNG meets the features and requirements to effectively serve as a cathode catalyst for the high-temperature polymer electrolyte membrane fuel cell (HT-PEMFC).

- The realistic system level validation of the Pt/3DNG catalyst has been performed by testing a single cell of high temperature PEMFC (HT-PEMFC). The electrode fabrication was performed by adopting the newly developed *in situ* ionomer preparation method over the conventional process which uses the Nafion ionomer. The UV-light induced free-radical polymerization resulted into *in-situ* generation of a fluorine-free ionomer with entrapped H_3PO_4 moieties. This strategy helped to infiltrate the ionomer into the interstitial space created by the 3D morphology of the catalyst by maintaining a fairly uniform catalyst-ionomer interface.
- The single-cell analysis of the membrane electrode assembly (MEA) based on the Pt/3DNG catalyst as the cathode with the *in situ* formed ionomer interface (Pt/3DNG-p) resulted to a peak power density of 982 mW cm^{-2}, which is higher than that obtained from the Nafion ionomer based MEA (860 mW cm^{-2}). The higher mass transport efficiency of the Pt/3DNG-p system helped to achieve excellent performance in the working conditions. Further, the activity tuning achieved through the *in situ* ionomer generation protocol could be confirmed from the measured low charge transfer resistance of the Pt/3DNG-p based MEA (0.007 Ω) over the one based on Pt/3DNG-n, which contains Nafion as the ionomer (0.010 Ω).

Three-Dimensionally Interconnected Graphitic Carbon Enriched with Iron Carbide Core-Shell Particles as a Highly Active Electrocatalyst for Oxygen Reduction Reaction in Acidic and Alkaline Media

This work explains the development of a 3D non-precious metal catalyst which displayed high performance for ORR in acidic medium and alkaline media. A template assisted synthesis strategy was adapted to prepare the interconnected bilayer structure consisting of the carbon nitride backbone wrapped by the graphitic carbon layer which holds the incorporated iron carbide particles (3D-FePDC). The prepared non-precious metal-based catalyst has shown excellent activity for ORR in both acidic and basic media. The single-cell of a PEMFC

constructed by using 3D-FePDC as the cathode catalyst delivered a maximum power density of 278 mW cm^{-2} by displaying the characteristic current-voltage polarization feature. The major highlights of the work are listed below:

- The catalyst synthesis involved a two-step process. The polydopamine with the iron precursor was anchored over the melamine foam, which was annealed at 900 ^{o}C at an argon atmosphere for the graphitization of the material. Thus formed catalyst possesses a bilayer architecture based on the 3D interconnected carbon nitride tetrapods wrapped by a layer of nitrogen-doped graphitic carbon enriched with the iron carbide core-shell particles. The complete wrapping of the graphitic carbon layer ensures the retention of the 3D morphology without leading to crumbling of the structure during the annealing process.

- The interconnected 3D architecture of the catalyst system provided morphological advantages in terms of more exposure of the active sites and mass transfer. The catalyst recorded a higher BET surface area of 1027.8 m^2 g^{-1} which is nine fold higher than its 2D counterpart system prepared without using a melamine foam template. Also, the 3D morphology helped the catalyst to expose more active sites towards the reaction interphase along with the advantage of offering improved mass diffusion in the system.

- The 3D-FePDC catalyst displayed ORR activity in both the acidic and basic media. In the acidic medium, it shows an overpotential of 60 mV compared to that of the *state-of-the-art* Pt/C catalyst. However, in the basic medium, the system displayed improved performance with an overlapping ORR feature of the Pt/C catalyst. In both the pH conditions, the material displayed high durability and structural integrity.

- The active sites created by the iron coordination and nitrogen doping helped the 3D-FePDC system to attain high electrochemical activity. The morphological advantage also helped the system to attain high performance by facilitating reactant and product diffusion. Thus, the morphological and structure tuning inherited in the system makes it an active and viable catalyst system to perform ORR in a better way.

- Finally, the system level validation of the catalyst could be performed by fabricating a single cell of a PEMFC with 3D-FePDC as the cathode in the MEA. The MEA recorded

a maximum power density of 278 mW cm^{-2} in the current-voltage polarization plot which possesses the characteristic features.

$NiCo_2O_4$ Nanoarray on CNT Sponge: a Bifunctional Oxygen Electrode Material for Rechargeable Zn-Air Battery

A highly efficient bifunctional catalyst for ORR and oxygen evolution reaction (OER) was synthesised and used as an air electrode in a rechargeable Zn-air battery. A template-assisted synthesis strategy was adapted to prepare the 3D interconnected nanostructure (NCS) consisting of $NiCo_2O_4$ nanoarray over the CNT modified melamine foam. The precious metal-free catalyst has shown low overpotential for both ORR and OER in alkaline medium. The system level demonstration of the catalyst could be performed by the fabrication of the rechargeable Zn-air battery. The Zn-air battery constructed with NCS outperformed the *state-of-the-art* system both in terms of performance and stability. The key aspects of the work are listed below:

- The synthesis of the catalyst involves a simple two-step process. The melamine foam is used as a template for the construction of the 3D interconnected framework. The catalyst possesses a three-layer structure which consists of the melamine foam backbone, CNT layer wrapping and $NiCo_2O_4$ array over it. The CNT layer gives the electronic conductivity to the system, which helps to grow the third layer of $NiCo_2O_4$ nanoarray over it. The 3D morphology with the interconnected channels with the $NiCo_2O_4$ nanoarray on the surface improves the reactant product distribution with its enhanced interface structure.
- NCS shows the OER activity in basic medium with a low overpotential of 300 mV @ 10 mA cm^{-2}, which is further brought down to 280 mV by the use of the 3D electrode. The overpotential of the NCS electrode is lower than the other recent reported systems. The interconnected 3D morphology of NCS provides more active reaction centre density, which is found to be playing a major role in lowering the overpotential associated with OER.
- The NCS catalyst also has shown better ORR activity in the same basic medium. It suffers only 80 mV overpotential compared to the *state-of-the-art* Pt/C system. The overall oxygen electrode activity (OEA) of the catalyst was calculated by comparing the OER and ORR activities. The OEA overpotential of the NCS electrode is 0.83 V, which

is lower than that reported on the commercial RuO_2 and Pt/C systems; OEA of the commercial RuO_2 and Pt/C was calculated to be 0.87 and 0.92 V, respectively.

- The enhanced activity of the catalyst is credited to its three-layer structure. The backbone structure provides the 3D interconnected morphology and this architectures helps the system to improve the passage of the reactants and products in the electrode matrix. At the same time. The CNT layer gives electronic support to the $NiCo_2O_4$ layer, which accelerates the rate of the intermediate reaction by assisting electron donation. Further, the outer layer of $NiCo_2O_4$ provides the active sites for binding the reactant species on the catalyst surface.
- NCS has good intrinsic properties like the high electrochemical surface area and high exchange current density. RRDE technique was used to calculate the faradaic efficiency of OER and intermediate formation of ORR. All these analyses support the excellent bifunctional activity of NCS. Apart from the bifunctional activity, NCS shows high stability in basic medium towards the corrosive oxygen electrode reactions.
- Real-life application of the bifunctional catalyst could be validated by fabricating a rechargeable Zn-air (ZAB) battery with the NCS coated air electrode. The ZAB possessing the NCS electrode outperformed the system based on the Pt/C electrode with a higher energy density of 706 Wh kg^{-1} against 686 Wh kg^{-1} recorded for the later one. The NCS based ZAB has a low charge-discharge voltage gap (0.89 V), which is retained even after the 1000 charge-discharge cycles. However, in the case of the cell based on the commercial electrode, the voltage gap was found to be increased and reached to 1.18 V from the initial value of 0.96 V.

Future prospects

The 3D carbon morphologies developed in this thesis work have the great potential to contribute to the sustainable energy production. The catalysts prepared have shown exceptional activity for the electrochemical water cycle reactions and they possess significant structural advantages of improving mass diffusion along with high performance. The practical complexities that existed in the *state-of-the-art* systems could be overcome up to a major extent by the current catalyst development. The cost-effective synthesis strategies and high durability make them more fascinating towards the realistic system level explorations. The catalyst prepared in Chapter 2

showed high activity for HER in acidic environment. However, the catalysts that can perform the counter OER reaction in acidic medium are still under development stage, which makes the development of the proton exchange membrane water electrolyzer more challenging. Also, the performance of the above catalysts in the other reaction media is not that much encouraging. In the prospect of commercialization, the catalysts that are giving HER activity in neutral pH or saline water are more interesting. In this context, the catalyst prepared in Chapter 2 can further be tuned by decorating suitable active species over its matrix to get desired performances in a wide range of the pH conditions. The morphology of this catalyst is one of the advantages favouring its application in the water electrolyzer. The catalyst by retaining the same morphology with added up active centres is expected to be a good choice for the generation of H_2 for industrial purposes.

Pt decoration on the 3D graphene proved itself as a good catalyst for the PEMFC cathode application. The 3D graphene could overcome the existing issues related to the stability of the carbon support. The *in situ* ionomer strategy adopted during the electrode fabrication helped to achieve enhanced Pt utilization during the PEMFC operation. This method can be extended to the other catalytic systems where it is a challenge to establish the triple phase boundary. Also, the as prepared *in situ* ionomer holds H_3PO_4, which finds a solution for the electrolyte flooding issue in HT-PEMFCs. The development of an MEAs based on the *in situ* ionomer generation strategy is expected to increase the efficiency of HT-PEMFCs in future. The 3D-FePDC prepared in Chapter 4 has shown overlapping performance with the *state-of-the-art* Pt/C catalyst in basic medium. It can be used in the commercial fuel cells by replacing the expensive Pt catalyst with an aim to improve the cost competitiveness of PEMFCs in the energy market. However, due to the low ionic conductivity and stability limitations of the anion exchange membranes (AEMs), successful demonstration of such a highly active catalyst in alkaline medium is still challenging. Hence, AEM research should be focused more to utilize the low-cost catalysts that are active in the basic medium.

The metal-air batteries have gained significant attention as a potential candidate in the path of sustainable energy development due to their high energy density. The 3D bifunctional catalyst prepared in Chapter 5 proved that it could improve the mass diffusion characteristics in the catalyst matrix which leads to up-gradation in the performance of the system. However, if we

want to explore such materials in the next-generation electronic applications, the mechanical flexibility of the battery is going to be an important factor of consideration. The prepared catalyst with the interconnected structure could be used as an air electrode; however, the lack of a flexible anion conducting solid electrolyte withholds the further development potential of realizing the flexible rechargeable air-breathing batteries.

The present dissertation is focused on the development of the catalytic or electrode part of the electrochemical energy devices such as water electrolyzer, PEMFC and Zn-air battery. The absence of concomitant developments in the other critical components required for bringing in futuristic features in the next generation energy devices hinders further exploration of the developed systems to effectively utilize their application potential. With more advancements in the development of the other critical components in future, the prepared catalysts and electrodes in this study are expected to achieve new space for many advanced applications.

List of Publications

1. Nitrogen-Doped Graphene with a Three-Dimensional Architecture Assisted by Carbon Nitride Tetrapods as an Efficient Metal-Free Electrocatalyst for Hydrogen Evolution. **Gangadharan, P. K.**; Unni, S. M.; Kumar, N.; Ghosh, P.; Kurungot, S., ***ChemElectroChem 2017, 4 (10), 2643-2652***.

2. $NiCo_2O_4$ nanoarray on CNT sponge: a bifunctional oxygen electrode material for rechargeable Zn–air batteries. **Gangadharan, P. K.**; Bhange, S. N.; Kabeer, N.; Illathvalappil, R.; Kurungot, S., ***Nanoscale Adv. 2019, 1 (8), 3243-3251***.

3. In situ preparation of ionomer as a tool for triple-phase boundary enhancement in 3D graphene supported Pt catalyst. **Gangadharan, P. K.**; Vijayakumar, V.; Nediyirakkal, S. A.; Fernandez, R. T.; Siddharthan, A.V.; Kurungot, S., ***Adv. Sustain. Syst. 2021, 5 (1), 2000125.***

4. Toward pH Independent Oxygen Reduction Reaction by Polydopamine Derived 3D Interconnected, Iron Carbide Embedded Graphitic Carbon. **Gangadharan, P. K.**; Pandikassala, A.; Kurungot, S., ***ACS Appl. Mater. Interfaces* 2021, *13* (7), 8147-8158.**

5. Layer-separated distribution of nitrogen doped graphene by wrapping on carbon nitride tetrapods for enhanced oxygen reduction reactions in acidic medium. Unni, S. M.; Illathvalappil, R.; **Gangadharan, P. K.;** Bhange, S. N.; Kurungot, S., ***Chem. Commun., 2014, 50 (89), 13769-13772.***

6. High-index faceted Au nanocrystals with highly controllable optical properties and electrocatalytic activity. Rajendra, R.; **Gangadharan, P. K.**; Tripathi, S.; Kurungot, S.; Ballav, N., ***Nanoscale 2016, 8 (46), 19224-19228***.

7. Cubic Palladium Nanorattles with Solid Octahedron Gold Core for Catalysis and Alkaline Membrane Fuel Cell Applications. Singh, P.; Sonika; **Gangadharan, P. K.**; Khan, Z.; Kurungot, S.; Jaiswal, A., ***ChemCatChem 2019, 11 (17), 4383-4392***.

8. Wet-Chemical Deposition of Pt on Au Nanocrystals: The Ag Lining. Roy, D.; Rajendra, R.; **Gangadharan, P. K.**; Kurungot, S.; Ballav, N., (***Manuscript communicated***)

9. Polydopamine Derived Iron Doped Hollow Carbon Nanorods for Simultaneous Generation of Hydrogen and Electricity. Pandikassala, A.; **Gangadharan, P. K.**; Kurungot, S., (***Manuscript under preparation***)

Erratum